# Modelling and simulation of fluid-saturated granular materials with application to sedimentation flows

DAVIDE MONSORNO

THESIS PRESENTED AS PART OF THE REQUIREMENTS FOR THE PHD DEGREE IN ENGINEERING SCIENCES (SCIENCES DE L'INGÉNIEUR)

*Institut de Mécanique, Matériaux et Génie Civil*
*Université catholique de Louvain*

| | |
|---|---|
| *advisors* | PROF. M.V. PAPALEXANDRIS |
| | PROF. A.A. DIMAS |
| *jury committee* | PROF. A. HOLEYMAN *(president)* |
| | PROF. S. SOARES FRAZAO |
| | DR. B. SPINEWINE |
| | DR. C. VARSAKELIS |

UCL
Université catholique de Louvain

**Abstract**

This PhD thesis is concerned with the continuum modelling of fluid-saturated granular mixtures, with particular emphasis on constant-density stratified flows. It tackles the theoretical description of these mixtures (which are treated as non-Brownian granular suspensions), the development of suitable computational algorithms and the simulation of flows of interest.

The first Chapter of this thesis contains a brief introduction to suspension modelling, and delineates its application to a continuum description of sedimentation processes. The motivation for this work is presented and the final objectives are discussed.

In the second Chapter, test problems of granular transport are studied with the help of a recently-developed two-phase continuum model. More specifically, this Chapter concerns channel flows over compacted granular beds. The predictive capabilities of the model and its limits are investigated; particular attention is devoted to the evolution equation for the volume fraction, which is of primary importance in the description of sedimentation and erosion phenomena.

The third Chapter is concerned with the derivation of a new model for two-phase flows of granular suspensions. This model, which is based on a generalization of the classical theory of irreversible processes, is developed in order to account for a number of physical phenomena that are of particular relevance to granular transport; notably, it accounts for compaction, which has a profound impact on granular rheology.

The fourth Chapter presents the application of the newly-derived model to channel flow at low-Reynolds number. This flow is chosen as a benchmark since particle migration plays a crucial role in the definition of its particle-concentration profile. Numerical results are compared with existing experimental measurements and particle-resolved simulations, finding good agreement. Further, the role of intergranular and nonlocal stresses in particle migration is investigated.

The fifth Chapter describes the derivation of a general numerical algorithm, based on a two-phase fractional-step projection method, which can be applied to the governing equations of the proposed flow model for the description of unsteady multi-dimensional flows. The specific numerical challenges presented by the new equations are discussed and a suitable treatment is proposed.

The sixth Chapter presents numerical results relative to sedimentation processes. First, the sedimentation and settling of a suspension into a granular bed is investigated in order to validate the particle-migration model. Subsequently, computations are presented relative to the collapse of a granular column submerged under water. This flow is used to validate the modelling of suspension rheology, and further to provide insight into a benchmark flow for applications involving granular transport due to gravity.

# Acknowledgments

This work is the result of a four-year research period at Universitè catholique de Louvain, performed as part of the requirements for a PhD degree in Engineering Sciences. Financial support was provided by the European Commission and by Université catholique de Louvain, through the Marie Curie FP7 project SEDITRANS (grant agreement no. 607394) and the FSR-2016 UCL project *"modèlisation et simulation des milieux granulaires saturès par un fluide appliquèes au transport des sèdiments"*.

I was able to accomplish this work with the help and support of many people, and to all of them I express my gratitude, apologizing in advance in the event that I forget to mention somebody. To begin with, I would like to thank my advisor, Prof. Miltiadis Papalexandris, for his guidance and support during my research. His integrity, scientific rigor and work ethics have been a constant example to me, and I am grateful for the opportunity of participating in his research group.

My sincere thanks go to my co-advisor, Prof. Athanassios Dimas; I am elated to have spent a visiting period in his group at the University of Patras, which contributed greatly to the material presented in this work. In addition, I would like to thank Prof. Sandra Soares-Frazao and Dr. Benoit Spinewine, who supervised my PhD program as members of the doctoral committee, and with whom I had the pleasure of interacting extensively through the SEDITRANS network. I am also thankful to Prof. Alain Holeyman for accepting the role of president of the jury committee and for his constructive comments on the initial manuscript.

The collaboration with colleagues is instrumental for a fruitful scientific activity; I am indebted to Dr. Christos Varsakelis, who mentored me during my first years of research and happily endured a never-ending stream of questions on various aspects of mathematical physics. In addition, I am grateful to Dr. Michail Georgiou, Dr. Panagiotis Antoniadis, Dr. Holger Grosshans and Mr. Christian Schmitz for their patience and encouragement, and further to all my colleagues at UClouvain, at UPatras and in the SEDITRANS network.

Finally, I must acknowledge the support of my family and friends, which did not falter in spite of my stroboscopic appearances at home over the years. When crunch time comes, doctoral students tend to differ from tolerable people; luckily I could count on my friends at Fight Off to keep me in line and further on Chantal, who can be much scarier than them independently of the color of their belt.

Davide Monsorno
Louvain-la-Neuve, January 2018

# Contents

# List of Figures

# Notation

| | |
|---|---|
| 1.1.1 | Numbers separated by dots denote Chapters, Sections and Subsections |
| (1.1) | Numbers inside parentheses denote Equations |
| $\hat{}$ | The hat superfix denotes dimensional quantities |

| | |
|---|---|
| $T_f$ | temperature of the fluid phase |
| $T_s$ | temperature of the granular phase |
| $e_f$ | specific internal energy of the fluid phase |
| $e_s$ | specific internal energy of the granular phase |
| $e_f^t$ | specific total energy of the fluid phase |
| $e_s^t$ | specific total energy of the granular phase |
| $p_f$ | pressure of the fluid phase |
| $p_s$ | pressure of the granular phase |
| $q_d$ | auxiliary pressure of the granular phase |
| $q_f'$ | auxiliary pressure of the fluid phase |
| $s_f$ | specific entropy of the fluid phase |
| $s_s$ | specific entropy of the granular phase |

| | |
|---|---|
| $\beta_s$ | integranular stress |
| $\gamma_s$ | scalar coefficient for the nonlocal stresses of the granular phase |
| $\delta$ | interphasial drag coefficient |

| | |
|---|---|
| $\zeta_f$ | second (bulk) viscosity coefficient of the fluid phase |
| $\zeta_s$ | second (bulk) viscosity coefficient of the granular phase |
| $\mu_c$ | compaction viscosity coefficient of the granular phase |
| $\mu_f$ | first (shear) viscosity coefficient of the fluid phase |
| $\mu_s$ | first (shear) viscosity coefficient of the granular phase |
| $\rho_f$ | density of the fluid phase |
| $\rho_s$ | density of the granular phase |
| $\phi_f$ | volume fraction of the fluid phase |
| $\phi_s$ | volume fraction of the granular phase |
| $\chi_a$ | coefficient in the nonlinear viscous stresses of the granular phase |
| $\chi_b$ | coefficient in the nonlinear viscous stresses of the granular phase |
| $\psi_f$ | specific Helmholtz free energy of the fluid phase |
| $\psi_s$ | specific Helmholtz free energy of the granular phase |

| | |
|---|---|
| $\mathbf{g}$ | gravity acceleration |
| $\mathbf{h}_s$ | vector coefficient for the nonlocal stresses of the granular phase |
| $\mathbf{u}_f$ | velocity of the fluid phase |
| $\mathbf{u}_s$ | velocity of the granular phase |

| | |
|---|---|
| $\mathbf{C}_s$ | configuration stress tensor of the granular phase |
| $\mathbf{V}_f$ | strain-rate tensor of the fluid phase |
| $\mathbf{V}_s$ | strain-rate tensor of the granular phase |
| $\mathbf{V}_f^d$ | deviatoric part of the strain-rate tensor of the fluid phase |
| $\mathbf{V}_s^d$ | deviatoric part of the strain-rate tensor of the granular phase |

# Chapter 1

# Introduction

## 1.1 Properties of granular materials

This thesis is concerned with the description of granular materials, defined as conglomerates of solid particles that present dissipative interactions [1]. An important characteristic of these materials is that they generate an extremely rich and unexpected phenomenology even when the physics of particle interaction at the granular level are well understood; one can for instance observe segregation, jamming, dilatancy. In fact, their behaviour at the macroscopic scale can be so different from what is common for liquids and solids, that it has been proposed to consider the granular state as a new state of matter [2].

Solid matter is often present in granular form, both in industrial environments and in nature, where it typically originates from mechanical fracturing of fragile materials such as rocks. As a matter of fact, the industrial processing of grains constitutes approximately 10% of the global energy consumption [1], and granular aggregates are the second most manipulated material after water [3].

Due to the rich phenomenology that granular materials present and because of the wealth of potential applications, different fields of research have been dedicated to the study of specific aspects of granular matter. This effort has generated an impressive body of literature which spans over a century since the appearance of seminal works such as the treatment of dilatancy due to Reynolds [4]. However, in spite of the attention received, an unequivocal theory remains elusive, with a direct impact on human activities: nearly 40% of the industrial capacity of transport and storage of granular materials is lost due to poorly developed theory [5].

A primary obstacle towards the development of a comprehensive framework is that problems related to granular matter can cover an extremely wide range of sizes, shapes, mechanical and chemical properties; as a result it is often difficult to determine *a priori* which physical phenomena are to be modeled and which can instead be neglected. In the case of small particles in air, for instance, electrostatic effects due triboelectric charging can play a significant role [6, 7]. For particles mixing with water, surface wetting is a complex phenomenon that can increase cohesion or result in the entrainment of air [8].

## 1.2 Modelling of granular suspensions

In most problems of practical interest, granular materials are immersed in a carrier fluid phase such as air or water. Even for dry compacted grains, the presence of air can seldom be neglected outside of statics [9–12]. In the presence of a dense liquid phase such as water, particle interactions are always fluid-mediated. The presence of a carrier fluid tends to increase the mobility of the granular phase, so that natural flows of sediment, which involve particle transport, generally concern suspensions in water. Conversely, combining particles with a fluid provides a practical way of transporting and handling granular matter; examples include the production of slurries, suspensions and pastes in the context of energy production, coatings, fluidized-bed reactors, pharmaceutical and agricultural processing. The picturesque example of a dredging ship in operation at sea is shown in Figure 1.1.

Figure 1.1: The Vasco Da Gama suction-dredging ship in operation. Dredging consists in the aquatic excavation of a granular bed; the increased fluid content of the mobilized sediment allows to easily manipulate it as a fluid.

This work is concerned with fluid-saturated granular materials; these can be seen as heterogeneous mixtures of two or more phases, consisting of solid particles in a fluid. In the case, common in applications, that particles are large enough for sedimentation, these mixtures can be classified as suspensions [13].

Focusing on suspensions allows for a great simplification of the flow physics; for example, electrostatic charging can typically be neglected for suspensions where the carrier fluid is water. Furthermore, the fact that particle interactions are fluid-mediated reduces the importance of the mechanical properties of the solid particles. Nevertheless the physics of suspensions is deceptively simple; for instance, even smooth rigid spheres exhibit a markedly non-Newtonian behaviour when they are suspended in a Newtonian liquid [14–16]. In addition, the range of possible flow conditions is still wide; the particle size and the properties of the carrier fluid can change over orders of magnitude, with a profound impact on the flow physics. As an example, Brownian motion typically becomes observable for particles below the micron scale; an entire field of research is dedicated to the study of these fine suspensions, which border on colloidal behaviour [17, 18]. In this respect, in view of the multitude of different definitions used in the literature, a clarification is made: the work presented in this thesis is concerned with non-Brownian suspensions in a Newtonian fluid, which are henceforth referred to as *granular suspensions*.

Flows of granular suspensions can differ sharply from flows of simple fluids: these mixtures can support shear stress at equilibrium, compact, clog, segregate, collapse in avalanches etc. Because of this complexity a considerable effort has been made towards their modelling, both from a discrete-element perspective and from the continuum point of view.

Discrete-element modelling has progressed to the point that significant insight can be gained into the rheological properties of flows at the laboratory scale [19–21]. However, the computational cost of particle-resolved discrete-element methods is currently far too high to model flows of practical interest. Moreover, even particle-resolved methods require a model for the short-range "lubrication" interactions that mediate contact between particles. The role of short-range interactions, which are known to play an important part in loss of reversibility and dissipation, is not completely clear yet [22–24].

A continuum description is often sufficient in applications, where one is not interested in the kinematics of single particles and all that is needed is global information. Continuum models can be derived either as limits of of kinetic theories, or alternatively via an axiomatic mixture-theoretic approach that treats the suspension as a multi-component continuum. In kinetic-theory-based modelling, spatial averaging is used in order to obtain expressions for the macroscopic variables [25]. An advantage of this approach is that it is based on first principles and, therefore, requires few initial postulates; the principal drawback is the necessity of modelling particle interactions, which is often performed in a rudimentary way. Moreover the averaging process relies on assumptions that are sometimes questionable. Mixture theories, on the other hand, derive balance equations for each phase by leveraging the entropy inequality, which expresses the second principle of thermodynamics [26–30]. This approach has the advantage of providing governing equations in a straightforward and elegant way; its limitations are scale-related, as the continuum hypothesis requires the length scale of the problem to be much greater than the particle size, cf. Figure 1.2. A self-contained presentation of both approaches can be found in [31] and [32].

Figure 1.2: A static pile of potatoes which is at the edge of applicability of continuum modelling: the position of a single potato is not fundamental for a global description of the geometry, yet the length scale corresponding to the diameter of a potato is still appreciable compared with the dimensions of the pile.

## 1.3 Application to sedimentation processes

A thorough understanding of the mechanisms of granular transport is a fundamental step towards the accurate modelling of flows which are stratified due to sedimentation, such as the geophysical flows describing the evolution of fluvial, lacustrine and coastal morphology. This type of flows typically involves mineral sediments and water, with the implication that grains are significantly denser than the fluid phase and tend to settle under gravity. As a result, these flows are generally stratified and present a lower dense region surmounted by a dilute region which is mainly occupied by the fluid phase; these regions are sometimes denoted as granular bed and fluid-flow region, respectively.

Motion inside the granular bed is limited as the grains are densely packed; in the fluid-flow region far from the bed, on the other hand, the particle concentration tends to be low due to gravity (which promotes sedimentation). As a result, if the water depth is sufficiently high, sediment transport is often limited to a layer close to the interface between the two regions. This transport layer is further subdivided in bed load, which represents a thin dense layer flowing over the interface, and suspended load, which refers to the particles kept in suspension by turbulence in the fluid-flow region [33].

This type of schematic description, which Figure 1.3 illustrates in a laboratory setting, has been the basis of a great number of research efforts aimed at characterizing the mechanisms of sediment transport. For bedload, classical approaches consider a single phase of clear water flow, coupled with an equation for bed evolution which employs empirical relations to compute the rate of sediment transport [34–36]. For suspended load, the theoretical framework of Rouse provides a description in equilibrium conditions [37]; this framework

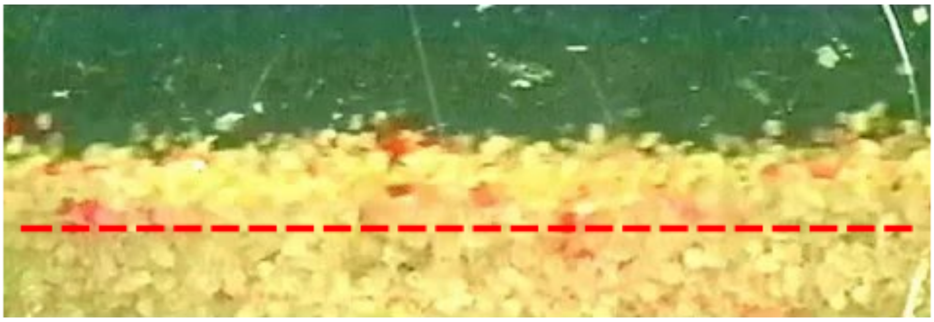

Figure 1.3: Granular transport over a compacted bed in a laboratory flume; suspended particles in the fluid-flow region are visible. In addition, the top half of the granular bed appears blurry in the picture since it is in motion; this corresponds to bedload transport. The red line marks the approximate depth of the mobile region. Image from a video of prof. G. Parker, University of Illinois.

has been used to develop a wide range of transport formulae. From a global perspective, however, there is no agreement on a general sediment transport formula to be adopted in numerical simulations [38].

More recently, the development of detailed rheological models for two-phase suspension flows has encouraged new modelling efforts towards a more detailed investigation of the transport layer [39–42]. This different approach, which aspires to develop a full-field continuum description of sediment transport, is supported by experimental observation suggesting that in many cases there is a smooth transition between the granular bed, the bed load and the fluid-flow region; in particular, one can observe particle suspension and sediment transport in laminar flow [43, 44].

As an example, the authors of [39] analyzed laminar flow with a two-phase suspension model. Their approach is based on the locally-averaged flow equations derived in [45], which are applicable to general three-dimensional flow; nevertheless, the analysis focuses on one-dimensional flow, as it exploits the specific flow structure. The authors tested different constitutive models for the stresses of the granular phase, including a Coulomb friction model and a more sofisticated inertial rheology, cf. [46], and were able to match experimental measurements for bed load transport in laminar pipe flow. This approach was extended in [40] to include turbulence modeling; the authors matched a turbulence model for the clear water region with a rheological description of the bed load; assuming a sheet-flow regime, the authors were able to capture the transition between the dense bed and the dilute suspension. A similar analysis was performed by the authors of [41], which relaxed some of the assumptions relative to the flow structure, and investigated the interaction between the bed load and the turbulent flow above it. In particular, they were able to capture the volume-fraction variations inside the bed load.

A full-field description of sediment transport is also desirable since it is the only practical approach to unsteady multi-dimensional flows, where one can not easily take advantage of simplifications due to geometry or flow regime. To this end, more general formulations have been proposed, based on a mixture-theoretic formalism, which are applicable to general flow [26, 47, 48]. While the resulting governing equations are currently too computationally-expensive to be directly applied to large-scale natural flows, these models serve two important functions. To begin with, they can be used to clarify the mechanisms of sediment transport and help develop more accurate correlations to be used in simplified models. In addition, fully-resolved simulations remain the only possible treatment for flows that are inherently three-dimensional. This is the case of many application of engineering interest where one is concerned with the flow around bluff bodies such as piles, locks and pipe outlets, and further of a myriad of natural flows such as those which generated the impressive erosion patterns shown in Figure 1.4.

Figure 1.4: The earth pyramids of Segonzano, Italy constitute a stunning example of three-dimensional erosive process. A number of stones compact and protect the ground below from erosion, resulting in the formation of columns with a maximum height of 40 meters.

## 1.4 Motivation and objectives of this work

The purpose of this thesis is to develop a general full-field flow model for granular suspensions that can be used to investigate the mechanics of particle transport in dense stratified flows and to perform numerical simulations of unsteady multi-dimensional flows. Simulations of unsteady flows at high particle concentration are currently a challenging endeavour, which requires specific assumptions both modelling- and algorithm-wise. The main impetus for the research presented herein is the enticing prospect of a description of particle transport which, on one hand, isolates the fundamental physics of suspension flow inside the transport layer and, on the other hand, avoids the strong modelling assumptions associated with a two-layer description of particle transport. The mixture-theoretic approach used in this work is not new; it is due to two main reasons that it is meaningful to undertake this effort now.

To begin with, a considerable number of experimental studies on the fundamental physics of suspension flow have become available in recent years [49–56]. This development has a direct impact on the derivation of flow models, as one of the main obstacles in this direction is that conclusive validation is unfortunately still difficult: suspensions are complex continua that require a wealth of information to be fully characterized, and it is problematic to provide constitutive relations that are univocally determined on the basis of simple flow experiments. In fact, the description of suspension rheology derived in Chapter 3 of this work has been formulated in light of experimental information [57–59] that was obtained only recently.

The other reason lies in the refinement of modelling ideas in the field of mixture-theory. As an example, models that consider each phase as a separate thermodynamic system have recently clarified the role of phasial-pressure nonequilibrium [26, 60, 61]. Another important development has been the clarification of the incompressible regime for suspensions [62]; it is quite surprising that a thorough consideration of incompressibility, in the form of low-Mach-number asymptotics, can actually provide useful information towards the modelling of dilatancy in constant-density flows of suspensions [63].

In order to attain the desired full-field description of granular suspensions, three primary objectives have to be reached. In particular, this work aims to:

**1)** develop a consistent continuum description of particle migration,

**2)** integrate a nonlinear rheology into the continuum formalism of mixture theory,

**3)** provide a numerical algorithm that can be used to study granular transport.

With respect to the first objective, it is important to notice that sedimentation and erosion processes inherently involve divergent flow, in the sense that the velocity fields of both the fluid and the particulate phases are not solenoidal (even though the velocity of the suspension is); this is an important aspect to be considered when modelling the evolution of the particle concentration. In particular, a theory that aims to provide a general description of sediment transport must necessarily deal with sediment suspension or deposition in the region between the granular bed and the fluid flow; these processes entail a non-solenoidal velocity field.

With respect to the second objective, one must take into account that in non-solenoidal flows normal stresses have a direct impact on the divergence of the velocity field, and consequently on the evolution of the particle concentration. Further, it is known from experiments that granular suspensions can exhibit dilatancy, developing viscous normal stresses as a response to shear (deviatoric) deformation [4]. Because of its potential influence on the evolution of the particle concentration, this non-Newtonian phenomenon has to be considered in detail; in fact there are flows where the non-Newtonian stresses are of primary importance, such as the low-Reynolds-number Poiseuille flow considered in Chapter 4. The determination of the functional dependence of the viscous stresses on the strain-rate has been the objective of a wealth of studies that rest on a wide body of experimental measurements, cf. also Section 3.1. This work aims to develop a thermodynamically-consistent formulation of suspension rheology which conforms with available experimental data, while resting on general physical assumptions which do not depend on a specific experimental geometry.

With respect to the third objective it is important to mention that a number of specific numerical challenges arise due to the fact that sedimentation is associated with non-solenoidal velocity fields for both the liquid carrier and the granular phase. In particular, popular algorithms developed for incompressible simple fluids are concerned with solenoidal flows, so that a different numerical treatment is in principle needed here in order to solve the resulting flow equations. Further, since non-Newtonian stresses can influence the divergence of the velocity fields and thus the evolution of the particle concentration, a suitable algorithm must account for the additional coupling displayed by the governing equations. For this reason, this work aims to develop numerical algorithms and procedures that can be applied to the numerical simulation of non-solenoidal constant-density flows.

The structure of this thesis is as follows. In Chapter 2 the two-phase continuum model of [26] is applied to channel flows over compacted granular beds. The numerical predictions of this model are evaluated, and the role of dilatancy with respect to granular transport is discussed. In Chapter 3 a new continuum model for two-phase flows of granular suspensions is developed, with the purpose of providing a more accurate description of granular compaction and dilatancy; this model provides a thermodynamically-consistent continuum description of suspension rheology. Further, equations for the important case of constant-density flow are derived from the low-Mach-number limit of the model. Finally, the model is applied to homogeneous Couette flow, where it is compared with existing modelling approaches. In Chapter 4 the proposed model is applied to channel flow at low-Reynolds number. The numerical predictions are validated against existing experimental measurements and particle-resolved simulations. In addition, parametric studies are performed in order to investigate the role of intergranular and nonlocal stresses with respect to particle migration. In Chapter 5 an algorithm is presented for the numerical solution of the governing equations which is applicable to general flow. This algorithm is based on a two-phase projection method and is tailored on the specific structure of the governing equations. In Chapter 6 the proposed algorithm is used to study example problems involving sedimentation processes; in addition, the collapse of a submerged granular column is studied numerically to provide further validation of the rheological model; the computed results are discussed and the predictions for the final shape of the column are compared with experimental data.

# Chapter 2

# A simple model of particle transport based on mixture theory

## 2.1 Mixture-theoretic modelling of granular suspensions

This work aims to develop a continuum description of granular suspensions which can be employed to perform numerical simulations of sedimentation processes; that is, of flows which exhibit significant concentration variations in time and space due to some external forcing such as gravity. To this end it relies on a mixture-theoretic approach, which considers each phase of a multi-component continuum as coexisting in space: all phases are present at every material point with a specific concentration, expressed by their local volume fraction. Classical mechanics provides local conservation laws for the mass, momentum and energy of each of phase; however additional constitutive relations, describing the material properties of the specific medium and the transport coefficients, have to be introduced in order to obtain a closed system of governing equations.

A non-equilibrium thermodynamic formalism, which exploits the second principle of thermodynamics, can be leveraged in order to constrain the constitutive relations that describe the complex behaviour of multi-phase continua. An important advantage of this type of modelling is that it provides a general framework for deriving constitutive relations, which does not invoke specific phenomenological or geometric assumptions. Depending on the thermodynamic formalism of choice, it is possible to describe a wide range of dissipative phenomena; for instance, the Theory of Irreversible Processes (TIP) has been succesfully employed in applications involving Newtonian flow, Fourier thermal conduction, thermoelectricity, piezoelectricity, thermochemistry etc. [64, 65].

---

The numerical results presented in this Chapter have been published in: C. Varsakelis, D. Monsorno, and M.V. Papalexandris, (2015), "Projection methods for two-velocity, two-pressure models for flows of heterogeneous mixtures", *Computers & Mathematics with Applications*, Vol.70, pp. 1024-1045.

In the case of suspensions, the primary task of mixture-theoretic modelling is describing the evolution of the granular volume fraction. This quantity plays a fundamental role in flows of suspensions and is generally recognized as a separate degree of freedom [27–30, 66–68]. Nevertheless the exact role of this quantity as a thermodynamic variable and, by extension, the form of the compaction equation (which describes the evolution of the volume fraction) are still under debate.

This Chapter discusses the capabilities of a specific model that applies the linearized approach of TIP to granular suspensions and explicitly takes into account the granular volume fraction as a state variable [26]. This approach is an approximation, since it is known that granular suspensions can exhibit non-Newtonian behaviour, with scalings that cannot be captured by a linear theory. Nevertheless, there are important conclusions to be drawn from this modelling effort. In particular, the corresponding governing equations provide a very simple description of granular rheology, which allows to focus on the evolution of the volume fraction. In this Chapter and in Chapter 3 it is shown that an accurate description of the volume fraction is a prerequisite for the development of a general rheological model. This is due to the fact that the viscosity coefficients are functions of the volume fraction and, conversely, to the fact that non-Newtonian stresses can contribute to the evolution of the volume fraction.

This Chapter is structured as follows. Section 2.2 provides a brief description of the flow model of choice for the case of constant-density flow (where the density of the fluid carrier and of the suspended particles can be assumed constant). Section 2.3 presents numerical results relative to fluid flow over compacted granular beds, which were obtained with a numerical algorithm specifically developed for this purpose. Finaly, Section 2.4 discusses the capabilities and shortcomings of the flow model and delineates the fundamental challenges involved with the numerical description of flows which are stratified due to sedimentation.

## 2.2 A two-phase modelling approach

In this Chapter, the model presented in [26] is employed in order to perform a preliminary study of test problems concerning flow over compacted granular beds. This model is a two-phase continuum description, which introduces the granular volume fraction and its gradient as thermodynamic state variables; this is done axiomatically through an extension of the Gibbs relations.

Without entering the details of the derivation, it is simply mentioned that the Gibbs relations provide a formal definition of the specific entropies $s_f$ and $s_s$ for the fluid and granular phases, respectively. Taking the time derivative of these relations and introducing the mass, momentum and energy balances, one obtains two expressions for the entropy production rates $\frac{\mathrm{d}s_f}{\mathrm{d}t}$ and $\frac{\mathrm{d}s_s}{\mathrm{d}t}$ which are constrained by the second principle of thermodynamics. By suitably exploiting this constrain, the model obtains constitutive relations which are used to provide closure for the system of governing equations. In particular, the model predicts a

Newtonian rheology law for both phases and Fourier heat conduction; in addition it provides an equation for the evolution of the granular volume fraction $\frac{\partial \phi_s}{\partial t}$.

### 2.2.1 Governing equations for constant-density flows

The governing equations derived in [26] apply to general compressible flow. However, flows of granular suspensions can often be considered at constant density; this is almost always the case in the context of sedimentation processes, which are typically concerned with solid particles suspended in a liquid. For this reason it is useful to consider simplified equations that are specific to the case of constant-density flow. This derivation is deceptively easy; proper care has to be taken when considering the relative magnitude, or scale, of the various terms in the equations. This is even more critical for granular suspensions when compared to the case of simple fluids, since multiple different scales, representing different physical phenomena, are involved.

One approach towards the specialization of the flow equations to the case of constant-density is to employ the so-called "rescaling method" [69]. This procedure essentially amounts to comparing the scale of the different terms in the equations, which are expanded in series with respect to a small parameter; in this case an asymptotic expansion is performed with respect to the Mach number. For the model proposed in [26], the constant-density limit has been derived in [62]. The resulting flow equations are listed here as reference in non-dimensional form; for a detailed description of the non-dimensionalization procedure the reader is referred to [62].

*Fluid phase*

$$
\begin{aligned}
\nabla \cdot (\phi_f(\mathbf{u}_s - \mathbf{u}_f)) &= 0\,, && (2.1)\\
\rho_f \frac{\partial \phi_f \mathbf{u}_f}{\partial t} + \rho_f \nabla \cdot (\phi_f \mathbf{u}_f \otimes \mathbf{u}_f) + \nabla(\phi_f p_f) &= \frac{1}{\mathrm{Re}} \nabla \cdot (2\mu_f \phi_f\, \mathbf{V}_f^d) \\
&\quad - p_f \nabla \phi_s - \delta\,(\mathbf{u}_f - \mathbf{u}_s) \\
&\quad + \rho_f \phi_f \boldsymbol{g}\,, && (2.2)
\end{aligned}
$$

*Granular phase*

$$
\begin{aligned}
\nabla \cdot \mathbf{u}_s &= 0\,, && (2.3)\\
\rho_s \frac{\partial \phi_s \mathbf{u}_s}{\partial t} + \rho_s \nabla \cdot (\phi_s \mathbf{u}_s \otimes \mathbf{u}_s) + \nabla(\phi_s p_s) &= \frac{1}{\mathrm{Re}} \nabla \cdot (2\mu_s \phi_s\, \mathbf{V}_s^d) \\
&\quad - \nabla \cdot (\gamma_s \nabla \phi_s \otimes \nabla \phi_s) \\
&\quad + p_f \nabla \phi_s + \delta\,(\mathbf{u}_f - \mathbf{u}_s) \\
&\quad + \rho_s \phi_s \boldsymbol{g}\,, && (2.4)
\end{aligned}
$$

*Compaction equation*

$$\frac{\partial \phi_s}{\partial t} + \mathbf{u}_s \cdot \nabla \phi_s \ = 0\,, \tag{2.5}$$

*Saturation relation*

$$\phi_f + \phi_s \ = \ 1\,, \tag{2.6}$$

In the above equations, the subscripts "*f*" and "*s*" denote the fluid and granular phase, respectively. The symbols $p_f$ and $p_s$ represent the "dynamic" pressures of the fluid and granular phases; they are the first-order terms of the pressures with respect to the low-Mach-number expansion, analogously to the pressure term that appears in the incompressible Navier-Stokes equations for a simple fluid. In addition, $\phi_f$ and $\phi_s$ are the fluid and granular volume fractions and $\mu_f$ and $\mu_s$ are the shear viscosities; it can be observed that the model predicts a Newtonian rheology for both the fluid and the granular phases. $\delta$ is the interphasial drag coefficient and $\rho_s$ is the solid density ($\rho_f = 1$ since the reference state used in the non-dimensionalization is relative to the fluid phase). The quantity $\gamma_s$ measures configuration stresses that arise due to concentration gradients. Finally, $\mathbf{u}_s$ and $\mathbf{u}_f$ are the velocity vectors, $\mathbf{g}$ is the gravity vector and $\mathbf{V}^d_\alpha$ stands for the deviatoric part of the strain-rate tensor of phase $\alpha$,

$$\mathbf{V}^d_\alpha \ = \ \frac{1}{2}\left(\nabla \mathbf{u}_a + (\nabla \mathbf{u})^{\mathrm{T}}_a\right) - \frac{1}{3}\nabla\cdot\mathbf{u}_a\,\mathbf{I}, \qquad \alpha = f, s, \tag{2.7}$$

where $\mathbf{I}$ is the identity tensor.

Physically, equations (2.1)–(2.2), and (2.3)–(2.4) describe the balance of mass and of linear momentum for the fluid and the granular phase, respectively. Also, the compaction equation (2.5) governs the evolution of the volume fraction $\phi_s$, whereas (2.6) is the saturation relation which expresses the assumption that the two phases saturate the space.

The combined term $p_f \nabla \phi_s + \delta(\mathbf{u}_f - \mathbf{u}_s)$ which appears, with opposite sign, on the right-hand side of the momentum equations (2.2) and (2.4) represents the momentum exchange between the two phases. More specifically, $\delta(\mathbf{u}_f - \mathbf{u}_s)$ models the interphasial drag exerted on the solid particles and can be identified with the interphasial drag coefficient. On the other hand, the term $p_f \nabla \phi_s$ models nozzling effects due to volume-fraction inhomogeneities [26, 29].

The term $\gamma_s \nabla \phi_s \otimes \nabla \phi_s$, whose divergence enters the momentum equation of the granular phase (2.4), describes Korteweg-type stresses[1] which are due to rearrangements of the

[1]This term is alternatively denoted as configuration stress or nonlocal stress in the literature. It expresses a component of the stress tensor which is of non-viscous nature and is essentially an interface term. By configuration it is meant that this stress depends on the granular microstructure; by nonlocal it is meant that it depends on a reference length related to the particle diameter, and that it describes interaction between particles at the mesoscopic level.

granular interfacial area density; it emerges due to the dependence of the free energy of the granular material on the gradient of the volume fraction $\nabla\phi_s$. At equilibrium it allows the granular material to support strain-rate independent shear stresses which are related to the normal stresses by a Coulomb-Mohr type criterion.

### 2.2.2 A compaction equation without particle migration

An interesting feature of the above model is the form of equation (2.3); in particular, this equation implies that the velocity field of the granular phase is solenoidal. The constant-density limit of the model presented in [26] does not allow a divergent velocity field for the granular phase, which is necessarily a feature of sedimentation processes. More specifically, mass conservation for the granular phase at constant density can be written as

$$\frac{\partial \phi_s}{\partial t} = -\mathbf{u}_s \cdot \nabla\phi_s - \phi_s \nabla \cdot \mathbf{u}_s. \tag{2.8}$$

The first term on the right-hand side of this equation represents advective transport due to bulk motion; in the case of uniform velocity, it is the only term present. The second term describes additional variations of the volume fraction which are associated with a divergent velocity field. Particle migration is described by this term, which is assumed to vanish in the compaction equation (2.5).

Equation (2.5) expresses a fundamental property of the model; it predicts that the granular phase flows solenoidally as an incompressible fluid (with material properties that depend on the local value of the volume-fraction). Several numerical methods are available to tackle solenoidal flow of simple fluids, among which a popular choice is the Chorin-Temam fractional-step projection method [70, 71]. An algorithm based on an extension of this method has been developed in [42], which can be used to solve equations (2.1)–(2.6); it is presented in Appendix A. In the following Section 2.3 this algorithm is used to analyze test flows of granular suspensions and further investigate the implications of equation (2.5).

## 2.3 Numerical results

This Section discusses the outcome of a number of numerical tests, performed in order to assess the predictive capacity of the flow equations (2.1)–(2.6). These tests, which were originally conceived with the primary purpose of validating the numerical algorithm presented in Appendix A, actually provide significant insight into the implications of the compaction equation (2.5). In fact, the outcome of these tests is one of the reasons for the development of a more general flow model which is presented in Chapter 3.

### 2.3.1 Mixture parameters

The material properties of the suspension considered in the tests of this Section are listed here; the hat symbol ˆ is used to denote dimensional quantities. The suspension consists of monodisperse sand in water, with a grain diameter $\hat{d}_p = 3.5 \times 10^{-4}\,\mathrm{m}$; the densities of sand and water are $\hat{\rho}_s = 2500\ \mathrm{kg/m^3}$ and $\hat{\rho}_f = 1000\ \mathrm{kg/m^3}$, respectively.

For the shear viscosity coefficient of the granular phase a Krieger-Dougherty type correlation is used,

$$\hat{\mu}_s = \frac{\hat{\mu}'_s \phi_s}{(\phi_m - \phi_s)^2}\,, \tag{2.9}$$

where the parameter $\phi_m$ represents the value of the volume fraction at maximum packing. Following [72], these parameters are set as $\hat{\mu}'_s = 720\ \mathrm{kg/(m \cdot s)}$ and $\phi_m = 0.635$. Equation (2.9) is quite stiff and diverges as $\phi_s \to \phi_m$. This divergence expresses the jamming phenomenon that the grains experience upon reaching their maximum packing; for such concentrations the motion of the granular conglomerate resembles that of a rigid body. From the physical point of view, it is worth noting that the above relation and its subsequent extensions have been successfully tested against numerous experimental measurements for a multitude of suspensions. The interstitial fluid, water, is treated as a Newtonian fluid, with constant viscosity $\hat{\mu}_f = 1 \times 10^{-3}\ \mathrm{kg/(m \cdot s)}$.

Choosing an expression for the configuration stress coefficient $\gamma_s$ is less straightforward. This quantity is a material property of the granular continuum (it is a derivative of the Helmholtz free energy with respect to $|\nabla\phi_s|$, cf. [26] and the related discussion in Chapter 3). For this reason its functional expression should be given by experimentally-acquired state equations. However, to the best of the author's knowledge, systematic experimental measurements for $\gamma_s$ have yet to appear in the literature. Thus, various authors have employed ad hoc relations, which nonetheless satisfy the convexity requirements for the stability of thermodynamic equilibria. In this Section the functional relation proposed in [28] is adopted. In that article the authors argue that, as $\phi_s \to \phi_m$, $\gamma_s$ should diverge to infinity at the same rate as $\mu_s$. On this premise, and since they employed a Krieger-Dougherty rheology law for the granular rheology, they propose the following relation,

$$\hat{\gamma}_s = \frac{\hat{\gamma}_0 \phi_s}{(\phi_m - \phi_s)^2}\,. \tag{2.10}$$

Here, $\hat{\gamma}_0$ is a (strictly positive) material-dependent constant. In view of the results of [73], who estimated numerically the value of $\hat{\gamma}_0$ by computing the equilibrium distributions of granular materials and the forces acting on them, this value is set as $\hat{\gamma}_0 = 4 \times 10^{-5}\ \mathrm{kg \cdot m/s^2}$.

The last expression to be specified is for the drag coefficient $\hat{\delta}$. Herein the expression proposed in the numerical study of [74] is adopted, which constitutes a generalization of the well-known Stokes law for the case of suspensions,

$$\hat{\delta} \;=\; \phi_s \, 18 \, \frac{\hat{\mu}_f}{\hat{d}_p^2} \, Q(\mathrm{Re}_p)\,, \tag{2.11}$$

where $Q(\mathrm{Re}_p)$ is given by the following empirical relationship, [75],

$$Q(\mathrm{Re}_p) \;=\; \begin{cases} 1 + 0.15\,\mathrm{Re}_p^{0.687}, & \mathrm{Re}_p < 1000\,, \\ 0.01833\,\mathrm{Re}_p, & \mathrm{Re}_p \geq 1000\,. \end{cases} \tag{2.12}$$

In the above relation, $\mathrm{Re}_p$ is the particle Reynolds number, defined with respect to the relative grain velocity, *i.e.*,

$$\mathrm{Re}_p \;=\; \frac{\hat{\rho}_f \, \hat{d}_p}{\hat{\mu}_f} |\hat{\boldsymbol{u}}_s - \hat{\boldsymbol{u}}_f|\,. \tag{2.13}$$

### 2.3.2 Poiseuille flow over a granular bed

This test simulates Poiseuille flow of water over and through a dense granular bed. The flow domain is a horizontal channel in the $x, y$-Cartesian plane with height $\hat{h}_{\mathrm{ref}} = 0.015\ m$, which is taken as the reference length for the problem. The bottom third of the channel is occupied by the granular bed, with a particle concentration $\phi_{\mathrm{bed}} = 0.58$. The initial concentration in the water stream, above the bed, is set at $\phi_{\mathrm{stream}} = 5.8 \times 10^{-7}$; with this choice the viscosity of the granular material is approximately $10^{-10}$ so that contribution of grains to the flow is negligible. Both phases are initially at rest and motion is induced by a horizontal forcing term $f$ so that, in the Poiseuille approximation with respect to the distance between the top wall and the bed, the Reynolds number is $\mathrm{Re} = 1000$. More precisely, the forcing is applied to the fluid phase as a uniform body force with magnitude $\phi_f f$, while for the granular phase this is $\phi_s f$. Accordingly, the reference velocity is taken as $\hat{u}_{\mathrm{ref}} = \frac{\mathrm{Re}\cdot\hat{\mu}_f}{\hat{\rho}_f \cdot \hat{h}_{\mathrm{ref}}}$. In order to decrease computing time, the flow is initially accelerated with a forcing term $f_{acc} = 5 \times 10^3 f$ until the fluid velocity reaches the value $u_{f_x} = 1$ at the centerline, and then evolves under a forcing term $f$.

As regards boundary conditions, the flow is assumed to be periodic in the streamwise direction with period $\hat{L}$. The top and bottom boundaries are modelled as solid, impermeable walls; more specifically, at these boundaries wall boundary conditions are imposed on both the granular and the fluid velocities whereas a zero-Neumann condition is prescribed for the volume fraction.

Preliminary simulations indicate that, for this value of the Reynolds number, the variations of the quantities are confined to the normal direction independently of the value of $\hat{L}$ and of the resolution in the streamwise direction. For this reason, the numerical predictions presented herein are obtained with a uniform one-dimensional grid with $1024$ cells across the channel. Figures 2.1a–2.1d show the granular and fluid streamwise component of the velocities at $t = 1, 5, 10$, and $200$; in this test the wall-normal component of the velocity vanishes. Due to the very high viscosity of the granular material inside the bed, the motion therein is very slow. This implies that the material interface essentially imposes a solid–wall boundary condition to the above–flowing fluid, so that the flow over the bed constitutes a good approximation of a classical Poiseuille flow. Consequently, in the stream region and as the flow evolves, both the granular and the fluid velocity become parabolic with height. Further,due to interphasial drag, the differences between the phasial velocities are non-negligible only in the vicinity of the material interface; away from it the velocities are practically equal. The simulation is continued up to $t = 200$, at which point the the forcing pressure term and the wall shear stress are balanced up to $0.1\%$.

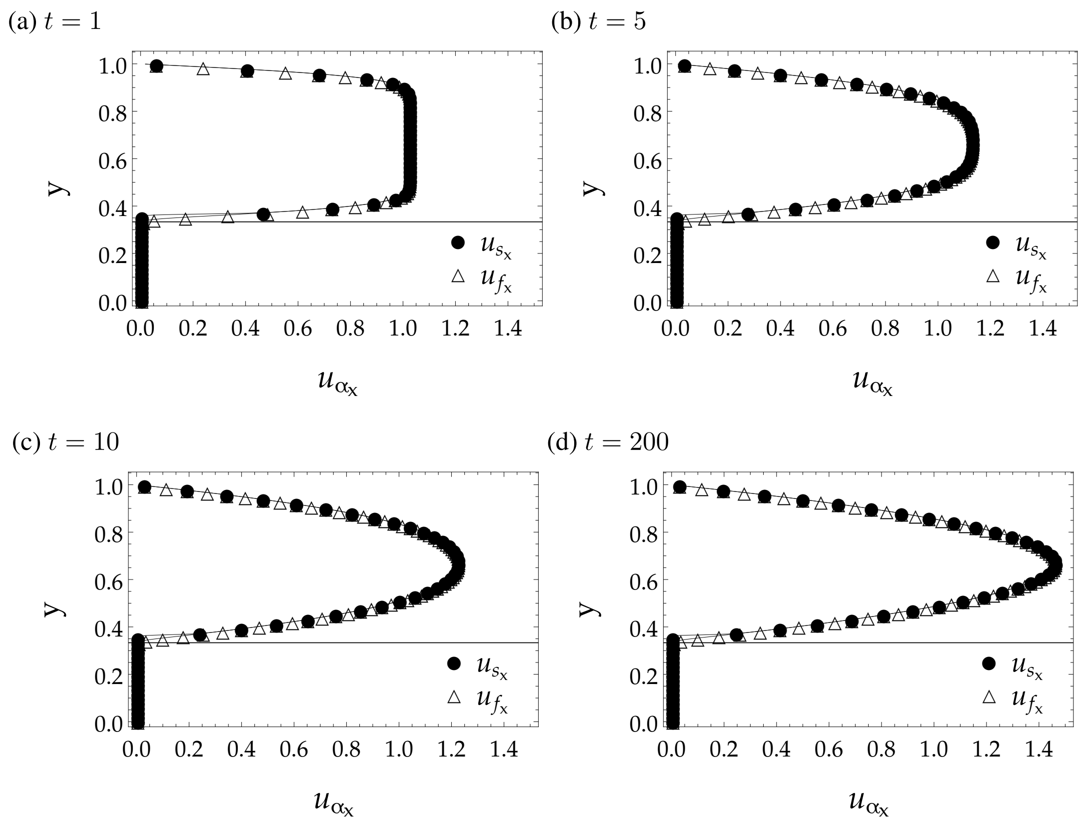


Figure 2.1: Profiles of superimposed granular and fluid streamwise velocities, $u_{s_x}$ and $u_{f_x}$ plotted against height $y$ at $t = 1, 5, 10, 200$. The continuous horizontal line represents the position of the material interface. Inside the granular bed, the phasial velocities are negligible. In the pure-fluid region, as the flow evolves, both velocities assume the familiar parabolic profiles. Moreover, due to interphasial drag, disparities between $u_{s_x}$ and $u_{f_x}$ are confined in the neighborhood of the material interface.

Figure 2.2 depicts the profiles of the phasial pressures $p_s$ and $p_f$ and that of the mixture $p_m = \phi_s p_s + \phi_f p_f$, superimposed to the (scaled) concentration profile. In order to facilitate comparison, the integration constants stemming from the solution of the Neumann problems are set so that $p_s = p_f = 0$ at the top boundary. First, it is observed that the fluid pressure

$p_f$ is linear. In fact, for this particular flow and due to the presence of the nozzling term in the momentum equation of the fluid phase (2.2), jumps in the granular concentration are irrelevant to the determination of the fluid pressure. The granular pressure inside the bed is also linear with slope equal to $\rho_s g$. At the material interface, $p_s = p_f$, a property that is dictated by the balance of linear momentum along the normal direction, cf. (2.4). Indeed, since the flow is one–dimensional and the normal component of the phasial velocities is zero, momentum conservation across the material interface implies that $\phi_s \cdot (p_s - p_f) \approx 0$ and hence $p_s \approx p_f$. The mixture pressure $p_m$, being the weighted average of $p_s$ and $p_f$, is piecewise linear and its slope is equal to $(\rho_s\phi_s + \rho_f\phi_f)g$ which, away from the material interface, constitutes a piecewise constant function.

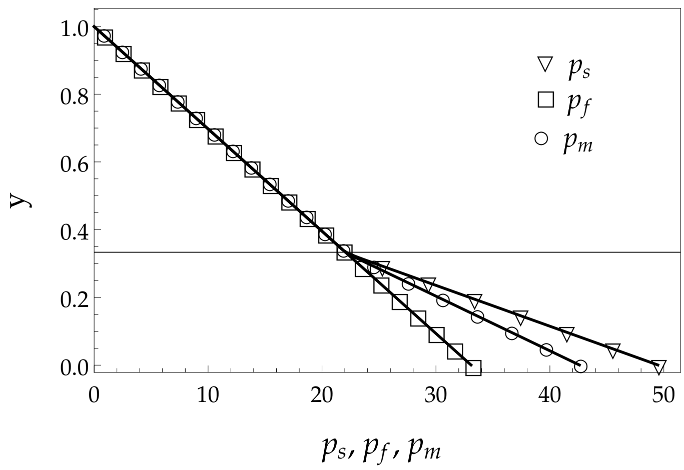


Figure 2.2: Predicted phasial pressures $p_s$, $p_f$ and mixture pressure $p_m$ plotted against height at $t = 200$. The continuous horizontal line represents the position of the material interface. Inside the bed, the granular pressure $p_s$ is linear and, due to conservation of momentum, it equals $p_f$ at the material interface. The fluid pressure $p_f$ is linear both inside the bed and in the stream region; its variation is independent of the concentration due to the nozzling term. On the other hand, the mixture pressure $p_m$ is piecewise-linear with a slope equal to $(\rho_s\phi_s + \rho_f\phi_f)g$.

### Numerical grid-convergence study

For this test, a grid-convergence study has also been performed in order to validate the numerical algorithm; the outcome is reported here as reference. More specifically, the normalized, mesh-dependent $L^2$-norm of the error is computed for the granular pressure $p_s$ and the phasial velocities $\mathbf{u}_s$ and $\mathbf{u}_f$ at $t = 200$. This error norm is defined as follows,

$$Err(H) = \sqrt{\frac{\frac{1}{N^2}\sum_{i=1}^{N}|h_i - H_i|^2}{\frac{1}{N^2}\sum_{i=1}^{N}|H_i|^2}}\,. \tag{2.14}$$

Here, $N$ stands for the total number of computational cells while $h$ is the numerical prediction for the corresponding resolution. In this study, grids with 32, 64, 128 and 256 points have been employed. Further, $H$ is the "true" solution, which in this study is replaced by the numerical prediction obtained on a finer grid with 1024 points.

The results of the grid–convergence study are reported in Figure 2.3. It can be readily inferred that the error decreases with the density of the grid, suggesting numerical convergence. The data shows a convergence rate that varies between $O(\Delta x)$ and $O(\Delta x^2)$.

**Interface thickness**

The algorithm of Appendix A, which is employed in the computations of this Chapter, adopts a parabolic regularization method in order to treat sharp interfaces for the volume fraction, such as the transition between the granular bed and the fluid region. Numerical solutions obtained by parabolic regularization methods have an inherent dependence on the thickness of the regularized interface. For this reason, simulations have been run with different interface thicknesses in order to exemplify the role of this parameter. Figure 2.4 illustrates the effect of the interface thickness on the velocity profile. It can be seen that, while the shape of the velocity profile is qualitatively unchanged, there is a difference with respect to the magnitude of the corresponding maxima. This behavior is rationalized as follows: as is well known, the Poiseuille parabolic profile attains a maximum that depends quadratically on the channel width. Variations of the interface thickness translate into channels with slightly different widths and thus different velocity maxima. In the limit of vanishing interface thickness, the velocity maximum is expected analytically to reach the maximum value $u_{s_x} = u_{f_x} = 1.5$; according to Figure 2.4, this is also verified with good approximation.

### 2.3.3 Couette flow over a granular bed

This test simulates unidirectional Couette flow of water over and through a dense granular bed. The geometry of the flow, the boundary and the initial conditions are identical to the one used for the Poiseuille flow discussed in the previous Subsection. However, in this case, the motion of the suspension is induced by the impulsive acceleration of the upper plane, which is presumed to move at a constant horizontal velocity $U_\mathrm{w} = 0.1\,\mathrm{m/s}$; this constitutes the reference velocity for this problem. With these values, the shear rate of the flow is $10\,s^{-1}$ and the Reynolds number of the fluid is 1000. As for the Poiseuille flow case, with this parameters the flow is one-dimensional and the wall-normal velocity component vanishes.

Figure 2.5 shows the predicted velocity profiles $u_{s_x}$ and $u_{f_x}$ at $t = 200$, at which point the simulation has reached steady state. The velocity profiles are piecewise linear, and inside the bed they are very close to zero due to the high viscosity in that region. Similarly to the Poiseuille case, due to interphasial drag, the differences between the phasial velocities are small and limited to the vicinity of the material interface.

The phasial and the mixture pressure distributions are shown in Figure 2.6. The results are completely analogous to the Poiseuille flow case; the reasons for this similarity are dis-

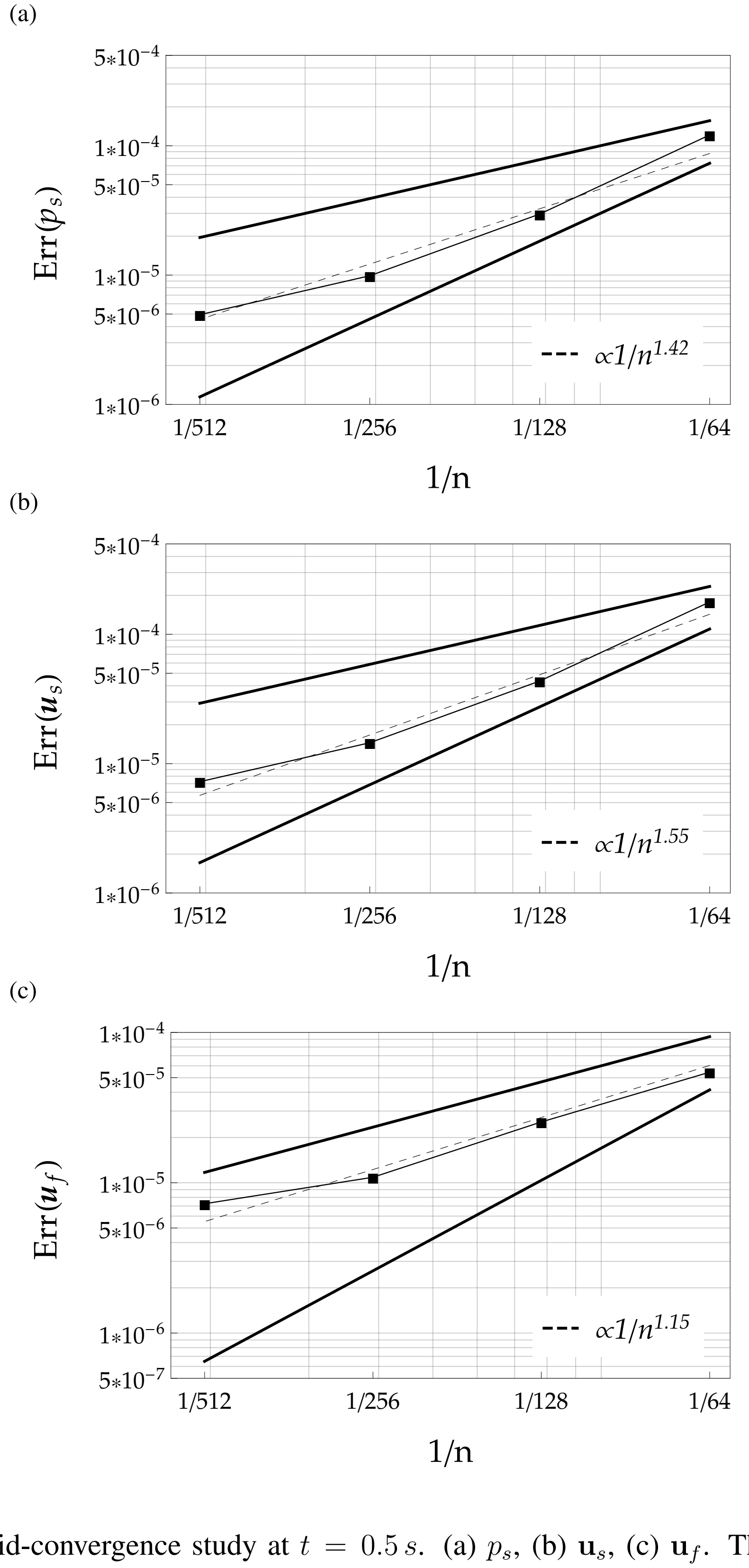


Figure 2.3: Grid-convergence study at $t = 0.5\,s$. (a) $p_s$, (b) $\mathbf{u}_s$, (c) $\mathbf{u}_f$. The dashed line slopes are obtained with least-square interpolation.

cussed in more detail in Section 2.4. From a numerical perspective, this test shows that the algorithm recovers the requirement that $p_s = p_f$ at the interface very accurately, in spite of

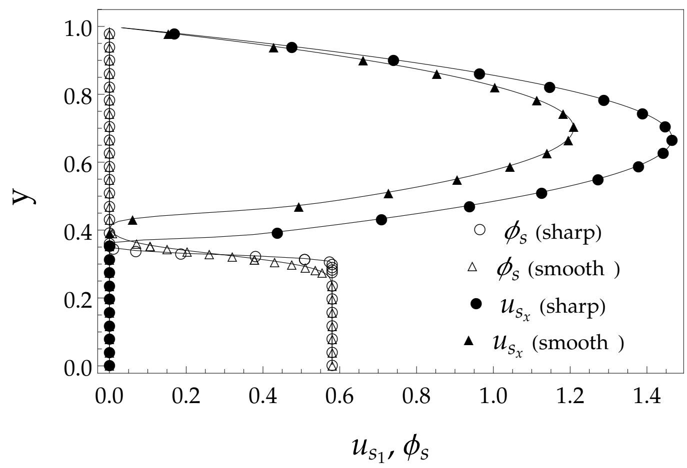


Figure 2.4: Predicted granular velocity and volume fraction profiles plotted against height $y$ for different interface thicknesses. The qualitative trend remains invariant with changes in the interface thickness. However, due to the nonlinear dependence of the maximum velocity with respect to the height of the domain, the resulting maxima differ. This result adduces that the choice of the thickness of the interface has to be the result of a specific analysis, which takes into account the length of the domain and the density of the grid.

the interface regularization method.

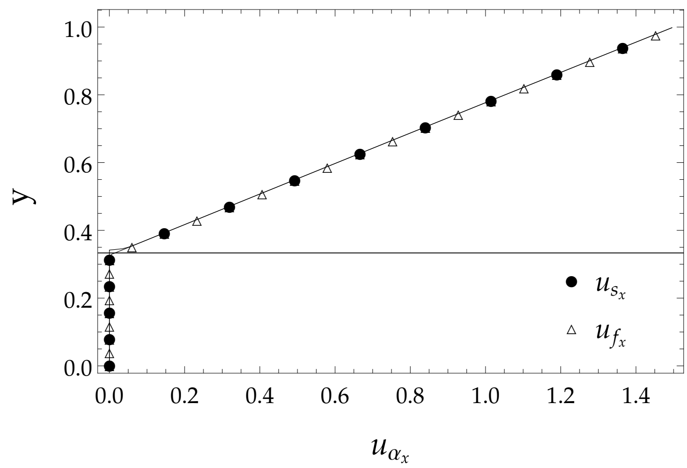


Figure 2.5: Predicted granular and fluid streamwise velocities, $u_{s_x}$ and $u_{f_x}$ plotted against height $y$ at $t_{ad} = 200$. The continuous horizontal line represents the position of the material interface. The velocities are piecewise linear but inside the bed their values are very small. The interphasial drag maintains small the difference between the two velocities everywhere in the domain, away from the material interface.

### 2.3.4 Transient flow over two-dimensional dunes

This test simulates forced flow of water over and through two–dimensional sinusoidal dunes. The previous tests show no discernible vertical movement of the granular phase in the case of

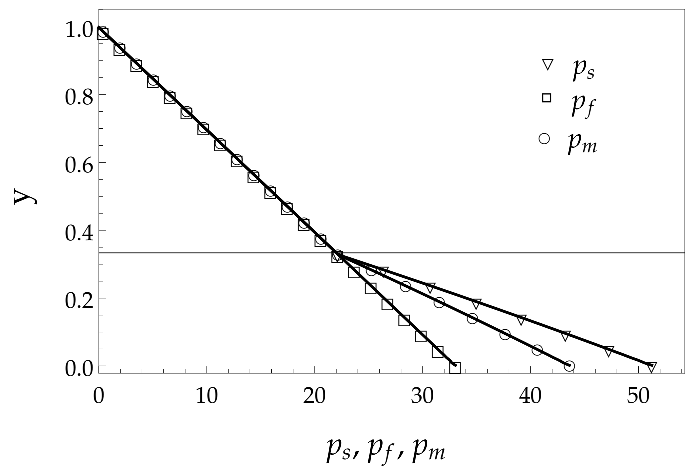


Figure 2.6: Predicted granular, fluid and mixture pressures, $p_s$, $p_f$ and $p_m$ plotted against height $y$ at $t_{ad} = 200$. The continuous horizontal line represents the position of the material interface. The profiles are completely analogous to those obtained for Poiseuille flow. Further, even though the numerical interface is quite steep, the requirement that $p_s = p_f$ (at the limit of discontinuity) is very accurately recovered.

flow over a flat bed, in the sense that they predict the wall-normal velocity to be negligible. This is an important feature of the model proposed in [26] which is further discussed in Section 2.4. In order to investigate if the shape of the bed surface plays a role with respect to particle suspension in laminar flow, this test considers a sinusoidal interface. The flow is confined in an horizontal channel of height $\hat{h}_{ref} = 0.1$ m. A dense granular bed with constant concentration $\phi_s = 0.58$ is placed at the bottom of the flow domain. The material interface is given by a sinusoidal wave of amplitude $0.0125\,\mathrm{m}$ and the average bed thickness is $0.02$ m. The flow is assumed to be periodic with a period of $0.1\,\mathrm{m}$. A resolution of $128 \times 128$ points is used. The concentration value in the stream above the bed is $\phi_{stream} = 5.8 \times 10^{-7}$.

In this test, the two phases are initially at rest and motion is induced by an horizontal forcing term $f$ such that, in the Poiseuille approximation with respect to the average height of the channel, the Reynolds number is $\mathrm{Re} = 2000$; this induces the reference velocity $\hat{u}_{\mathrm{ref}} = \frac{\mathrm{Re} \cdot \hat{\mu}_f}{\hat{\rho}_f \cdot \hat{h}_{\mathrm{ref}}}$. The flow is initially accelerated with a forcing term $f_{acc} = 10^3 f$ to a maximum non-dimensional velocity $u_{f_x} = 1$, and then evolves under a forcing term $f$. At the top and bottom of the domain wall boundary conditions are imposed for both phases; a zero-Neumann boundary condition is prescribed for the volume fraction.

Figure 2.7 shows the vorticity field of the fluid phase at various non-dimensional times. One observes that, due to the acceleration of the fluid phase, a shear layer is formed at the material interface. However, the phasial velocities inside the bed remain very small throughout the duration of the simulation. The abrupt change of the fluid velocity across the material interface results in the onset of a Kelvin-Helmholtz instability and thus the formation of vortical structures. These structures detach from the crests and propagate downstream, inducing counter–vortices while convected over the throughs. Subsequently, these vortices reach the

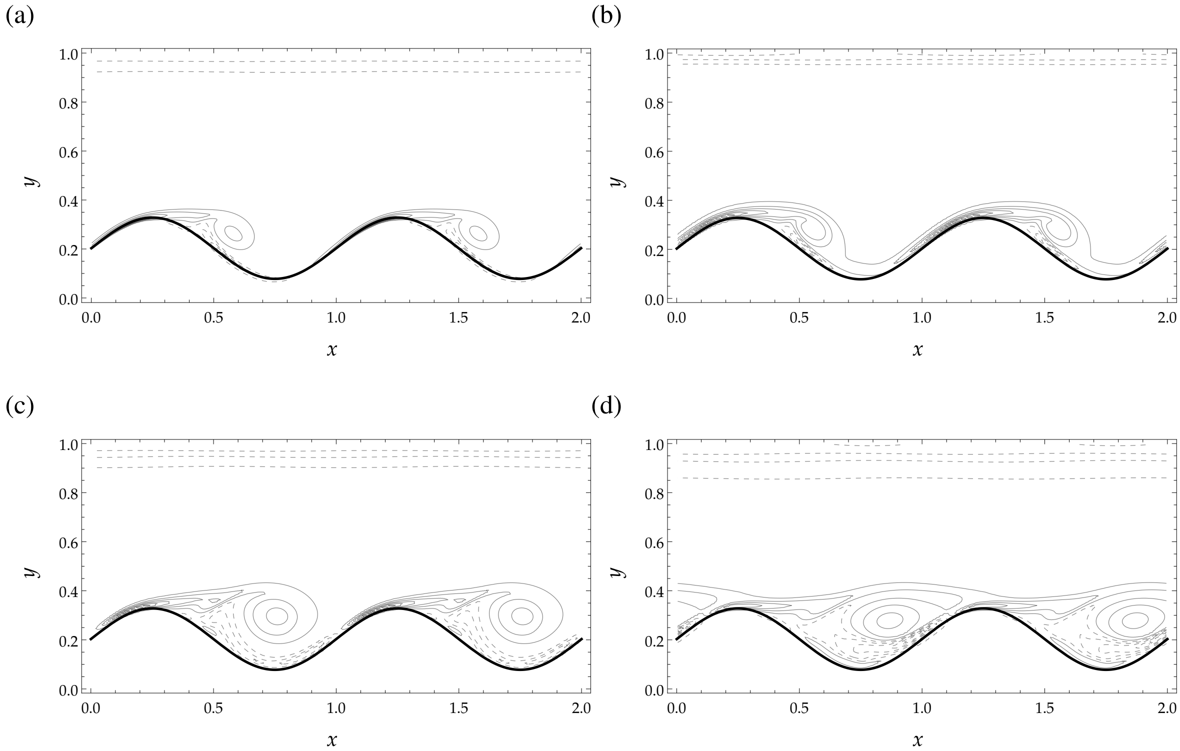

Figure 2.7: Contour plots of the fluid vorticity at $t = 0.9$, $1.8$, $2.7$ and $3.6$. Two periods in the streamwise direction are shown. Negative and positive vorticity values are represented by continuous and dashed contour lines, respectively. Further, the thick continuous line represents the material interface. Due to the fluid velocity differences inside the bed and at the stream region a Kelvin-Helmholtz instability is onset. The resulting vortices propagate downstream, give rise to counter-vortices while in the troughs and are confined in the neighborhood of the dunes.

downstream dune; interestingly, they do not move upwards (towards the center of the channel), but remain confined to the vicinity of the material interface.

In all three tests performed so far, the phasial velocities normal to the interface are negligible right at the interface throughout the simulation; consequently there is no transport of grains away from the interface. The next Section discusses the origin of this behaviour, which is at odds with experimental data showing particle transport even in the laminar regime [43, 76].

## 2.4 A critical examination of modelling issues

The flow model expressed by (2.1)–(2.5) has the desirable property of providing a two-phase continuum description of suspension flow which is numerically tractable; for instance, the algorithm proposed in [42] can be used for the solution of these equations for general flow. This model has been used with success to describe flows where particle transport is primarily due to advection [74, 77].

On the other hand, the numerical tests of Section 2.3 show that this model does not capture particle entrainment from the surface of a granular bed. This is a consequence of equation (2.3), which essentially forces the component of the granular velocity normal to the bed surface to vanish on the bed surface; to be more precise, if the normal component of the velocity on the bottom side of the interface between the granular bed and the fluid-flow region vanishes (as is usually the case since the granular bed is very densely packed) then this component vanishes on the top side as well. In the case where the flow is one-dimensional with wall boundary conditions, such as in the case of Poiseuille and Couette flow, equation (2.3) actually implies that the vertical velocity component of both phases vanishes throughout the flow domain.

By the same token, the interface treatment is deceptively simple: the initial thickness of the interface has to be specified as an arbitrary parameter which for one-dimensional flows, does not vary in time. In particular, gravity does not generate a vertical velocity component and thus it does not have a direct effect on the vertical distribution of the volume fraction, so that the interface can not vary its thickness and "settle". It follows that, although the results shown in Subsection 2.3.2 compare favorably against the experimental results of [39, 40] throughout the channel width, within the interface region the results rely on the choice of a predetermined interface thickness.

Another consequence of the vanishing wall-normal velocities is the similarity of the pressure profiles for the Poiseuille and Couette tests shown in Figures 2.2 and 2.6. In particular, in the wall-normal direction there can not be any interphasial momentum exchange due to drag, so that, in both cases, the fluid and granular pressures simply increase with slope $\rho_f g$ and $\rho_s g$ according to equations (2.2) and (2.4). In this respect, it is important to notice that equations (2.2) and (2.4) express a Newtonian rheology law, so that there are no viscous stresses in the wall-normal direction.

Finally, an important limitation of models that present the solenoidality constraint (2.3) is related to the fact that particle migration is not only important in the context of granular transport, but also plays an important role with respect to granular rheology. In fact, there is a class of flows where volume-fraction variations are important even when granular transport is negligible; this is due to the fact that the viscosity coefficients of the granular phase are nonlinear functions of the volume fraction. Near maximum packing, small variations of the volume fraction can induce significant viscosity variations; in dense granular flows, it can be necessary to capture viscosity variations which are quite small relative to the actual volume fraction. The limited scope of equation (2.3) is also apparent if one considers the non-Newtonian character of suspensions, since they exhibit normal stresses due to shear that can change the volume fraction. In other words they exhibit dilatancy, which necessarily implies a divergent velocity field: the granular phase can dilate and reduce its volume-fraction under the influence of non-Newtonian stresses. Under the constraint of equation (2.3) this phenomenon is not possible.

### Collapse of a submarine granular column

In order to elucidate some of the implications of the solenoidality constraint (2.3) on granular rheology, an additional numerical test case is considered: a two-dimensional column of sand, submerged under water, collapses due to gravity. In this flow, viscosity variations in the dense regime are of paramount importance. In fact, if the initial particle concentration inside the column is sufficiently close to maximum packing, the collapse presents a complicated structure which exhibits different flow regimes: a central portion of the sand column remains essentially rigid, whereas the sides of the column flow freely to the bottom [78–81]. This configuration provides a good test of rheological models, as it is very sensitive to viscosity variations and allows to draw qualitative comparisons between different rheological descriptions.

Figure 2.8 compares numerical predictions obtained with two different rheology formulations. The initial shape of the two-dimensional granular column is shown in Figure 2.8a. In one case the volume-fraction-dependent rheology expressed by (2.9) is employed; the state of the collapse at a representative time instant is shown in Figure 2.8b. The other case employs the well-known $\mu(I)$ inertial rheology formulation, which provides a direct connection between shear and normal stresses [46, 82–84]; a representative instant of the collapse for this case is shown in Figure 2.8c.

It is known from experiments that, if the initial column is sufficiently dense, a static pile is left after the collapse, with steep sides at an inclination that resembles the angle of repose [79, 80]. This is incompatible with the behaviour predicted by the Newtonian rheology shown in Figure 2.8b. The main reason for this discrepancy lies in the description of the volume-fraction evolution expressed by equation (2.5). According to this equation, the volume fraction inside the dense column, initially uniform, remains uniform; as a result that the viscosity of the suspension inside the column remains uniform, and the column behaves as a very viscous simple fluid, slowly relaxing to the bottom.

The second test, which employs a $\mu(I)$ formulation, shows better agreement with experiments in the sense that it presents both a central region that does not move during the collapse, and it leaves a static pile when the collapse is complete, with two vortices that propagate away from the point of collapse. It is not surprising that this type of rheology law performs well for this test problem, where it has been shown to be a good representation [78]. In fact, this flow satisfies a fundamental assumption of the $\mu(I)$ formulation: volume-fraction variations inside the dense column are fairly limited [83]; the dense region remains dense throughout the collapse and volume-fraction variations are only relevant because they correspond to variations of the viscosity coefficients. In this case, the $\mu(I)$ rheology formulation allows to bypass entirely the volume-fraction dependency of the viscosity coefficients by expressing the shear stresses directly as a function of normal stresses. There is, however, a price to pay for this simplicity: it is conceptually difficult to reconciliate the $\mu(I)$ inter-

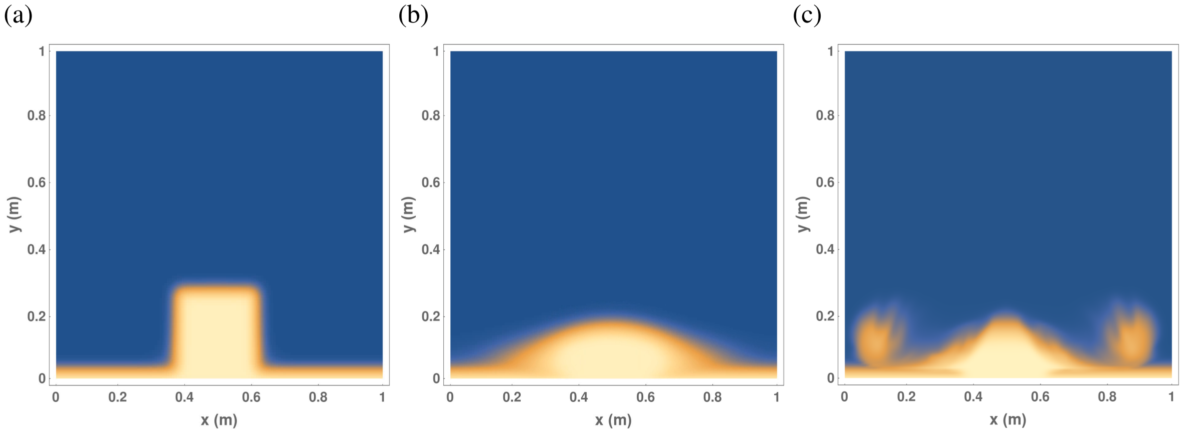


Figure 2.8: Collapse of a submarine granular column. (a) initial condition, (b) collapsed shape with a Newtonian volume-fraction dependent viscosity, (c) collapsed shape with $\mu(I)$ rheology.

tial rheology formulation with a continuum formalism that is thermodynamically-consistent, such as the one of TIP. Furthermore, it has been shown that this type of rheology is not always well-posed from a mathematical perspective [85]; it is not yet clear if the two issues are connected.

The comparison of the two different formulations of granular viscosity is particularly interesting since it has been shown that, at least for the simple case of homogeneous Couette flow, the two formulations should be equivalent [57]. In order for this to hold, the volume fraction can not follow exactly equation (2.5). Its evolution has to be linked with the phasial stresses, so that the contribution of the normal stresses mirrors the behaviour predicted by the $\mu(I)$ rheology. It turns out that it is indeed possible to derive, on theoretical grounds, a compaction equation which is thermodynamically-consistent and depends explicitely on the phasial pressures; such a model is presented in Chapter 3. Finally, it is useful to provide some context relative to the compaction equation (2.5), in order to clarify its origin from a modelling standpoint, and to further comment on its implications.

#### Incompressibility and dilatancy

The model proposed in [26], derived for general compressible flow, actually provides an evolution equation for the volume fraction which explicitly depends on the phasial stresses, and more specifically on the phasial pressures. In fact, the compaction equation (2.5) originates from the low-Mach-number limit of the energy balance for the granular phase [62]. The reason why equation (2.5) is used in place of the low-Mach-number limit of the compaction equation, is that this limit is dependent on the phasial temperatures and, in particular, it couples mechanical and thermal degrees of freedom; this complicates the solution of the resulting governing equations. It is, in fact, quite peculiar that the energy balance of the granular phase simplifies to equation (2.5); one could reasonably expect, in analogy to what happens for incompressible flow of multiphase simple fluids, some sort of heat transport equation for this phase.

It turns out that the specific form of equation (2.5) is a consequence of a choice relative to the characterization of dissipative phenomena, which is made in the derivation of the model presented in [26]. In particular, the second principle allows some freedom in this characterization, and it is possible to proceed in a different way [63, 86]. More precisely, it is possible to derive a compaction equation which decouples pressures and temperatures in the low-Mach limit, and which maintains an explicit dependence on the phasial pressures in this limit. Moreover, this alternative approach provides an energy balance with a low-Mach-number limit which is essentially a heat transport equation. The flow model presented in Chapter 3 conforms to this different derivation. It is remarkable that the two approaches produce models with a very similar structure for general compressible flow, while for incompressible flow they exhibit a fundamental difference; this unexpected property has been discussed in [63].

# Chapter 3

# A new thermomechanical model for granular suspensions

## 3.1 Introduction

This Chapter is concerned with the derivation of a continuum model for two-phase flows of granular suspensions. This derivation, which is based on an ad hoc modification of the framework of classical irreversible thermodynamics, is performed in order to obtain a flow description that accounts for granular dilatancy. The outcome of this derivation is a flow model that i) describes divergent flows, ii) links the compaction equation with the pressures of the fluid and granular phases, and iii) describes the non-Newtonian suspension rheology in a thermodynamically-consistent manner.

### 3.1.1 Overview of continuum modelling of granular materials

An important preliminary question to be considered concerns the relevance of continuum modelling. In other words, whether a collection of macrosopic particles can be described as a continuum, and its constitutive relations be properly accommodated into a comprehensive continuum theory, and if yes then what the predictive capacity of such a theory is. This question has a long history, as attempts to develop continuum theories for the mixtures of interest go back more than 50 years ago and are still ongoing; see, for example, [26], [28], [30, 66], [87], [88], [89] and references therein. However, providing a conclusive answer has proven to be an extremely challenging task. In fact, since an unequivocally accepted continuum theory for granular suspensions does not exist, to a large extent this question remains open [16, 24].

The results presented in this Chapter have been published in: D. Monsorno, C. Varsakelis, and M.V. Papalexandris, (2016), "A thermomechanical model for granular suspensions", *Journal of Fluid Mechanics*, Vol.808, pp. 414-440.

Ever since the onset of the development of continuum theories for granular suspensions, it has been recognized that the volume fraction of the particles constitutes a separate degree of freedom [90–92]. However, these early modelling efforts were unsuccessful in coupling this kinematic independence with their theoretical framework and thus suffered from underdeterminacy problems [93]. Employing additional assumptions as a remedy such as, for example, pressure equilibrium between the granular material and the fluid, turned out to be problematic as well since it often resulted in ill-posed systems [94]. The authors of [27] were probably the first that assigned to the volume fraction its own evolution equation. Although this equation was postulated essentially on an ad hoc basis, pre-assuming the existence of a balance law that the volume fraction obeys (balance of equilibrated forces), it nonetheless provided the necessary closure to the system of balance laws. This approach was subsequently employed, among others, in [28] and [30, 66].

It is interesting to note that in their later work, the authors of [27] tried to remove the ad hoc character of the balance of equilibrated forces by resorting to variational arguments [95]. Still, this issue was resolved in [96], by asserting that the balance of equilibrated forces can be recovered if one assumes that the volume fraction is an internal degree of freedom. A similar approach was employed by the authors of [67], who were able to derive an equation for the volume fraction based on purely entropic arguments. Interestingly, this study contains certain inconsistencies related to the consequences of introducing the volume fraction as a thermodynamic variable which were identified and rectified in [29]. This point of view, *i.e.* treating the volume fraction as an internal degree of freedom, has been also adopted in [26] and [68]. Nonetheless, the status of the volume fraction as a thermodynamic variable and, by extension, the form of the compaction equation are still under debate.

An additional challenge concerns the rationalization of the constitutive relations for the dissipative properties, and in particular for the granular rheology, in a way that is consistent with the second law. Experimental measurements [49–54, 97, 98] and numerical simulations [21, 99–107] have produced an extensive load of data; see, also [17] for a succinct review. Based on these data, various theoretical analyses have been carried. These analyses assert that empirical correlations for the viscosity coefficients having the volume fraction of the particles and the shear rate as control parameters accord very well to the data [16, 24].

However, no study has thus far incorporated these constitutive relations into a continuum theory that is additionally thermodynamically consistent. In fact, available continuum theories typically ignore the normal viscosity of the granular phase [26, 28, 30, 89], employ them in an ad hoc fashion [19, 40, 41, 108], or obtain scalings that do not match experimental data [109, 110]. This can be traced to the fact that the normal viscosity is associated with a shear-induced pressure that engenders a non-Newtonian behavior. From shear-flow experiments it is known that, for a large range of shear rates $\dot{\gamma}$, shear-induced pressure scales linearly with $|\dot{\gamma}|$ [102, 108, 111]. This range is usually referred to as the *viscous regime*. As commented in [112], this observed scaling cannot be described by a simple linear relation between the viscous stress and strain-rate tensors, which is often assumed in existing modelling efforts. Existing thermodynamic frameworks for other types of non-Newtonian fluids, e.g. polymer melts, are also of little help to granular suspensions as the scalings are utterly different; indeed, for such fluids normal-stress differences scale quadratically with the shear rate.

An alternative point of view was proposed by the authors of [46] and [82], which is based on a dimensional analysis of homogeneous shear flows of dry granular materials. These collective efforts resulted in the scalar version of the popular $\mu(I)$-rheology that was subsequently extended to 3D in [83, 84]. The $\mu(I)$-rheology provides a representation of the granular viscous stresses in terms of the shear rate and the normal stress (pressure). In other words, the $\mu(I)$-rheology is a type of friction law and thus the control parameter is no longer the volume fraction but the pressure. The satisfactory agreement between experimental data for shear flows and the predictions of the $\mu(I)$-rheology led to a number of subsequent generalizations [113–115], and to its extension to granular suspensions [57]. A rationalization of one of these extensions, that takes into account nonlocal effects, into a continuum mechanical framework was performed in [116].

The results reported in [57] are of particular interest since, for the case of homogeneous shear flow, they demonstrate the equivalence between the two representations: the $\mu(I)$-rheology law and the "traditional" one that utilize the pressure and the volume fraction as the control variable, respectively. Thus, in principle, when developing continuum theories or performing numerical simulations, one may opt for either of the two representations. However, some caution needs to be exercised prior to making the choice of the representation. Indeed, in [85] it is reported that the $\mu(I)$-rheology can exhibit an ill-posed behavior in certain flow regimes. Moreover, when implementing the $\mu(I)$-rheology in an incompressible solver, as done in [78], certain artificial modifications are required so that the negativity of the pressure field does not conflict with the constitutive relation. On the other hand, it is well known that viscosity correlations based on the volume fraction representation have a singularity at the jamming transition point where they diverge to infinity. This singularity can cause severe numerical issues and the reader is referred to [42] for a thorough discussion.

### 3.1.2 A thermodynamically-consistent approach

This Chapter presents the derivation of a thermomechanical, two-phase model for granular suspensions that properly accommodates the constitutive relations for the granular stresses in a thermodynamically-consistent manner. The approach is based on the non-equilibrium thermodynamic formalism for immiscible two-phase mixtures proposed in [26]. According to this formalism, the carrier fluid and the granular material are treated as two separate thermodynamic continua but the latter is endowed with an augmented state vector so that its microstructure can be captured. Constitutive relations for the dissipative and relaxation phenomena, including granular viscous dissipation, are derived by exploiting the constraints imposed by the entropy inequality on the entropy production rate. The resulting theory is general enough to account for thermal, mechanical and kinematic non-equilibrium between the phases. It is, therefore, conforming to the analysis of [117], which argues that flowing suspensions constitute systems out of equilibrium and, as such, display differences between the intensive thermodynamic variables of the fluid and particulate phases. Moreover, the resulting model, being endowed with a compaction equation for the granular volume fraction, captures both compaction and dilatational effects.

Opting for the rationalization of the constitutive expressions into a thermodynamically-consistent theory offers a number of compelling advantages over their direct inclusion into the pre-constitutive governing equations. Indeed, even though shear-flow experiments constitute the starting point for many efforts to describe the non-Newtonian behavior of granular suspensions, the majority of them relies heavily on the specific properties of this flow. As a consequence, extending the corresponding models to other types of flows is not straightforward. By contrast, when constitutive relations are derived, and in a way that conforms with the second law, the resulting post-constitutive equations are formally valid for a broad class of flows. This is well exemplified by the thermodynamic theories for polymer melts where efforts to properly accommodate the non-Newtonian rheological characteristics provided important insights into their properties [65].

As mentioned above, in order to derive the constitutive relations that conform *a priori* to the observed scaling, one needs to depart from the usual linear current-force relations and consider more elaborate expressions. The present theory utilizes a subtle, non-linear coupling between thermodynamic currents and forces and a thorough *a posteriori* exploitation of the resulting phenomenological coefficients. The complexity of this analysis is necessary to remove undesirable aspects such as singularities and to guarantee the vanishing of the viscous stresses at thermodynamic equilibrium. On the other hand, it is in view of this complexity that additional corollaries are obtained. For example, as a by-product one obtains a result against the validity of a Stokes hypothesis for the bulk viscosity. In turn, this result theoretically corroborates the numerical analysis reported in [106].

In the development of the present thermomechanical model it is not assumed that the particulate phase or the fluid have a constant density. Rather, one starts from a fairly general setting where compressibility effects are allowed and then arrives at the incompressible and constant-density limits via multi-phase low-Mach-number asymptotics [62]. Although it is possible to proceed under the constant-density assumption, the passage from compressible to incompressible and then to constant-density flows entails a number of details and critical points that have to be underlined.

The proposed two-phase model is quite general, however, its strengths and advantages become more evident when dealing with flows that involve concentration gradients, the onset of hydrodynamic instabilities and a strong non-equilibrium between the two phases. Typical examples of such flows include the erosion of granular beds and the subsequent formation of dunes or ripples, subaqueous granular column collapses and suspension flows in channels. Consequently, this model is well-adapted for the modelling and simulation of natural phenomena like sediment transport in coastal and fluvial environments, avalanches and pyroclastic density currents. Furthermore, the two-phase theory is applicable to a number of industrial and technological applications that involve fluidized beds, dense particulate flows inside bead mills, transport of bulk agricultural materials and others.

The derivation of the thermomechanical model is presented according to the following structure. Section 3.2 presents the basic principles and balance laws of thermomechanics of granular suspensions based on the mixture-theoretic approach that has been adopted. Section 3.3 presents the derivation of constitutive relations for granular suspensions, with particular emphasis on the description of the viscous stresses acting on the granular phase. Section 3.4 presents the complete, post-constitutive form of the proposed thermomechanical model. Section 3.5 presents the incompressible limit of the complete model, derived via low-Mach-number asymptotics. The reduced equations for the important special case of constant-density flows are also shown. Section 3.7 discusses the model predictions for the case of steady shear flow. Section 3.6 compares the model description of particle migration with two existing popular approaches. Finally, Section 3.8 concludes.

## 3.2 Thermomechanics of granular suspensions

This derivation considers a two-phase mixture consisting of a granular material and a carrier fluid. The assumptions upon which this mixture-theoretic formalism is based are the following.

- **i.** Each phase is treated as a continuum thermodynamic system.
- **ii.** The two thermodynamic continua are immiscible but occupy the same space. More specifically, they fill completely the space that they occupy (saturation condition).
- **iii.** The two thermodynamic continua are open to each other and at non-equilibrium. As such, they interact with each other in the form of momentum and energy exchanges. Herein, the absence of chemical reactions or phase transformations is assumed.
- **iv.** The momentum and energy exchanges between the two continua are pure, *i.e.* their sum vanishes.
- **v.** The postulate of phase separation holds. In other words, dissipative phenomena associated with only one phase depend exclusively on the variables of this phase.
- **vi.** Both phases are macroscopically isotropic.

As in the previous Chapter, the indices $f$ and $s$ are used to denote quantities attributed to the fluid and granular phase, respectively. $\phi_f$ and $\phi_s$ stand for the volume fractions of the two phases. Then, the saturation condition of Assumption (ii) reads

$$\phi_f + \phi_s = 1\,. \tag{3.1}$$

The local form of the mass, momentum and energy balance laws for each phase are derived in the standard manner, *i.e.* by first writing the integral balance laws over an arbitrary control volume and then by applying successively the Reynolds transport and divergence theorems. As shown in [31], this procedure yields the following equations,

$$\frac{\partial(\rho_\alpha\phi_\alpha)}{\partial t} + \nabla\cdot(\rho_\alpha\phi_\alpha\mathbf{u}_\alpha) = 0\,, \tag{3.2}$$

$$\frac{\partial(\rho_\alpha\phi_\alpha\mathbf{u}_\alpha)}{\partial t} + \nabla\cdot(\rho_\alpha\phi_\alpha\mathbf{u}_\alpha\otimes\mathbf{u}_\alpha) + \nabla(p_\alpha\phi_\alpha) = \nabla\cdot(\phi_\alpha\mathbf{P}_\alpha) + \mathbf{f}_\alpha\,, \tag{3.3}$$

$$\frac{\partial(\rho_\alpha\phi_\alpha e^t_\alpha)}{\partial t} + \nabla\cdot(\rho_\alpha\phi_\alpha e^t_\alpha\mathbf{u}_\alpha) + \nabla\cdot(p_\alpha\phi_\alpha\mathbf{u}_\alpha) = \nabla\cdot(\phi_\alpha\mathbf{P}_\alpha\cdot\mathbf{u}_\alpha) - \nabla\cdot(\phi_\alpha\mathbf{q}_\alpha) + \mathcal{E}_\alpha\,. \tag{3.4}$$

In the above equations $\alpha = f,\, s$. Using standard notation, $\rho_\alpha$, $\mathbf{u}_\alpha$, $p_\alpha$, and $e^t_\alpha$, denote the density, velocity vector, thermodynamic pressure and total energy, respectively, of phase $\alpha$. Further, $\mathbf{P}_\alpha$ stands for the (*pressure-less*) stress tensor and $\mathbf{q}_\alpha$ for the heat-flux vector of phase $\alpha$. Finally, $\mathbf{f}_\alpha$ and and $\mathcal{E}_\alpha$ represent the interphasial momentum and energy exchanges, respectively.

In view of Assumption (iii) the following relations are set,

$$\mathbf{f} \triangleq \mathbf{f}_f = -\,\mathbf{f}_s\,, \tag{3.5}$$

$$\mathcal{E} \triangleq \mathcal{E}_f = -\,\mathcal{E}_s\,. \tag{3.6}$$

It is also convenient to decompose the interphasial energy exchange into a term related to the momentum exchange plus a remaining part,

$$\mathcal{E} = E + \mathbf{f}\cdot\mathbf{u}_s\,. \tag{3.7}$$

Next, the total energy of each phase is expressed as the sum of internal and kinetic energies, $e^t_\alpha = e_\alpha + \frac{1}{2}\mathbf{u}^2_\alpha$. Then, the above balance laws for the fluid phase are written as,

$$\frac{\mathrm{d}(\rho_f\phi_f)}{\mathrm{d}t_f} + \rho_f\phi_f\nabla\cdot\mathbf{u}_f = 0, \tag{3.8}$$

$$\rho_f\phi_f\frac{\mathrm{d}\mathbf{u}_f}{\mathrm{d}_f t} + \nabla(p_f\phi_f) = \nabla\cdot(\phi_f\mathbf{P}_f) - \mathbf{f}, \tag{3.9}$$

$$\rho_f\phi_f\frac{\mathrm{d}e_f}{\mathrm{d}_f t} + p_f\phi_f\nabla\cdot\mathbf{u}_f = \phi_f\mathbf{P}_f : \mathbf{V}_f - \nabla\cdot(\phi_f\mathbf{q}_f) - E - \mathbf{f}\cdot(\mathbf{u}_s - \mathbf{u}_f)\,, \tag{3.10}$$

whereas the balance laws for the granular phase are written as,

$$\frac{\mathrm{d}(\rho_s\phi_s)}{\mathrm{d}_s t} + \rho_s\phi_s\nabla\cdot\mathbf{u}_s = 0, \tag{3.11}$$

$$\rho_s\phi_s\frac{\mathrm{d}\mathbf{u}_s}{\mathrm{d}_s t} + \nabla(p_s\phi_s) = \nabla\cdot(\phi_s\mathbf{P}_s) + \mathbf{f}, \tag{3.12}$$

$$\rho_s\phi_s\frac{\mathrm{d}e_s}{\mathrm{d}_s t} + p_s\phi_s\nabla\cdot\mathbf{u}_s = \phi_s\mathbf{P}_s : \mathbf{V}_s - \nabla\cdot(\phi_s\mathbf{q}_s) + E. \tag{3.13}$$

In the above equations, $\mathbf{V}_\alpha$ denotes the strain-rate tensor, $\mathbf{V}_\alpha = \frac{1}{2}\left(\nabla\mathbf{u}_\alpha + \nabla\mathbf{u}_\alpha^{\mathrm{T}}\right)$. Also, the double-dot symbol, $(:)$, represents the double interior product between two second-order tensors. Finally, the material time derivative with respect to the velocity of phase $\alpha$ is defined as,

$$\frac{\mathrm{d}(\cdot)}{\mathrm{d}_\alpha t} = \frac{\partial(\cdot)}{\partial t} + \mathbf{u}_\alpha\cdot\nabla(\cdot)\,. \tag{3.14}$$

One might argue that the energy equations in (3.4) are symmetric whereas equations (3.10) and (3.13) are not. However, this is merely an apparent asymmetry and is due to the particular decomposition of $\mathcal{E}$ that was introduced in (3.7). More specifically, it is straightforward to show that all decompositions of the form $\mathcal{E} = E + \mathbf{f}\cdot(c_1\mathbf{u}_s + c_2\mathbf{u}_f)$, with $c_1$ and $c_2$ constants, result in the same constitutive relations. In other words, the particular choice of the constants $c_1$ and $c_2$ is inconsequential to the final results.

The thermodynamic state of each phase is specified by its state vector and thus its Gibbs relation. The fluid phase is assumed to consists of a simple, homogeneous fluid. As such, its state vector is $(e_f, \rho_f)^T$ and the corresponding Gibbs relations reads,

$$T_f\mathrm{d}s_f = \mathrm{d}e_f - \frac{p_f}{{\rho_f}^2}\mathrm{d}\rho_f\,, \tag{3.15}$$

where $s_f$ stands for the entropy of the fluid.

As regards the granular phase, one must consider that it can perform additional reversible work due to its microstructure and that this work will depend on the volume that grains occupy and on the properties of the fluid-granular conglomerate interface. For this reason, an adequate description of the state of the granular material requires additional field variables. The exact number of such variables remains an open question but a consensus in literature is being built that the standard state vector of simple fluids, here $(e_s, \rho_s)^T$, should be augmented by at least two variables: the volume fraction, $\phi_s$, and its gradient, $\nabla\phi_s$, [26–28, 30, 48, 66, 72, 89, 96, 118–120]. Then, the usual Gibbs relation is modified to accommodate the reversible work of the additional variables as follows,

$$T_s \mathrm{d}s_s = \mathrm{d}e_s - \frac{p_s}{{\rho_s}^2}\mathrm{d}\rho_s - \frac{\beta_s}{\rho_s\phi_s}\mathrm{d}\phi_s - \frac{1}{\rho_s\phi_s}\mathbf{h}_s \cdot \mathrm{d}(\nabla\phi_s)\,. \tag{3.16}$$

In this equation $s_s$ stands for the entropy of the granular phase. The quantities $\beta_s$ and $\mathbf{h}_s$ are defined as the partial derivatives of $s_s$ with respect to $\phi_s$ and $\nabla\phi_s$, respectively. They can equivalently be defined with respect to the Helmholtz free energy $\psi_s$ of the solid phase, so that

$$\beta_s = \rho_s\phi_s\left(\frac{\partial\psi_s}{\partial\phi_s}\right)_{T_s,\rho_s,\nabla\phi_s}, \quad \mathbf{h}_s = \rho_s\phi_s\left(\frac{\partial\psi_s}{\partial\nabla\phi_s}\right)_{T_s,\rho_s,\phi_s}. \tag{3.17}$$

According to the Gibbs relation (3.16), $\beta_s$ is the force conjugate to the variable $\phi_s$ to $\phi_s$. It is often referred to as intergranular stress or configuration pressure; see, for example, [27], [121] and [122] for dry granular materials, as well as [28], [30, 66] and [123] for fluid-saturated ones. Physically, it describes the continuum manifestation of contact stresses resulting from strains due to integranular interactions and, in particular, the resistance of grains to compaction. Herein, these contact stresses are modeled as purely elastic ones and thus the third term on the right-hand-side of the Gibbs relation (3.16) accounts for the total work of these stresses; a more elaborate discussion can be found in [29]. Quasi-static compaction experiments have shown that $\beta_s \geq 0$ [124, 125]. In other words, the intergranular stress is of purely repulsive nature.

As regards $\mathbf{h}_s$, the presumed macroscopic isotropy of the granular material implies that its free energy is an isotropic function, so that $\mathbf{h}_s$ can be written as

$$\mathbf{h}_s = \gamma_s\nabla\phi_s\,, \qquad \gamma_s = 2\rho_s\phi_s\left(\frac{\partial\psi_s}{\partial|\nabla\phi_s|^2}\right)_{T_s,\rho_s,\phi_s}. \tag{3.18}$$

In this manner, the term $\gamma_s$ is the quantity conjugate to $|\nabla\phi_s|^2$. This quantity is related to stresses that are developed due to rearrangements of the interfacial area density. At this point, a couple of comments regarding the introduction of $\nabla\phi_s$ as an additional variable are due. First it is noted that, as shown in [31], $\nabla\phi_s$ is a measure of the interfacial area density and, as such, relates directly to the microstructure of the system. Also, as demonstrated by [126], the description of stresses related to variations of the interfacial area density within thermodynamically consistent theories requires that the free energy of the material is a function of the volume fraction gradient. As regards the physical meaning of these stresses, it should be noted that macroscopically the interface between a granular material and the interstitial fluid is not a sharp discontinuity; instead it has a non-zero thickness, thus constituting a thin transition layer. Within this layer, the steep volume fraction gradients result in Korteweg stress, *i.e.* a weak interfacial tension that resembles surface tension, [127].

Finally, with respect to the Gibbs relation for the granular phase, it is remarked that this work is concerned with granular suspensions that are by definition non-colloidal, *i.e.* the Péclet numbers are high. For this reason, the Gibbs relation (3.16) does not contain any term related to Brownian effects.

Next, the mass-averaged density $\rho$, velocity $\mathbf{u}$ and entropy $s$ of the mixture are defined as follows,

$$\rho = \rho_s \phi_s + \rho_f \phi_f \,, \tag{3.19}$$

$$\mathbf{u} = \frac{\rho_s \phi_s \mathbf{u}_s + \rho_f \phi_f \mathbf{u}_f}{\rho} \,, \tag{3.20}$$

$$s = \frac{s_s \rho_s \phi_s + s_f \rho_f \phi_f}{\rho} \,. \tag{3.21}$$

As is the case for any observable field, the mixture entropy obeys a balance law of the form

$$\rho \frac{\mathrm{d}s}{\mathrm{d}t} + \nabla \cdot \mathbf{J}^s = \sigma \,, \tag{3.22}$$

where $\mathbf{J}^s$ represents the entropy flux and $\sigma$ the entropy production rate. In this relation the material derivative of the entropy is taken with respect to the mass-averaged velocity, that is,

$$\frac{\mathrm{d}(\cdot)}{\mathrm{d}t} = \frac{\partial(\cdot)}{\partial t} + \mathbf{u} \cdot \nabla(\cdot). \tag{3.23}$$

According to the second thermodynamic axiom, the entropy production rate is non-negative,

$$\sigma \geq 0 \,. \tag{3.24}$$

Upon combination of equations (3.8) and (3.11) with the definitions of the mass-averaged quantities (3.19), (3.20) and (3.21), the following expression for the material derivative of the mixture entropy $s$ is obtained.

$$\rho \frac{\mathrm{d}s}{\mathrm{d}t} = \nabla \cdot \left( \rho_f \phi_f s_f (\mathbf{u}_f - \mathbf{u}) + \rho_s \phi_s s_s (\mathbf{u}_s - \mathbf{u}) \right) + \rho_f \phi_f \frac{\mathrm{d}s_f}{\mathrm{d}t_f} + \rho_s \phi_s \frac{\mathrm{d}s_s}{\mathrm{d}t_s} \,. \tag{3.25}$$

## 3.3 Derivation of the constitutive relations

In this Section constitutive relations are derived for the dissipative and relaxation phenomena that occur in granular suspensions, by exploiting the constraints imposed by the second thermodynamic axiom (3.24).

The starting point is the rate equation for the mixture entropy (3.25). This equation can be expanded further upon introduction of the Gibbs relations (3.15) and (3.16) and the balance laws (3.8) – (3.13). By doing so and by collecting terms, one obtains the balance equation for the mixture entropy. This equation has the form of (3.22) with the entropy flux $\mathbf{J}^s$ given by

$$\mathbf{J}^s = \rho_f \phi_f s_f (\mathbf{u}_f - \mathbf{u}) + \rho_s \phi_s s_s (\mathbf{u}_s - \mathbf{u}) + \frac{\phi_f}{T_f}\mathbf{q}_f + \frac{\phi_s}{T_s}\mathbf{q}_s + \frac{\gamma_s}{T_s}\frac{\mathrm{d}\phi_s}{\mathrm{d}_s t}\nabla\phi_s\,,$$

and the entropy production rate $\sigma$ given by

$$\begin{aligned}\sigma =& E\left(\frac{1}{T_s} - \frac{1}{T_f}\right) + \frac{\mathrm{d}\phi_s}{\mathrm{d}t_s}\left(\frac{p_s - \beta_s}{T_s} - \frac{p_f}{T_f} + \nabla\cdot\left(\frac{\gamma_s}{T_s}\nabla\phi_s\right)\right) + \mathbf{f}\cdot\left(\frac{\mathbf{u}_f}{T_f} - \frac{\mathbf{u}_s}{T_s}\right) - \\ & \frac{p_f}{T_f}\nabla\phi_s\cdot(\mathbf{u}_f - \mathbf{u}_s) + \phi_f\mathbf{q}_f\cdot\nabla\left(\frac{1}{T_f}\right) + \phi_s\mathbf{q}_s\cdot\nabla\left(\frac{1}{T_s}\right) + \frac{\phi_f}{T_f}\mathbf{P}_f : \mathbf{V}_f + \\ & \frac{1}{T_s}\left(\phi_s\mathbf{P}_s + \mathbf{C}_s\right) : \mathbf{V}_s\,. \end{aligned} \tag{3.26}$$

In the last equation, the second-order tensor $\mathbf{C}_s$ is defined as

$$\mathbf{C}_s \triangleq \mathbf{h}_s \otimes \nabla\phi_s = \gamma_s \nabla\phi_s \otimes \nabla\phi_s\,. \tag{3.27}$$

where the symbol $\otimes$ denotes the dyadic product between two vectors.

The next step follows the proposition of [29], who advocated to treat the differences $(T_s - T_f)$, $(p_s - \beta_s - p_f)$, and $(\mathbf{u}_s - \mathbf{u}_f)$ as independent forces that drive the system toward equilibrium. This amounts to collecting the terms related to these differences in the expression for $\sigma$ above. Accordingly, the following two decompositions are performed,

$$\left(\frac{p_s}{T_s} - \frac{p_f}{T_f}\right) = \left(\frac{1}{T_s} - \frac{1}{T_f}\right)p_f + \frac{1}{T_s}(p_s - p_f), \tag{3.28}$$

$$\left(\frac{\mathbf{u}_s}{T_s} - \frac{\mathbf{u}_f}{T_f}\right) = \left(\frac{1}{T_s} - \frac{1}{T_f}\right)\mathbf{u}_s + \frac{1}{T_f}(\mathbf{u}_s - \mathbf{u}_f). \tag{3.29}$$

As will be shown below, these decompositions have important implications to the rate equation for $\phi_s$, especially in the incompressible limit; see also [63]. To be more explicit, this decomposition was chosen so as, in the limit, the thermomechanical model be able to predict dilatancy of the granular medium; see Section 3.5 below. By contrast, in the model proposed by [26] this particular grouping of terms was not introduced. Consequently, that model cannot predict dilatancy of the granular material for constant-density flows, as has been mentioned in Chapter 2; cf. also [62].

Further, the deviatoric parts of $\mathbf{V}_f$ and $\mathbf{P}_f$ are denoted as $\mathbf{V}_f^d$ and $\mathbf{P}_f^d$, respectively. They are defined by the standard decompositions

$$\mathbf{V}_f^d = \mathbf{V}_f - \frac{1}{3}(\mathrm{tr}\mathbf{V}_f)\,\mathbf{I}, \qquad \mathbf{P}_f^d = \mathbf{P}_f + p_f^v\,\mathbf{I}\,, \tag{3.30}$$

with $p_f^v$ being the bulk viscous pressure of the fluid phase. The reason for not applying this decomposition to the granular phase will become evident below in the Chapter. By substituting relations (3.28), (3.29) and (3.30) to (3.26), the following expression is obtained for $\sigma$,

$$\begin{aligned}\sigma = &\left(E + \frac{\mathrm{d}\phi_s}{\mathrm{d}_s t}p_f\right)\left(\frac{1}{T_s} - \frac{1}{T_f}\right) + \frac{\mathrm{d}\phi_s}{\mathrm{d}t_s}\left(\frac{p_s - \beta_s - p_f}{T_s} + \nabla\cdot\left(\frac{\gamma_s}{T_s}\nabla\phi_s\right)\right) - \\ &\frac{\phi_f}{T_f}p_f^v\nabla\cdot\mathbf{u}_f + \frac{1}{T_f}\left(\mathbf{f} - p_f\nabla\phi_s\right)\cdot(\mathbf{u}_f - \mathbf{u}_s) + \phi_f\mathbf{q}_f\cdot\nabla\left(\frac{1}{T_f}\right) + \phi_s\mathbf{q}_s\cdot\nabla\left(\frac{1}{T_s}\right) + \\ &\frac{\phi_f}{T_f}\mathbf{P}_f^d : \mathbf{V}_f^d + \frac{1}{T_s}\left(\phi_s\mathbf{P}_s + \mathbf{C}_s\right) : \mathbf{V}_s\,.\end{aligned} \tag{3.31}$$

Next it is observed that, in view of (3.31), the entropy production rate is expressed as a sum of products with each product being associated to a particular dissipative process. In other words, the entropy production rate $\sigma$ can be written as

$$\sigma = \sum_{i=1}^{8} X_i Y_i\,. \tag{3.32}$$

In this expression, the quantities $X_i$ are identified as the *thermodynamic forces*, while the quantities $Y_i$ are identified as the *thermodynamic currents*. More specifically, in view of (3.31), the thermodynamic forces are

$$\begin{aligned}X_i \in \Bigg\{ &\left(\frac{1}{T_s} - \frac{1}{T_f}\right),\ \frac{1}{T_s}\left(p_s - \beta_s - p_f + T_s\nabla\cdot\left(\frac{\gamma_s}{T_s}\nabla\phi_s\right)\right),\ \nabla\cdot\mathbf{u}_f, \\ &(\mathbf{u}_f - \mathbf{u}_s),\ \nabla\left(\frac{1}{T_f}\right),\ \nabla\left(\frac{1}{T_s}\right),\ \mathbf{V}_f^d,\ \mathbf{V}_s\Bigg\},\end{aligned} \tag{3.33}$$

whereas the thermodynamic currents are

$$\begin{aligned}Y_i \in \Bigg\{ &\left(E + \frac{\mathrm{d}\phi_s}{\mathrm{d}_s t}p_f\right),\ \frac{\mathrm{d}\phi_s}{\mathrm{d}_s t},\ -\frac{\phi_f}{T_f}p_f^v,\ \frac{1}{T_f}\left(\mathbf{f} - p_f\nabla\phi_s\right),\ \phi_f\mathbf{q}_f,\ \phi_s\mathbf{q}_s,\ \frac{\phi_f}{T_f}\mathbf{P}_f^d, \\ &\frac{1}{T_s}(\phi_s\mathbf{P}_s + \mathbf{C}_s)\Bigg\}.\end{aligned} \tag{3.34}$$

It should be noted that both thermodynamic forces and currents vanish at equilibrium. Moreover, the entropy inequality (3.24) is written as

$$\sigma = \sum_{i=1}^{8} X_i Y_i \geq 0\,. \tag{3.35}$$

At this point the thermodynamic currents are expressed as function of the forces. For all but the last of the currents above linear relationships between currents and forces are assumed. This is equivalent to considering the Taylor expansions of these currents with respect to the forces around an equilibrium state and keeping the first-order terms of these expansions. In this manner the following relation is obtained,

$$Y_i = \sum_j L_{ij} X_j, \quad i = 1, \ldots 7\,. \tag{3.36}$$

The coefficients $L_{ij}$ are the so-called phenomenological coefficients. By virtue of the presumed macroscopic isotropy of the two phases and of the representation theorem of linear isotropic tensors, the phenomenological coefficients above are scalars. Actually, the decompositions given by (3.30) were introduced so as to make more convenient the application of the representation theorem for the viscous stresses acting on the fluid.

As regards the off-diagonal elements of the matrix of phenomenological coefficients, it is remarked that coefficients that couple a current and a force of difference tensorial order vanish; this is a consequence of the representation theorem of linear isotropic tensors. Further, according to the principle of phase separation, coefficients that couple currents related to only one phase (such as the heat fluxes $\mathbf{q}_f$ and $\mathbf{q}_s$) with forces that depend on state variables of the other phase, vanish as well. Consequently, the only non-vanishing off-diagonal phenomenological coefficients are $L_{12}$ and $L_{21}$. Also, by assuming the validity of Onsager reciprocity relations, these two coefficients are equal. Then, the only non-zero phenomenological coefficients are the following,

$$L_{ii}\,,\ i = 1, \ldots 7\,, \quad \text{and} \quad L_{12} = L_{21}\,. \tag{3.37}$$

By virtue of the above equation and the linear relations (3.36), the entropy inequality (3.35) yields

$$\sigma = \sum_{i=1}^{7} L_{ii} X_i^2 + 2L_{12} X_1 X_2 + X_8\, Y_8 \geq 0\,, \tag{3.38}$$

with

$$X_8 = \mathbf{V}_s, \quad Y_8 = \frac{1}{T_s}(\phi_s \mathbf{P}_s + \mathbf{C}_s)\,. \tag{3.39}$$

The current $Y_8$ has been singled out and will be treated separately because it represents the viscous stresses acting on the granular phase (divided by $T_s$). These stresses have a manifestly non-Newtonian behaviour that cannot be described by a purely linear theory. Accordingly, the detailed derivation of their constitutive relations is provided separately in the next Subsection. For the time-being it is remarked that, by the principle of phase separation, $Y_8$ can only be a function of $X_8$ and possibly $X_6 = \nabla T_s^{-1}$. If the dependence on temperature gradients is assumed to be linear then, by virtue of the representation theorem of linear isotropic tensors, the dependence of $Y_8$ on $X_6$ vanishes. Therefore, $Y_8$ becomes a function of $X_8$ only.

Furthermore, since $X_8$ is independent of the other thermodynamic forces, the entropy inequality (3.38) requires that the matrix of phenomenological coefficients $L_{ij}$ be positive definite and that the product $X_8 Y_8$ be positive. In other words, the entropy inequality (3.38) is equivalent to the following conditions that should be independently satisfied,

$$\begin{cases} L_{ii} \geq 0\,, \quad i = 1, \ldots 7\,, \\ L_{12}^2 \leq L_{11} L_{22}\,, \\ X_8 Y_8 \geq 0\,. \end{cases} \tag{3.40}$$

Finally, before deriving the constitutive relation for $Y_8$, it is worth pointing out that the phenomenological coefficients $L_{ii}$ and $L_{12}$ can be recast in terms of transport coefficients. Those involving only one phase can be written as

$$L_{44} = \phi_f T_f^2\, \kappa_f\,, \quad L_{55} = \phi_s T_s^2\, \kappa_s\,, \quad L_{66} = \frac{\phi_f}{T_f}\, \zeta_f\,, \quad L_{77} = \frac{\phi_f}{T_f}\, \mu_f\,. \tag{3.41}$$

where $\kappa_f$ and $\kappa_s$ are the thermal conductivities of the two phases, while $\mu_f$ and $\zeta_f$ are the first and second viscosity coefficients of the Newtonian stress tensor of the fluid phase, respectively.

The remaining phenomenological coefficients are related to interactions between the two phases and can be cast in the form of transport coefficients via the following definitions,

$$L_{11} = T_f T_s\, \xi, \quad L_{22} = \phi_f \phi_s T_s \frac{1}{\mu_c}, \quad L_{33} = \frac{1}{T_f}\, \delta, \quad L_{12} = L_{21} = T_f T_s \phi_f \phi_s \lambda. \tag{3.42}$$

In the above, $\xi$ represents the interphasial heat transfer coefficient while $\delta$ represents the coefficient of interphasial drag. Also, $\mu_c$ has dimensions of viscosity and is commonly referred to as *compaction viscosity*. It expresses responsiveness of the granular material to compaction. Finally, $\lambda$ is a coefficient for cross effect of the variation of $\phi_s$ due to thermal non-equilibrium between the two phases; in other words, $\lambda$ expresses the capacity of the granular material to compact due to thermal loadings. According to the first of inequalities (3.40), all these transport coefficients are positive except for $\lambda$ whose sign cannot be constrained on the basis of thermodynamics. Nonetheless, its amplitude is constrained by the second of inequalities (3.40) according to which,

$$\lambda^2 \leq \frac{\xi}{\phi_s \phi_f \, T_f \, \mu_c} \, . \tag{3.43}$$

### 3.3.1 Constitutive relations for the viscous stresses of the granular phase

As mentioned above, the current $Y_8$ is a function of $X_8$ only. The starting point for the derivation of a constitutive relation for $Y_8$ is the general representation theorem for isotropic tensors, [128]. According to it, the expression for $Y_8$ reads,

$$Y_8 = \frac{1}{T_s}(\phi_s \mathbf{P}_s + \mathbf{C}_s) = \mathcal{G}(\mathbf{V}_s) = g_0 \mathbf{I} + g_1 \mathbf{V}_s + g_2 \mathbf{V}_s \cdot \mathbf{V}_s \, , \tag{3.44}$$

where the coefficients $g_0$, $g_1$ and $g_2$ are functions of the principal invariants of the strain-rate tensor $\mathbf{V}_s$ and of the state variables of the granular phase.

In the derivation of the sought-after nonlinear constitutive expression for $Y_8$ it is further required that $Y_8$ be non-singular and tend to zero as $\mathbf{V}_s$ vanishes, *i.e.* at equilibrium. It is also noted that the component $\mathbf{C}_s$ of $Y_8$ is a function of the state variable $\nabla \phi_s$, cf. definition (3.27), which implies that it describes elastic stresses. As such, $\mathbf{C}_s$ does not vanish at equilibrium. In other words, the pressure-less stress tensor $\mathbf{P}_s$ consists of an elastic component stemming from $\mathbf{C}_s$ plus a viscous component stemming from $Y_8$ which should tend to zero at equilibrium.

Additionally, according to accumulated experimental and numerical evidence, the viscous stresses acting on granular suspensions admit a "first-order scaling" with respect to the shear rate $\dot{\gamma}$. More specifically, in experiments of simple shear flow in the viscous regime, these stresses are found to be linear with respect to $|\dot{\gamma}|$, [57], [58] and [59]. The same has also been predicted in the simulations of [102], [108] and [103] that were based on Stokesian dynamics.

Guided by this evidence, a constitutive relation is sought for $Y_8$ that extends this scaling with respect to the shear rate to more general flows. Actually, this idea is not new and has been examined before by, among others, [129] and [83] who proposed a linear scaling with $\sqrt{\mathbf{V}_s : \mathbf{V}_s}$. It should be noted, however, that a scaling with this quantity cannot provide by itself a tensorial representation of the stresses because this quantity is a scalar.

Herein, it is proposed to extend this scaling to the tensorial representation (3.44) by considering positive homogeneous functions of degree one in $\mathbf{V}_s$, so that

$$\mathcal{G}(k \, \mathbf{V}_s) = k \, \mathcal{G}(\mathbf{V}_s) \, , \quad \forall \, k \geq 0 \, . \tag{3.45}$$

Next, the following invariants $l_1$, $l_2$ and $l_3$ of $\mathbf{V}_s$ are introduced,

$$l_1 = \mathrm{I}_{\mathbf{v}_s}, \quad l_2 = (J_{\mathbf{v}_s})^{\frac{1}{2}} = (-2\,\mathrm{II}_{\mathbf{v}_s} + \frac{2}{3}{\mathrm{I}_{\mathbf{v}_s}}^2)^{\frac{1}{2}}, \quad l_3 = (\mathrm{III}_{\mathbf{v}_s})^{\frac{1}{3}}, \tag{3.46}$$

where $\mathrm{I}_{\mathbf{v}_s}$, $\mathrm{II}_{\mathbf{v}_s}$ and $\mathrm{III}_{\mathbf{v}_s}$ are the principal invariants of $\mathbf{V}_s$. It can be directly verified that $l_1$, $l_2$ and $l_3$ are homogeneous of degree one. Also, the following identity holds for $J_{\mathbf{v}_s}$,

$$J_{\mathbf{v}_s} \triangleq \mathbf{V}_s^d : \mathbf{V}_s^d. \tag{3.47}$$

Since $J_{\mathbf{v}_s}$ is positive, there are bijective relations between the following invariant triplets,

$$(\mathrm{I}_{\mathbf{v}_s}, \mathrm{II}_{\mathbf{v}_s}, \mathrm{III}_{\mathbf{v}_s}) \iff (\mathrm{I}_{\mathbf{v}_s}, J_{\mathbf{v}_s}, \mathrm{III}_{\mathbf{v}_s}) \iff (l_1, l_2, l_3) \tag{3.48}$$

so that the quantities $g_0$, $g_1$ and $g_2$ appearing in equation (3.44) can be considered as functions of the invariants $l_1$, $l_2$ and $l_3$. Further, in view of the tensorial representation (3.44), equation (3.45) implies the following homogeneity constraints on these quantities,

$$g_0(kl_1, kl_2, kl_3) = k\, g_0(l_1, l_2, l_3), \tag{3.49}$$

$$g_1(kl_1, kl_2, kl_3) = g_1(l_1, l_2, l_3), \tag{3.50}$$

$$g_2(kl_1, kl_2, kl_3) = \frac{1}{k}\, g_2(l_1, l_2, l_3)\,. \tag{3.51}$$

Since $g_2$ is homogeneous of degree $-1$, one has to verify that the boundedness constraint of $Y_8$ holds for any finite $\mathbf{V}_s$. To this it is noted that, since

$$\mathbf{V}_s : \mathbf{V}_s = \left( \frac{l_1^2}{3} + l_2^2 \right), \tag{3.52}$$

one can define

$$\tilde{g}_2 = g_2 \sqrt{\frac{l_1^2}{3} + l_2^2}\,, \tag{3.53}$$

with $\tilde{g}_2$ homogeneous of degree zero. Then, the third term on the right-hand side of (3.44) is written as

$$g_2 \mathbf{V}_s \cdot \mathbf{V}_s = \frac{\tilde{g}_2}{\sqrt{\frac{l_1^2}{3} + l_2^2}} \mathbf{V}_s \cdot \mathbf{V}_s\,. \tag{3.54}$$

According to this equation, if $\tilde{g}_2$ is bounded, then the term $g_2 \mathbf{V}_s \cdot \mathbf{V}_s$ is always bounded and vanishes as $\mathbf{V}_s \to 0$.

A simple choice to satisfy the homogeneity requirements on $g_0$, $g_1$ and $\tilde{g}_2$ would be to take the series expansions of these quantities up to the degree of homogeneity. This would yield

$$g_0 = (c_1 l_1 + c_2 l_2 + c_3 l_3), \quad g_1 = c_4, \quad \tilde{g}_2 = c_5\,, \tag{3.55}$$

with the coefficients $c_i$ being functions of the state variables of the granular phase but independent of $\mathbf{V}_s$. However, as it turns out, this simple choice is unsatisfactory because it leads to the appearance of the third-order term

$$(\mathbf{V}_s \cdot \mathbf{V}_s) : \mathbf{V}_s = \frac{3}{2} l_1 l_2^2 + l_3^3 \tag{3.56}$$

in the product $X_8 Y_8$.The sign of this term is undetermined and so would be the sign of the product $X_8 Y_8$, since (3.56) is the highest-order term. This, in turn, implies that the entropy inequality would not be satisfied.

This conundrum can be circumvented by modifying the expressions (3.55), so as to remove the third-order term (3.56) from the entropy inequality. This is achieved by splitting the term (3.56) into two components and by subtracting one component from $g_0$ and the other component from $g_1$, respectively. In this manner, the proposed expressions for $g_0$ and $g_1$ read,

$$g_0 = (c_1 l_1 + c_2 l_2 + c_3 l_3) - \frac{3}{2} \frac{\tilde{g}_2}{\sqrt{\dfrac{l_1^2}{3} + l_2^2}} l_2^2 \tag{3.57}$$

$$g_1 = c_4 - \tilde{g}_2 \frac{l_3^3}{\left(\frac{l_1^2}{3} + l_2^2\right)^{\frac{3}{2}}}\,. \tag{3.58}$$

By introducing the above expressions for $g_0$ and $g_1$ and the aforementioned expression $\tilde{g}_2 = c_5$, one arrives at the following expression for the pressure-less stress tensor $\mathbf{P}_s$,

$$\begin{aligned}(\phi_s \mathbf{P}_s + \mathbf{C}_s) = &\left( c_1 l_1 + c_2 l_2 + c_3 l_3 - c_5 \frac{3\, l_2^2}{2\sqrt{\dfrac{l_1^2}{3} + l_2^2}} \right) \mathbf{I} + \\ &\left( c_4 - c_5 \frac{l_3^3}{\left(\dfrac{l_1^2}{3} + l_2^2\right)^{\frac{3}{2}}} \right) \mathbf{V}_s + c_5 \frac{1}{\sqrt{\dfrac{l_1^2}{3} + l_2^2}} \mathbf{V}_s \cdot \mathbf{V}_s\,. \end{aligned} \tag{3.59}$$

It is straightforward to verify that this representation satisfies the homogeneity requirements (3.49)–(3.51). Furthermore, it is continuous with respect to its arguments, non-singular and tends to zero at equilibrium.

Also, with the above representation, the third inequality in (3.40) stemming from the second thermodynamic axiom reads,

$$\frac{1}{T_s}(\phi_s \mathbf{P}_s + \mathbf{C}_s) : \mathbf{V}_s = \frac{1}{T_s}(c_1 l_1 + c_2 l_2 + c_3 l_3) l_1 + \frac{1}{T_s} c_4 \left( \frac{{l_1}^2}{3} + {l_2}^2 \right) \geq 0. \tag{3.60}$$

This implies the following constraints on the coefficients $c_i$,

$$c_3 = 0, \quad c_4 \geq 0, \quad \left( c_1 + \frac{c_4}{3} \right) \geq 0, \quad {c_2}^2 \leq 4 c_4 \left( c_1 + \frac{c_4}{3} \right). \tag{3.61}$$

Next, the second term on the right-hand side of (3.59) can be decomposed into a deviatoric and an isotropic component so that this equation is written in the following form,

$$\begin{aligned}(\phi_s \mathbf{P}_s + \mathbf{C}_s) \; = \; & \left( c_1 + \frac{c_4}{3} - \frac{c_5}{3} \frac{\det \mathbf{V}_s}{(\mathbf{V}_s : \mathbf{V}_s)^{\frac{3}{2}}} \right) (\nabla \cdot \mathbf{u}_s) \, \mathbf{I} + \\ & \left( c_4 - c_5 \frac{\det \mathbf{V}_s}{(\mathbf{V}_s : \mathbf{V}_s)^{\frac{3}{2}}} \right) \mathbf{V}_s^d + \\ & \left( c_2 \sqrt{\mathbf{V}_s^d : \mathbf{V}_s^d} - \frac{3}{2} c_5 \frac{\mathbf{V}_s^d : \mathbf{V}_s^d}{\sqrt{\mathbf{V}_s : \mathbf{V}_s}} \right) \mathbf{I} + \\ & \left( c_5 \frac{1}{\sqrt{\mathbf{V}_s : \mathbf{V}_s}} \right) \mathbf{V}_s \cdot \mathbf{V}_s \, . \end{aligned} \tag{3.62}$$

According to the above relation, two *generalized* Newtonian stress components can be identified by setting,

$$\zeta_s \phi_s = \left( c_1 + \frac{c_4}{3} - \frac{c_5}{3} \frac{\det \mathbf{V}_s}{(\mathbf{V}_s : \mathbf{V}_s)^{\frac{3}{2}}} \right), \quad 2 \mu_s \phi_s = \left( c_4 - c_5 \frac{\det \mathbf{V}_s}{(\mathbf{V}_s : \mathbf{V}_s)^{\frac{3}{2}}} \right). \tag{3.63}$$

The coefficients $\mu_s$ and $\zeta_s$ are interpreted as the first and second (bulk) viscosity of the granular phase. It is interesting to observe that the representation (3.62) reduces to that of a Newtonian fluid when $c_2 = c_5 = 0$. In this limiting case, the constraints (3.61) translate to $\mu_s \geq 0$ and $\zeta_s \geq 0$, as expected. Nonetheless, according to (3.63), in the general case and for three-dimensional flows where $\det \mathbf{V}_s \neq 0$, there are additional contributions to $\mu_s$ and $\zeta_s$ that depend on the strain rate.

Also, the sum of the remaining terms in (3.62),

$$\left( c_2 \sqrt{\mathbf{V}_s^d : \mathbf{V}_s^d} - \frac{3}{2} c_5 \frac{\mathbf{V}_s^d : \mathbf{V}_s^d}{\sqrt{\mathbf{V}_s : \mathbf{V}_s}} \right) \mathbf{I} + \left( c_5 \frac{1}{\sqrt{\mathbf{V}_s : \mathbf{V}_s}} \right) \mathbf{V}_s \cdot \mathbf{V}_s \, , \tag{3.64}$$

represents additional non-Newtonian viscous stresses of the granular phase. Its isotropic component is commonly referred to as the *suspension pressure*, see for example [108], and is responsible for the shear-induced dilatancy that is a characteristic feature of granular suspensions. Also, its deviatoric component gives rise to *normal stress differences* under simple shear that are discussed in Section 3.7.

It is also noted that, in view of (3.63), if the bulk viscosity was assumed to be zero, then the following conditions would be true: $c_5 = 0$ and $(c_1 + \frac{c_4}{3}) = 0$. These conditions must hold simultaneously because the coefficients $c_i$ do not depend on the velocity gradients. But then, the fourth constraint in (3.60), implies that $c_2 = 0$ also. In this case, the non-Newtonian viscous stresses given by (3.64) should vanish as well. However, this goes against preponderant experimental evidence that has established shear-induced dilatancy and normal-stress differences in granular suspensions. One can therefore conclude that this model excludes the possibility of a Stokes-type hypothesis for the granular phase. Bulk viscosity is notoriously difficult to measure but the prediction of a non-zero bulk viscosity is consistent with the findings of [106] who predicted non-zero $\zeta_s$ via Stokesian dynamics simulations.

Finally, for the sake of clarity of exposition, the following short-hand notation is introduced,

$$\phi_s\chi_a = \left( c_2\sqrt{\mathbf{V}_s^d : \mathbf{V}_s^d} - \frac{3}{2}c_5\frac{\mathbf{V}_s^d : \mathbf{V}_s^d}{\sqrt{\mathbf{V}_s : \mathbf{V}_s}} \right), \quad \phi_s\chi_b = c_5\frac{1}{\sqrt{\mathbf{V}_s : \mathbf{V}_s}}\,, \tag{3.65}$$

which allows to express the stress tensor $\mathbf{P}_s$ in a concise manner,

$$(\phi_s\mathbf{P}_s + \mathbf{C}_s) \; = \phi_s\zeta_s(\nabla \cdot \mathbf{u}_s)\,\mathbf{I} \, + \, 2\phi_s\mu_s\mathbf{V}_s^d \, + \, \phi_s\chi_a\mathbf{I} \, + \, \phi_s\chi_b\mathbf{V}_s \cdot \mathbf{V}_s\,. \tag{3.66}$$

It should be stressed that since the coefficients $c_i$ are functions of the state variables, so are the coefficients $\zeta_s$, $\mu_s$, $\chi_a$ and $\chi_b$. In particular, they can depend on both $\phi_s$ and $\nabla\phi_s$.

## 3.4 Post-constitutive equations

The balance laws for the two phases, (3.8)–(3.10) and (3.11)–(3.13), supplemented by the constitutive equations (3.36) and (3.66), the saturation condition (3.1), and by appropriate equations of state for each phase, constitute a closed system of governing equations for granular suspensions. Further, by combining these relations, and upon introduction of the expressions for the transport coefficients (3.41) and (3.42), the following post-constitutive equations are obtained,

*Fluid phase*

$$\frac{\mathrm{d}(\rho_f\phi_f)}{\mathrm{d}_f t} + \rho_f\phi_f\nabla \cdot \mathbf{u}_f = 0, \tag{3.67}$$

$$\rho_f\phi_f\frac{\mathrm{d}\mathbf{u}_f}{\mathrm{d}_f t} + \nabla(p_f\phi_f) = \nabla \cdot \left( (\zeta_f\nabla \cdot \mathbf{u}_f)\,\phi_f\mathbf{I} + 2\mu_f\phi_f\mathbf{V}_f^d \right) - \left(\delta(\mathbf{u}_f - \mathbf{u}_s) + p_f\nabla\phi_s\right), \tag{3.68}$$

$$
\begin{aligned}
\rho_f\phi_f\frac{\mathrm{d}e_f}{\mathrm{d}_f t} + p_f\phi_f\nabla\cdot\mathbf{u}_f = {} & 2\mu_f\phi_f\mathbf{V}_f^d : \mathbf{V}_f^d + \zeta_f\phi_f(\nabla\cdot\mathbf{u}_f)^2 + \\
& \nabla\cdot(\kappa_f\phi_f\nabla T_f) - \xi(T_f - T_s) + \\
& (\delta(\mathbf{u}_f - \mathbf{u}_s) + p_f\nabla\phi_s)\cdot(\mathbf{u}_f - \mathbf{u}_s) + p_f\frac{\mathrm{d}\phi_s}{\mathrm{d}_s t} - \\
& \lambda T_f\phi_f\phi_s\left(p_s - \beta_s - p_f + T_s\nabla\cdot\left(\frac{\gamma_s}{T_s}\nabla\phi_s\right)\right). \qquad (3.69)
\end{aligned}
$$

*Granular phase*

$$
\frac{\mathrm{d}(\rho_s\phi_s)}{\mathrm{d}_s t} + \rho_s\phi_s\nabla\cdot\mathbf{u}_s = 0, \qquad (3.70)
$$

$$
\begin{aligned}
\rho_s\phi_s\frac{\mathrm{d}\mathbf{u}_s}{\mathrm{d}_s t} + \nabla(p_s\phi_s) = {} & \nabla\cdot\big(\left(\zeta_s\nabla\cdot\mathbf{u}_s + \chi_a\right)\phi_s\mathbf{I} + 2\mu_s\phi_s\mathbf{V}_s^d + \chi_b\phi_s\mathbf{V}_s\cdot\mathbf{V}_s\big) - \\
& \nabla\cdot\mathbf{C}_s + \left(\delta(\mathbf{u}_f - \mathbf{u}_s) + p_f\nabla\phi_s\right)\,, \qquad (3.71)
\end{aligned}
$$

$$
\begin{aligned}
\rho_s\phi_s\frac{\mathrm{d}e_s}{\mathrm{d}_s t} + p_s\phi_s\nabla\cdot\mathbf{u}_s = {} & 2\mu_s\phi_s\mathbf{V}_s^d{:}\mathbf{V}_s^d + \zeta_s\phi_s(\nabla\cdot\mathbf{u}_s)^2 + \chi_a\phi_s\nabla\cdot\mathbf{u}_s - \\
& \mathbf{C}_s : \mathbf{V}_s + \chi_b\phi_s(\mathbf{V}_s\cdot\mathbf{V}_s) : \mathbf{V}_s + \nabla\cdot(\kappa_s\phi_s\nabla T_s) + \\
& \xi(T_f - T_s) - p_f\frac{\mathrm{d}\phi_s}{\mathrm{d}_s t} + \\
& \lambda T_f\phi_f\phi_s\left(p_s - \beta_s - p_f + T_s\nabla\cdot\left(\frac{\gamma_s}{T_s}\nabla\phi_s\right)\right). \qquad (3.72)
\end{aligned}
$$

*Compaction equation*

$$
\frac{\mathrm{d}\phi_s}{\mathrm{d}_s t} = \frac{\phi_s\phi_f}{\mu_c}\left(p_s - \beta_s - p_f + T_s\nabla\cdot\left(\frac{\gamma_s}{T_s}\nabla\phi_s\right)\right) + \lambda\,\phi_f\phi_s(T_f - T_s). \qquad (3.73)
$$

The compaction equation (3.73) describes the evolution of the volume fraction of the granular phase. It is remarked that this equation is not derived by a conservation principle; instead it is follows directly from the constitutive relations (3.36) between thermodynamic currents and forces.

An interesting property of the system is that at the limit $\phi_s \to 0$, all terms in equations (3.70)–(3.72) for the granular phase become zero, while equations (3.67)–(3.69) for the fluid reduce to the compressible Navier-Stokes equations.

It is also worth commenting on the form of the term that describes the interphasial momentum exchanges. This term reads

$$
\mathbf{f} \;=\; \delta(\mathbf{u}_f - \mathbf{u}_s) + p_f\nabla\phi_s\,, \qquad (3.74)
$$

with $\delta$ being the interphasial drag coefficient, cf. (3.42). [130] proposed the decomposition of the interphasial momentum exchange into a drag and an Archimedean-type force that actually agrees with (3.74). This expression was subsequently employed by a number of modelling efforts, such as, for example, in [40] and [41], which further report that this decomposition is really a postulate. The results of this chapter, however, show that this decomposition is dictated by the second law of thermodynamics. More specifically, discarding this term leads to a system of governing equations that violates the positivity of the entropy production rate $\sigma$. In other words, the particular form of (3.74) is not an ad hoc assumption but a necessary condition for thermodynamic consistency.

Actually, the inclusion of the term $p_f \nabla \phi_s$ has a long history that seems to be underestimated by some contemporary studies. This term is usually referred to as *nozzling term* or *non-conservative product*; see the discussion in [68] and [131]. Further, in [29] it is remarked that changes in the volume fraction can accelerate or decelerate the flow, thereby acting as a nozzle. In turn, this can engender a relative motion between the two phases. The labeling of $p_f \nabla \phi_s$ as a non-conservative product is also of interest. If one considers the inviscid limit of the above equations, then it is straightforward to show that, due to the presence of $p_f \nabla \phi_s$, these equations cannot be cast into a conservative form. As a consequence, even weak solutions cannot be defined and the corresponding Riemann problem is ill posed [132].

At this point, some remarks about the calibration of the various parameters that appear in the post-constitutive equations are appropriate. The parameters related to the fluid phase are the shear and bulk viscosities, $\mu_f$ and $\zeta_f$, and the thermal conductivity $\kappa_f$. They have been measured for a wide class of Newtonian fluids in a variety of thermodynamic conditions and their values are readily available. The situation with the parameters related to the granular phase is more complex. Due to the structure of this phase at the grain (mesoscopic) level, these parameters generally depend on $\phi_s$. For constant-density flows, various expressions for the viscosities $\mu_s$, $\chi_a$ and $\chi_b$ are available, mostly derived from shear flow experiments; see, for example, [58] , [83] and [108]. On the other hand, data for the bulk viscosity $\zeta_s$ are available only for very dilute mixtures, [106]. Also, the variation of these viscosities with temperature is largely unexplored. For the thermal conductivity $\kappa_s$, experimental correlations are available in the literature, cf. [133] and [134]. As regards $\beta_s$, relations based on quasi-static compaction experiments have been provided in [124] and [125]; see also the analysis in [29]. By contrast, no detailed experimental data are available for $\gamma_s$. For this reason, people often assume a power-law dependence on $\phi_s$ based mostly on physical intuition. As regards the parameters related to phase interactions, various correlations have been proposed for the interphasial drag and heat-transfer coefficients, $\delta$ and $\xi$, that are readily available in the literature. Much less is known for the compaction viscosity $\mu_c$. It is often considered to be a constant whose magnitude is approximated via simplified transport models, [67]. Similarly, no data are available for the off-diagonal coefficient $\lambda$. In many situations, however, one may assume that the evolution of the volume fraction $\phi_s$ depends only weakly on the thermal non-equilibrium between the two phases, especially in view of constraint (3.43). In any case, it is expected that numerical simulations based on this model, combined with available and forthcoming experimental data, will yield more accurate estimations of these parameters.

This Section is concluded with a discussion on the boundary conditions that are needed to close the above system of equations. The assignment of boundary conditions for the variables related to the fluid phase, $\mathbf{u}_f$ and $p_f$ does not pose any problem and it can be performed in the same way as in single-phase flows. For example, at rigid walls, one can assume zero slip for the fluid velocity and Neumann condition for the fluid pressure. The same is true for the pressure of the granular phase $p_s$. On the other hand, the assignment of boundary condition for $\mathbf{u}_s$ at walls requires more attention because of the possibility of slip. Appropriate slip conditions are hard to derive and are material dependent; nonetheless, some data is available in the literature [135]. Similarly, the derivation of wall conditions for the volume fraction $\phi_s$ is quite challenging. Often a Neumann condition is employed, but the value of the normal derivative is determined via the compaction equation or is zet to zero. However, these choices are dictated by convenience and the issue is still open; additional physical evidence is required in order to derive more accurate boundary conditions for $\phi_s$. Finally, as regards thermal boundary conditions at walls, quite often one may assume that the two phases are in thermal equilibrium since they are both in contact with the walls. Then, the prescription of thermal conditions can be performed in a similar manner as in single-phase flows.

## 3.5 The incompressible limit

The thermomechanical model given by equations (3.67)–(3.73) is valid for both compressible and incompressible flows. Nonetheless, in many practical applications, the velocities of the two phases are very small with respect to the speed of sound of the two phases and, consequently, compressibility effects are negligible. This is identified as the incompressible limit. In this case, one can employ the square of the smallest of the two Mach numbers as a perturbation parameter and perturb the governing equations with respect to this parameter. The result of this procedure is a system of equations, referred to as the "low-Mach-number approximation", that is simpler than the original one in several important aspects.

In this Section, the derivation of the low-Mach-number approximation for the model given by (3.67)–(3.73) is presented. The procedure is laborious but straightforward. For this reason, herein only the basic steps and the final result are described. For a more detailed explanation on the low-Mach-number approximation for two-phase flow models, the reader is referred to [62].

*Step 1.* A reference length $l_r$ and a reference velocity $u_r$ are specified. Also, for the purpose of non-dimensionalization, one considers reference values of the thermodynamic variables $\rho_r$, $T_r$, $p_r$, specific heats $c_{p_r}$ and $c_{vr}$, and transport coefficients $\mu_r$ and $\kappa_r$ with respect to a reference state of the phase with the smallest speed of sound. In most practical cases, this is the fluid phase. Herein this assumption is made as well.

*Step 2.* Equations of state are introduced for each phase. For example, the fluid can be considered to obey the ideal-gas law, so that $p_r = (c_{p_r} - c_{vr})\,\rho_r T_r$.

*Step 3.* A reference Mach number $M$ is defined as the ratio between the reference velocity and the fluid speed of sound at the reference state. Under the ideal-gas law,

$$M = \frac{u_r}{\sqrt{\frac{\hat{\gamma} p_r}{\rho_r}}}\,, \qquad \hat{\gamma} = \frac{c_{p_r}}{c_{vr}}\,. \tag{3.75}$$

Then, the perturbation parameter $\epsilon$ is defined as

$$\epsilon \triangleq \hat{\gamma} M^2\,, \tag{3.76}$$

*Step 4.* The governing equations and the equations of state are non-dimensionalized with respect to the reference quantities.
*Henceforth in this Chapter, in order to avoid the introduction of additional symbols, every variable is understood to be non-dimensionalized (except for the reference quantities).*

*Step 5.* All variables are expanded in perturbation series of powers of $\epsilon$. For example,

$$p_s = p_s^0 + \epsilon p_s^1 + \dots\,, \qquad \mathbf{u}_s = \mathbf{u}_s^0 + \epsilon \mathbf{u}_s^1 + \dots\,, \qquad \text{etc.} \tag{3.77}$$

where the superscript refers to the order of a term in the expansion.

*Step 6.* The perturbation expansions of all variables are inserted into the governing system of equations and the terms of the same order are collected.

The results are presented below. *Henceforth, in order to avoid unnecessary complexity in the notation, all quantities are supposed to represent the zero-order term of the expansions and, therefore, the superscript zero is dropped.* For example, $p_s^0$ is now written as $p_s$ etc. The only exception to this convention is for the first-order terms of the pressures which will still be denoted as $p_s^1$ and $p_f^1$. These are typically referred to as "dynamic pressures", whereas the zeroth-order terms are referred to as "thermodynamic pressures".

At order $O(\epsilon^{-1})$ the momentum equations of the two phases (3.68) and(3.71) yield,

$$\nabla(p_f \phi_f) + p_f \nabla(\phi_s) = 0\,, \tag{3.78}$$

$$\nabla(p_s \phi_s) - p_f \nabla(\phi_s) = 0\,. \tag{3.79}$$

Since $p_f$, $p_s$ and $\phi_s$ are independent variables, equations (3.78) and (3.79) reduce to

$$\nabla p_s = 0 = \nabla p_f\,, \quad \text{and} \quad p \triangleq p_s(t) = p_f(t)\,. \tag{3.80}$$

Also, in view of this equation, the compaction equation is identically satisfied at order $O(\epsilon^{-1})$. Further, at order $O(1)$, one obtains the following equations.

*Fluid phase*

$$\frac{\mathrm{d}(\rho_f\phi_f)}{\mathrm{d}_f t} + \rho_f\phi_f\nabla\cdot\mathbf{u}_f = 0\,, \tag{3.81}$$

$$\rho_f\phi_f\frac{\mathrm{d}\mathbf{u}_f}{\mathrm{d}_f t} + \nabla(p_f^1\phi_f) = \frac{1}{\mathrm{Re}}\nabla\cdot\big(\left(\zeta_f\nabla\cdot\mathbf{u}_f\right)\phi_f\mathbf{I} + 2\mu_f\phi_f\mathbf{V}_f^d\big) - \big(\delta(\mathbf{u}_f-\mathbf{u}_s) + p_f^1\nabla\phi_s\big)\,, \tag{3.82}$$

$$\rho_f\phi_f\frac{\mathrm{d}h_f}{\mathrm{d}_f t} = \frac{1}{\mathrm{Re}\,\mathrm{Pr}}\nabla\cdot(\kappa_f\phi_f\nabla T_f) - \xi(T_f - T_s) + \phi_f\frac{\hat\gamma-1}{\hat\gamma}\frac{\partial p}{\partial t}\,. \tag{3.83}$$

*Granular phase*

$$\frac{\mathrm{d}(\rho_s\phi_s)}{\mathrm{d}_s t} + \rho_s\phi_s\nabla\cdot\mathbf{u}_s = 0\,, \tag{3.84}$$

$$\rho_s\phi_s\frac{\mathrm{d}\mathbf{u}_s}{\mathrm{d}_s t} + \nabla(p_s^1\phi_s) = \frac{1}{\mathrm{Re}}\nabla\cdot\big(\left(\zeta_s\nabla\cdot\mathbf{u}_s + \chi_a\right)\phi_s\mathbf{I} + 2\mu_s\phi_s\mathbf{V}_s^d + \chi_b\phi_s\mathbf{V}_s\cdot\mathbf{V}_s\big) - \nabla\cdot\mathbf{C}_s + \big(\delta(\mathbf{u}_f-\mathbf{u}_s) + p_f^1\nabla\phi_s\big)\,, \tag{3.85}$$

$$\rho_s\phi_s\frac{\mathrm{d}h_s}{\mathrm{d}_s t} = \frac{1}{\mathrm{Re}\,\mathrm{Pr}}\nabla\cdot(\kappa_s\phi_s\nabla T_s) + \xi(T_f - T_s) + \phi_s\frac{\hat\gamma-1}{\hat\gamma}\frac{\partial p}{\partial t}\,. \tag{3.86}$$

*Compaction equation*

$$\frac{\mathrm{d}\phi_s}{\mathrm{d}_s t} = \mathrm{Re_c}\,\phi_s\phi_f\left(p_s^1 - \beta_s - p_f^1 + T_s\nabla\cdot\left(\frac{\gamma_s}{T_s}\nabla\phi_s\right)\right) + \lambda\,\phi_f\phi_s(T_f - T_s)\,. \tag{3.87}$$

In the above equations, $h_f$ and $h_s$ stand for the specific enthalpies of the two phases. Also $\mathrm{Re}$ and $\mathrm{Pr}$ stand for the Reynolds and Prandtl number, respectively, based on the reference variables. Further, the non-dimensional number $\mathrm{Re_c}$ is the Reynolds number based on the compaction viscosity, $\mu_c$. Finally, it is noted that in the derivation of these results, it is assumed that $\beta_s$ and $\gamma_s$ scale with $\rho_r u_r^2$ and $\rho_r u_r^2 l_r^2$, respectively; see the relative discussion in [62].

The most important simplification in the incompressible limit is that the thermodynamic pressures no longer appear in the momentum equations. In this sense, the energy equation for each phase is essentially decoupled from the corresponding momentum equation. An interesting feature of the model is that it predicts thermal non-equilibrium between the two phases even at low-Mach numbers, cf. (3.83) and (3.86). Moreover, when the thermodynamic pressure $p$ remains constant, as in the case of open domains, the energy equations above reduce to the standard advection-diffusion equations for $T_f$ and $T_s$ with the additional relaxation term representing interphasial heat exchange.

### 3.5.1 Special case: constant-density flows

The important special case is now considered, where the densities of the two phases are constant and the two temperatures $T_s$ and $T_f$ are also constant and equal to each other. Then, the energy equations (3.83) and (3.86) are trivially satisfied and the remaining equations simplify to the following system,

$$\frac{\mathrm{d}\phi_f}{\mathrm{d}_f t} + \phi_f \nabla \cdot \mathbf{u}_f = 0\,, \tag{3.88}$$

$$\rho_f \phi_f \frac{\mathrm{d}\mathbf{u}_f}{\mathrm{d}_f t} + \nabla(p_f^1 \phi_f) = \frac{1}{\mathrm{Re}} \nabla \cdot \left( (\zeta_f \nabla \cdot \mathbf{u}_f)\, \phi_f \mathbf{I} + 2\mu_f \phi_f \mathbf{V}_f^d \right) - \left( \delta(\mathbf{u}_f - \mathbf{u}_s) + p_f^1 \nabla \phi_s \right)\,, \tag{3.89}$$

$$\frac{\mathrm{d}\phi_s}{\mathrm{d}_s t} + \phi_s \nabla \cdot \mathbf{u}_s = 0\,, \tag{3.90}$$

$$\rho_s \phi_s \frac{\mathrm{d}\mathbf{u}_s}{\mathrm{d}_s t} + \nabla(p_s^1 \phi_s) = \frac{1}{\mathrm{Re}} \nabla \cdot \left( (\zeta_s \nabla \cdot \mathbf{u}_s + \chi_a)\, \phi_s \mathbf{I} + 2\mu_s \phi_s \mathbf{V}_s^d + \chi_b \phi_s \mathbf{V}_s \cdot \mathbf{V}_s \right) - \nabla \cdot \mathbf{C}_s + \left( \delta(\mathbf{u}_f - \mathbf{u}_s) + p_f^1 \nabla \phi_s \right)\,, \tag{3.91}$$

$$\frac{\mathrm{d}\phi_s}{\mathrm{d}_s t} = \mathrm{Re_c}\, \phi_s \phi_f \left( p_s^1 - \beta_s - p_f^1 + \nabla \cdot (\gamma_s \nabla \phi_s) \right). \tag{3.92}$$

The above constant-density model has the important property that it does not constrain the velocity field of either phase to be divergence-free. This is a direct consequence of the compaction equation (3.92) which stipulates that the volume fraction $\phi_s$ is not conserved along streamlines of the granular phase. It is further noted that, in a manner analogous to the Navier-Stokes equations which require that the dynamic pressure be determined only up to an additive constant, the above model requires that the two dynamic pressures $p_s^1$ and $p_f^1$ be determined up to the *same* additive constant. This is due to the structure of the compaction equation (3.92) which requires that the difference $(p_s^1 - p_f^1)$ be uniquely determined.

Also, the above model has the property that at the single-phase limit, $\phi_s \to 0$, the equations for the fluid phase reduce to the Navier-Stokes equations, as they should. Finally, it is worth mentioning that algorithms for the numerical integration of systems of equations of this type have been recently proposed in [77] and [42].

## 3.6 Comparison with other particle-migration models

In this Section the structure of the compaction equation (3.92) for the constant-density model is compared with two popular descriptions of particle migration, the diffusive-flux model proposed in [136] and the suspension-balance model proposed in [108]. Equation (3.92) consists of an advection-diffusion equation for the volume fraction that contains the difference between the phasial pressures and the integranular stress, $p_s - p_f - \beta_s$, as a source term.

The diffusive flux model proposed in [136], when applied to non-colloidal suspensions, provides an evolution equation for $\phi_s$ which, in non-dimensional form, reads

$$\begin{aligned}\frac{\partial \phi_s}{\partial t} + \mathbf{u} \cdot \nabla \phi_s = & \frac{d_p^2}{2} K_c \nabla \cdot \left( \phi_s^2 \nabla \cdot \mathbf{V} + \phi_s \mathbf{V} \nabla \phi_s \right) + \\ & \frac{d_p^2}{2} K_\mu \nabla \cdot \left( \phi_s^2 \frac{1}{\mu} \frac{\partial \mu}{\partial \phi_s} \mathbf{V} \nabla \phi_s \right) . \end{aligned} \tag{3.93}$$

In this equation $d_p$ is the particle diameter, $\mathbf{V}$ is the strain-rate tensor for the suspension and $\mu$ is the suspension viscosity. Also $K_c$ and $K_\mu$ are two empirically determined constants.

A notable similarity between the two models is that they both contain a diffusion operator for the volume fraction $\phi_s$. On the other hand, an important difference is that the advection term for the model presented in this Chapter, equation (3.92), involves the velocity of the granular phase $\mathbf{u}_s$, whereas (3.93) is written in terms of the suspension velocity $\mathbf{u}$. This is due to the fact that, in the present model, each phase is endowed with its own velocity. For certain flows, the two phasial velocities $\mathbf{u}_s$ and $\mathbf{u}_f$ can be assumed equal. However, this is not always the case; typical examples are flows with significant density ratios between the two phases, such as sedimentation processes.

An additional difference is that the strain-rate tensor $\mathbf{V}$ appears in all terms on the right-hand side of (3.93), whereas it does not appear at all in equation (3.92). It is worth noting that since the terms on the right-hand side of (3.93) are linear with respect to $\mathbf{V}$, they vanish when $\mathbf{V}$ goes to zero. Consequently, the diffusive-flux model does not incorporate any mechanism for resisting particle migration in flow regions where the shear rate is zero. As an example, as mentioned in [136], equation (3.93) predicts that, in pressure-driven channel flows at low Reynolds number, $\phi_s$ attains a cusp at the centerline where it reaches the maximum packing treshold $\phi_m$; however, such a cusp has not been observed in experiments. On the other hand, the right-hand side of (3.92) does not vanish with the shear rate and, consequently, the diffusion operator therein does not allow the formation of cusps. This point is further discussed in Chapter 4, where pressure-driven flow is considered in detail.

The formalism behind the derivation of the governing system (3.88)– (3.92) is conceptually closer to the suspension-balance approach, in the sense that each phase is assigned its own momentum equation. In both approaches, the migration model consists of an equation for the material derivative of $\phi_s$ with respect to the velocity of the granular phase $\mathbf{u}_s$. Also, in both cases, the right-hand side of the migration model involves stresses acting on the granular phase. For example, the suspension-balance model proposed in [108] reads, neglecting body forces,

$$\frac{\partial \phi_s}{\partial t} + \mathbf{u} \cdot \nabla \phi_s \;=\; -\frac{d_p^2}{18} \mathrm{Re}\, \nabla \cdot \left( f(\phi_s) \nabla \cdot \Sigma_s \right) . \tag{3.94}$$

In this equation $\Sigma_s$ stands for the stress tensor of the granular phase and it is given by

$$\Sigma_s \;=\; -\mu_n \sqrt{2\mathbf{V}_s : \mathbf{V}_s}\, \mathbf{Q} + 2\mu_s \mathbf{V}_s \,, \tag{3.95}$$

where $\mathbf{Q}$ is a constant tensor that takes into account the anisotropy of normal viscous stresses. Also, $f(\phi_s)$ is the so-called "sedimentation hindrance function" and its expression is provided in [108].

One difference between the two models is that the right-hand side of (3.94) contains the divergence of the viscous stress tensor of the granular phase, whereas the present model (3.92) contains the difference of the phasial pressures $p_s - p_f$.

Further, similarly to equation (3.93), the right-hand side of (3.94) also becomes zero at flow regions with zero shear rate. As explained above, this leads to the prediction of cusps in the profiles of $\phi_s$ with in these regions. Recent variants of the suspension-balance model (3.94) - (3.95), such as the one proposed in [60], address this issue with the introduction of additional nonlocal stresses that depend on a suitable correlation length linked to the particle diameter $d_p$. In the present model, such nonlocal phenomena are represented via the quantity $\gamma_s$ that appears in the diffusion term in (3.92). As already mentioned above, $\gamma_s$ appears in the expression (3.27) for the configuration stress tensor $\mathbf{C}_s$, which describes nonlocal stresses related to the interaction between particles at the mesoscopic level.

A final observation is that the expression for the viscous stresses, equation (3.95), relies on information relative to the flow direction for determining $\mathbf{Q}$. On the other hand, the present model does not depend on such information.

## 3.7 Example: steady shear flow

In this Section, in order to gain insight into the structure and the predictive capacity of the model, the constant-density equations (3.88)–(3.92) are applied to steady homogeneous shear flow between parallel plates. More specifically, in this example the bottom plate remains at rest whereas the upper plate is moving at a constant (non-dimensional) velocity. The shear rate, $\dot{\gamma}$, is then defined as the ratio between the velocity of the upper plate divided by the distance between the two plates. Assuming no-slip boundary conditions at the wall, it is easy to verify that the solution to this problem consists of linear velocity profiles given by

$$\mathbf{u}_s = \mathbf{u}_f = \dot{\gamma}\, y\, \hat{\mathbf{e}}_x \,, \tag{3.96}$$

$\mathbf{e}_x$ being the unit vector pointing to the streamwise direction. The dynamic pressures and solid volume fraction $\phi_s$ are also constant and satisfy the following relation,

$$p_s^1 - p_f^1 = \beta_s(\phi_s) = const. \tag{3.97}$$

By virtue of the above relation, the compaction equation (3.92) is also satisfied. Then, the strain-rate tensors are given by

$$\mathbf{V}_f = \mathbf{V}_s = \dot{\gamma} \begin{pmatrix} 0 & \frac{1}{2} & 0 \\ \frac{1}{2} & 0 & 0 \\ 0 & 0 & 0 \end{pmatrix} \tag{3.98}$$

and have the following invariants, cf. (3.46).

$$l_1 = 0\,, \quad l_2 = \frac{1}{\sqrt{2}}|\dot{\gamma}|\,, \quad l_3 = 0\,. \tag{3.99}$$

Further, the non-dimensional stress tensors reduce to the following expressions, cf. (3.62),

$$\mathbf{P}_f = \frac{\dot{\gamma}}{\mathrm{Re}} \begin{pmatrix} 0 & 1 & 0 \\ 1 & 0 & 0 \\ 0 & 0 & 0 \end{pmatrix}, \tag{3.100}$$

$$\mathbf{P}_s = \frac{\mu_s \dot{\gamma}}{\mathrm{Re}} \begin{pmatrix} 0 & 1 & 0 \\ 1 & 0 & 0 \\ 0 & 0 & 0 \end{pmatrix} - \frac{\mu_n |\dot{\gamma}|}{\mathrm{Re}} \begin{pmatrix} 1 & 0 & 0 \\ 0 & 1 & 0 \\ 0 & 0 & \frac{c_2 - \frac{3}{2}c_5}{c_2 - c_5} \end{pmatrix}. \tag{3.101}$$

In the last expression, the shear viscosity of the granular phase $\mu_s$ is given by (3.63). Morevoer, $\mu_n$ is the so-called *normal viscosity*, defined by [108]. In the context of the proposed thermomechanical model, $\mu_n$ is given by

$$\mu_n = \frac{1}{\sqrt{2}\,\phi_s}(c_5 - c_2)\,. \tag{3.102}$$

Herein, both $\mu_s$ and $\mu_n$ are understood to have been non-dimensionalized by shear viscosity of the fluid.

The stress tensor of the granular phase $\phi_s \mathbf{P}_s$ can also be written as a function of the *anisotropy coefficients*, following the procedure of [108]. Accordingly, the expression for $\mathbf{P}_s$ reads,

$$\mathbf{P}_s = \frac{2\,\mu_s}{\mathrm{Re}} \mathbf{V}_s^d - \frac{\mu_n |\dot{\gamma}|}{\mathrm{Re}} \hat{\mathbf{Q}}\,, \quad \text{with} \quad \hat{\mathbf{Q}} = \begin{pmatrix} 1 & 0 & 0 \\ 0 & \lambda_2 & 0 \\ 0 & 0 & \lambda_3 \end{pmatrix}, \tag{3.103}$$

where $\lambda_2$ and $\lambda_3$ are the anisotropy coefficients. For the presented model, their values are the following.

$$\lambda_2 = 1\,, \qquad \lambda_3 = \frac{c_2 - \frac{3}{2}c_5}{c_2 - c_5}\,. \tag{3.104}$$

Then, the first and second normal-stress differences become proportional to $(\lambda_2 - 1)$ and $(\lambda_3 - \lambda_2)$, respectively.

As regards the *second* normal-stress difference, which scales with $(\lambda_3 - \lambda_2)$, it is remarked that in the present model $\lambda_3$ depends on the ratio $c_5/c_2$ which has to be measured experimentally. Nonetheless, if one sets

$$c_5 = \frac{1}{2} c_2 , \tag{3.105}$$

then $\lambda_3 = 0.5$, which gives the same normal stresses that are predicted by the model of [102]. There is also a general agreement that $\lambda_3 = 0.5$ and that the value of $\lambda_2$ is close to unity, which is the prediction of this model. For example, [129] and [137] set explicitly $\lambda_2 = 1$ in their computations and [138] reached a similar conclusion with the constitutive model that they proposed. On the other hand, the experimental measurements of [49], [50] and [58] are compatible with $\lambda_2 \simeq 0.85$ and $\lambda_3 = 0.5$. Also, the simulations of [108] are in good agreement with these values of the anisotropy coefficients.

As regards the *first* normal-stress difference, since it scales with $(\lambda_2 - 1)$, this model predicts that it equals to zero. Actually, it can be shown that the representation theorem (3.44), upon which this model is based, implies *a priori* that is zero. It is noted that this has been explicitly assumed in a number of previous studies. In any case, there is a consensus that the first normal-stress difference is much smaller than the second one. However, while definite conclusions cannot be drawn yet, there is experimental evidence that the first normal-stress difference admits a small albeit non-zero value; see, for example, [49], [50] and [58].

A likely cause is the slow relaxation of the internal ordering of the granular phase. In fact, as is known from experimental observations and discrete-element simulations, flowing granular suspensions present a partially-ordered structure because the macroscopic motion of the particles cannot be completely decoupled from their microscale configuration; a review on this issue has been provided by [139]. In the derivation of this model, the assumption that $\mathbf{P}_s$ is an algebraic function of $\mathbf{V}_s$ is equivalent to assuming that the dynamics controlling the microscale configuration are very fast with respect to the characteristic time-scales of the flow. In other words, this assumption implies that any additional internal degree of freedom at the grain level relaxes very fast with respect to the flow time-scales, so that effectively the stresses are determined by $\phi_s$, $\nabla\phi_s$ and the deformation tensor $\mathbf{V}_s$.

This assumption, however, can be removed by the introduction of an additional tensorial order parameter that relates to the microstructure of the granular phase; say $\mathbf{A}_s$. Possible candidates of such an order parameter include fabric tensors, [140], [141] and [142], a microstructure tensor based on the mean-free path length, [47], and others. This approach allows for the description of time-dependent stresses related to relaxation phenomena. It is remarked that within the framework of non-equilibrium thermodynamics, the introduction of an order parameter $\mathbf{A}_s$ provides an extra term to the Gibbs equation, $-\mathbf{B}_s : \mathrm{d}\mathbf{A}_s$, with $\mathbf{B}_s$

being the partial derivative of the Helmholtz free energy of the granular phase with respect to $\mathbf{A}_s$. Consequently, by exploiting the entropy inequality, one can derive a rate equation for $\mathbf{A}_s$ and a constitutive equation for $\mathbf{P}_s$ that depend both on $\mathbf{V}_s$ and on $\mathbf{B}_s$. This procedure has already been used in [117] and [143] for the case of colloidal suspensions.

In the present work, the choice has been made to refrain from the introduction of a tensorial order parameter related to the granular microstructure for the following two reasons. First, currently there exists no univocal definition of such a tensorial order parameter and, to the best of the author's knowledge, there is not sufficient experimental guidance about how the free energy of the granular phase should depend on it. Second, from a trade-off point of view, the first normal-stress difference has been measured to be quite small, yet the introduction of a tensorial order parameter would increase considerably the complexity of the governing equations.

## 3.8 Conclusions

This Chapter presented a mixture-theoretic formalism for granular suspensions, *i.e.* for mixtures of a granular material and a carrier fluid at high Péclet numbers. According to this formalism, the two phases are treated as coexisting but open thermodynamic continua that interact with each other. As such, each phase is endowed with its own set of thermodynamic variables and conservation laws. This formalism has been applied for the derivation of a thermomechanical model for the mixtures of interest. Constitutive equations for the dissipative and relaxation phenomena occurring in both phases are derived by exploiting the constraints imposed by the entropy inequality when applied to the entire mixture.

The proposed model is valid for both compressible and incompressible flows. Herein, the incompressible limit of the model has also been derived via low-Mach asymptotic expansion. The resulting system of equations is substantially simpler than the full model and, therefore, more convenient for flows where compressibility effects are negligible. For the important special case of constant-density flows, the reduced equations have also been presented and discussed.

In the derivation, particular emphasis has been placed on three objectives. First, the model should be able to handle thermal non-equilibrium even at low-Mach numbers. To this end, each phase has been endowed with its own temperature field. Second, the model should provide an evolution equation for the solid volume fraction. Moreover, this evolution equation should yield divergent velocity fields even for constant density flows so that the dilatancy of the granular phase can be predicted. To this end, the solid volume fraction has been introduced as an additional thermodynamic variable. Then, both the first and second objectives have been achieved by writing the entropy-production rate in a convenient form of sum of products. The third objective is to capture as accurately as possible the non-Newtonian behavior of the viscous stresses acting on the granular phase. To this end, the general representation theorem of isotropic tensors has been leveraged and the following requirements have been imposed: i) the representation should yield the same scaling with respect to the shear rate as the one observed in experiments, ii) it should remain bounded at equilibrium, and iii) it should satisfy the entropy inequality. This provides a well defined, shear-rate dependent constitutive relation for the granular viscous stress tensor.

When compared with existing particle-migration models for constant-density flows, the predictions of this model for the evolution of the granular volume fraction present a number of important differences. In particular, when comparing the compaction equation (3.92) with the diffusive-flux model presented in [136], it is shown that the present model can predict phasial velocity nonequilibrium and avoid singularities in the limit of vanishing shear-rate, which can not be achieved with that model. The case of vanishing shear-rate is also relevant to the comparison with the suspension-balance model presented in [108]; in fact that model has more recently been modified in this sense [60]. In addition, that model connects directly the viscous stresses to the evolution of the volume fraction, whereas the present model predicts a connection with the phasial pressures through equation (3.92).

When applied to the problem of steady shear flow, the present model predicts a zero value for the first normal-stress difference and a negative value for the second one. These predictions match previous numerical studies and are in good agreement with experimental observations. However, available experimental data show a small non-zero value for the first normal-stress difference. A likely explanation for this discrepancy is the presence of relaxation phenomena at the grain level that are unaccounted for in the present model. Even though the macroscopic effects of these phenomena are expected to be small, they can in principle be captured via the introduction of an additional order parameter of tensorial character that is related to the microstructure of the granular phase.

# Chapter 4

# Channel flow of a dense suspension

## 4.1 Introduction

In this Chapter, the flow model developed in Chapter 3 is used to numerically investigate the plane Poiseuille flow of a dense granular suspension at low Reynolds numbers. The objective of this analysis is two-fold: first, to provide additional validation of the proposed model via comparisons with existing experimental data and numerical results. Second, to provide new insight into the physics of particle migration; particular attention is devoted to the interplay between the various mechanisms that contribute to particle migration towards the central region of the channel. To this end, the role of non-Newtonian viscous stresses and of nonlocal stresses is investigated, including the case of suspensions close to the jamming transition.

In Section 3.7 the governing equations for constant-density flow have been applied to plane Couette flow, where it has been shown that the predictions for viscous stresses and granular rheology are in good agreement with experimental data. The Poiseuille flow considered in this Chapter is another convenient benchmark that is still relatively simple to describe, yet presents a varying velocity gradient which allows to observe particle migration due to the presence of non-Newtonian stresses. Over the years, this flow has been the subject of numerous experimental studies, ranging from early works such as [144] to the well-known studies reported in [145], [146] and [147]. More recent experimental results have been obtained by the group of Gilchrist, cf. [55] and [56]. Experimental measurements of the group of Gilchrist and numerical results obtained via a discrete-element method have recently been reported in [20]. Herein the predictions of the model are compared against those results.

A first reason for which fully-developed flows at low Reynolds numbers have been the

The results presented in this Chapter have been published in: D. Monsorno, C. Varsakelis, and M.V. Papalexandris, (2017), "Poiseuille flow of dense non-colloidal suspensions: the role of intergranular and nonlocal stresses in particle migration", *Journal of Non-Newtonian Fluid Mechanics*, Vol.247, pp. 229-238.

object of a wealth of relevant studies is that they can be consistently reproduced in an experimental setting; this ease of reproduction has contributed to the availability of a reliable set of experimental results. In addition, fully-developed flows afford a relatively simple mathematical description. Indeed, for such flows, governing equations typically reduce to a set of time-independent ordinary differential equations that are easier to treat numerically.

Another reason that renders such flows representative paradigms is the fact that, despite their conceptual simplicity, they exhibit complex features that typify the behaviour of suspensions. For example, in the early study of pipe-flow reported in [144], the authors observed the formation of a central plug region. Further, shear-induced particle migration was observed and investigated both in plane-flow [145, 147] and pipe-flow measurements [146]; see also the more recent experimental results in [55] and [56]. Additionally, experimental measurements assert that the particle concentration (equivalently, the granular volume fraction) exhibits a peak at the centerline due to particle migration from the walls towards the bulk of the channel. Another interesting observation is that this peak is not very sharp but, instead, fairly smooth. Moreover, for moderate concentrations, this peak is bounded below the critical value $\phi_m$ of the volume fraction at the jamming transition.

As elucidated in [136], capturing the aforementioned features via continuum modelling is far from trivial. In fact the authors of [136], whose study is based on a diffusive-flux model, remarked that the volume fraction cannot be bounded below $\phi_m$ by viscous terms alone.

Further challenges are induced by the fact that particle interactions result in the development of additional stresses that must also be taken into account in a continuum model. These stresses are of nonlocal nature in the sense that they depend on the size of the particles which is finite, i.e. non-zero. Typically, diffusive-flux models tackle this issue with the introduction of stress terms that depend on a suitable correlation length, [148]. Suspension-balance type models also include extra terms for the description of these stresses. For example, in [19] the representation of these additional stresses was given in terms of the granular temperature, which is closely related to the shear rate. In [108] an additional stress component was introduced by means of a nominal shear rate. Subsequently, this approach was adopted in a number of studies; see, for instance, [60] and references therein.

A well-established approach for taking into account mesoscopic phenomena is the introduction of suitable order parameters. As regards suspensions, this translates into the introduction of order parameters for the representation of the additional stresses acting on the granular phase. This methodology was followed in [47], where these additional stresses are represented in terms of a tensorial order parameter that depends on the mean free path of the particles. Also, in [149] the authors combined the equations for the granular stresses proposed in [47] with the migration model proposed in [60], to which they added an extra term that depends on the gradient of the volume fraction. The gradient of the volume fraction can also be introduced as an order parameter. In fact, it has been frequently employed in such a context for the derivation of continuum theories of granular suspensions [26–28, 30, 62].

This Chapter is structured as follows. In Section 4.2 the continuum model developed in Chapter 3 is specialized to its unidirectional, constant-density, steady-state limit. Further, this Section contains a discussion on the choice of boundary conditions for fully-developed channel flows. Section 4.3 presents the numerical results, and the comparisons with experimental data and with computations based on a particle-resolved method reported in [20]. This Section also includes an analysis of the role of the stresses acting on the granular phase. Finally, Section 4.4 concludes.

## 4.2 Governing equations

### 4.2.1 Equations for Poiseuille flow

The study presented in this Chapter is based on the two-phase continuum model derived in Chapter 3, and more specifically on the constant-density equations (3.88)–(3.92). In principle one can solve these equations directly as a system for the unknown velocity vectors $\mathbf{u}_f$ and $\mathbf{u}_s$, the phasial dynamic pressures $p_f^1$ and $p_s^1$ and the granular volume fraction $\phi_s$; algorithms for the numerical integration of systems of equations of this type have been recently proposed in [42, 77].

In this Chapter, however, the simple geometry of Poiseuille flow is exploited with the purpose of simplifying this system and providing an easier numerical treatment. More specifically, in order to derive the reduced equations that govern plane Poiseuille flow, time-independent solutions of these equations are sought that are in addition unidirectional, i.e. the variables are functions of the wall-normal coordinate only. Given that the problems considered in this Chapter are at small channel size and high particle concentrations, following experimental observation the flow is assumed laminar and the effect of gravity is neglected [20, 55, 56].

In addition, further simplification can be achieved with respect to the modelling of non-Newtonian rheology: one can take advantage of the numerous experimental measurements of the second normal-stress difference that suggest a link between the coefficients $\chi_a$ and $\chi_b$ in equation (3.91), as per the relative discussion in Section 3.7 and in particular equations (3.65) and (3.105). More specifically, following equation (3.105) one obtains simplified expressions for $\chi_a$ and $\chi_b$ as follows,

$$\chi_a = -\sqrt{2}\,\mu_n \left( 2\sqrt{\mathbf{V}_s^d : \mathbf{V}_s^d} - \frac{3}{2}\frac{\mathbf{V}_s^d : \mathbf{V}_s^d}{\sqrt{\mathbf{V}_s : \mathbf{V}_s}} \right), \tag{4.1}$$

$$\chi_b = -\frac{\sqrt{2}\,\mu_n}{\sqrt{\mathbf{V}_s : \mathbf{V}_s}}, \tag{4.2}$$

where the double-dot symbol : denotes the double interior product between two second-order tensors. These expressions both depend on the single scalar coefficient $\mu_n$, which is denoted as *normal stress viscosity*, according to the terminology introduced by the authors of [108].

The above assumptions are now introduced into equations (3.88)–(3.92). To begin with, the unidirectionality requirement implies that the velocity vectors are aligned in the streamwise direction $\mathbf{e}_x$, so that

$$\mathbf{u}_f = u_f(y)\,\mathbf{e}_x, \quad \mathbf{u}_s = u_s(y)\,\mathbf{e}_x\,, \tag{4.3}$$

with $x$ and $y$ denoting the streamwise and wall-normal coordinates, respectively. Next, for the granular volume fraction one has $\phi_s = \phi_s(y)$.

The above assumptions, together with equation (3.92), imply that the phasial pressures $p_f^1$ and $p_s^1$ can be decomposed as follows,

$$p_f^1 = p_f(y) - Fx, \quad p_s^1 = p_s(y) - Fx, \tag{4.4}$$

where $F$ represents the constant pressure gradient in the streamwise direction that drives the flow. Integration of the momentum equation of the fluid phase along the $y$-direction then yields that $p_f$ is constant. Without loss of generality, one can set its constant value equal to zero so that

$$p_f = 0\,. \tag{4.5}$$

In view of the above relations, the continuity equations (3.88) and (3.90) are satisfied identically, whereas equations (3.89), (3.91) and (3.92), combined with equations (4.1) and (4.2), reduce to the following system.

*Fluid phase*

$$\frac{1}{\mathrm{Re}}\frac{\mathrm{d}}{\mathrm{d}y}\left((1-\phi_s)\frac{\mathrm{d}u_f}{\mathrm{d}y}\right) = \delta\,(u_f - u_s) - F\,(1-\phi_s)\,, \tag{4.6}$$

*Granular phase*

$$\frac{1}{\mathrm{Re}}\frac{\mathrm{d}}{\mathrm{d}y}\left(\mu_s\phi_s\frac{\mathrm{d}u_s}{\mathrm{d}y}\right) = -\,\delta(u_f - u_s) - F\,\phi_s\,, \tag{4.7}$$

$$\frac{1}{\mathrm{Re}}\frac{\mathrm{d}}{\mathrm{d}y}\left(\mu_n\phi_s\left|\frac{\mathrm{d}u_s}{\mathrm{d}y}\right|\right) = -\,\frac{\mathrm{d}}{\mathrm{d}y}\left(\gamma_s\left(\frac{\mathrm{d}\phi_s}{\mathrm{d}y}\right)^2\right) - \frac{\mathrm{d}}{\mathrm{d}y}\left(p_s\phi_s\right)\,, \tag{4.8}$$

*Compaction equation*

$$p_s - \beta_s + \frac{\mathrm{d}}{\mathrm{d}y}\left(\gamma_s\frac{\mathrm{d}}{\mathrm{d}y}\phi_s\right) = 0\,. \tag{4.9}$$

Equations (4.6)–(4.9) constitute a system of coupled, nonlinear ODEs for the four unknowns $u_f$, $u_s$, $p_s$, and $\phi_s$. This system is closed once appropriate experimental correlations are provided for the material parameters; this is done below.

#### Material parameters

In order to be solved numerically, the system of equations (4.6) - (4.9) requires to be supplemented with correlations for the transport coefficients $\delta$, $\mu_s$, $\mu_n$ and with appropriate expressions for the thermodynamic derivatives $\beta_s$ and $\gamma_s$. The relations employed in this numerical study are listed here.

For the drag coefficient $\delta$, the Hill-Koch-Ladd correlation proposed in [150] is chosen; this correlation is applicable for a wide range of Reynolds numbers and volume fractions. According to it, the coefficient $\delta$ is a function of the local volume fraction $\phi_s$, the particle diameter $d_p$ and the particle Reynolds number $\mathrm{Re}_p$ (which is defined in terms of the particle diameter and the slip velocity $\|\mathbf{u}_f - \mathbf{u}_s\|$),

$$\delta = f(\phi_s, d_p, \mathrm{Re_p})\,. \tag{4.10}$$

The exact expression for (4.10) is too long and cumbersome to reproduce herein, comprising several cases and containing various numerical constants, Still, the authors of [150] undertook the challenge to write their correlation in a code-friendly manner so the interested reader is directly referred to this work for more information.

For the viscosity coefficients $\mu_s$ and $\mu_n$ the formulation proposed in [108] has been employed. The adaptation of this formalism to the two-phase flow model of Chapter 3 results in the following expressions, non-dimensionalized with respect to the shear velocity of the carrier fluid,

$$\mu_s = \frac{2.5}{\phi_m - \phi_s} + 0.1\,\frac{\phi_s}{(\phi_m - \phi_s)^2}\,, \tag{4.11}$$

$$\mu_n = 0.75\,\frac{\phi_s}{(\phi_m - \phi_s)^2}\,, \tag{4.12}$$

where $\phi_m$ represents the critical value of the granular volume fraction at the jamming transition; in this study the value $\phi_m = 0.6$ is assumed. The above expressions have the advantage of being simple yet sufficiently accurate for the flows under study. More elaborate experimental correlations can be found in [58, 59].

As regards $\beta_s$ and $\gamma_s$, it is first remarked that these quantities are defined as thermodynamic derivatives, so that constitutive relations for them have to be derived via experimental measurements; see the relevant discussions in [27, 29, 62, 63, 73]. Also, since they relate to the microstructure of the granular phase, their constitutive relations should depend on the parameters that characterize this microstructure.

Further, the intergranular stress $\beta_s$ expresses the resistance of solid particles to compaction and, at least for rigid particles, is expected to vanish for small values of $\phi_s$ and to diverge at $\phi_m$ [84, 121, 122]. In this study the following expression has been employed, which is based on the relation proposed in [122],

$$\beta_s = -\beta_0 \log\left(\frac{\phi_m - \phi_s}{\phi_m}\right), \quad \beta_0 = 2.08 \times 10^3. \tag{4.13}$$

The coefficient $\beta_0$ also depends on the microstructure of the particulate phase. The above (non-dimensional) value $\beta_0$ has been calibrated with respect to the experimental data reported in [20] that are used in the comparisons presented in Section 4.3 below.

Experimental measurements for $\gamma_s$ are particularly scarce. This quantity, which is defined in the second of (3.17) as the derivative of the Helmholtz free energy of the granular phase with respect to $\nabla\phi_s$, enters the expression (3.27) for $\mathbf{C}_s$, a stress-tensor component that appears in the momentum equation (3.91) for the granular phase. This tensor describes Korteweg-type stresses which are developed in the granular phase due to variations in the contact-area density between grains. Although few data is available regarding $\gamma_s$, this quantity is also expected to vanish as $\phi_s \to 0$. Moreover, since it is a thermodynamic derivative, it has to increase monotonically with $\phi_s$ in order to satisfy the convexity requirement for stability of equilibrium states of the granular medium [62]. In this study, due to lack of available experimental data, a simple power law is assumed, namely,

$$\gamma_s = -\gamma_0 \phi_s^r, \quad \gamma_0 = 5.2 \times 10^4, \tag{4.14}$$

with $r$ a positive exponent. Different exponents were tested and better agreement with experiments was found for higher values of $r$. In particular, the numerical results presented in this Chapter have been obtained with $r = 6$. It is worth mentioning that linear expressions for $\gamma_s$ have been used in a number of earlier studies [74, 151]. Expressions that diverge at $\phi_m$ have also been employed [28, 127, 152]. This study refrains from adopting the later approach due to absence of conclusive evidence regarding the behaviour of $\gamma_s$ near the point of jamming transition.

**The low-Reynolds limit**

Since this study deals with flows at low Reynolds number, it is appropriate to examine how the various stresses scale at the limit $\mathrm{Re} \to 0$. To this end, the scaling of the terms in the momentum equation of the granular phase (4.8) is considered; it is remarked that in this equation there are two non-dimensional groups. These are the Reynolds number Re, and the coefficient $\gamma_0$ which enters (4.8) by virtue of the expression (4.14) for $\gamma_s$. These two groups are given by

$$\mathrm{Re} \;=\; \frac{\hat{u}_r\,\hat{l}_r\,\hat{\rho}_r}{\hat{\mu}_r}\,, \qquad \gamma_0 \;=\; \frac{\hat{\gamma}_0}{\hat{\rho}_r\,\hat{u}_r^2\,\hat{l}_r^2}\,, \tag{4.15}$$

where the hat symbol ^ denotes dimensional quantities. The second of (4.15) is essentially the non-dimensionalisation of $\hat{\gamma}_0$; see for example the discussion in [62, 86]. On a side note, this scaling suggests that if the particle diameter is the only characteristic length of the microstructure of the granular phase, then $\hat{\gamma}_0$ scales quadratically with the particle diameter.

On the basis of (4.15), the ratio between the viscous and nonlocal stress in (4.8) is determined by the following non-dimensional group

$$r \;\triangleq\; \gamma_0 \mathrm{Re} \;=\; \frac{\hat{\gamma}_0}{\hat{\mu}_r \hat{u}_r\,\hat{l}_r}\,. \tag{4.16}$$

Considering that the fluid density $\hat{\rho}_r$ cannot be zero, the limit $\mathrm{Re} \to 0$ can be attained by letting the reference length $\hat{l}_r$ or the reference velocity velocity $\hat{u}_r$ go to zero, or by letting the fluid viscosity $\hat{\mu}_r$ go to infinity. Then, in view of (4.16), one distinguishes the following cases.

i) $\hat{\mu}_r \to \infty$. In this case $r \to 0$, which means that the viscous stresses dominate over the nonlocal stresses.

ii) $\hat{l}_r \to 0$. Then $r \to \infty$, which means that the nonlocal stresses become dominant over the viscous stresses.

iii) $\hat{u}_r \to 0$. In this case $r \to \infty$ and, therefore, the nonlocal stresses dominate over the viscous stresses. At this limit, relation (4.8) essentially reduces to the balance of forces for hydrostatics of granular mixtures, *i.e.* when both phases are at rest [73, 153].

It should be clarified that since these estimates are based on scaling arguments, *i.e.* on dimensional considerations, they do not necessarily hold at boundary layers or interfaces because therein one term may dominate due to high gradients of $u_s$ or $\phi_s$. Finally it is remarked that, since the Reynolds number does not enter the compaction equation (4.9), the contribution of the integranular stress $\beta_s$ cannot be neglected even at the limit of low Reynolds number.

### 4.2.2 Boundary conditions

Numerical solution of the system of equations (4.6) - (4.9) requires the assignment of suitable boundary conditions. First it is remarked that, since the half-width of the channel is taken as reference length for the non-dimensionalisation purposes, the walls are located at $y = \pm 1$. A no-slip condition is applied for the velocities of both phases at the walls, i.e.

$$u_f(\pm 1) \;=\; 0\,, \quad u_s(\pm 1) = 0\,. \tag{4.17}$$

This boundary condition is often employed in numerical studies of moderately dense suspensions [28, 30, 60, 83]. It is considered to be a good approximation for wall-bounded flows insofar as the granular volume fraction near the walls is not too close to maximum packing; this is corroborated by the experimental measurements reported in [135]. Evidently, it is possible for non-zero grain slip to occur in certain types of granular flows. The derivation of appropriate wall conditions for granular media is an area of active study, which however goes beyond the scope of the present work.

The boundary condition for the volume fraction $\phi_s$ requires more attention because, from a physical standpoint, it is generally not possible to control $\phi_s$ at the wall. Nevertheless, due to its simplicity, a Dirichlet condition has been imposed in a number of previous studies, e.g. [30, 154]. When the migration model can be cast in conservative form, a number of authors apply zero particle flux, i.e. impermeability, across solid boundaries. This approach has been implemented for diffusive-flux [136, 148] and suspension-balance models [60, 149].

In the present case however, the compaction equation (4.9) cannot be cast in conservative form, which renders the application of that approach cumbersome. For this reason, a different strategy is adopted that takes into account the one-dimensional character of the flow and the knowledge of the average particle concentration. More specifically, an integral constraint is applied for $\phi_s$, with the additional requirement that the values of $\phi_s$ at the two channel walls be equal,

$$\int_{-1}^{+1} \phi_s \, \mathrm{d}y \; = \; 2\,\overline{\phi}_s, \qquad \phi_s(-1) = \phi_s(+1)\,, \tag{4.18}$$

where $\overline{\phi}_s$ is the $y$-averaged volume fraction and is assumed to be known *a priori*. In the present case, for the comparisons with experiments included in Section 4.3 below, this value is determined by the experimental data. It should be clarified that this integral constraint is to be employed in a discrete sense, i.e. for numerical purposes. More specifically, the discretization of the above integral provides a relation for the values of $\phi_s$ at the wall in terms of the average volume fraction $\overline{\phi}_s$. This choice has the additional advantage of not being affected by the well-documented uncertainties regarding the interpretation of measurements of $\phi_s$ at very short distances from the wall (distances at the order of the particle diameter) that have been documented in [20, 60, 146, 147].

It is worth noting that mass continuity could also be used as an integral constraint for $\phi_s$. More specifically, one could impose

$$\int_{-1}^{+1} \phi_s u_s \, \mathrm{d}y \; = const., \tag{4.19}$$

where the value of the integral is again determined from experimental data. In this study it is chosen to employ equation (4.18) as an additional constraint for $\phi_s$ instead of equation (4.19) because the iterative algorithm for the system (4.6)–(4.9) converged faster when equation

(4.18) was used.

The prescription of boundary condition for the granular pressure $p_s$ also requires attention. Inside the flow domain the compaction equation (4.9) links $p_s$ with $\phi_s$. Then, if the flow variables are sufficiently smooth up to the boundary, one can obtain a boundary condition for $p_s$ by assuming that the compaction equation remains valid at the boundary. This provides a value for $p_s$ at the wall through extrapolation of $\phi_s$. More specifically, for the computations of this chapter the following condition for $p_s$ is set,

$$p_s \;=\; \beta_s - \frac{\mathrm{d}}{\mathrm{d}y}\left(\gamma_s \frac{\mathrm{d}}{\mathrm{d}y}\phi_s\right)\,, \quad \text{at} \quad y = 1\,, \tag{4.20}$$

where the right-hand side of the above equation is discretized via one-sided differences.

## 4.3 Numerical results

The present study examines the same flow considered in the discrete-element simulations of [20] which, in turn, replicate the experimental studies of [55] and [56] and their more recent extensions performed by Gilchrist and his collaborators. The first part of this Section presents a comparison of the numerical results with the experimental data reported in [20]. In the second part the role of the intergranular and nonlocal stresses is investigated via a series of parametric studies.

### 4.3.1 Comparison with experiments

In the experiments of Gilchrist that have been reported in [20], an initially homogeneous granular suspension with a mean particle diameter of $1\,\mu m$ is pumped through a long channel with a width of $40\,\mu m$. Herein, the channel width is discretized on a uniform grid of 500 points and the governing system (4.6)–(4.9) is integrated numerically via an iterative under-relaxation algorithm; the outline of this algorithm is provided in the Appendix to this Chapter. The Reynolds number of the flows under study is very small; its value is not mentioned in [20] but similar experiments presented in [55] were conducted at $\mathrm{Re} = 1.2 \times 10^{-4}$ with respect to the centerline velocity. This is the value of the Reynolds number that is used in the computations of this Section.

Fig. 4.1 presents the profiles of $\phi_s$ for two different average volume fractions, namely $\overline{\phi}_s = 0.298$ and $\overline{\phi}_s = 0.411$. For comparison purposes the experimental data of Gilchrist for the same values of $\overline{\phi}_s$ is also included, as well as the numerical results of [20] for slightly different values of average volume fractions ($\overline{\phi}_s = 0.30$ and $\overline{\phi}_s = 0.40$, respectively). From the plots of the experimental data one can clearly observe the formation of a zone of high particle concentration in the central region of the channel. The phenomenon is explained as follows. As the flow develops, the velocity gradients become higher near the walls, which implies that the amplitude of the normal viscous stresses acting on the granular phase varies across the channel. This, in turn, causes particle migration from the wall region towards the centerline of the channel. As a result, the volume fraction $\phi_s$ at the centerline increases progressively until the full development of the flow. The clear symmetry of the experimental profiles adduces the assumption to treat the suspension as neutrally buoyant.

It can readily be inferred that the model predictions match very well the experimental data for the volume fraction $\phi_s$ in the bulk of the channel and that the concentration peak at the centerline is accurately computed. Reproducing this peak is not a trivial task, as it requires to take into account the (Korteweg-type) nonlocal stresses that are developed during inter-particle interactions, [60, 148]. As mentioned above, in the present model, this is taken into account via the introduction of the configuration stress tensor $\mathbf{C}_s$, cf. equation (3.27).

On the other hand, there is a noticeable discrepancy in the vicinity of the wall. In this region, the experimental data show a large drop of the volume fraction whereas the computations of the present study predict a much milder decrease. These computations also differ from those of [20] that predict a drop of $\phi_s$ to zero at the wall, albeit in an oscillatory manner. One may ostensibly associate this discrepancy with the choice of boundary conditions for $\phi_s$. Nonetheless, previous numerical studies, based on different continuum models and with different boundary conditions, [60, 136, 148, 149, 151, 155] resulted in similar predictions. The collective inability to capture this concentration drop underscores the difficulty in prescribing accurate boundary conditions at solid boundaries. On the other hand, it should not go unnoticed that the region where the numerical predictions deviate from the experimental data spans only 2 to 3 grain diameters. This suggests that the observed discrepancy might as well be attributed to the inherent limitation of continuum theories to capture structures at the particle scale. Finally, as discussed in a wide number of studies [55, 60, 145, 147, 149, 155], the volume fraction in the wall region is notoriously difficult to measure, which could also contribute to the observed deviation.

The velocity profiles for the two cases mentioned above are plotted in Fig. 4.2. In this figure, the parabolic profile for the corresponding pure-fluid flows are also superimposed. It can be observed that, with respect to the latter, the velocity profiles exhibit some flattening in the vicinity of the centerline. This flattening, which is somewhat more pronounced in the case of higher $\phi_s$, is attributed to the increase of the viscosity coefficients in areas of high particle concentrations, cf. equations (4.11) and (4.12). Another interesting point is that the profiles of the two phasial velocities, $u_f$ and $u_s$, almost coincide. In fact, in the flows under consideration, the suspension is quite dense and the particle diameter is very small. As a result, the interphasial drag force becomes important, which leads to velocity equilibration during the development of the flow. The effect of the drag coefficient on the velocity profiles is discussed further in Section 4.3.2. Also, from Fig. 4.2 one can readily infer that the present numerical results for the velocity profiles agree very well with the ones of [20]. The small differences between these two sets of computations can be attributed to the fact that

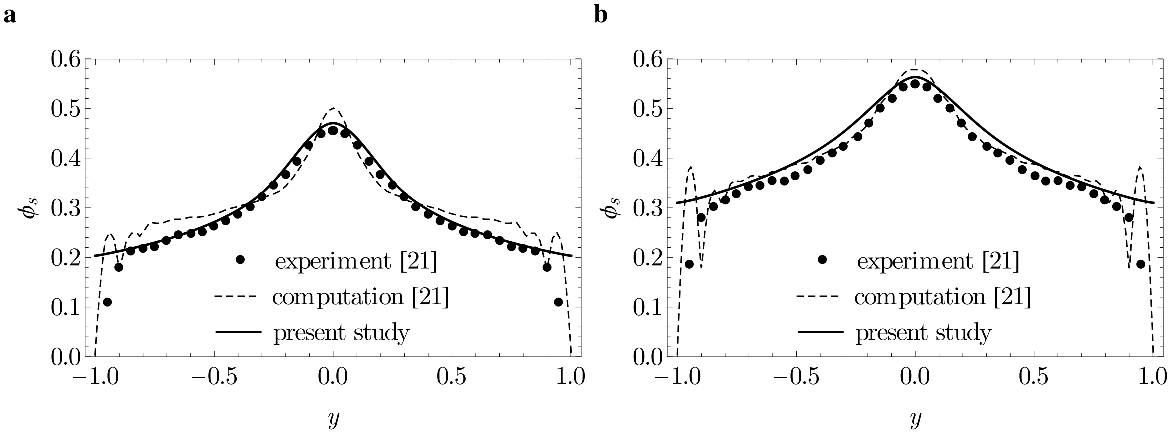


Figure 4.1: Volume fraction profiles for fully-developed channel flow of granular suspensions. Comparison between the computations of the present study and the results reported in [20]. (a) $\overline{\phi}_s = 0.298$. (b) $\overline{\phi}_s = 0.411$. The computations of [20] were performed for $\overline{\phi}_s = 0.3$ and $\overline{\phi}_s = 0.4$, respectively.

the computations of [20] were performed at slightly different average volume fractions.

### 4.3.2 The role of integranular and nonlocal stresses

This Section presents the results of an analysis regarding the role of the intergranular and nonlocal stresses in particle migration. First, it examines the balance of stresses acting on the granular phase in the $y$ direction for the two cases discussed above, i.e. $\overline{\phi}_s = 0.298$ and $\overline{\phi}_s = 0.411$. To this end, Fig. 4.3 shows the profiles of the amplitude of all terms entering equation (4.8) normalized by the applied streamwise pressure gradient $F$. In this figure it can be observed that in both cases the normal viscous stress is almost constant and much higher than the other stresses, except in the central region where it drops rapidly. This drop is explained by the fact that the velocity gradients become smaller approaching the centerline, whereas the normal viscosity $\mu_n$ remains bounded since the granular phase is away from the jamming transition. In fact, right at the center, the velocity gradient vanishes and the value of the normal viscous stress drops to zero.

On the other hand, the pressure term $p_s\phi_s$ follows exactly the opposite trend. In particular, at the wall it is considerably smaller than the viscous stress and increases slowly moving towards the centerline. However, in the central region of the channel, which is characterized by high values $\phi_s$ due to particle migration, the term $p_s\phi_s$ starts to increase significantly as soon as the amplitude of the viscous stress starts to drop. Consequently, the term $p_s\phi_s$ becomes dominant in the central region of the channel with high particle concentration.

Further, it can be observed that the amplitude of the nonlocal stress $\gamma_s(\frac{\mathrm{d}\phi_s}{\mathrm{d}y})^2$, is very small. More precisely, its value is close to zero everywhere except for the central region of high particle concentration. Finally, it is remarked that the normalized stress profiles shown in Fig. 4.3 are similar for both cases, i.e. $\overline{\phi}_s = 0.298$ and $\overline{\phi}_s = 0.411$. However,

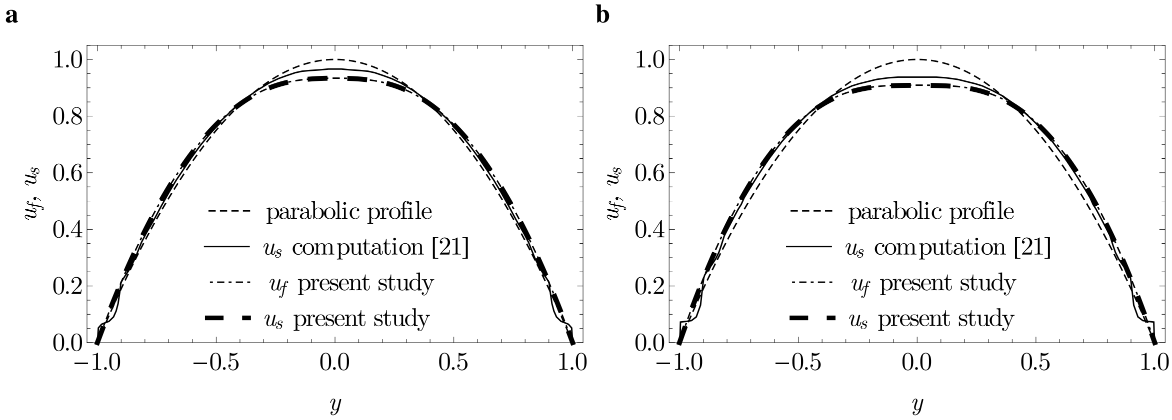


Figure 4.2: Profiles of the non-dimensional phasial velocities $u_f$ and $u_s$ across the channel. (a) $\overline{\phi}_s = 0.298$. (b) $\overline{\phi}_s = 0.411$. The numerical predictions of [20] were obtained for $\overline{\phi}_s = 0.3$ and $\overline{\phi}_s = 0.4$, respectively.

the amplitude of these stresses in absolute terms rises significantly with the average particle volume fraction. For example, when $\overline{\phi}_s = 0.298$, the normal viscous stress at the wall is approximately 9% of the applied pressure gradient $F$. However, when the average volume fraction is increased to $\overline{\phi}_s = 0.411$, then the normal viscous stress at the wall becomes equal to 25% of $F$.

Next, the sensitivity of the particle concentration profiles with respect to $\gamma_s$ is examined. As mentioned above, this quantity plays the role of a thermodynamic derivative and appears in the expression for the nonlocal stress tensor of the granular phase $\mathbf{C}_s = \gamma_s \nabla\phi_s \otimes \nabla\phi_s$, as well as in the diffusion operator $\nabla \cdot (\gamma_s \nabla\phi_s)$ on the right-hand side of the compaction equation (3.92). Herein the case with average volume fraction $\overline{\phi}_s = 0.298$ is considered and the value of the coefficient $\gamma_0$ is varied, cf. (4.14).

The computed profiles of the volume fraction for different values of $\gamma_0$ are plotted in Figure 4.4. It can be observed that the variations in $\gamma_0$ do not impact at all the volume fraction close to the wall but have a dramatic effect in the central region of the channel. More specifically, as $\gamma_0$ decreases, the peak of $\phi_s$ at the centerline become steeper and sharper. By contrast, higher values of $\gamma_0$ result in lower gradients of $\phi_s$ and in more diffuse profiles.

In other words, $\gamma_s$ influences significantly the distribution of the volume fraction across the channel despite the fact that, as shown above, the nonlocal stress $\gamma_s(\frac{\mathrm{d}\phi_s}{\mathrm{d}y})^2$ is much smaller than both the granular pressure and the normal viscous stress. Actually, $\gamma_s$ exerts this influence via the diffusion operator in the compaction equation (3.92). This implies that $\gamma_0$ essentially plays the role of a diffusivity constant that controls the amplitude of the volume fraction gradients in regions of particle agglomeration and clustering. It is remarked that this analysis is based solely on the specific correlation (4.14) that is used for $\gamma_s$, which is a simple power law of $\phi_s$. Nonetheless, other correlations that have appeared in the literature also assume that $\gamma_s$ increases with $\phi_s$ [28, 30]. For this reason, one can anticipate a similar trend to be observed even for different correlations.

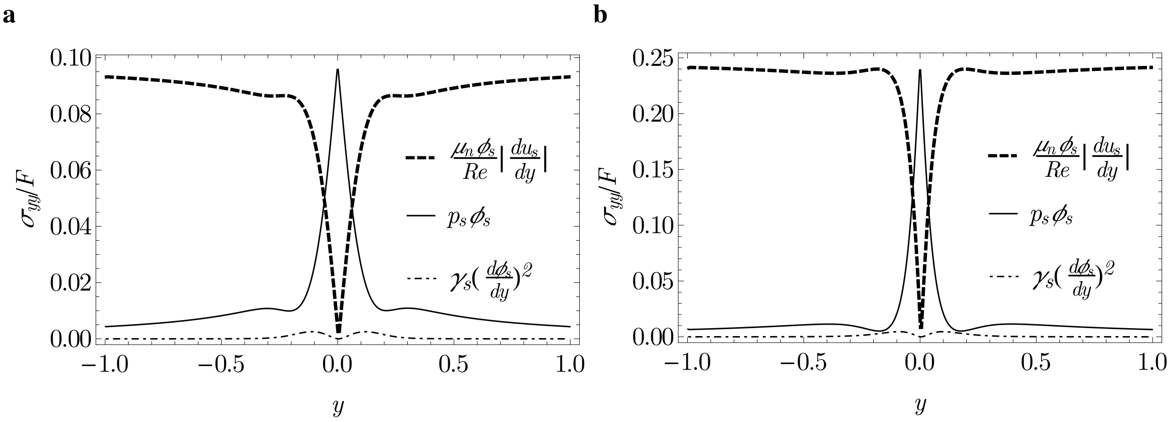


Figure 4.3: Balance of stresses in the normal direction: profiles of the amplitude of the terms entering the momentum equation (4.8) normalized by the streamwise pressure gradient $F$. (a) $\overline{\phi}_s = 0.298$. (b) $\overline{\phi}_s = 0.411$.

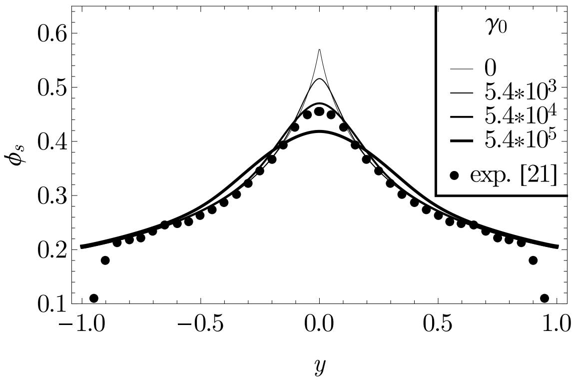


Figure 4.4: Dependence of the profile of the volume fraction accross the channel on the amplitude of the nonlocal stresses. Average volume fraction $\overline{\phi}_s = 0.298$. The dots show the experimental data reported in [20].

Next, the parameter $\beta_0$ is considered, which controls the amplitude of the intergranular stress $\beta_s$, cf. equation (4.13). The computed volume fraction profiles for different values of $\beta_0$ are plotted in Fig. 4.5. One can observe that as $\beta_0$ increases, particle migration is inhibited and the volume fraction in the central region of the channel, where particles agglomerate, becomes smaller. Also, the maximum value and the gradient of $\phi_s$ decrease. In other words, the increase of $\beta_0$ flattens out the volume fraction profiles. From a physical standpoint, this is to be expected since $\beta_s$ expresses the resistance of grains to compaction. Further, it is noted that $\beta_s$ does not appear in the momentum balance law of the granular phase, but only in the compaction equation (3.92) as a negative source term (sink) that mediates particle migration, which corroborates the observed trend.

The role of the interphasial drag coefficient $\delta$ is now considered. In the previous Subsection it was mentioned that, for the flows considered herein, this coefficient is so stiff that the velocities of the two phases equilibrate during the development of the flow. It is therefore interesting to examine the sensitivity of the velocity equilibration with respect to $\delta$. To this

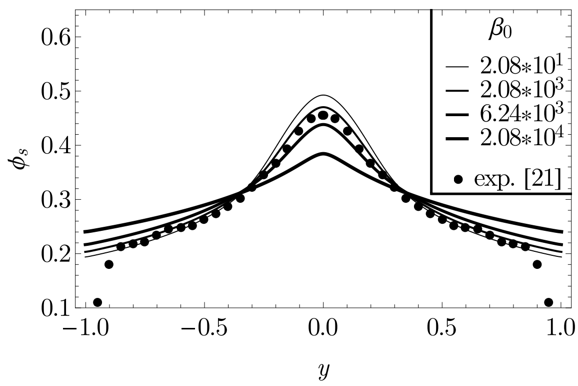


Figure 4.5: Dependence of the profile of the volume fraction across the channel on the amplitude of the integranular stress. Average volume fraction $\overline{\phi}_s = 0.298$. The dots show the experimental data reported in [20].

end, the computations for the case of $\overline{\phi}_s = 0.298$ are repeated by multiplying the value of $\delta$ with a shrinkage factor $\varepsilon$.

In Fig. 4.6 the velocity and volume fraction profiles are presented for $\varepsilon = 1$, which corresponds to the physical value of $\delta$ for $\overline{\phi}_s = 0.298$, as well as $\varepsilon = 0.01$ and 0.001. From these figures one can observe that the volume fraction and the velocity of the granular phase $u_s$ remain practically unaffected by the shrinkage of the drag coefficient. Also, it can be seen that for $\varepsilon = 0.01$ the two phasial velocities remain equilibrated. In fact, $\delta$ has to be contracted by three orders of magnitude, i.e. $\varepsilon = 0.001$, in order to observe a significant difference between $u_s$ and $u_f$. More specifically, from the plots shown in Fig 4.6(a), it can be observed that for $\varepsilon = 0.001$ the fluid velocity $u_f$ is uniformly higher than $u_s$. Also in this case and in the central region of the channel with high particle concentrations, $u_f$ is almost constant and approximately 10% higher than the maximum value of $u_s$ at the centerline. On the other hand it should be acknowledged that $\varepsilon = 0.001$ represents an extreme and, most likely, physically unrealistic case. One may therefore conclude that, in the flows under consideration, the phasial velocities remain equilibrated.

The analysis of this Section concludes with the presentation of computations at very high particle concentrations, close to the maximum packing treshold $\phi_m$. This parameter enters the expressions for the viscosity coefficients of the granular phase, cf. Equations (4.11) and (4.12), as well as the correlation for the integranular stress $\beta_s$, cf. (4.13). All three of these quantities diverge as $\phi$ approaches $\phi_m$. In the cases examined so far, the values of the volume fraction were sufficiently below the critical value $\phi_m$; it would therefore be informative to see how the flow profiles change as the particle concentration approaches maximum packing. To this end computations are repeated with $\phi_s = 0.3$, 0.4 and 0.5. The numerical results for the volume fraction and velocity $u_s$ are shown in Fig. 4.7a. It is interesting to observe that in fact for $\phi_s = 0.5$ the volume fraction at the central region of the channel is almost uniform and very close to the critical value $\phi_m$. Further, it can be observed that the velocity profile in this area is almost uniform. In other words, one has the formation of an effectively

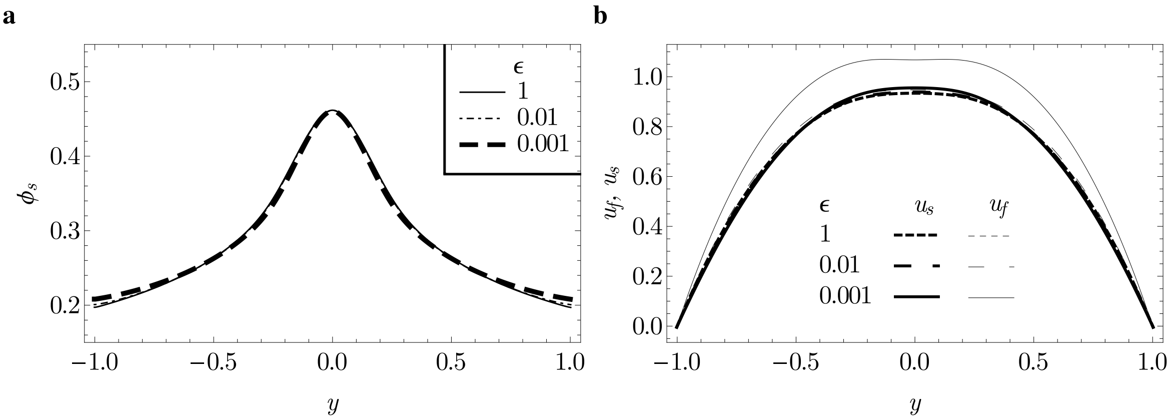


Figure 4.6: Sensitivity analysis with respect to the drag coefficient $\delta$. The value of $\delta$ is multiplied by a shrinkage factor $\varepsilon$. (a) volume fraction $\phi_s$. (b) non-dimensional phasial velocities $u_s$ and $u_f$. It can be observed that $\phi_s$ and $u_s$ remain practically unaffected by the shrinkage of the drag coefficient. Further, appreciable differences between the two phasial velocities appear only when $\delta$ is contracted by a factor of $\varepsilon = 0.001$.

rigid plug moving at constant velocity. This is a well known phenomenon which has been often reported in the literature since the early works [144] and [154]. It is interesting to mention that the central rigid plug is formed independently of the actual value of $\gamma_0$. In fact computations were repeated for $\gamma_0 = 0$ and still predicted the formation of this plug.

It is also worth mentioning that $\phi_s$ gets very close to critical value $\phi_m$ but it does not become equal to it anywhere in the flow domain. This is due to the presence of the intergranular stress $\beta_s$ in the compaction equation (4.9) which also diverges at $\phi_m$. More specifically, according to the algorithm presented in Appendix B, the profile of $\phi_s$ is computed via a Poisson equation that contains $\beta_s$ on its right-hand side. As $\phi_s$ approaches the jamming value $\phi_m$, the right hand side of the Poisson equation becomes negative due to $\beta_s$, which prevents $\phi_s$ from reaching $\phi_m$. It should be noted, however, that this is not a numerical cutoff; on the contrary, the presence of $\beta_s$ in (4.9) expresses the physical property of granular materials to resist compaction. In incompressible flows of rigid particles, when the concentration approaches the maximum packing treshold, the resistance of particles to further compaction can become arbitrarily large.

## 4.4 Conclusions

This Chapter presented a numerical study of Poiseuille flow of dense non-colloidal suspensions in a narrow channel. This study is based on the two-phase continuum model developed in Chapter 3. The computations capture accurately the particle migration towards the central region of the channel and are in good agreement with experimental data and earlier discrete-element computations. Also, for very dense suspensions, they predict the formation of an effectively rigid plug in the central region of the channel moving at constant velocity, in ac-

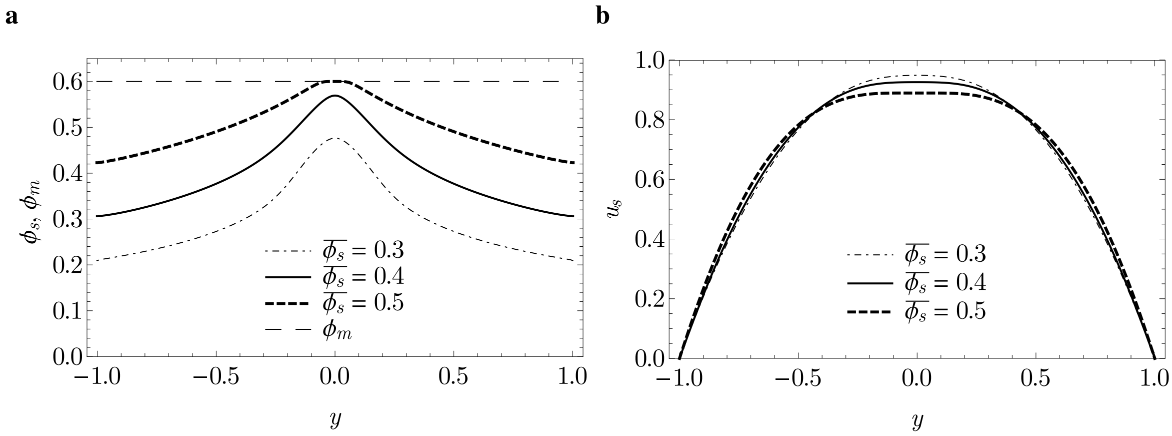


Figure 4.7: Flow profiles for different average volume fractions $\overline{\phi}_s$. (a) volume fraction $\phi_s$. (b) non-dimensional velocity of the granular phase $u_s$. For $\overline{\phi}_s = 0.5$ one can observe the formation of an effectively rigid plug moving at constant velocity.

cordance with existing experimental observations. The study has been supplemented by an analysis of the role of the integranular and nonlocal stresses acting on the granular phase. According to it, both of these parameters influence significantly particle migration, hence the concentration profiles across the channel. In particular, when their amplitude increases, particle migration becomes weaker thereby resulting in smoother concentration profiles.

# Chapter 5

# A numerical algorithm for the solution of the proposed two-phase flow model

## 5.1 Introduction

The system of governing equations (3.88)–(3.92), which express the model of Chapter 3 for the case of constant density, possess a complex structure that requires specific consideration in order to be solved numerically. In particular, when attempting to devise a numerical algorithm for the integration of this system, one is confronted with the following issues.

**i. Size and complexity**. With the saturation relation $\phi_f = 1 - \phi_s$, three scalar and two vector differential equations remain to be solved in space and time. It is not obvious how to discretize the system in time and space and, in particular, there are multiple choices relative to the order in which to integrate the various equations.

**ii. Equation coupling**. The governing equations are strongly coupled. Most notably, the phasial dynamic pressures $p_s^1$ and $p_f^1$ appear explicitly on the right-hand side of the compaction equation (3.92), and the nonconservative product $p_f^1 \nabla \phi_s$ appears on the right-hand side of the momentum equations (3.89) and (3.91). This can be contrasted with the Navier-Stokes equations for a simple fluid, where only the gradient of the pressure appears, and only in the momentum balance. These differences considerably complicate the numerical solution, as further discussed in Section 5.3.

**iii. Nonlinear rheology**. The momentum equation for the granular phase (3.91) contains a nonlinear expression for the viscous stresses of the granular phase, which must be considered with care due to the high viscosity of dense suspensions.

**iv. Stiff material coefficients**. The majority of the experimental expressions for the material properties of the granular phase are stiff nonlinear functions of the volume fraction $\phi_s$ which present a singularity at maximum packing, requiring specific numerical treatment.

v. **Divergent velocity fields**. From the continuity equations (3.88) and (3.90) and the compaction equation (3.92), it can be seen that the velocity fields $\mathbf{u}_s$ and $\mathbf{u}_f$ are not solenoidal even in the constant-density limit. In particular, the divergence of $\mathbf{u}_s$ can be expressed as the following non-vanishing expression,

$$\nabla \cdot \mathbf{u}_s = -\mathrm{Re_c}\,\phi_f \left(p_s^1 - \beta_s - p_f^1 + \nabla \cdot (\gamma_s \nabla \phi_s)\right). \tag{5.1}$$

Projection methods, originally developed by Chorin [70] and independently by Temam [71] for the solution of the incompressible Navier-Stokes equations, have been shown to be capable of treating divergent flows of simple fluids. In fact there are extensions of the standard Chorin-Temam method, which leverage the Helmholtz decomposition of vector fields, [156], that apply to variable-density low-Mach-number flows [157–159]. These approaches provide a way to to cope with the source term $\frac{\partial \rho}{\partial t}$ which appears in the elliptic equation for the pressure if the flow is not solenoidal, as this term can be destabilizing with respect to time integration [160].

In the same vein, algorithms for two-phase flow have been developed. In [42] a suitable generalization of the projection method, based on Ladyzhenskaya's decomposition theorem [161], was shown to be applicable to two-phase flow equations such as the system (2.1)–(2.6). In fact this is the algorithm which was used in the numerical computations of Chapter 2. This algorithm is particularly interesting since, with the only exception of a different rheology formulation, the new equations (3.88)–(3.92) reduce to equations (2.1)–(2.6) in the limit $\mathrm{Re}_c \to 0$ where compaction is negligible.

One could then attempt to extend the method presented in [42] to equations (3.88)–(3.92). In fact, this Chapter presents such an attempt and proposes an algorithm for the integration of the system (3.88)–(3.92), which describes two-phase divergent flow of suspensions. It should be stressed, however, that such extension is not direct, as there are a number of fundamental differences to be addressed. In particular the coupling between the various equations, mentioned in point (ii) above, proves to be particularly challenging.

The structure of the Chapter is as follows. First, a comprehensive description of the algorithm is given in Section 5.2; the time and space discretizations are discussed and integration techniques for the various terms in the equations are proposed. Then, in Section 5.3, a more detailed analysis of time-integration is performed, with the aim of providing insight into the behaviour of the compaction equation (3.92). This is particularly important since this equation presents a peculiar structure that does not appear in previous flow models: it couples directly the evolution of the volume fraction with the phasial pressures. It turns out that this coupling generates a peculiar interaction with the projection method, which has not been previously addressed in the literature and requires specific numerical treatment.

## 5.2 Structure of the algorithm

### 5.2.1 Selection of unknown variables

Projection algorithms for the Navier-Stokes equations solve these equations whith respect to the velocity and pressure variables; in the case of (3.88)–(3.92), there is more flexibility in the choice of solution variables. One can, in principle, proceed analogously and solve the system (3.88)–(3.92) with respect to the phasial velocities $\mathbf{u}_f$ and $\mathbf{u}_s$, the phasial pressures $p_f$ and $p_s$ and volume fractions $\phi_f$ and $\phi_s$. However, as discussed in [42], such choice might not be desirable for a number of reasons. Most notably, the momentum equations (3.89) and (3.91) contain the non-conservative product $p_f^1 \nabla\phi_s$ on their right-hand side; this can jeopardize the performance of a projection method because, in general, $p_f$ is not bounded in the $L^\infty$-norm; cf. [161] for theoretical and [77] for numerical evidence. In addition, in many cases of practical interest, equations (3.88)–(3.92) include a term expressing the gravitational acceleration which can be dominant, so that it is convenient to group it directly with the phasial pressures before solving the system.

To this end, the system (3.88)–(3.92) is rearranged. More specifically, the gravity vector g and the body-force terms $\rho_f\phi_f\mathbf{g}$ and $\rho_s\phi_s\mathbf{g}$, corresponding to the fluid and granular phases, are introduced, and the auxiliary variables $p_d$ and $p'_f$ are defined as follows,

$$p_d = (p_s^1 - p_f^1)\phi_s, \qquad p'_f = p_f^1 - \rho_f\Phi, \quad \text{with} \quad \Phi = \textstyle\int \mathbf{g}\cdot \mathrm{d}\mathbf{x}. \tag{5.2}$$

In the above expression the integration constant for the potential $\Phi$ is immaterial, as only the gradient of $p'_f$ enters the equations; for instance, denoting the components of $\mathbf{g} = (g_1, g_2, g_3)$, One can set $\Phi = (g_1x_1, g_2x_2, g_3x_3)$. The system (3.88)–(3.92) can then be cast into the following equations for the unknowns $\mathbf{u}_f$, $\mathbf{u}_s$, $p'_f$, $p_d$ and $\phi_s$,

$$\frac{\mathrm{d}\phi_f}{\mathrm{d}_f t} + \phi_f \nabla\cdot\mathbf{u}_f \;=\; 0\,, \tag{5.3}$$

$$\rho_f\phi_f\frac{\mathrm{d}\mathbf{u}_f}{\mathrm{d}_f t} + \phi_f\nabla p'_f \;=\; \frac{1}{\mathrm{Re}}\nabla\cdot\mathbf{T}_f \;-\delta(\mathbf{u}_f-\mathbf{u}_s)\,, \tag{5.4}$$

$$\frac{\mathrm{d}\phi_s}{\mathrm{d}_s t} + \phi_s\nabla\cdot\mathbf{u}_s \;=0\,, \tag{5.5}$$

$$\rho_s\phi_s\frac{\mathrm{d}\mathbf{u}_s}{\mathrm{d}_s t} + \nabla p_d \;=\frac{1}{\mathrm{Re}}\nabla\cdot\mathbf{T}_s - \nabla\cdot\mathbf{C}_s + \delta(\mathbf{u}_f-\mathbf{u}_s) - \phi_s\nabla p'_f + (\rho_s-\rho_f)\phi_s\mathbf{g}\,, \tag{5.6}$$

$$\frac{\mathrm{d}\phi_s}{\mathrm{d}_s t} = \mathrm{Re}_c\,\phi_s\phi_f\left(\frac{p_d}{\phi_s} - \beta_s + \nabla\cdot(\gamma_s\nabla\phi_s)\right)\,. \tag{5.7}$$

This system is supplemented by the saturation relation,

$$\phi_f + \phi_s \;=\; 1\,. \tag{5.8}$$

In the above system the following shorthand notation has been employed for the viscous components of the stress tensors $\mathbf{T}_f$ and $\mathbf{T}_s$ and for the nonlocal stresses $\mathbf{C}_s$,

$$\begin{aligned}
\mathbf{T}_f &= (\zeta_f \nabla \cdot \mathbf{u}_f)\, \phi_f \mathbf{I} + 2\mu_f \phi_f \mathbf{V}_f^d, && (5.9)\\
\mathbf{T}_s &= ((\zeta_{s1}+\zeta_{s2})\nabla\cdot\mathbf{u}_s + \chi_a)\, \phi_s \mathbf{I} + 2(\mu_{s1}+\mu_{s2})\phi_s \mathbf{V}_s^d + \chi_b \phi_s \mathbf{V}_s\cdot\mathbf{V}_s, && (5.10)\\
\mathbf{C}_s &= \gamma_s \nabla\phi_s \otimes \nabla\phi_s. && (5.11)
\end{aligned}$$

In equation (5.10), the terms $\mu_{s1}$, $\mu_{s2}$, $\zeta_{s1}$ and $\zeta_{s2}$ are obtained by splitting the generalized Newtonian viscosity coefficients $\mu_s = \mu_{s1} + \mu_{s2}$ and $\zeta_s = \zeta_{s1} + \zeta_{s2}$ which were defined in (3.63),

$$\mu_{s1} = \frac{c_4}{2\phi_s}, \quad \mu_{s2} = -\frac{c_5}{2\phi_s}\frac{\det \mathbf{V}_s}{(\mathbf{V}_s : \mathbf{V}_s)^{\frac{3}{2}}}, \quad \zeta_{s1} = \frac{3c_1 + c_4}{3\phi_s}, \quad \zeta_{s2} = -\frac{c_5}{3\phi_s}\frac{\det \mathbf{V}_s}{(\mathbf{V}_s : \mathbf{V}_s)^{\frac{3}{2}}}. \qquad (5.12)$$

The above decomposition is performed in order to separate the nonlinear components $\mu_{s2}$ and $\zeta_{s2}$, which depend on the velocity gradients, since these components are treated separately with respect to time integration, cf. also Subsection 5.2.3. According to the analysis of Section 3.7, $\mu_{s1}$ and $\zeta_{s1}$ can be identified with the Newtonian viscosity coefficients measured for planar flow, whereas $\mu_{s2}$ and $\zeta_{s2}$ can be expressed as functions of $\mathbf{V}_s$ and of a single *normal viscosity* coefficient $\mu_n$ according to equations (3.102) and (3.105),

$$\mu_{s2} = \frac{\mu_n}{\sqrt{2}}\frac{\det \mathbf{V}_s}{(\mathbf{V}_s : \mathbf{V}_s)^{\frac{3}{2}}}, \quad \zeta_{s2} = \frac{\mu_n\sqrt{2}}{3}\frac{\det \mathbf{V}_s}{(\mathbf{V}_s : \mathbf{V}_s)^{\frac{3}{2}}}. \qquad (5.13)$$

The terms $\chi_a$ and $\chi_b$ in equation (5.10) assume the analogous expressions derived in equations (4.1) and (4.2). It is important to notice that all the nonlinear expressions $\mu_{s2}$, $\zeta_{s2}$, $\chi_a$ and $\chi_b$ are proportional to the single viscosity coefficient $\mu_n$, so that the rheological description is completely defined by the three coefficients $\mu_{s1}$, $\zeta_{s1}$ and $\mu_n$.

Further, it can be observed that in equations (5.4) and (5.6) only the gradients of the phasial pressures appear. In addition, gravity does not explicitly enter the equations for the fluid phase, and its effect is limited to a buoyancy term appearing on the right-hand side of the momentum equation (5.6) for the granular phase; in particular, if the two phases have the same density, this term vanishes.

### 5.2.2 Time discretization

The algorithm presented herein is, as usual for projection algorithms, a fractional-step method. To this end, a semi-implicit time-marching scheme is employed; the flowchart of this scheme is summarized now for the case of an equidistant temporal mesh with time-step $\Delta t$[1]. The superscripts $n$, and $n+1$ are used to denote values computed at time $n\,\Delta t$ and $(n+1)\Delta t$, respectively.

1) The updated value of the volume fraction $\phi_s^{n+1}$ is computed from the compaction equation (5.7) with the following scheme,

$$\frac{\phi_s^{n+1}-\phi_s^n}{\Delta t} = \frac{1}{2}\mathrm{Re_c}\,\phi_s^n\phi_f^n\nabla\cdot\left(\gamma_s^n\nabla\phi_s^{n+1}+\gamma_s^n\nabla\phi_s^n\right)+\mathrm{Res}_\phi^{n+1/2}, \tag{5.14}$$

where the residual $\mathrm{Res}_\phi$ corresponds to the following expression,

$$\mathrm{Res}_\phi = -\,\mathbf{u}_s\cdot\nabla\phi_s+\mathrm{Re_c}\,\phi_f\left(p_d-\phi_s\beta_s\right)\,. \tag{5.15}$$

2) The time-integration scheme for the velocity of the granular phase is as follows,

$$\begin{aligned}\frac{\phi_s^{n+1}\mathbf{u}_s^{n+1}-\phi_s^n\mathbf{u}_s^n}{\Delta t}+\frac{\nabla p_d^{n+1/2}}{\rho_s} =& \frac{1}{\rho_s\mathrm{Re}}\nabla\cdot\left(\mu_{s1}^{n+1}\phi_s^{n+1}(\mathbf{V}_s^d)^{n+1}+\mu_{s1}^n\phi_s^n(\mathbf{V}_s^d)^n\right)+\\ &\frac{1}{2\rho_s\mathrm{Re}}\nabla\cdot\left(\zeta_{s1}^{n+1}\phi_s^{n+1}(\nabla\cdot\mathbf{u}_s)^{n+1}\mathbf{I}+\zeta_{s1}^n\phi_s^n(\nabla\cdot\mathbf{u}_s)^n\mathbf{I}\right)+\\ &\mathbf{Res}_s^{n+1/2}+\frac{\rho_s-\rho_f}{\rho_s}\phi_s^{n+1}\mathbf{g}\,,\end{aligned} \tag{5.16}$$

where the residual $\mathbf{Res}_s$ is given by,

$$\begin{aligned}\mathbf{Res}_s =& -\nabla\cdot\left(\phi_s\mathbf{u}_s\otimes\mathbf{u}_s\right)+\nabla\cdot\left(\frac{\gamma_s}{\rho_s}\nabla\phi_s\otimes\nabla\phi_s\right)-\phi_s\nabla\left(\frac{p_f'}{\rho_s}\right)+\frac{\delta}{\rho_s}\left(\mathbf{u}_f-\mathbf{u}_s\right)\\ &+\frac{1}{\rho_s\mathrm{Re}}\nabla\cdot\left((\zeta_{s2}\nabla\cdot\mathbf{u}_s+\chi_a)\phi_s\mathbf{I}+2\mu_{s2}\phi_s\mathbf{V}_s^d+\chi_b\phi_s\mathbf{V}_s\cdot\mathbf{V}_s\right)\,.\end{aligned} \tag{5.17}$$

In order to avoid the inversion of the nonlinear equation (5.16), a fractional projection is employed. In a preliminary "advection–diffusion step", a provisional value of the granular velocity $\tilde{\mathbf{u}}_s$ is computed as follows,

$$\phi_s^{n+1}\tilde{\mathbf{u}}_s-L_s = \phi_s^n\mathbf{u}_s^n+R_s+\Delta t\,\mathbf{Res}_s^{n+1/2} \tag{5.18}$$

with $L_s$ and $R_s$ defined as

$$L_s = \frac{\Delta t}{\rho_s\mathrm{Re}}\nabla\cdot\left(\mu_{s1}^{n+1}\phi_s^{n+1}\tilde{\mathbf{V}}_s^d\right)+\frac{\Delta t}{2\rho_s\mathrm{Re}}\nabla\cdot\left(\zeta_{s1}^{n+1}\phi_s^{n+1}(\nabla\cdot\tilde{\mathbf{u}}_s)\mathbf{I}\right) \tag{5.19}$$

$$R_s = \frac{\Delta t}{\rho_s\mathrm{Re}}\nabla\cdot\left(\mu_{s1}^n\phi_s^n(\mathbf{V}_s^d)^n\right)+\frac{\Delta t}{2\rho_s\mathrm{Re}}\nabla\cdot\left(\zeta_{s1}^n\phi_s^n(\nabla\cdot\mathbf{u}_s)^n\mathbf{I}\right) \tag{5.20}$$

It can be observed from equation (5.18) that the proposed method belongs to the class of pressure-free methods.

[1] For the sake of simplicity, the algorithm is presented here as a simple fractional-step time iteration. This algorithm can be directly cast in terms of a predictor-corrector method, by repeating the iteration twice; to this end, it is sufficient to mirror the procedure described in [77].

Subsequently, the projection step is performed,

$$\phi_s^{n+1}\tilde{\mathbf{u}}_s \;=\; \phi_s^{n+1}\mathbf{u}_s^{n+1} + \frac{\Delta t}{\rho_s}\nabla q_d^{n+1} - \Delta t\frac{\rho_s - \rho_f}{\rho_s}\phi_s^{n+1}\mathbf{g}\,. \tag{5.21}$$

The quantity $q_d^{n+1}$ is not the same as the pressure $p_d^{n+1/2}$ appearing in (5.16). Rather, it is an auxiliary numerical variable that enforces the Helmholtz decomposition and is denoted as "granular auxiliary pressure" in this Chapter. Of course, $q_d^{n+1}$ and $p_d^{n+1/2}$ are closely related; in fact $q_d$ and $p_d$ can be identified up to first order in time, [162],

$$p_d^{n+1/2} \;=\; q_d^{n+1} + \epsilon_d^{n+1}, \qquad \epsilon_d = O(\Delta t). \tag{5.22}$$

Later in this Section, a second-order accurate expression is obtained for $\epsilon_d$. Nevertheless, the computation of this quantity is quite cumbersome in the present case, due to the fact that a Poisson equation has to be solved for this quantity at each time step (with third-order differential operators in the source term on the right-hand side). For this reason, and in view of the complexity of the system, in what follows, $p_d^{n+1/2}$ is identified with $q_d^{n+1}$, so that the proposed algorithm computes the pressure field with first-order accuracy.

Further, it can be seen that equations (5.21) contains the gravity term on the right-hand side, which might come as a surprise because its presence is not customary in the literature of projection methods; typically, this term is incorporated in the computation of the provisional velocity $\tilde{\mathbf{u}}_s$. The rationale behind this choice is that it allows an efficient implementation of boundary conditions, as elaborated in the discussion of boundary conditions below. In this respect, it can be observed that (5.21) actually constitutes the Helmholtz–Marsden decomposition of the vector field $\phi_s\tilde{\mathbf{u}}_s + \Delta t\frac{\rho_s-\rho_f}{\rho_s}\phi_s\mathbf{g}$, cf. also [156].

The granular auxiliary pressure $q_d^{n+1}$ is computed as the solution to the elliptic problem that emerges upon projecting equation (5.21) over the subspace of fields with a specified divergence. More specifically, by virtue of the continuity and compaction equations (5.5) and (5.7), at every time step the term $\nabla\cdot(\phi_s\mathbf{u}_s)$ has to satisfy the following relation,

$$\nabla\cdot(\phi_s\mathbf{u}_s) \;=\; \mathbf{u}_s\cdot\nabla\phi_s - \mathrm{Re_c}\,\phi_s\phi_f\left(\frac{q_d}{\phi_s}\beta_s + \nabla\cdot(\gamma_s\nabla\phi_s)\right). \tag{5.23}$$

Consequently, taking the divergence of equation (5.21) allows to enforce the divergence constraint (5.23). The following equation is obtained,

$$\nabla\cdot(\phi_s^{n+1}\tilde{\mathbf{u}}_s)=\mathbf{u}_s^n\cdot\nabla\phi_s^{n+1}-\mathrm{Re_c}\,\phi_s^{n+1}\phi_f^{n+1}\left(\frac{q_d^{n+1}}{\phi_s^{n+1}}-\beta_s^{n+1}+\nabla\cdot(\gamma_s^{n+1}\nabla\phi_s^{n+1})\right)$$
$$+\frac{\Delta t}{\rho_s}\nabla^2 q_d^{n+1}-\Delta t\frac{\rho_s-\rho_f}{\rho_s}\nabla\phi_s^{n+1}\cdot\mathbf{g}\,. \tag{5.24}$$

This specific choice of time integration is crucial for the performance of the method; in particular, it is remarked that the value of $q_d$ on the right-hand side of the divergence constraint (5.23) is computed implicitly with respect to time. The implications of this choice are further discussed in Section 5.3.

Equation (5.24) is rearranged in order to obtain the following elliptic problem for $q_d^{n+1}$,

$$\nabla^2 q_d^{n+1}-\frac{\rho_s\mathrm{Re_c}\,\phi_f^{n+1}}{\Delta t}\,q_d^{n+1}=\frac{\rho_s\mathrm{Re_c}\,\phi_s^{n+1}\phi_f^{n+1}}{\Delta t}\left(\nabla\cdot(\gamma_s^{n+1}\nabla\phi_s^{n+1})-\beta_s^{n+1}\right)+$$
$$(\rho_s-\rho_f)\nabla\phi_s^{n+1}\cdot\mathbf{g}+\frac{\rho_s}{\Delta t}\nabla\cdot(\phi_s^{n+1}\tilde{\mathbf{u}}_s)\,. \tag{5.25}$$

Once the granular auxiliary pressure $q_d^{n+1}$ has been calculated as the solution of the corresponding linear system, the granular velocity is updated via (5.21),

$$\mathbf{u}_s^{n+1}\;=\;\tilde{\mathbf{u}}_s-\frac{\Delta t}{\rho_s\phi_s^{n+1}}\nabla q_d^{n+1}+\Delta t\frac{\rho_s-\rho_f}{\rho_s}\mathbf{g}\,. \tag{5.26}$$

3) In analogy to the granular phase, the time–integration scheme for the fluid phase reads,

$$\begin{aligned}\frac{\phi_f^{n+1}\mathbf{u}_f^{n+1}-\phi_f^n\mathbf{u}_f^n}{\Delta t}\;=\;&-\frac{\phi_f^{n+1}}{\rho_f}\nabla p_f'^{\,n+1/2}\\&+\frac{1}{\rho_f\mathrm{Re}}\nabla\cdot\left(\mu_f^{n+1}\phi_f^{n+1}(\mathbf{V}_f^d)^{n+1}+\mu_f^n\phi_f^n(\mathbf{V}_f^d)^n\right)\\&+\frac{1}{2\rho_f\mathrm{Re}}\nabla\cdot\left(\zeta_f^{n+1}\phi_f^{n+1}(\nabla\cdot\mathbf{u}_f)^{n+1}\mathbf{I}+\zeta_f^n\phi_f^n(\nabla\cdot\mathbf{u}_f)^n\mathbf{I}\right)\\&+\mathbf{Res}_f^{n+1/2}\,,\end{aligned} \tag{5.27}$$

where the residual $\mathbf{Res}_f$ is given by,

$$\mathbf{Res}_f\;=\;-\nabla\cdot(\phi_f\mathbf{u}_f\otimes\mathbf{u}_f)-\frac{\delta}{\rho_f}(\mathbf{u}_f-\mathbf{u}_s)\,. \tag{5.28}$$

In the "advection–diffusion" step of the fluid phase, the provisional fluid velocity $\tilde{\mathbf{u}}_f$ is computed as follows,

$$\phi_f^{n+1}\tilde{\mathbf{u}}_f-L_f=\phi_f^n\mathbf{u}_f^n+R_f+\Delta t\,\mathbf{Res}_f^{n+1/2} \tag{5.29}$$

with $L_f$ and $R_f$ defined as

$$L_f = \frac{\Delta t}{\rho_f \mathrm{Re}} \nabla \cdot (\mu_f^{n+1} \phi_f^{n+1} \tilde{\mathbf{V}}_f^d) + \frac{\Delta t}{2\rho_f \mathrm{Re}} \nabla \cdot (\zeta_f^{n+1} \phi_f^{n+1} (\nabla \cdot \tilde{\mathbf{u}}_f) \mathbf{I}) \tag{5.30}$$

$$R_f = \frac{\Delta t}{\rho_f \mathrm{Re}} \nabla \cdot (\mu_f^n \phi_f^n (\mathbf{V}_f^d)^n) + \frac{\Delta t}{2\rho_f \mathrm{Re}} \nabla \cdot \left(\zeta_f^n \phi_f^n (\nabla \cdot \mathbf{u}_f)^n \mathbf{I}\right) \tag{5.31}$$

The projection step for the fluid phase assumes the form,

$$\phi_f^{n+1} \tilde{\mathbf{u}}_f \;=\; \phi_f^{n+1} \mathbf{u}_f^{n+1} + \Delta t \frac{\phi_f^{n+1}}{\rho_f} \nabla q_f'^{n+1}, \tag{5.32}$$

where, analogously to the granular phase, $q_f'$ is the "fluid auxiliary pressure". From equations (5.3), (5.5) and (5.8), one obtains that the term $\nabla \cdot (\phi_s \mathbf{u}_f)$ has to satisfy the following relation,

$$\nabla \cdot (\phi_f^{n+1} \mathbf{u}_f^{n+1}) \;=\; -\nabla \cdot (\phi_s^{n+1} \mathbf{u}_s^{n+1}). \tag{5.33}$$

Since $\mathbf{u}_s^{n+1}$ has been already updated, equation (5.33) can be used to compute the fluid auxiliary pressure directly. More precisely, the fluid auxiliary pressure is computed as the solution of the following elliptic problem,

$$\nabla \cdot (\phi_f^{n+1} \nabla q_f'^{n+1}) \;=\; \frac{\rho_f}{\Delta t} \nabla \cdot (\phi_f^{n+1} \tilde{\mathbf{u}}_f) + \frac{\rho_f}{\Delta t} \nabla \cdot (\phi_s^{n+1} \mathbf{u}_s^{n+1}). \tag{5.34}$$

Following the computation of the fluid auxiliary pressure $q_f'^{n+1}$, the fluid velocity is updated via (5.32),

$$\mathbf{u}_f^{n+1} \;=\; \tilde{\mathbf{u}}_f^{n+1} - \frac{\Delta t}{\rho_f} \nabla q_f'^{n+1}. \tag{5.35}$$

**Explicit integration of the residuals $\mathrm{Res}_\phi$, $\mathbf{Res}_s$ and $\mathbf{Res}_f$**

The time-marching scheme just described is essentially a Crank-Nicolson method for the integration of the diffusive operator inside the compaction equation (5.7) and for the Newtonian component of the viscous fluxes of both phases.

On the other hand the remaining residuals, denoted as $\mathrm{Res}_\phi$, $\mathbf{Res}_s$ and $\mathbf{Res}_f$ in equations (5.14), (5.16) and (5.27), are evaluated explicitly at $n + 1/2$. $\mathrm{Res}_\phi$ contains the convective term $\mathbf{u}_s^n \cdot \nabla \phi_s^n$ and the source term $\mathrm{Re}_\mathrm{c}\, \phi_f\, (q_d - \phi_s \beta_s)$, while $\mathbf{Res}_s$ and $\mathbf{Res}_f$ contain the convective fluxes $\nabla \cdot (\phi_\alpha \mathbf{u}_\alpha \otimes \mathbf{u}_\alpha)$ as well as source terms that describe the momentum exchange between the phases, the nonlinear rheology and the divergence of the configuration stress tensor $\gamma_s \nabla \phi_s \otimes \nabla \phi_s$. Following [163], the approximation of these terms is performed with a second-order Adams-Bashforth scheme so that,

$$\mathrm{Res}_\phi^{n+1/2} \approx \frac{3}{2}\mathrm{Res}_\phi^{n} - \frac{1}{2}\mathrm{Res}_\phi^{n-1}\,, \tag{5.36}$$

$$\mathbf{Res}_\alpha^{n+1/2} \approx \frac{3}{2}\mathbf{Res}_\alpha^{n} - \frac{1}{2}\mathbf{Res}_\alpha^{n-1}, \qquad \alpha = s, f\,. \tag{5.37}$$

**Boundary conditions**

The use of a Crank-Nicolson scheme, and actually of any implicit or semi-implicit scheme, for the time integration of the diffusive operator in equation (5.14) and of the viscous fluxes in (5.16) and (5.27) presumes that the volume fraction $\phi_s$ and the provisional velocities $\tilde{\mathbf{u}}_a$ be endowed with appropriate boundary conditions. For the volume fraction the prescription of boundary conditions concerns an advection-diffusion scalar equation and is not particularly problematic from a numerical perspective; on the other hand, the choice of proper boundary conditions for the provisional velocity is crucial for the correct implementation of tangential boundary conditions for the true velocity [162].

An application of the analysis of [162] to equations (5.3)–(5.8) dictates that the tangential components of the provisional velocities be assigned the following boundary conditions,

$$\tilde{\mathbf{u}}_s^{n+1}|_{\partial\Omega}\cdot\boldsymbol{\tau} = \mathbf{u}_s^{n+1}|_{\partial\Omega}\cdot\boldsymbol{\tau} + \frac{\Delta t}{\rho_s\phi_s^{n+1}}\nabla q_d^{n+1}|_{\partial\Omega}\cdot\boldsymbol{\tau} - \Delta t\frac{\rho_s-\rho_f}{\rho_s}\mathbf{g}\cdot\boldsymbol{\tau}\,, \tag{5.38}$$

$$\tilde{\mathbf{u}}_f^{n+1}|_{\partial\Omega}\cdot\boldsymbol{\tau} = \mathbf{u}_f^{n+1}|_{\partial\Omega}\cdot\boldsymbol{\tau} + \frac{\Delta t}{\rho_f}\nabla q_f'^{n+1}|_{\partial\Omega}\cdot\boldsymbol{\tau}\,, \tag{5.39}$$

where $\partial\Omega$ denotes the boundary of the domain $\Omega$ and $\boldsymbol{\tau}$ is a versor oriented as the velocity component tangential to the boundary. In fact, relations (5.38) and (5.39) simply express the tangential component of equations (5.26) and (5.35), respectively.

The quantities $\mathbf{u}_s^{n+1}|_{\partial\Omega}\cdot\boldsymbol{\tau}$ and $\mathbf{u}_f^{n+1}|_{\partial\Omega}\cdot\boldsymbol{\tau}$ are known since they are specified as boundary conditions; $\phi_s^{n+1}$ is also known, as the volume fraction is the first variable to be updated. However, neither $q_d^{n+1}$ nor $q_f'^{n+1}$ are known at this stage of the algorithm and, therefore, they need to be approximated. It can be shown that employing $q_d^n$ and $q_f'^n$ instead of $q_d^{n+1}$ and $q_f'^{n+1}$ in equations (5.38) and (5.39) does not alter significantly the convergence properties of the scheme, cf. also the relevant discussion in [163]; this choice is followed here. Thus, the boundary conditions for the tangential components of $\tilde{\mathbf{u}}_s$ and $\tilde{\mathbf{u}}_f$ read,

$$\tilde{\mathbf{u}}_s^{n+1}|_{\partial\Omega}\cdot\boldsymbol{\tau} = \mathbf{u}_{s_b}\cdot\boldsymbol{\tau} + \frac{\Delta t}{\rho_s\phi_s^{n+1}}\nabla q_d^{n}|_{\partial\Omega}\cdot\boldsymbol{\tau} - \Delta t\frac{\rho_s-\rho_f}{\rho_s}\mathbf{g}\cdot\boldsymbol{\tau}\,, \tag{5.40}$$

$$\tilde{\mathbf{u}}_f^{n+1}|_{\partial\Omega}\cdot\boldsymbol{\tau} = \mathbf{u}_{f_b}\cdot\boldsymbol{\tau} + \frac{\Delta t}{\rho_f}\nabla q'^{n}_{f}|_{\partial\Omega}\cdot\boldsymbol{\tau}\,. \tag{5.41}$$

On the other hand, the boundary conditions for the normal components of $\tilde{\mathbf{u}}_s$ and $\tilde{\mathbf{u}}_f$ are inherited from the Helmholtz decomposition and, in particular, from the requirement that the decomposition is orthogonal. One obtains

$$\tilde{\mathbf{u}}_s^{n+1}|_{\partial\Omega} \cdot \boldsymbol{n} \;= \mathbf{u}_s^{n+1}|_{\partial\Omega} \cdot \boldsymbol{n} \;=\; \mathbf{u}_{s_b} \cdot \boldsymbol{n}\,, \tag{5.42}$$

$$\tilde{\mathbf{u}}_f^{n+1}|_{\partial\Omega} \cdot \boldsymbol{n} \;= \mathbf{u}_f^{n+1}|_{\partial\Omega} \cdot \boldsymbol{n} \;=\; \mathbf{u}_{f_b} \cdot \boldsymbol{n}\,, \tag{5.43}$$

where $\boldsymbol{n}$ denotes the versor normal to the boundary. Finally, as regards the boundary conditions for the phasial pressures, they are directly induced by combining (5.42) and (5.43) with (5.26) and (5.35), respectively. This yields,

$$\nabla q_d^{n+1}|_{\partial\Omega} \cdot \boldsymbol{n} \;= \phi_s^{n+1}(\rho_s - \rho_f)\mathbf{g} \cdot \boldsymbol{n}, \tag{5.44}$$

$$\nabla q_f'^{n+1}|_{\partial\Omega} \cdot \boldsymbol{n} \;= 0\,. \tag{5.45}$$

In other words, each phase is endowed with a different Neumann problem.

### A note on the role of the auxiliary pressures

The relation between the auxiliary pressures $q_d^n$ and $q_f'^n$ and the pressures $p_d^n$ and $p_f'^n$ is quite delicate and constitutes one of the most difficult parts in the analysis of projection methods. In order to clarify this point it is first noted that, for the case of the Navier-Stokes equations, the pressure term computed by projection methods can exhibit artificial boundary layers due to the boundary conditions that it inherits from the Helmholtz decomposition. More specifically, the normal component of the momentum equation at the wall provides a constraint for the pressure which depends on residual terms such as the viscous stresses and is not necessarily compatible with the constant Neumann condition which is imposed on the Helmholtz decomposition. A detailed analysis of this point is performed in [164], the authors of which additionally establish the thickness of such layers as a function of $\Delta t$. As shown in [165], the computed pressure converges to the solution only on the average, a type of convergence for which boundary layers are inconsequential.

The same manifestation of boundary layers in the pressure fields is expected for the governing system (5.3)–(5.8) as well. More precisely, this is due to the fact that $\nabla p_f'$ and $\nabla p_d$ are constrained by equations (5.4) and (5.6), which are not automatically compatible with boundary conditions on $\nabla q_f'$ and $\nabla q_d$ imposed through equations (5.26) and (5.35). For the case of the Navier-Stokes equations, the discrepancy between the auxiliary pressure that is used in the projection and the actual pressure is not a fundamental issue since the algorithm only requires the auxiliary pressure for time integration; if one is not interested in the value of the pressure field it is not even necessary to compute it. On the other hand, for the system (5.3)–(5.8), the values of the phasial pressures $p_d^{n+1/2}$ and $p'^{n+1/2}$ are required in order to advance the algorithm, since they enter the expressions for $\mathbf{Res}_\phi$ and $\mathbf{Res}_s$ in equations (5.14) and (5.16), respectively. As mentioned with respect to equation (5.22), these quantities do not exactly coincide with $q_d^{n+1}$ and $q'^{n+1}$, as they differ by first-order terms in $\Delta t$,

$$p_d^{n+1/2} = q_d^{n+1} + \epsilon_d^{n+1}, \qquad p'^{n+1/2} = q'^{n+1} + \epsilon'^{n+1}, \tag{5.46}$$

with $\epsilon_d$ and $\epsilon'$ of order $O(\Delta t)$. Following the procedure proposed in [162], it is possible to obtain second-order accurate expressions for the gradient of the quantities $\epsilon_d^{n+1}$ and $\epsilon'^{n+1}$. These are derived by combining equations (5.16), (5.18) and (5.26), as well as equations (5.27), (5.29) and (5.35). The following relations are obtained,

$$\nabla\epsilon_d^{n+1} = -\frac{\Delta \mathrm{t}}{2\rho_s \mathrm{Re}} \nabla\cdot\left(\mu_{s1}^{n+1}\phi_s^{n+1}\mathbf{Q}_d + \zeta_{s1}^{n+1}\phi_s^{n+1}\mathbf{R}_d\right), \tag{5.47}$$

$$\nabla\epsilon'^{n+1} = -\frac{\Delta \mathrm{t}}{2\rho_f\phi_f \mathrm{Re}} \nabla\cdot\left(\mu_f^{n+1}\phi_f^{n+1}\mathbf{Q}' + \zeta_f^{n+1}\phi_f^{n+1}\mathbf{R}'\right), \tag{5.48}$$

where,

$$\mathbf{Q}_d = \nabla\left(\frac{\nabla(q_d^{n+1})}{\phi_s^{n+1}}\right) + \nabla\left(\frac{\nabla(q_d^{n+1})}{\phi_s^{n+1}}\right)^T - \frac{2}{3}\nabla\cdot\left(\frac{\nabla(q_d^{n+1})}{\phi_s^{n+1}}\right)\mathbf{I}, \tag{5.49}$$

$$\mathbf{R}_d = \nabla\cdot\left(\frac{\nabla(q_d^{n+1})}{\phi_s^{n+1}}\right)\mathbf{I}, \tag{5.50}$$

$$\mathbf{Q}' = \nabla\nabla q_f'^{n+1} + \left(\nabla\nabla q_f'^{n+1}\right)^T - \frac{2}{3}\nabla\cdot(\nabla q_f'^{n+1})\mathbf{I}, \tag{5.51}$$

$$\mathbf{R}' = \nabla\cdot\left(\nabla(q'^{n+1})\right). \tag{5.52}$$

As shown in [162], in the case of the Navier-Stokes equations the same procedure is sufficient to obtain second-order accuracy for the pressure term, due to the fact that only the gradient of the pressure correction appears in the equations. In the present case, on the other hand, the auxiliary pressures $p_d$ and $p'$ appear directly in the governing equations (5.3)–(5.8), so that it is not sufficient to know the gradients of $\epsilon_d$ and $\epsilon'$ and the values of $\epsilon_d$ and $\epsilon'$ have to be known instead. In order to determine them, taking the divergence of equations (5.47) and (5.48) provides two Poisson equations for $\epsilon_d$ and $\epsilon'$, which can be used to compute these quantities if appropriate boundary conditions are known. However, this is not a trivial task: for instance, Neumann conditions for $p_d$ and $p'$ are not sufficient: these boundary conditions provide Neumann conditions for $\epsilon_d$ and $\epsilon'$ through equations (5.44), (5.45) and (5.46), but the integration constants remain to be determined. In view of this complexity, and further of the fact that it is challenging to compute accurately the right-hand sides of equations (5.47) and (5.48) since they contain third-order differential operators, the pressure-correction terms $\epsilon_d$ and $\epsilon'$ are neglected in the computation of the following numerical results presented in Chapter 6. In the case that second-order convergence for the pressure terms must be enforced, it is preferable to cast the proposed algorithm as a predictor-corrector method, cf. [77, 158].

### 5.2.3 Spatial discretization

In order to describe the spatial discretization, a uniform mesh is introduced on a rectangular domain. More precisely this mesh consists of a finite collection of equidistant 3-dimensional rectangles $K_{i,j,k}$, $i = 1, ...M_{x_1}$, $j = 1, ..., M_{x_2}$, $k = 1, ..., M_{x_3}$, lexicographically ordered with respect to the Cartesian coordinates of their cell centers $(x_{1_i}, x_{2_j}, x_{3_k})$. The length of the cells in each dimension is denoted by $\Delta x_1$, $\Delta x_2$ and $\Delta x_3$, respectively. Throughout this Section, the following standard notation convention is adopted: for every quantity $f$,

$$f(i,j,k) \equiv f(x_{1_i}, x_{2_j}, x_{3_k}), \tag{5.53}$$

$$f(i \pm \tfrac{1}{2}, j \pm \tfrac{1}{2}, k \pm \tfrac{1}{2}) \equiv f(x_{1_i} \pm \tfrac{\Delta x_1}{2}, x_{2_j} \pm \tfrac{\Delta x_2}{2}, x_{3_j} \pm \tfrac{\Delta x_3}{2}). \tag{5.54}$$

Further, two discrete operators are introduced. First, the finite-difference operator acting on a function $f(x_{1_i}, x_{2_j}, x_{3_k})$. When applied to the $x_1$-direction is given by,

$$\frac{\delta_n f(i,j,k)}{\delta x_1} = \frac{f(x_{1_i} + n\frac{\Delta x_1}{2}, x_{2j}, x_{3_k}) - f(x_{1i} - n\frac{\Delta x_1}{2}, x_{2j}, x_{3k})}{n\Delta x_1}. \tag{5.55}$$

Second, the linear interpolation operator, whose action along the $x_1$-direction reads,

$$\overline{f}^{nx_1}(i,j,k) = \frac{f(x_{1_i} + n\frac{\Delta x_1}{2}, x_{2_j}, x_{3_k}) + f(x_{1_i} - n\frac{\Delta x_1}{2}, x_{2_j}, x_{3_k})}{2}. \tag{5.56}$$

Expressions for the above operators acting on the other directions can be directly obtained by symmetry.

#### Compaction equation and volume-fraction regularization

The time integration of the compaction equation (5.7) requires to compute the advective transport term in $\mathbf{Res}_\phi$ which appears in equation (5.14). Since the volume fraction $\phi_s$ can formally be a discontinuous function and, even from a physical standpoint, exhibits very sharp variations in problem of practical interest, an adequate treatment of the convective term is required. This can be accomplished with an upwind scheme such as the Corner-Transport-Upwind (CTU) algorithm proposed in [166], which constitutes a second-order generalization of the standard upwind scheme to multiple dimensions.

Discontinuities in the volume fraction $\phi_s$ are also problematic since most coefficients in the system (5.3)–(5.8) depend on the volume fraction $\phi_s$. In turn, discontinuities can trigger severe numerical instabilities that may not be remedied unless a prohibitively small time–step $\Delta t$ is adopted. Moreover, from the analytical point of view, there is no *a priori* guarantee that the governing equations are well-posed for discontinuous values of $\phi_s$. For these reasons, a treatment of these instabilities is performed with a regularization method.

The idea behind any regularization method is to replace the values of the discontinuous function in the vicinity of the discontinuity by those of a smoother, and preferably compactly supported, one. These methods, usually referred to as *diffuse–interface* methods, are backed with a solid theoretical framework; see, for example, the recent discussions of [167, 168] and references therein. In particular, the perturbations induced by the use of the regularization lead to well-posed problems whilst the corresponding numerical schemes converge to the original solutions as the support of the regularization approaches zero.

However, despite their conceptual simplicity, regularization methods are not easy to implement when the interface is multi-dimensional and time-evolving. Moreover, the width of the regularization and its dependence on the spatial resolution of the numerical method remain a contentious topic, [77, 169].

In the present case a simple regularization technique is employed, which is easy to implement and able to treat complicated geometries: the so-called parabolic regularization. More specifically, at every step of the algorithm, and following the update of the volume fraction $\phi_s^{n+1}$, the next sequence of operations is performed.

1) For every computational cell $K_{ijk}$, the differences between the value of $\phi_s^{n+1}$ in $K$ with the values of $\phi_s^{n+1}$ in the adjacent cells $|\phi_s^{n+1}(K_{ijk}) - \phi_s^{n+1}(K')|$, is computed, *i.e.* compute for all cells $K'$ that possess a common face with $K_{ijk}$. An interface exists in the direction normal to the common face of $A$ and $B$ if,

$$|\phi_s^{n+1}(K_{ijk}) - \phi_s^{n+1}(K')| > \delta_1 \,,$$

where $\delta_1 > 0$ is the parameter that differentiates between a discontinuity and a regular transition.

2) Regularized values $\phi_s^r$ are computed by iterating the following parabolic problem,

$$\frac{\phi_s^{r+1} - \phi_s^r}{\Delta t} = \epsilon \, \nabla^2 \phi_s^r \,, \tag{5.57}$$

$$\phi_s^0 = \phi_s^{n+1} \,, \tag{5.58}$$

where $\epsilon$ is a suitably chosen regularization parameter until,

$$|\phi_s^{r+1}(K_{ijk}) - \phi_s^{r+1}(K')| \;\leq\; \delta_2 \,, \quad \forall K_{ijk}. \tag{5.59}$$

In this expression $\delta_2 \leq \delta_1$. If $\delta_2 = \delta_1$ the regularization procedure can potentially performed at every time iteration; by choosing a lower $\delta_2$ the amount of artificial diffusion can be controlled depending on the specific problem.

3) The regularized values $\phi_s^{r+1}$ are used as updated values of the volume fraction.

### Convective fluxes and odd-even decoupling

The numerical computations presented in this work have been performed with finite differences on a collocated grid. It is well-known that this type of spatial discretization requires additional treatment in order to cope with a velocity-pressure numerical instability usually denoted as "odd-even decoupling". Herein a specific interpolation of the convective fluxes is employed, the Rhie-Chow interpolation, which addresses this issue in a systematic way [170–174].

The core idea of this procedure is to compute the velocity at the cell interfaces by combining values of both the velocity and the gradient of the pressure. In this case, an interpolation scheme can be deduced from equations (5.21) and (5.32). Indeed, conservation of momentum dictates that (5.21) and (5.32) are valid both at the cell centers and interfaces. For the sake of brevity, the consequences of this fact are listed below for an interface normal to the $(x_1, x_2)$ plane. At such interface, equations (5.21) and (5.32) assume the following form,

$$\begin{aligned}
\phi_s^n(i,j,k\pm\tfrac{1}{2})u_{s_3}^n(i,j,k\pm\tfrac{1}{2}) &= \phi_s^n(i,j,k\pm\tfrac{1}{2})\tilde{u}_{s_3}^n(i,j,k\pm\tfrac{1}{2}) \\
&\quad - \frac{\Delta t}{\rho_s}\frac{\partial q_d^n}{\partial x_3}(i,j,k\pm\tfrac{1}{2}) \\
&\quad + \Delta t\frac{\rho_s-\rho_f}{\rho_s}\phi_s^n(i,j,k\pm\tfrac{1}{2})\mathbf{e}_3\cdot\mathbf{g}\,, \qquad (5.60) \\
\phi_f^n(i,j,k\pm\tfrac{1}{2})u_{f_3}^n(i,j,k\pm\tfrac{1}{2}) &= \phi_f^n(i,j,k\pm\tfrac{1}{2})\tilde{u}_{f_3}^n(i,j,k\pm\tfrac{1}{2}) \\
&\quad - \frac{\Delta t}{\rho_f}\phi_f^n(i,j,k\pm\tfrac{1}{2})\frac{\partial q_f'^n}{\partial x_3}(i,j,k\pm\tfrac{1}{2})\,. \qquad (5.61)
\end{aligned}$$

in these equations and in what follows, all instances of the $\pm$ symbol in each equation specify the same sign (either all positive or all negative). The quantities on the right-hand side of the above equations can be approximated as follows,

$$\phi_s^n(i,j,k\pm\tfrac{1}{2})\tilde{u}_{s_3}^n(i,j,k\pm\tfrac{1}{2}) \approx \overline{\phi_s^n(i,j,k\pm\tfrac{1}{2})\,\tilde{u}_{s_3}^n(i,j,k\pm\tfrac{1}{2})}^{1x_3}\,, \qquad (5.62)$$

$$\phi_f^n(i,j,k\pm\tfrac{1}{2})\tilde{u}_{f_3}^n(i,j,k\pm\tfrac{1}{2}) \approx \overline{\phi_f^n(i,j,k\pm\tfrac{1}{2})\,\tilde{u}_{f_3}^n(i,j,k\pm\tfrac{1}{2})}^{1x_3}\,, \qquad (5.63)$$

$$\frac{\partial q_d^n}{\partial x_3}(i,j,k\pm\tfrac{1}{2}) \approx \frac{\delta^1 q_d^n(i,j,k\pm\tfrac{1}{2})}{\delta x_3}\,, \qquad (5.64)$$

$$\phi_f^n(i,j,k\pm\tfrac{1}{2})\frac{\partial q_f'^n}{\partial x_3}(i,j,k\pm\tfrac{1}{2}) \approx \overline{\phi_f^n(i,j,k\pm\tfrac{1}{2})}^{1x_3}\,\frac{\delta^1 q_f'^n(i,j,\pm\tfrac{1}{2})}{\delta x_3}\,, \qquad (5.65)$$

$$\phi_s^n(i,j,k\pm\tfrac{1}{2})\mathbf{e}_3\cdot\mathbf{g} \approx \overline{\phi_s^n(i,j,k\pm\tfrac{1}{2})}^{1x_3}\mathbf{e}_3\cdot\mathbf{g}\,. \qquad (5.66)$$

Next, the following short-hand notation is introduced,

$$\begin{aligned} M_s^3(i,j,k\pm\tfrac{1}{2}) &= \overline{\phi_s^n(i,j,k\pm\tfrac{1}{2})\,\tilde{u}_{s_3}^n(i,j,k\pm\tfrac{1}{2})}^{1x_3} - \frac{\Delta t}{\rho_s}\frac{\delta^1 q_d^n(i,j,k\pm\frac{1}{2})}{\delta x_3} \\ &+ \Delta t\frac{\rho_s-\rho_f}{\rho_s}\overline{\phi_s^n(i,j,\pm\tfrac{1}{2})}^{1x_3}\mathbf{e}_3\cdot\mathbf{g}\,, \end{aligned} \tag{5.67}$$

$$\begin{aligned} M_f^3(i,j,k\pm\tfrac{1}{2}) &= \overline{\phi_f^n(i,j,k\pm\tfrac{1}{2})\,\tilde{u}_{f_3}^n(i,j,k\pm\tfrac{1}{2})}^{1x_3} \\ &- \frac{\Delta t}{\rho_f}\overline{\phi_f^n(i,j,k\pm\tfrac{1}{2})}^{1x_3}\,\frac{\delta^1 q_f'^n(i,j,\pm\frac{1}{2})}{\delta x_3}\,. \end{aligned} \tag{5.68}$$

Then, by combining (5.60), (5.61) with (5.67) and (5.68), one readily obtains the following interpolation for $\phi_a\mathbf{u}_a$,

$$\phi_s(i,j,k\pm\tfrac{1}{2})u_{s_3}(i,j,k\pm\tfrac{1}{2}) \approx M_s^3(i,j,k\pm\tfrac{1}{2})\,, \tag{5.69}$$

$$\phi_f(i,j,k\pm\tfrac{1}{2})u_{f_3}(i,j,k\pm\tfrac{1}{2}) \approx M_f^3(i,j,k\pm\tfrac{1}{2})\,. \tag{5.70}$$

The quantities $M_\alpha^1(i,j,k\pm\frac{1}{2})$ and $M_\alpha^2(i,j,k\pm\frac{1}{2})$ can be defined by direct analogy. Then, the final expressions for cell interfaces normal to the other planes assume the following form,

$$\phi_\alpha(i\pm\tfrac{1}{2},j,k)u_{\alpha_3}(i\pm\tfrac{1}{2},j,k) \approx M_\alpha^1(i\pm\tfrac{1}{2},j,k)\,, \tag{5.71}$$

$$\phi_\alpha(i,j\pm\tfrac{1}{2},k)u_{\alpha_3}(i,j\pm\tfrac{1}{2},k) \approx M_\alpha^2(i,j\pm\tfrac{1}{2},k)\,,\quad \alpha=s,f\,. \tag{5.72}$$

The interpolation scheme provided by equations (5.69)–(5.72) introduces a coupling between the phasial velocities and pressures that is sufficient to remedy the odd-even decoupling problem. In particular, the divergence theorem yields, for an arbitrary cell $K_{ijk}$,

$$\int_{K_{i,j,k}}\nabla\cdot(\phi_\alpha\mathbf{u}_\alpha\otimes\mathbf{u}_\alpha)\mathrm{d}\mathbf{x} = \int_{\partial K_{i,j,k}}\phi_\alpha\mathbf{u}_\alpha\otimes\mathbf{u}_\alpha\cdot\,\mathrm{d}\mathbf{S}\,,\quad \alpha=s,f\,. \tag{5.73}$$

Then, by combining (5.69)–(5.72) with the right-hand side of (5.73), the following discretization scheme for the convective fluxes is obtained,

$$\begin{aligned} \int_{\partial K_{i,j,k}}\phi_\alpha\mathbf{u}_\alpha\otimes\mathbf{u}_\alpha\cdot\mathrm{d}\mathbf{S} \approx\; & \frac{M_\alpha^1(i+\frac{1}{2},j,k)\overline{\mathbf{u}}_\alpha^{1x_1}(i+\frac{1}{2},j,k)-M_\alpha^1(i-\frac{1}{2},j,k)\overline{\mathbf{u}}_\alpha^{1x_1}(i-\frac{1}{2},j,k)}{\Delta x_1}+ \\ & \frac{M_\alpha^2(i,j+\frac{1}{2},k)\overline{\mathbf{u}}_\alpha^{1x_2}(i,j+\frac{1}{2},k)-M_\alpha^2(i,j-\frac{1}{2},k)\overline{\mathbf{u}}_\alpha^{1x_2}(i,j-\frac{1}{2},k)}{\Delta x_2}+ \\ & \frac{M_\alpha^3(i,j,k+\frac{1}{2})\overline{\mathbf{u}}_\alpha^{1x_3}(i,j,k+\frac{1}{2})-M_\alpha^3(i,j,k-\frac{1}{2})\overline{\mathbf{u}}_\alpha^{1x_3}(i,j,k-\frac{1}{2})}{\Delta x_3}\,. \end{aligned} \tag{5.74}$$

#### Diffusive fluxes

For the discretization of the second-order linear operators, conservative second-order centered finite differences are employed; this is the typical choice in the literature of projection methods. More specifically, this is done for the operators $\mathbf{V}_\alpha^d$, $\nabla\cdot\mathbf{u}_\alpha$ and $\nabla\cdot(\gamma_s\nabla\phi_s)$ appearing in equations (5.4), (5.6) and (5.7).

The partial viscosities $\mu_f\phi_f$, $\zeta_f\phi_f$, $\mu_{s1}\phi_s$ and $\zeta_{s1}\phi_s$, and the coefficient $\gamma_s$ have to be computed at the cell interfaces; this matter is not trivial, since these expressions are nonlinear functions of the volume fraction $\phi_s$ which can exhibit large variations near the jamming limit. For the flows considered in this thesis, preliminary computations were performed in order to compare linear and harmonic interpolation, showing only minor differences. As a result, herein linear interpolation is chosen.

#### Nonlinear viscous stresses

The present model predicts that the granular phase exhibits non-Newtonian viscous stresses; more precisely, the following term is part of the viscous stress $\mathbf{T}_s$ on the right-hand side of equation (5.6),

$$\frac{1}{\rho_s\mathrm{Re}}\nabla\cdot\big((\zeta_{s2}\nabla\cdot\mathbf{u}_s+\chi_a)\phi_s\mathbf{I}+2\mu_{s2}\phi_s\mathbf{V}_s^d+\chi_b\phi_s\mathbf{V}_s\cdot\mathbf{V}_s\big)\,, \tag{5.75}$$

and enters the expression for the residual $\mathbf{Res}_s$ in equation (5.16). The following shorthand notation is introduced,

$$tr\mathbf{V}_s=a_1,\quad \mathbf{V}_s:\mathbf{V}_s=a_2,\quad \det\mathbf{V}_s=a_3. \tag{5.76}$$

Then, the term in (5.75) can be written as

$$\frac{1}{\rho_s\mathrm{Re}}\nabla\cdot(\mu_n\phi_s\mathbf{N}) \tag{5.77}$$

where $\mathbf{N}$ denotes the following quantity,

$$\mathbf{N}=\left(\frac{\sqrt{2}}{3}\frac{a_3}{a_2^{3/2}}\nabla\cdot\mathbf{u}_s+\frac{3a_2-a_1^2}{\sqrt{2a_2}}-2\sqrt{2}\sqrt{a_2-\frac{a_1^2}{3}}\right)\mathbf{I}+\sqrt{2}\frac{a_3}{a_2^{3/2}}\mathbf{V}_s^d-\sqrt{\frac{2}{a_2}}\mathbf{V}_s\cdot\mathbf{V}_s. \tag{5.78}$$

In order to compute this expression, the derivatives of the velocity field $\mathbf{u}_s$ have to be obtained at the cell faces. Linear interpolation is employed, together with conservative second-order centered finite differences, analogously to the scheme used for the computation of the diffusive fluxes.

An important consideration regards the stability of the expression (5.78) in the limit $a_2\to 0$, as this quantity appears in the denominators of this expression. From a mathematical standpoint there is no singularity in this limit, as explained in Subsection 3.3.1. However, the numerical behaviour of the discretized expression is not as clear-cut due to truncation errors relative to the specific implementation. For this reason expression (5.78) is regularized with the introduction of a treshold $\tau$ for $a_2$. More precisely, in pseudo-code notation, $a_2 = max(a_2, \tau)$. This treshold can typically be set as a very small number; as an example, the computation of Chapter 6 have been obtained with $\tau = 10^{-10}$.

Finally, it is remarked that the viscosity coefficients of suspensions close to maximum packing can assume extremely high values, cf. for instance the expression (4.12) for $\mu_n$. This implies the necessity of considering the following parabolic-type constraint,

$$\Delta t \lesssim \frac{\mathrm{Re} \min \Delta x_j{}^2}{\mu_n}, \qquad j = 1, ..., 3, \tag{5.79}$$

which can become quite stringent in the case of dense small-scale flows. It is often the case in applications that flow is limited to regions where the volume fraction is far from maximum packing, and that the region which is densely packed can be considered immobile relatively to the time scale of the primary flow. In this case, an artificial treshold for the coefficient $\mu_n$ can be introduced close to maximum packing in order to mitigate the issue. For example, in pseudo-code notation, the treshold $\mu_n = min(\mu_n, \mu_n|_{\phi_s=0.59})$ has been used for the computations discussed in Section 6.4.

### Configuration stress tensor

The divergence of the configuration stress tensor $\nabla \cdot (\gamma_s \nabla \phi_s \otimes \nabla \phi_s)$ is a highly nonlinear differential operator and, as such, its discretization requires particular attention. Herein the following identity is employed,

$$\nabla \cdot (\gamma_s \nabla \phi_s \otimes \nabla \phi_s) = (\nabla \cdot (\gamma_s \nabla \phi_s)\mathbf{I} + \gamma_s \mathbf{H}(\phi_s)) \nabla \phi_s, \tag{5.80}$$

where $\mathbf{H}(\phi_s)$ is the Hessian of $\phi_s$; the discretization is then performed as follows. The diagonal tensor $\nabla \cdot (\gamma_s \nabla \phi_s)\mathbf{I}$ is approximated via the divergence theorem,

$$\begin{aligned}
&\nabla \cdot (\gamma_s(i,j,k) \nabla \phi_s(i,j,k))\mathbf{I} \simeq \\
&\left( \frac{\overline{\gamma}^{1x_1}(i+\frac{1}{2},j,k)\frac{\delta^1 \phi_s(i+\frac{1}{2},j,k)}{\delta x_1} - \overline{\gamma_s}^{1x_1}(i-\frac{1}{2},j,k)\frac{\delta^1 \phi_s(i-\frac{1}{2},j,k)}{\delta x_1}}{\Delta x_1} \right. \\
&+ \frac{\overline{\gamma_s}^{1x_2}(i,j+\frac{1}{2},k)\frac{\delta^1 \phi_s(i,j+\frac{1}{2},k)}{\delta x_2} - \overline{\gamma_s}^{1x_2}(i,j-\frac{1}{2},k)\frac{\delta^1 \phi_s(i,j-\frac{1}{2},k)}{\delta x_2}}{\Delta x_2} \\
&\left. + \frac{\overline{\gamma_s}^{1x_3}(i,j,k+\frac{1}{2})\frac{\delta^1 \phi_s(i,j,k+\frac{1}{2})}{\delta x_3} - \overline{\gamma_s}^{1x_3}(i,j,k-\frac{1}{2})\frac{\delta^1 \phi_s(i,j,k-\frac{1}{2})}{\delta x_3}}{\Delta x_3} \right) \mathbf{I}.
\end{aligned} \tag{5.81}$$

Both the diagonal and the off-diagonal components of the Hessian operator $\mathbf{H}(\phi_s)$ are approximated via cell centered, second-order finite differences. Finally, the multiplier $\nabla\phi_s$ is also approximated via the divergence theorem as follows,

$$\begin{pmatrix} \frac{\partial\phi_s(i,j,k)}{\partial x_1} \\ \frac{\partial\phi_s(i,j,k)}{\partial x_2} \\ \frac{\partial\phi_s(i,j,k)}{\partial x_3} \end{pmatrix} \approx \begin{pmatrix} \frac{1}{2}\left(\frac{\delta^1\phi_s(i+\frac{1}{2},j,k)}{\delta x_1} + \frac{\delta^1\phi_s(i-\frac{1}{2},j,k)}{\delta x_1}\right) \\ \frac{1}{2}\left(\frac{\delta^1\phi_s(i,j+\frac{1}{2},k)}{\delta x_2} + \frac{\delta^1\phi_s(i,j-\frac{1}{2},k)}{\delta x_2}\right) \\ \frac{1}{2}\left(\frac{\delta^1\phi_s(i,j,k+\frac{1}{2})}{\delta x_3} + \frac{\delta^1\phi_s(i,j,k-\frac{1}{2})}{\delta x_3}\right) \end{pmatrix} \tag{5.82}$$

## 5.3 Coupling between compaction and projection

As previously mentioned in Subsection 5.2.2, the specific time discretization of equation (5.24) has a profound impact on the performance of the numerical algorithm. In fact, the application of a projection method to the system of equations (5.3)–(5.8) entails a peculiar structure which is, to the best of the author's knowledge, new to the literature. More precisely, the compaction equation (5.7) explicitly contains the phasial pressures, which results in a strong coupling with the projection equation (5.24). In this Section the interaction of equations (5.7) and (5.24) is investigated, in order to gain insight into its implications from the numerical standpoint. Identifying $p_d$ and $q_d$ in equation (5.22), the compaction equation (5.7) can be written as

$$\frac{\partial\phi_s}{\partial t} = -\mathbf{u}_s\cdot\nabla\phi_s + \mathrm{Re_c}\,\phi_s\phi_f\left(\frac{q_d}{\phi_s} - \beta_s + \nabla\cdot(\gamma_s\nabla\phi_s)\right). \tag{5.83}$$

Further, combining the projection equation (5.21) with mass conservation for the granular phase, (2.8), the elliptic problem for $q_d$ can be written as

$$\nabla^2 q_d^{n+1} = \frac{\rho_s}{\Delta t}\left[\nabla(\phi_s^{n+1}\tilde{\mathbf{u}}_s) + \frac{\partial\phi_s}{\partial t}\right] + (\rho_s - \rho_f)\phi_s\mathbf{g}. \tag{5.84}$$

The right-hand side of equation (5.83) explicitly contains the auxiliary granular pressure $q_d$ and, in turn, the left-hand side of this equation is a source term in the elliptic equation (5.84) for $q_d$. This direct coupling constitutes a fundamental difference with respect to existing algorithms for solenoidal flows such as the one employed in Chapter 2 and described in Appendix A; it turns out that it can originate a strong numerical instability, and that a specific treatment is required. In particular, the presence of the time derivative of the volume fraction $\frac{\partial\phi_s}{\partial t}$ inside equation (5.84) can not be avoided, whereas in the case of solenoidal flow it is possible to obtain a Poisson equation for $q_d$ by dividing the projection equation by $\phi_s$ and exploiting the constraint $\nabla\cdot\mathbf{u}_s = 0$, cf. also the corresponding equation (A.14).

### Time-integration properties

In order to contextualize the numerical treatment implemented in Subsection 5.2.2, a linear stability analysis is performed. In principle, one should evaluate the entire system (3.88)–(3.92), as all the equations in that system are coupled; this is a long and tedious task due to the complexity of the system, especially if the semi-implicit time-integration scheme of 5.2.2 is maintained. Nevertheless, on the basis on numerical experiments, it is possible to identify the terms whose integration is problematic; in turn, this allows to analyze explicitly a simplified system which maintains only the important terms.

In the present case, the challenge stems from the coupling of equations (5.83) and (5.84), and the important terms appear in the following reduced versions of equations (5.83) and (5.84),

$$\frac{\partial \phi_s}{\partial t} = \mathrm{Re_c}\,\phi_s\phi_f\left(\frac{q_d}{\phi_s} - \beta_s + \nabla\cdot(\gamma_s\nabla\phi_s)\right), \tag{5.85}$$

$$\nabla^2 q_d = \frac{\rho_s}{\Delta t}\frac{\partial \phi_s}{\partial t}. \tag{5.86}$$

In these equations, the terms involving velocities and body force have been dropped. The rationale behind this choice is that, according to numerical experiments, the time integration of equations (5.83) and (5.84) is problematic due to a strong instability that is present irrespectively of these terms. This reduced system is sufficiently tractable that it can be analyzed explicitly, yet it maintains the terms of the original system that are challenging to integrate.

The behaviour of the system (5.85)–(5.86) is examined for a perturbation around equilibrium at uniform volume fraction $\phi_s$,

$$\frac{q_d}{\phi_s} = \beta_s, \quad \phi_s = \phi_0, \quad q_d = q_0. \tag{5.87}$$

This simple state is a solution of both equations (5.85)–(5.86) and of the original system (3.88)–(3.92), and corresponds to a suspension at rest with uniform concentration. A small perturbation in $\phi_s$ and $q_d$ is considered,

$$\phi_s = \phi_0 + \epsilon_\phi(\mathbf{x},t), \quad q_d = q_0 + \epsilon_q(\mathbf{x},t). \tag{5.88}$$

After linearization around the equilibrium state, replacing the time derivative in equation (5.86) through equation (5.85), one obtains

$$\frac{\partial \epsilon_\phi}{\partial t} = \mathrm{Re_c}\,\phi_0(1-\phi_0)\left(\frac{\epsilon_q}{\phi_0} - \epsilon_\phi\frac{\partial\beta_s}{\partial\phi_s} + \gamma_s\nabla^2\epsilon_\phi\right), \tag{5.89}$$

$$\nabla^2\epsilon_q = \frac{\mathrm{Re_c}\,\phi_0(1-\phi_0)\rho_s}{\Delta t}\left(\frac{\epsilon_q}{\phi_0} - \epsilon_\phi\frac{\partial\beta_s}{\partial\phi_s} + \gamma_s\nabla^2\epsilon_\phi\right). \tag{5.90}$$

It is now possible to compare different time-integration schemes. The above system is linear in $\epsilon_\phi$ and $\epsilon_q$; a perturbation mode of wavenumber $\lambda$ in direction $x$ is considered, so that

$$\epsilon_\phi \;=\; c_\phi(\lambda,t)e^{i\lambda x}, \quad \epsilon_q \;=\; c_q(\lambda,t)e^{i\lambda x}. \tag{5.91}$$

To begin with, an explicit time-integration scheme is examined,

$$\epsilon_\phi^{n+1} \;=\; \epsilon_\phi^n + \Delta t \mathrm{Re_c}\, \phi_0(1-\phi_0)\left(\frac{\epsilon_q^n}{\phi_0} - \epsilon_\phi^n \left.\frac{\partial\beta_s}{\partial\phi_s}\right|_{\phi_0} + \gamma_s|_{\phi_0}\nabla^2\epsilon_\phi\right), \tag{5.92}$$

$$\nabla^2\epsilon_q^{n+1} \;=\; \frac{\mathrm{Re_c}\,\phi_0(1-\phi_0)\rho_s}{\Delta t}\left(\frac{\epsilon_q^n}{\phi_0} - \epsilon_\phi^n \left.\frac{\partial\beta_s}{\partial\phi_s}\right|_{\phi_0} + \gamma_s|_{\phi_0}\nabla^2\epsilon_\phi\right). \tag{5.93}$$

This scheme constitutes the natural generalization of a fractional-step projection algorithm for solenoidal flows such as the one described in Appendix A. Introducing the perturbation mode (5.91), and employing centered second-order differences with uniform spacing $\Delta x$ for the space discretization of the Laplacian operator, the following linear system is obtained for the modal coefficients $c_\phi$ and $c_q$,

$$\begin{pmatrix} c_\phi^{n+1} \\ c_q^{n+1} \end{pmatrix} \;=\; M_1 \begin{pmatrix} c_\phi^{n} \\ c_q^{n} \end{pmatrix}, \tag{5.94}$$

where the matrix $M_1$ is given by

$$M_1 = \begin{pmatrix} 1+\Delta t \mathrm{Re_c}\phi_0(1-\phi_0)\left(-\left.\frac{\partial\beta_s}{\partial\phi_s}\right|_{\phi_0} + \frac{2\gamma_s|_{\phi_0}(\cos(\lambda x)-1)}{\Delta x^2}\right) & \Delta t\mathrm{Re_c}(1-\phi_0) \\ -\frac{\mathrm{Re_c}\,\phi_0(1-\phi_0)\rho_s}{\Delta t}\frac{\Delta x^2}{2(\cos(\lambda x)-1)}\left.\frac{\partial\beta_s}{\partial\phi_s}\right|_{\phi_0} + \frac{\mathrm{Re_c}\,\phi_0(1-\phi_0)\rho_s\,\gamma_s|_{\phi_0}}{\Delta t} & \frac{\mathrm{Re_c}(1-\phi_0)\rho_s}{\Delta t}\frac{\Delta x^2}{2(\cos(\lambda x)-1)} \end{pmatrix}. \tag{5.95}$$

A necessary requirement for stability is that the modulus of the eigenvalues of $M_1$ can not exceed one. However, this can not be guaranteed for small wavenumber $\lambda$: the expression $\cos(\lambda x)-1$ is present in the denominators of the entries of the row relative to $c_q$. In particular, the zero-th order mode corresponding to $\lambda = 0$ is singular.

An alternative approach to the integration of the system (5.85)–(5.86) is to exploit its linearity and solve the second equation implicitly with respect to $q^{n+1}$, so that

$$\epsilon_\phi^{n+1} = \epsilon_\phi^n + \Delta t\mathrm{Re_c}\,\phi_0(1-\phi_0)\left(\frac{\epsilon_q^n}{\phi_0} - \epsilon_\phi^n\left.\frac{\partial\beta_s}{\partial\phi_s}\right|_{\phi_0} + \gamma_s|_{\phi_0}\nabla^2\epsilon_\phi\right), \tag{5.96}$$

$$\nabla^2\epsilon_q^{n+1} - \frac{\mathrm{Re_c}(1-\phi_0)\rho_s}{\Delta t}\epsilon_q^{n+1} = -\frac{\mathrm{Re_c}\phi_0(1-\phi_0)\rho_s}{\Delta t}\left(\epsilon_\phi^n\left.\frac{\partial\beta_s}{\partial\phi_s}\right|_{\phi_0} + \gamma_s|_{\phi_0}\nabla^2\epsilon_\phi^n\right). \tag{5.97}$$

This approach is the basis for the time-integration algorithm that was previously proposed in 5.2.2. One obtains the following matrix $M_2$ for the system relative to the mode of wavenumber $\lambda$,

$$M_2 = \begin{pmatrix} 1+\Delta t \mathrm{Re}_\mathrm{c}\phi_0(1-\phi_0)\left(-\left.\frac{\partial\beta_s}{\partial\phi_s}\right|_{\phi_0} + \frac{2\,\gamma_s|_{\phi_0}(\cos(\lambda x)-1)}{\Delta x^2}\right) & \Delta t \mathrm{Re}_\mathrm{c}(1-\phi_0) \\ \frac{\mathrm{Re}_\mathrm{c}\,\phi_0(1-\phi_0)\rho_s\Delta x^2}{2\Delta t\left(\cos(\lambda x)-1-\frac{\mathrm{Re}_\mathrm{c}(1-\phi_0)\rho_s\Delta x^2}{2\Delta t}\right)}\left(-\left.\frac{\partial\beta_s}{\partial\phi_s}\right|_{\phi_0} + \frac{2\,\gamma_s|_{\phi_0}(\cos(\lambda x)-1)}{\Delta x^2}\right) & 0 \end{pmatrix}. \tag{5.98}$$

In this case, the denominator of the term on the $c_q$ line now contains the factor $\cos(\lambda x) - 1 - \frac{\mathrm{Re}_\mathrm{c}(1-\phi_0)\rho_s\Delta x^2}{2\Delta t}$, which is never singular. In the limit of $\Delta t \to 0$, the matrix $M_2$ converges to the following matrix,

$$M_2' = \begin{pmatrix} 1-\Delta t \mathrm{Re}_\mathrm{c}\phi_0(1-\phi_0)\left.\frac{\partial\beta_s}{\partial\phi_s}\right|_{\phi_0} & \Delta t \mathrm{Re}_\mathrm{c}(1-\phi_0) \\ \phi_0\left(\left.\frac{\partial\beta_s}{\partial\phi_s}\right|_{\phi_0} - \frac{2\,\gamma_s|_{\phi_0}(\cos(\lambda x)-1)}{\Delta x^2}\right) & 0 \end{pmatrix}. \tag{5.99}$$

One of the eigenvalues of $M_2'$ tends to one, while the other one is proportional to $\Delta t$, so that the solution scheme is conditionally stable in the $\Delta t \to 0$ limit. In fact, with the additional assumption that the coefficient $\gamma_s$ is negligible (which is often the case in applications, as $\gamma_s$ is inversely proportional to the squares of the reference length and velocity), the eigenvalues can be computed explicitly. More precisely, the matrix $M_2'$ then reduces to the following matrix,

$$M_2'' = \begin{pmatrix} 1-\Delta t \mathrm{Re}_\mathrm{c}\phi_0(1-\phi_0)\left.\frac{\partial\beta_s}{\partial\phi_s}\right|_{\phi_0} & \Delta t \mathrm{Re}_\mathrm{c}(1-\phi_0) \\ \phi_0\left.\frac{\partial\beta_s}{\partial\phi_s}\right|_{\phi_0} & 0 \end{pmatrix}, \tag{5.100}$$

which presents the two eigenvalues 1 and $\phi_0(\phi_0-1)\mathrm{Re}_\mathrm{c}\Delta t$, respectively.

Although it would be desirable to devise a scheme where both eigenvalues vanish for $\Delta t \to 0$, the discretization expressed by equations (5.96) and (5.97) turns out to be sufficiently stable to handle several flows of practical interest, due to stabilization by numerical viscosity. In any case, given the approximate nature of the above considerations and the complexity of the complete system of equations (5.3)–(5.8), the applicability of the above integration scheme has to be verified for the cases of interest. In particular, herein this algorithm is employed with success in the computations of Chapter 6.

# Chapter 6

# Numerical results for sedimentation flows

In Chapter 4 of this thesis, a numerical study was presented for pressure-driven channel flow where the width of the channel was only two orders of magnitude greater than the grain diameter; as a result, this was effectively a neutrally-buoyant flow. However, the relevant length scales in geophysical phenomena and in many practical applications are much larger than the grain diameter, so that buoyancy effects can not usually be neglected. In fact, when the granular phase undergoes sedimentation, the resulting hydrostatic pressure promotes compaction and one observes stratification, with a high particle concentration at the bottom of the flow domain and a low concentration at the top. For instance, one can observe this behaviour at lake- or sea beds, where stratification is so strong that the granular bed is compacted almost to maximum packing, and the interface between the highly-compacted bed and the clear water above it is as thin as few grain diameters.

In the present Chapter, the projection algorithm of Chapter 5 is applied to example problems concerning compacted granular beds, with two main objectives. On one hand, the analysis constitutes an important test for the proposed algorithm, in conditions that are closer to practical applications concerning sediment transport. In particular, modelling can be challenging due to the presence of sharp interfaces where the volume fraction (and the material coefficients that depend on it) changes abruptly. Furthermore, several material coefficients depend nonlinearly on the volume fraction and can vary by orders of magnitude between the high-concentration and dilute regions of the flow, requiring specific numerical treatment.

On the other hand, the governing equations for constant-density flow (5.3)–(5.8) allow to describe granular compaction with a higher level of detail than generally available to earlier models, such as the one of [26] which was used in the computations of Chapter 2. More specifically, the results of this Chapter show that the proposed model can capture the relaxation mechanism associated with the settling of a dense granular layer into a compacted bed. This relaxation can have an important effect on the rheological properties of dense suspensions, [80], due to the stiff dependence of the viscosity coefficients on the volume fraction close to maximum packing [58, 59, 108].

The structure of this Chapter is as follows. Section 6.1 provides a brief description of an implementation of the algorithm of Chapter 5, which is used for the following computations. Section 6.2 contains a numerical study of the settling of a dense submerged granular bed, and further a discussion of the convergence properties of the integration algorithm. Section 6.3 is concerned with the analysis of the sedimentation of an initially uniform suspension into a dense granular bed. In addition, in this flow a sharp volume-fraction interface is formed at the top of the dense bed; for this reason it is also used as a test in order to evaluate the impact of the interface-regularization method. Finally, Section 6.4 presents computations relative to the collapse of a granular column submerged under water. This test showcases the capabilities of the proposed flow model with respect to unsteady stratified flows, in a geometry that is a benchmark for applications involving gravity-induced granular transport.

## 6.1 Towards an efficient algorithm implementation

The solution algorithm described in Chapter 5 is fairly demanding from a computational perspective. To begin with, at each time iteration five linear systems have to be solved (which correspond to second-order elliptic problems): one system for each of the semi-implicit computations of $\phi_s$, $\tilde{\mathbf{u}}_s$ and $\tilde{\mathbf{u}}_f$ expressed by equations (5.14), (5.16) and (5.27), plus two systems for the elliptic equations (5.25) and (5.34) for the auxiliary pressures $q_d$ and $q_f'$. In addition, the explicit computation of the residuals $\mathrm{Res}_\phi$, $\mathbf{Res}_s$ and $\mathbf{Res}_f$, which appear in equations (5.14), (5.16) and (5.27), requires a considerable number of operations, and the arrays that store the matrices for all the linear systems have to be updated at each iteration.

In order to achieve reasonable performance under such circumstances, it is currently necessary to combine a fast linear solver with a parallelization technique. The performance of the linear solver is especially critical, since it turns out that the linear systems associated with the elliptic problems for the velocities and pressures are the bottleneck of the algorithm. Furthermore, due to the fact that the matrices of the linear systems need to be updated at every iteration, the usage of direct solvers is impractical and an iterative procedure is preferable. The well-known PETSc toolkit, [175–177], contains a wide selection of iterative Krylov solvers in a convenient MPI implementation designed for computing purposes. In addition, it provides a practical way of indexing the arrays corresponding to the matrices of the linear systems, a task which can otherwise be challenging since the algorithm of Chapter 5 requires to populate a great number of entries (it uses a box stencil). For this reasons PETSc is choosen as the basis for the development of a solver program specifically tailored to equations (5.3)–(5.8).

The solver has been developed as part of this thesis at Université Catholique de Louvain and at the University of Patras under a secondment for SEDITRANS, an ITN project of the Marie Curie Actions of the 7th Framework Programme. It is written in C/C++ and inherits the MPI capabilities of the underlying PETSc environment. For the computations of this

Chapter, it employs a Biconjugate-Gradient-Stabilized method with Jacobi preconditioning in order to solve the linear systems appearing in the integration algorithm.

### 6.1.1 Physical parameters

In order to be solved numerically, the system of governing equations for constant-density flow, (5.3)–(5.8) requires to be supplemented with experimental correlations for the material and transport coefficients. The relations employed in the computations of this Chapter are listed here as reference; the hat symbol ˆ is used to denote dimensional quantities.

#### Densities, granulometry and drag

A monodispersed granular suspension of sand in water is considered, with a grain diameter $\hat{d}_p = 3.5 \times 10^{-4}\,\mathrm{m}$ and maximum packing at $\phi_m = 0.6$. The mass density of the fluid phase is $\hat{\rho}_f = 10^3\,\mathrm{kg/m^3}$, while the density of the granular phase is $\hat{\rho}_s = 2.5 \times 10^3\,\mathrm{kg/m^3}$. The gravity acceleration is $\hat{g} = |\hat{\mathbf{g}}| = 9.81\,\mathrm{m/s^2}$. For the interphasial drag coefficient $\hat{\delta}$, the same formulation is used as in the computations of Chapter 4. In particular, the Hill-Koch-Ladd correlation proposed in [150] is used for $\hat{\delta}$, cf. (4.10). The functional form of this correlation is quite cumbersome, and the reader is referred directly to [150] for a code-friendly representation. Nevertheless, it is interesting to notice that, for sufficiently small particle Reynolds number $\mathrm{Re}_p$, the drag coefficient $\hat{\delta}$ depends quadratically on the particle diameter $\hat{d}_p$.

#### Microstructural parameters

For the parameters $\hat{\beta}_s$ and $\hat{\gamma}_s$ which measure the intergranular stress and the nonlocal stresses, the same approach used in Subsection 4.2.1 is followed, with expressions analogous to (4.13) and (4.14). However, some additional considerations are needed here in order to account for the fact that the suspension considered here has a larger grain diameter $\hat{d}_p$ than the suspension considered in Chapter 4, and further to comment on the modelling of the intergranular stress close to the maximum packing.

Following the scaling considerations of Subsection 4.2.1, it is assumed that $\hat{\beta}_s$ does not depend on $\hat{d}_p$, whereas $\hat{\gamma}_s$ depends quadratically on it; this follows from the hypothesis that the grain diameter is the only characteristic length for the microstructure. Then, the following expressions are derived from (4.13) and (4.14),

$$\hat{\beta}_s \;=\; -\,\hat{\beta}_0 \log\left(\frac{\phi_m - \phi_s}{\phi_m}\right), \quad \hat{\beta}_0 \;=\; 1.0 \times 10^{-1}\,\mathrm{Pa}\,, \tag{6.1}$$

$$\hat{\gamma}_s \;=\; -\,\hat{\gamma}_0\,\phi_s^6, \quad \hat{\gamma}_0 \;=\; 1.2 \times 10^{-4}\,\mathrm{N}. \tag{6.2}$$

Expression (6.1) presents a stiff behaviour with respect to the volume fraction $\phi_s$, with a logarithmic asymptote at the maximum-packing treshold $\phi_m$. It is useful to comment further on this behaviour, as the intergranular stress $\hat{\beta}_s$ encodes an important part of the granular dynamics. In particular, in the case where the particles can be assumed rigid, $\hat{\beta}_s$ is expected to vanish for small values of $\phi_s$ and to present a singularity corresponding with the maximum-packing treshold $\phi_m$ [84, 121, 122]. The singularity at $\phi_m$ expresses the experimental observation that rigid grains can not be compacted over a certain volume-fraction (the actual value of $\phi_m$ is somewhat dependent on the randomness of the packing, for rigid spheres one can assume $0.55 < \phi_m < 0.65$).

Herein the assumption that the grains are rigid is encoded in (6.1), which also implies that grain deformation and fracturing are neglected. It is stressed that this assumption is additional to considering that the flow is incompressible, and has to be verified depending on the specific application. In particular it is known that, under strong compression, particles can actually deform or fracture [124, 125], so that a different constitutive law for $\hat{\beta}_s$ may be required in those circumstances.

The stiffness of the integranular stress close to maximum-packing can present a significant numerical challenge. In fact, at equilibrium, the compaction equation (5.7) predicts that the integranular stress is of the same order of magnitude as the phasial pressures; then, the constitutive law (6.1) for the intergranular stress implies that the difference $\phi_m - \phi_s$ is exponentially small with respect to this magnitude.

One possible way to tackle the numerical integration of (6.1) is to artificially reduce its stiffness close to jamming, with a milder divergence that is amenable to numerical treatment. A modified intergranular stress $\beta_s'$ is defined,

$$\hat{\beta}_s' = \begin{cases} \hat{\beta}_s & : \phi_m - \phi_s \geq \epsilon \\ \hat{\beta}_0 \left( 0.5 \frac{\epsilon^2}{(\phi_m - \phi_s)^2} - \log(\frac{\epsilon}{\phi_m}) - 0.5 \right) & : \phi_m - \phi_s < \epsilon \end{cases} , \tag{6.3}$$

where $\epsilon$ is a small parameter that controls the width of the modified region; herein the value $\epsilon = 10^{-2}$ is used, which corresponds to modifying the original expression (6.1) in the interval $0.59 < \phi_s < 0.6$. This expression essentially connects, at $\phi_s = 0.59$, the original expression for $\hat{\beta}_s$ with a second-order asymptote at $\phi_m$.

The above expression (6.3) replaces the logarithmic asymptote with a polynomial one which can be handled by the numerical method, and maintains a maximum-packing treshold. This is a computational compromise: resistance to compaction is artificially increased in the regularization interval $\phi_m - \epsilon < \phi_s < \phi_m$, which is controlled by the value of the regularization parameter $\epsilon$ in (6.3).

Another way of treating the stiff coefficient $\hat{\beta}_s$ is to introduce a cutoff for the volume fraction $\phi_s$, so as to remove the stiff parameter region; this approach is easy to implement and allows to employ the unmodified expression (6.1). Furthermore, it permits significantly faster numerical integration due to the possibility of a larger time step $\Delta t$. However, the cutoff effectively limits the intergranular stress and, due to the stiffness of (6.1), practical cutoff tresholds, e.g. $\phi_{max} = 0.599$, do not typically resolve hydrostatic equilibrium in large-scale applications. This drawback can be tolerated if compaction after the cutoff limit does not have to be resolved, however the choice depends on the specific application.

In the following sections, both treatments are tested; the modified expression (6.3) for $\hat{\beta}'_s$ is used in the next Section 6.2, where it is important to capture the transition to equilibrium conditions. In Sections 6.3 and 6.4 the faster cutoff method is employed, and the differences between the two treatments of the integranular stress are discussed.

**Viscosity coefficients**

The shear viscosity of the water phase is $\hat{\mu}_f = 8.9 \times 10^{-4}\,\mathrm{Pa}$, while its bulk viscosity is assumed three times greater at $\hat{\zeta}_f = 2.7 \times 10^{-3}\,\mathrm{Pa}$, [178]. The bulk viscosity has to be specified *a priori* since the fluid velocity is not solenoidal, so that the contribution of this parameter can potentially be significant (in contrast to flows of simple fluids, where a Stokes hypothesis is usually well justified).

For the viscosity coefficients of the granular phase the situation is more complex. In the flows considered in this Chapter, $\det \mathbf{V}_s \equiv 0$ and there is no ambiguity in the selection of an empirical law for the generalized Newtonian viscosities $\hat{\mu}_s = \hat{\mu}_{s1}$ and $\hat{\zeta}_s = \hat{\zeta}_{s1}$, cf. (5.12); in other words, the generalized Newtonian viscosities coincide with the Newtonian viscosities. However, a general expression for the bulk viscosity $\hat{\zeta}_s$ is not easily obtained since this quantity is difficult to measure. It is expected that $\hat{\zeta}_s$ depends on $\phi_s$ similarly to $\hat{\mu}_s$, cf. also the relevant discussion in [106]; herein we assume this two quantities to be proportional with the proportionality constant $k$, so that $\hat{\zeta}_s = k\hat{\mu}_s$.

Nonetheless, some information can be gathered from the model derivation of Chapter 3, as the value of $\hat{\zeta}_s$ is constrained on thermodynamic grounds by the last of relations (3.61). More precisely, when $\det \mathbf{V}_s = 0$, this constraint can be expressed as

$$\hat{\zeta}_s \geq \frac{\hat{\mu}_n^2}{\hat{\mu}_s}. \tag{6.4}$$

For $\hat{\mu}_s$ and $\hat{\mu}_n$ the relations (4.11) and (4.12) that were proposed in [108] are employed, so that the inequality (6.4) above becomes

$$\hat{\zeta}_s \geq \hat{\mu}_f \frac{9\,\phi_s^2}{40\,(\phi_m - \phi_s)^3 + 1.6\,\phi_s(\phi_m - \phi_s)^2}. \tag{6.5}$$

From equation (6.5), in the limit $\phi_s \to \phi_m$ one obtains the constraint $k \geq \frac{45}{8}$. Herein the more conservative value $k = \frac{45}{2}$ is chosen, which is four times the minimum limit for $\phi_s \to \phi_m$.

Finally, one must specify an expression for the compaction viscosity $\hat{\mu}_c$; this quantity enters the compaction Reynolds number $\mathrm{Re}_c$ appearing in the compaction equation (5.7).

This is a particularly challenging task, as information about this coefficient is scarce; in fact, the appearance of $\mathrm{Re}_c$ in equation (5.7) is a novel feature of the proposed flow model. The compaction viscosity controls the relaxation of the volume fraction due to phasial-pressure nonequilibrium, a complex phenomenon that depends, a priori, on the microstructural properties of the specific suspension. Nevertheless, a comparison with existing suspension models both of the diffusive-flux and of the suspension-balance type, [60, 97, 108], suggest that this quantity may be proportional to $\hat{\mu}_f$; for sufficiently low particle-Reynolds number $\mathrm{Re}_p$, this scaling is plausible due to the fact that particle interaction is then dominated by viscous effects. Herein, in absence of more precise information, the constant value $\hat{\mu}_c = \hat{\mu}_f$ is chosen. Actually, the above-mentioned comparison suggests the (untested) hypothesis of a proportionality constant scaling as $(\hat{d}_p)^{-2}$, cf. also Section 3.6. This can be contrasted with the behaviour of the shear, normal and bulk viscosity coefficients, which do not depend on the particle diameter $\hat{d}_p$ [58, 83, 106, 108].

## 6.2 Compaction of a dense bed

The first flow case involves the compaction of a flat granular bed; a submerged dense layer, initially at uniform volume fraction, is allowed to settle under gravity until equilibrium is reached. The accurate computation of the settling process is challenging, due to the stiffness of the material coefficients with respect to the volume fraction. In fact, at equilibrium the suspension is highly compacted due to gravity, so that the volume fraction is close to maximum packing. In these conditions, even small variations of the volume fraction are associated with significant changes in the pressure and velocity distributions, due to the nonlinearity of material coefficients measuring viscosity, drag and resistance to compaction. This test allows to explore the capabilities of the particle-migration model with respect to compacted suspensions, and to gain insight into the stratification dynamics of dense granular beds.

### Problem set-up

A flat granular bed with an initial height of $0.2\,\mathrm{m}$ fills the bottom half of the flow domain; over the bed a clear water region with the same height is present. Due to the stable stratification of this initial condition the flow can be assumed to be one-dimensional; in fact this was tested in preliminary computations. Hence, a one-dimensional domain in the wall-normal direction is considered, with a height of $0.4\,\mathrm{m}$.

In the granular bed, interphasial drag is quite strong, which results in slow relaxation. In order to reduce the settling time to an extent that is practically computable, a very dense initial condition is considered with $\phi_s = 0.5998$, which is close to the maximum-packing treshold $\phi_m = 0.6$. In order to resolve compaction at such high concentration, in this test the modified expression for the intergranular stress $\hat{\beta}_s'$ defined in (6.3) is employed. The clear water region above the bed consists of practically pure water, with a volume fraction $\phi_s = 10^{-5}$. The interface separating the bed from the fluid above is regularized in order to present a smooth transition region. The resulting initial condition for $\phi_s$ as a function of the (non-dimensional) vertical coordinate $z$ is shown in Figure 6.1 for t = 0.

Both phases are initially at rest; the reference velocity for this problem is the uniform-flow sedimentation velocity at $\phi_s = 10^{-5}$ which is determined by the drag law and, at this low concentration, is approximately the sedimentation velocity of a single particle. With the physical parameters of Subsection 6.1.1, this reference velocity is $\hat{u}_r = 2.62 \times 10^{-2}\,\mathrm{m/s}$.

The domain presents a wall boundary condition at the bottom and a zero-Neumann condition at the top for both phasial velocities $\mathbf{u}_s$ and $\mathbf{u}_f$. For the volume fraction $\phi_s$ and the auxiliary pressures $q_d$ and $q_f'$, zero-Neumann conditions are used. The domain is discretized on a uniform grid with 512 points.

**Discussion of the numerical results**

Figure 6.1 shows the initial volume fraction profile as a function of the non-dimensional vertical coordinate, together with its evolution after 5 non-dimensional times. The granular phase moves downwards and, conversely, the fluid flows upwards; however, motion is quite limited due to the fact that the dense bed is already very close to maximum packing. The most visible effect is the evolution of the transition region between the compacted bed and the fluid, which becomes a sharp interface as the granular phase settles at the bottom. In fact, from a numerical standpoint, at t = 5 the interface is so sharp that the regularization treatment (which limits the maximum variation $\Delta\phi_s$ between successive nodes) impedes further evolution.

In order to observe the small variation of the volume fraction $\phi_s$ throughout the granular bed, Figure 6.1b provides a closeup near the maximum packing treshold $\phi_m = 0.6$. In particular the volume fraction, which was initially uniform, has increased throughout the granular bed and has reached a profile with finite slope which corresponds to hydrostatics. While the increase of $\phi_s$ inside the bed is limited, it nevertheless corresponds to a significant increase of the integranular stress $\hat{\beta}_s'$ and of the viscosity coefficients $\mu_s$, $\zeta_s$ and $\mu_n$; this is due to the fact that the expressions for these coefficients are stiff with respect to $\phi_s$. As an example, at the bottom of the domain (where $\phi_s$ is largest, cf. Figure 6.1b), all these coefficients increase by one order of magnitude between t = 0 and t = 5.

In order to better appreciate the transition to equilibrium, it is necessary to consider the evolution of the phasial velocities and pressures; Figure 6.2 shows the wall-normal component of the fluid and solid non-dimensional velocities at different times. Figure 6.2a refers to the early state of the flow, at t = 0.01. At this time, the bed has not yet settled and its relaxation is controlled by drag. In the fluid region above the bed the granular phase moves downward at the reference velocity, determined by drag, corresponding to settling at $\phi_s = 10^{-5}$; inside the bed the downward velocity is smaller due to the higher drag coefficient. Conversely, the

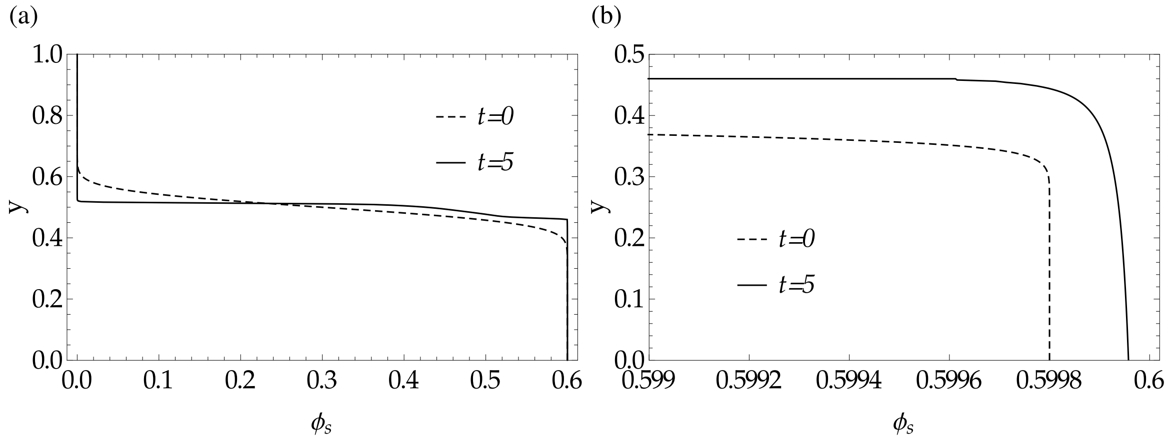


Figure 6.1: Initial and equilibrium volume-fraction profiles. (a) volume fraction as a function of the (non-dimensional) vertical coordinate, (b) close-up of the volume fraction profile near the maximum packing limit $\phi_m = 0.6$.

fluid phase moves upwards; in fact, inside the bed the volume fraction is almost constant down to the bottom wall, so that by continuity the phasial velocities are inversely proportional to the phasial volume fractions, $\phi_s \mathbf{u}_s + \phi_f \mathbf{u}_f \approx 0$. This can be readily observed in Figure 6.2a, for $z < 0.4$ .

Figure 6.2b shows the velocities at a later time, t = 2. At this time, most of the bed has settled, but the granular phase is still moving downwards in a wide transition region which occupies about a fifth the flow domain.

Finally, at t = 5 sufficient time has passed that the suspension has settled; the corresponding velocity profiles are shown in figure 6.2c. The transition region between the bed and the fluid has become a sharp interface. It is interesting to observe that, through the interface, there is a narrow peak of the fluid velocity which does not disappear with time; it is due to the continuous sedimentation of the dilute suspension at $\phi_s = 10^{-5}$ above the bed. From a physical perspective, this behaviour is a consequence of approximating the pure fluid above the bed with a dilute suspension; if the fluid were pure, with $\phi_s = 0$, the solid velocity would not be defined above the bed and the fluid velocity would vanish everywhere in the flow domain.

Figure 6.3 shows the phasial pressures $p_s$ and $p_f$, together with analytic expressions for the mixture pressure $p_m$ and the granular hydrostatic pressure $p_h$. The mixture pressure $p_m$ is herein defined as the pressure that would be present in a single-phase fluid with density equal to the average density of a compacted bed at maximum packing, while the granular hydrostatic pressure $p_h$ is the pressure that the granular phase would assume if the fluid

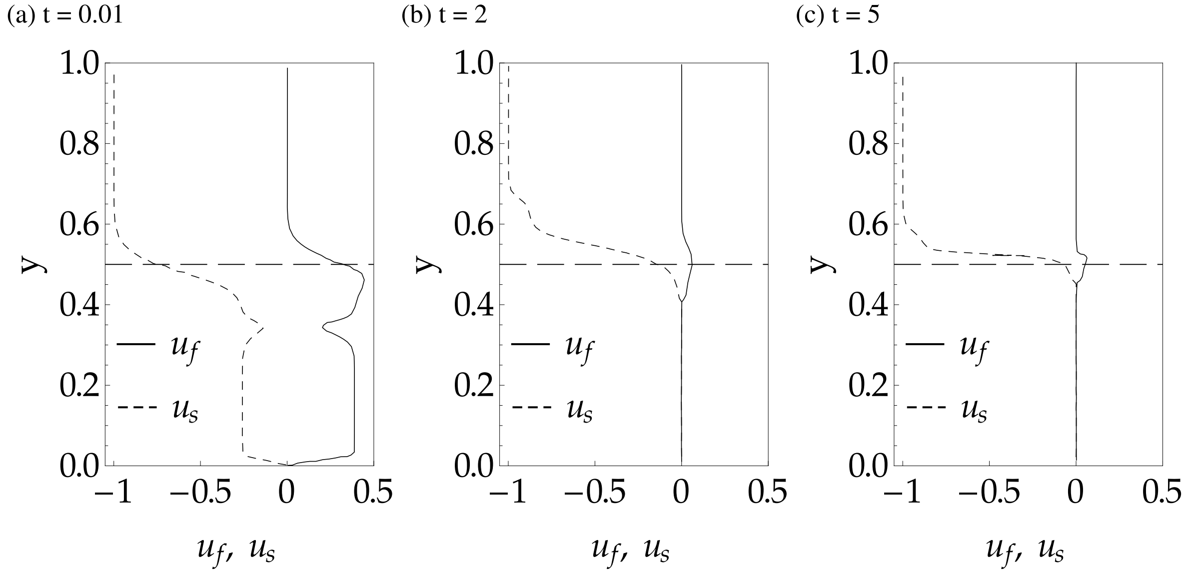


Figure 6.2: Evolution of the wall-normal non-dimensional phasial velocities $u_s$ and $u_f$. (a) at t = 0.01 the settling is controlled by drag and there is significant motion inside the granular bed. (b) at t = 2 the suspension has almost settled inside the granular bed, where the phasial velocities vanish; however the suspension is still settling in a wide transition region at the top of the bed which occupies approximately one fifth of the flow domain. (c) at t = 5 the suspension has settled, and a sharp transition region is present at the top of the bed. The dashed grid line at $y = 0.5$ in all figures marks the initial position of the granular bed.

phase were absent. More specifically, inside the granular bed they are defined as

$$p_m = p_f|_{y=y_{top}} + (\rho_f(1-\phi_m) + \rho_s\phi_m)g(y_{top} - y), \tag{6.6}$$

$$p_h = p_f|_{y=y_{top}} + \rho_s g(y_{top} - y), \tag{6.7}$$

where $y_{top}$ denotes the height of the granular bed, here $y_{top} = 0.5$.

The profiles of the phasial pressures $p_s$ and $p_f$ corroborate the analysis relative to the evolution of the velocity profiles; In particular, Figure 6.3a shows the pressure profiles at t = 0.01. At this time, buoyancy is entirely balanced by interphasial drag, and the two phases have the same pressure $p_s = p_f = p_m$. In Figure 6.3b the phasial pressures are shown at the later time t = 5. At this later time, the granular bed is at mechanical equilibrium and the bed has settled, cf. Figure 6.2c. Consequently the granular phase "supports itself"; more precisely, the buoyancy term in the momentum balance of the granular phase is counterbalanced by a corresponding increase in the granular pressure $p_s$, whose gradient is now $\rho_s g$ inside the dense bed. Since the interphasial momentum flux now vanishes inside the bed, the fluid phase $p_f$ increases differently from $p_s$, with gradient $\rho_f g$; this implies that a significant phasial pressure difference can exist for sufficiently deep granular beds in hydrostatic equilibrium.

The pressure plots of Figure 6.3 can be compared with the pressure profiles shown in Figures 2.2 and 2.6, which were obtained in Chapter 2 with a flow model that does not account for particle migration. In particular, it can be observed that the pressure profiles shown in 2.2 and 2.6 show the same structure as those of Figure 6.3b, and resemble the pressure profiles at equilibrium. This is a consequence of the fact that the flow model used in Chapter 2 predicts a solenoidal granular velocity, $\nabla \cdot \mathbf{u}_s = 0$, so that in this flow the phasial velocities vanish identically. On the other hand, the flow model employed herein provides a more accurate description of the settling process, as it captures the interphasial momentum transfer associated with phasial velocity differences.

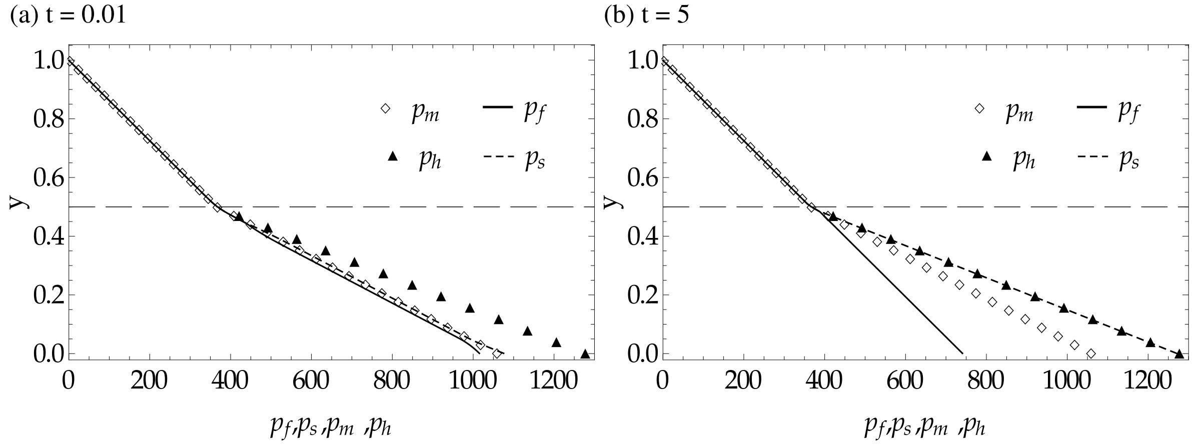


Figure 6.3: Evolution of phasial pressure profiles at (a) t = 0.01, (b) t = 5. The phasial pressures $p_f$ and $p_s$ are shown, together with the mixture pressure $p_m$ and the granular hydrostatic pressure $p_h$ defined in (6.6) and (6.7). The dashed grid line at $y = 0.5$ marks the position of the bed-fluid interface.

### Numerical grid-convergence study

In order to assess the performance of the solver, a grid-convergence study is performed for this flow case. More precisely, different grid resolutions are tested and the relative $L_2$ norm of the error with respect to a reference solution, which uses a refined grid with 1024 points, is evaluated at t = 1. As an example, for $\phi_s$ this value is $\mathrm{Err}(\phi_s) = \frac{||\phi_s - \phi_{ref}||_2}{||\phi_{ref}||_2}$, where $\phi_{ref}$ is the reference solution. The observed convergence rates for the volume fraction $\phi_s$, the granular velocity $u_s$ and the auxiliary pressure $p_d = \phi_s(p_s - p_f)$ are shown in Figure 6.4, together with two black lines corresponding to second- and third-order convergence.

The volume fraction and velocity plots exhibit a similar trend. In particular, at least 128 points are required in order to achieve the expected second-order convergence rate. Moreover, as the resolution increases, the convergence rate increases, due to the fact that the reference solution is not the exact one. For this reason the asymptotic convergence rates in these figures, corresponding to the dashed lines, are computed relative to the resolutions of 128, 180 and 256 points (with a least-square interpolation).

For the case of the phasial pressure difference $p_d$ the convergence is less regular; its plot is shown in Figure 6.4c. In particular, convergence is not monotonic at medium resolutions, and it appears that a resolution higher than 256 points should be used in order to avoid a local peak of the error.

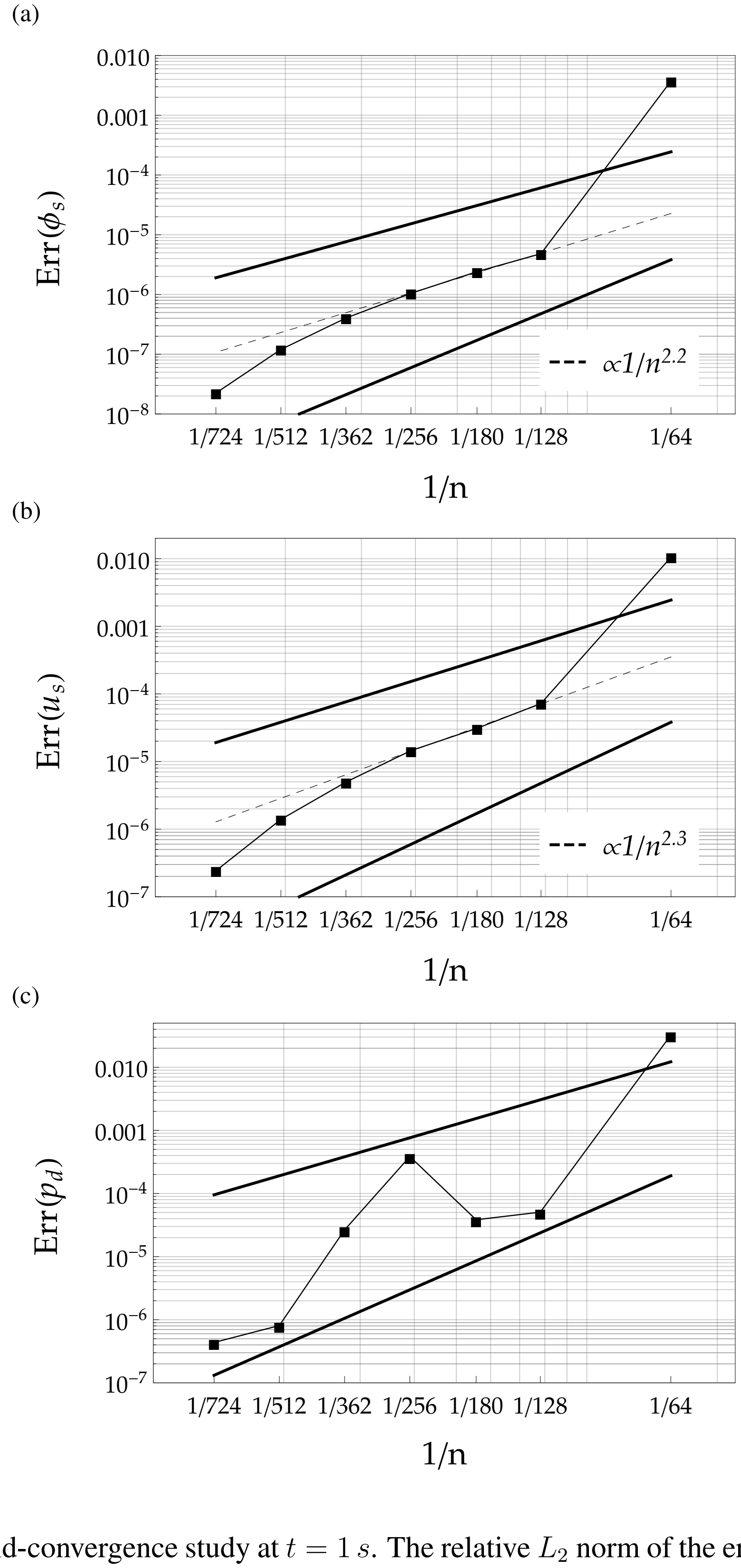


Figure 6.4: Grid-convergence study at $t = 1\,s$. The relative $L_2$ norm of the error with respect to a reference solution with 1024 points is shown for (a) $\phi_s$, (b) $\mathbf{u}_s$, (c) $p_d$. The two thick lines in all figures correspond to second- and third-order convergence. Further, the dashed line, shown for cases (a) and (b), is obtained with least-square interpolation relative to the resolutions of 128, 180 and 256 points.

## 6.3 Sedimentation of a dense suspension

This section considers the sedimentation of a dense suspension, which settles into a compacted granular bed. This test case serves to assess the efficiency of the algorithm in handling large volume-fraction variations, and also provides important insight into the numerical treatment of the intergranular stress $\beta_s$ near maximum packing. Further, as the granular bed is formed, the flow develops a sharp interface at the top of the bed; this interface is used as a benchmark in order to demonstrate the effects of the interface regularization treatment.

### Problem set-up

An initially uniform suspension with volume fraction $\phi_s = 0.1$ fills the entire flow domain, and the liquid and granular phases are initially at rest. The same domain geometry is used as in the previous analysis of Section 6.2; in particular, one-dimensional flow is considered in a domain with a height of $0.4\,\mathrm{m}$.

The boundary conditions are also similar, with a wall condition for the velocities at the bottom and zero-Neumann conditions elsewhere for all variables; the only exception is that a Dirichlet condition with $\phi_{top} = 10^{-5}$ is used for the volume fraction $\phi_s$ at the top boundary.

The properties of the suspensions also conform to the previous case, and the reference velocity is again the uniform-flow sedimentation velocity at $\phi_s = 10^{-5}$ (which is close to the sedimentation velocity of a single particle). For this test, however, the unaltered expression for the intergranular stress $\beta_s$ defined in (6.1) is used, and the maximum volume fraction is limited with a cutoff treshold at $\phi_{max} = 0.599$. As discussed in Subsection 6.1.1, this treatment of the intergranular stress improves the numerical tractability of compaction and allows to use a significantly larger time step, which is a desirable feature for the problem at hand since sedimentation can be a very slow process.

The domain is discretized on a uniform grid with 1024 points in the wall-normal direction. In addition, results for the volume fraction $\phi_s$ are also shown for coarser grids with 128, 256 and 512 points, in order to evaluate the impact of the interface regularization treatment.

### Discussion of the numerical results

The evolution of the volume fraction $\phi_s$ with time is shown in Figure 6.5, where it is labeled $\phi_{1024}$ since it is computed on a grid with 1024 points. Together, the variables $\phi_{128}$, $\phi_{256}$ and $\phi_{512}$ are shown, which represent the same quantity computed on coarser grids with 128, 256 and 512 points, respectively.

Initially, the volume fraction has the uniform distribution plotted in Figure 6.5a. Shortly after, at t = 1, sedimentation has progressed slightly; Figure 6.5b shows that boundary layers begin to form at the top and bottom boundary. The process is very slow due to the fact that the suspension experiences high interphasial drag; in fact, after 50 non-dimensional times, only half of the suspension has settled, as shown in Figure 6.5c. As the suspension settles, it leaves a layer of clear fluid on top of it. In the computations this is approximated by a dilute region at $\phi_s = 10^{-5}$; this value follows from the boundary condition for $\phi_s$ at the top boundary.

Figure 6.5d shows the final state of the process: after 80 non-dimensional times the entire suspension has stratified to the bottom of the domain and a compacted granular bed has beed formed, with a volume fraction close to the maximum-packing treshold $\phi_m$.

In the flow under consideration, a sharp interface for the volume fraction is naturally formed at the top of the granular bed. By comparing the predictions of the model at various resolutions, the effects of the interface regularization procedure described in Subsection 5.2.3 can be evaluated. In particular, it can be observed that this procedure has a notable impact at low resolutions if the flow exhibits strong stratification. According to Figure 6.5 the effect is minor when the volume fraction is still fairly uniform, however once the bed is compacted the interface becomes appreciably diffused for the lower resolution. It is well-known that the presence of discontinuities can degrade grid-convergence properties; in the case of Figure 6.5d, it appears that the interface regularization dominates the error for the lower resolution.

Computational errors with respect to the volume fraction directly affect mass conservation, since the mass of the granular phase inside the domain is proportional to the integral of its volume fraction. For the problem at hand, this integral should be constant, as the mass flow through the boundaries of the domain is negligible. In order to assess the mass-conservation properties of the implemented algorithm, the relative variation of this quantity has been computed at various resolutions. After an initial transient, the error is found to increase linearly with time for all resolutions considered; the relative error per time-step and the cumulative error per non-dimensional time are shown in Table 6.1. The numerical error can be compared with $(\Delta y)^2 = 9.5 \times 10^{-7}$ and $\Delta t = 5 \times 10^{-5}$, which are the characteristic values for the accuracy of the implemented algorithm (which is second-order in space, but first-order in time for the phasial pressures). In particular, it appears to scale weakly with $\Delta y$, but linearly with $\Delta t$. While the error per time-step is small compared with these quantities, the global error is not entirely negligible for the problem at hand after sufficient time has

| Resolution (pts.) | $\Delta t$ | Error per time-step | Error per non-dimensional time |
|---|---|---|---|
| 256 | $5 \times 10^{-5}$ | $9.8 \times 10^{-8}$ | $2.0 \times 10^{-3}$ |
| 512 | $1 \times 10^{-4}$ | $1.4 \times 10^{-7}$ | $2.9 \times 10^{-3}$ |
| 512 | $5 \times 10^{-5}$ | $7.2 \times 10^{-8}$ | $1.4 \times 10^{-3}$ |
| 1024 | $5 \times 10^{-5}$ | $5.9 \times 10^{-8}$ | $1.2 \times 10^{-3}$ |

Table 6.1: Mass-conservation properties: the relative variation of the granular phase inside the domain is computed at different resolutions. The data refer to asymptotic conditions: after an initial transient, the error is linear in time at all resolutions.

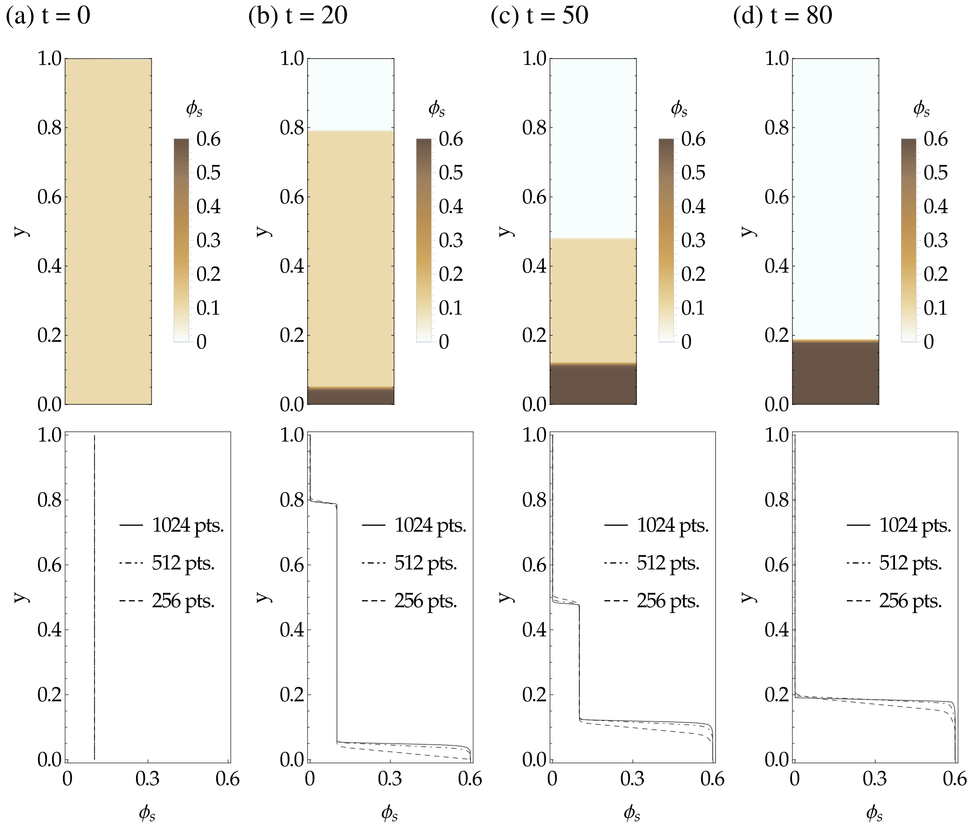


Figure 6.5: Granular volume fraction at t = 0, 20, 50, 80. The top figures show the volume fraction distributions, computed on a grid with 1024 points; the corresponding bottom figures compare this results with the results obtained at different resolutions. (a) the volume fraction is initially uniform, with a value of $0.1$ across the domain. (b,c) the granular phase settles on the bottom under gravity, leaving behind a region of clear fluid. (d) the final configuration presents a sharp interface at the top of the bed; the numerical thickness of the interface depends on the resolution due to the regularization treatment.

passed; this is due to the fact that it cumulates in time, and sedimentation lasts a long time in the case considered. In fact, a manifestation of the mass-conservation error can be seen in Figure 6.5d: after 80 non-dimensional times, which correspond to $1600000$ time-steps, the height of the granular bed is computed to be approximately $0.18$, whereas it should be approximately $1/6 \approx 0.17$ based on the initial condition for the volume fraction[1].

At the end of the sedimentation, for t = 80, the suspension inside the dense bed has compacted enough for the volume fraction $\phi_s$ to reach the cutoff value $\phi_{max} = 0.599$. While the cutoff is marginal with respect to the volume-fraction profile, it nevertheless has an important effect on the phasial velocities and pressures. To better appreciate the consequences, it is useful to consider the phasial velocity profiles. Figure 6.6 shows the non-dimensional

[1]It is possible that the gradual increase of mass is particularly noticeable due to the specific flow pattern considered in this analysis, in the sense that the error might not be cumulative for a less regular flow; nevertheless, this test shows that for simulations involving a significant number of non-dimensional times, mass conservation should be monitored closely.

velocity profiles at t = 80. In the fluid region above the dense bed, the granular phase moves downward at the reference velocity corresponding to sedimentation, as could be expected by analogy with the flow discussed in the previous Section. However, inside the granular bed the velocities do not exactly vanish and the granular phase continues to move downwards, albeit extremely slowly. This is due to the fact that the integranular stress $\beta_s$ is finite for $\phi_s = 0.599$, and its value is too low for the granular phase to "support itself". More precisely, at steady-state the auxiliary pressure $p_d = \phi_s(p_s - p_f)$ coincides with $\beta_s$ inside the bed, cf. (5.7). Then, the buoyancy term in the momentum equation for the granular phase can not be counterbalanced by the gradient of the auxiliary pressure $\nabla p_d$ (which vanishes in the cutoff region), and is instead opposed by interphasial drag.

The profiles of the phasial pressures are in agreement with the analysis of the phasial velocities; in particular, Figure 6.7 shows the phasial pressures for t = 80. Both $p_f$ and $p_s$ have the same value which coincides with $p_m$ , so that $p_d = \phi_s(p_s - p_f) \approx 0$. This pressure distribution is similar to that of Figure 6.3a, which refers to the early stages of settling of a granular bed. In that case the modified intergranular stress $\hat{\beta}'_s$ was used in order to resolve hydrostatics, so that the computed flow gradually transitioned to equilibrium. On the other hand, the numerical cutoff of the volume fraction employed herein, $\phi_{max} = 0.599$, does not allow to reach hydrostatic equilibrium and the bed is kept in a state of very slow relaxation.

## 6.4 Collapse of a submerged granular column

In this Section, the collapse of a two-dimensional dense granular column under water is investigated. As previously discussed in Section 2.4, this flow is particularly challenging from a modelling perspective, since the collapse exhibits a complex flow structure with different flow regimes [78–81]. More specifically, this problem is dominated by spatial variations of the viscosity coefficients: the compacted column is significantly more viscous than the surrounding fluid and, further, different regions of the column present different viscosity. As a result, an accurate representation of the granular rheology is necessary in order to capture even qualitatively the phenomenology that is observed in experiments. Therefore, this flow provides a useful validation of the proposed volume-fraction based rheology formulation for the case of unsteady stratified flows. Furthermore, this benchmark test provides insight into applications involving dense granular transport due to gravity.

#### Problem set-up

The flow domain is a two-dimensional rectangle, with a vertical height $\hat{h} = 0.3\,\mathrm{m}$ and a horizontal length of $1.8\,\mathrm{m}$. A square granular column with aspect ratio $a$ = 2 (the top *radius* is used in the literature to compute this value) stands at the center of this domain; the height of the column is $0.18\,\mathrm{m}$ and the volume fraction inside the column is $\phi_s = 0.59$. Additionally,

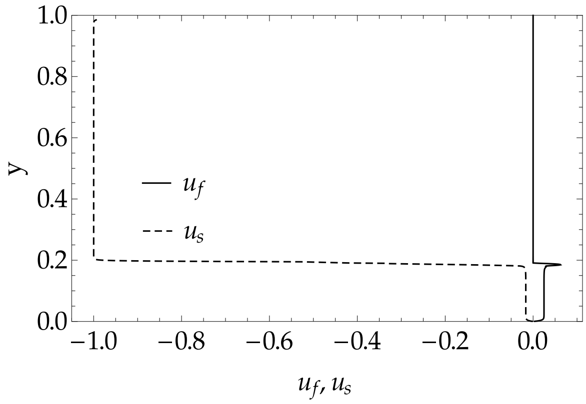


Figure 6.6: Wall-normal non-dimensional phasial velocities at t = 80. In the fluid region, the granular phase settles with the free-flow velocity at $\phi_s = 10^{-5}$, which is essentially the settling velocity of an isolated grain. Due to the artificial cutoff for the volume fraction at $\phi_{max} = 0.599$, in the dense granular bed the granular phase moves downwards with a very small, albeit non-vanishing, velocity, and the fluid correspondingly moves upwards.

on the bottom of the flow domain a dense granular layer is introduced, in order to circumvent the difficult problem of assigning continuum boundary conditions for the volume fraction on a bare wall. The height of this layer is $4 \times 10^{-2}$ m , with an initial volume fraction $\phi_s = 0.59$. The remaining part of the domain is essentially clear fluid, with a volume fraction $\phi_s = 10^{-5}$. At the beginning of the simulation, the interface between the dense and the dilute regions of the flow domain is smoothened with a parabolic regularization, until this interface covers 15 points. The two phases are initially at rest and the initial guesses $p'_f = 0$, $p_d = \beta_s$ are used for the auxiliary pressures. Due to the symmetry at the center of the domain, only the right half of the domain is simulated; the initial distribution of $\phi_s$ in this half-domain is shown in Figure 6.8a.

The half-domain, consisting of the right half of the original domain, is limited by wall boundary conditions for the phasial velocities on the top and bottom sides; on the same top and bottom sides the phasial pressures have a zero-Neumann condition, while the granular volume fraction has a zero-Neumann condition at the bottom and a Dirichlet condition at the top, $\phi_{top} = 10^{-5}$. On the left side of the half-domain, corresponding to the centerline of the column, a symmetry (mirror) condition is applied, with the horizontal component of the velocities set to zero and zero-Neumann conditions for the other variables; on the right side of the domain, a zero-Neumann condition is used for all variables. The half-domain is discretized with a uniform structured grid that consists of 256 points in the vertical direction and 512 points in the horizontal direction.

The properties of the suspension are the same as in the previous problem and are listed in Subsection 6.1.1. In particular, herein the unmodified expression for the intergranular stress $\beta_s$ is used and the maximum volume fraction is limited with a cutoff treshold at $\phi_{max} = 0.599$. In addition, in order to reduce the computational cost of the simulation, a

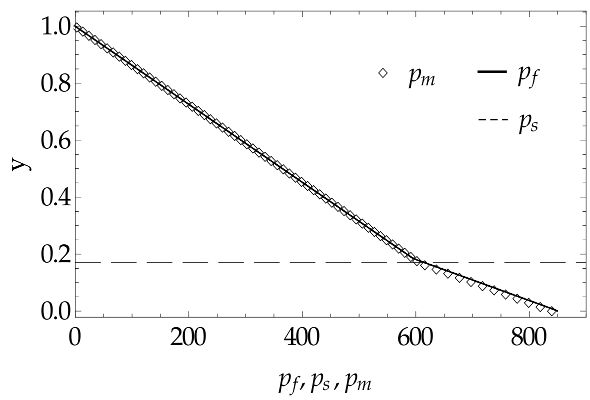


Figure 6.7: Profiles of the phasial pressures at t = 80. Due to the artificial cutoff for the volume fraction at $\phi_{max} = 0.599$, the integranular stress $\beta_s$ is bounded and buoyancy due to phasial density differences is balanced by interphasial drag. As a result, the two phases have the same pressure, which coincides with the mixture pressure $p_m$. The dashed grid line at $y = 0.17$ marks the final position of the bed-fluid interface that is predicted by mass conservation.

treshold is applied for the non-Newtonian stresses at $\phi_s = 0.59$ according to the procedure presented in Subsection 5.2.3. The reference velocity for the non-dimensionalization is $\hat{u}_r = (2\hat{g}\hat{h})^{0.5} = 2.4 \text{ m/s}$.

### Discussion of the numerical results

The evolution of the granular volume fraction in time is shown in Figure 6.8 at the successive instants t = 0, 2, 7, 14. Figure 6.8a shows the initial condition, consisting of a square column adjacent to a dense granular bed. The granular column begins to collapse, due to the fact that its sides are unsupported. Figure 6.8b shows a contour plot of $\phi_s$ during the early stages of the collapse, at t = 2. The lateral side of the column begins to slide to the bottom, with local instabilities forming along the sliding region. At the base of the column, a plume of ejected material rises due to the impact of the collapsing column wall. Figure 6.8c shows a further state of the collapse; at t = 7 enough material has moved that the column reduces to a pile of (half) triangular shape. The collapsing material does not enter the bulk of the flow domain and instead flows close to the surface of the adjacent granular bed, creating a vortex sheet parallel to the surface of the bed which generates a number of consecutive vortices. According to Figure 6.8d, at t = 14 the collapse is practically completed. This Figure shows that the initial column is reduced to a triangular pile that remains at the point of collapse, with a basal layer of flowing material propagating towards the right along the surface of the granular bed. The particle concentration of this moving layer remains dense, $\phi_s \approx 0.4$, and the mobile material is confined to the bottom half of the flow domain.

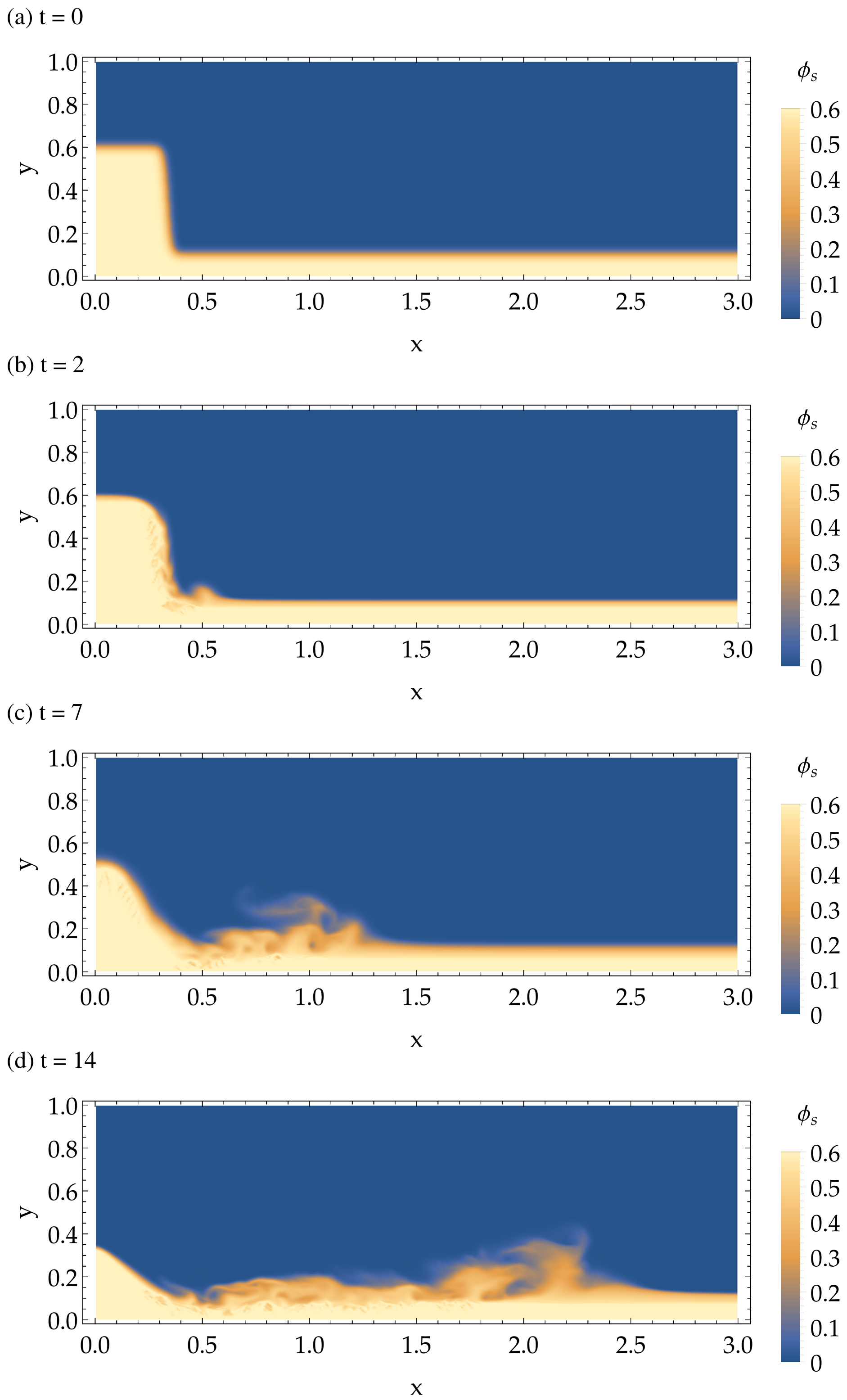


Figure 6.8: Collapse of a submarine granular column; distribution of volume fraction $\phi_s$ at t = 0, 2, 7, 14. (a) initial condition. (b) at an early stage, local instabilities form on the side of the column and a plume is ejected at the base. (c) at a later stage, the column morphs into a triangular shape, and the collapsed material flows away over the adjacent granular bed. (d) at the end of the collapse, a (half) triangular pile remains, with a dense mobile layer propagating away from the pile.

The computations predict that the remaning triangular pile has a slope of approximately $35°$, which is slightly reduced close to the apex. This can be compared with the experimental study reported in [79], in which the authors provide an extensive set of measurements for a wide range of aspect ratios, relative to non-cohesive quartz sand sorted for a grain diameter $\hat{d}_p < 5 \times 10^{-4}\,\mathrm{m}$. In particular, the authors of [79] report values of the apex angle that are scattered around $32°$ for two-dimensional column collapse under water at aspect ratios less than $a = 5$. Figure 6.9 shows contours for the granular volume fraction at t = 14, superimposed with a red dashed line at a slope of $32°$ corresponding to the experimental data for the apex angle. This line is in good agreement with the numerical results, especially if one observes that the lateral side of the pile is also slightly concave in the experiments.

Additionally, the height of the pile can be compared with the experimental data, although this is complicated by the fact that a shallow granular bed is present in the numerical simulation (which is not the case in the experiments). According to the computations of this Section, at t = 14 the height of the column is approximately $50\%$ of the initial height if measured with respect to the surface of the bottom layer and approximately $65\%$ of the initial height if measured with respect to the bottom wall. In the experiments a taller pile is observed at $74\%$ of the original height.

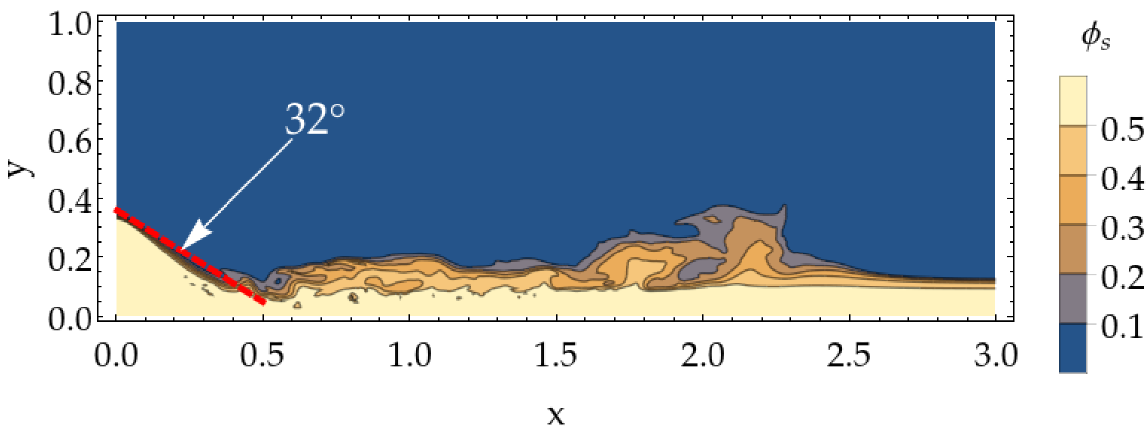


Figure 6.9: Contours of the granular volume fraction at t = 14; contour lines are drawn for $\phi_s = 0.1, 0.2, 0.3, 0.4, 0.5$. The inclination of the red dashed line is 32°, corresponding to the experimental data for the apex-angle reported in [79] relative to 2D collapse under water with aspect ratio $a = 2$.

A possible reason for the difference lies in the sensitivity of this value with respect to the initial volume fraction inside the granular column, [80, 81]. In fact, the authors of [80] conclude, on the basis of their experimental tests, that the initial volume fraction strongly influences the final height of the collapse; this factor was not considered in the measurements reported in [79]. As an example, both studies provide data for a column with aspect ratio $a = 0.67$; the authors of [79] observe a final height that is $100\%$ of the initial, while in [80] it is shown that a variation of initial volume fraction by 0.05 can change the final height by

50%. This observation agrees with the numerical simulations performed for this test case: several values of the initial concentration have been tested, and no final pile was observed for initial concentrations less than about $\phi_s = 0.55$, in which case the dense suspension that constitutes the column behaves as a simple fluid and slumps to the bottom.

This behaviour, which may seem puzzling at first, has a direct explanation related to the time scale of the flow. In particular, the viscosity is a nonlinear monotonic function of the volume fraction, and the final granular pile must be at high volume fraction in order to resist collapse. As discussed in Sections 6.2 and 6.3, the settling of a dense mixture is a slow process due to the high value of the interphasial drag coefficient. It turns out that, if the initial volume fraction is sufficiently low, the suspension inside the column does not have time to compact significantly (thus increasing its viscosity) before the collapse is complete, [81].

Next, the velocity fields are examined; for the flow under consideration, this analysis is particularly significant since the flow exhibits a characteristic structure that crucially depends on the rheological properties of the suspension. In fact, it is known from experimental observation that underwater collapse (in which the phasial densities are of the same order of magnitude) evolves very differently from collapse in air, although both cases end with the formation of a granular pile of similar shape [79, 179, 180]. More precisely, in the case of underwater collapse motion is limited to the lateral sides of the column, where the granular phase slides to the bottom and exhibits a peak of the downward velocity (on the other hand, for collapse in air the whole column flows at the same time). Recovering this feature is thus a primary task for the numerical method.

The computations for the phasial velocities, shown below, confirm that the solver is capable of capturing the experimentally-observed features of underwater collapse. In particular, Figure 6.10 shows a close-up of the column, with the vertical (y) component of the non-dimensional phasial velocities plotted at t = 2. It can be observed that motion in the vertical direction is essentially limited to the lateral side of the column, with a thin region of dense material close to the interface that "slides" off the side of the column. In this dense region interphasial drag is strong and, as a result, the velocity plots of both phases are similar.

At a later stage, the column collapses into a triangular pile; the non-dimensional vertical velocity of the granular phase is shown in Figure 6.11 at t = 7 and t = 14. For t = 7, Figure 6.11a shows that a significant portion of the lateral region of the column is still mobile; further, a series of alternating peaks on the surface of the adjacent granular bed are indicative of the presence of vortical structures where the collapsed material flows away from the column; in fact the presence of vortical structures is also visible in the corresponding volume-fraction plot of Figure 6.8c. On the other hand, at t = 14 the collapse is close to completion; Figure 6.11b shows that only a thin mobile layer remains at the surface of the pile, and the maximum value of the vertical velocity is reduced.

The analysis of the streamwise (x) velocity component also reveals an interesting detail.

In particular, the collapsed material has formed a dense layer over the surface of the adjacent granular bed, which has propagated quite far from the initial position and which maintains a high velocity at large distances compared with the dimensions of the column. This is visible in Figure 6.12, which shows the streamwise component of the phasial velocities at t = 14. The mobile region is fairly dense and, as a result, the phasial velocities are similar due to strong interphasial drag.

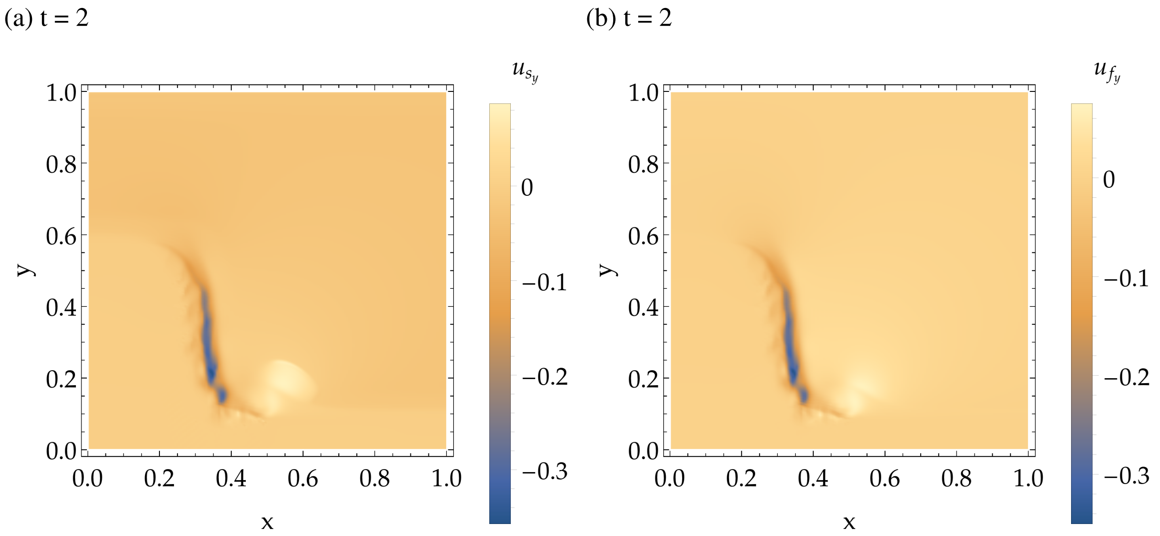


Figure 6.10: Collapse of a submarine granular column: vertical (y) component of the non-dimensional phasial velocities $u_{s_y}$ and $u_{f_y}$ at t = 2. Collapse is limited to the lateral interface of the column, where the suspension presents a lower viscosity. The velocities of the two phases are similar due to strong interphasial drag in the dense mobile region.

Finally, it is appropriate to investigate the interaction between the collapsing material and the granular bed adjacent to the column. During the collapse, the bed is scoured in proximity of the column; Figures 6.13 and 6.14 show the magnitude of the non-dimensional velocity field and the volume fraction in that region, respectively. In particular, in Figure 6.13 a significant velocity can be observed below the initial height of the bed, which indicates mobilization of the granular phase and thus erosion. Correspondingly, Figure 6.14 shows important variations of the granular volume fraction inside the bed. At t = 7, a flowing layer of collapsed material with a volume fraction $\phi_s \approx 0.4$ is visible for $0.05 \lesssim y \lesssim 0.15$; underneath the granular phase remains more compact. Later, at t = 14, most of the material of the column has been advected out of the region of interest; the interface of the bed is no longer flat, and low concentration regions are present below the initial position of the interface.

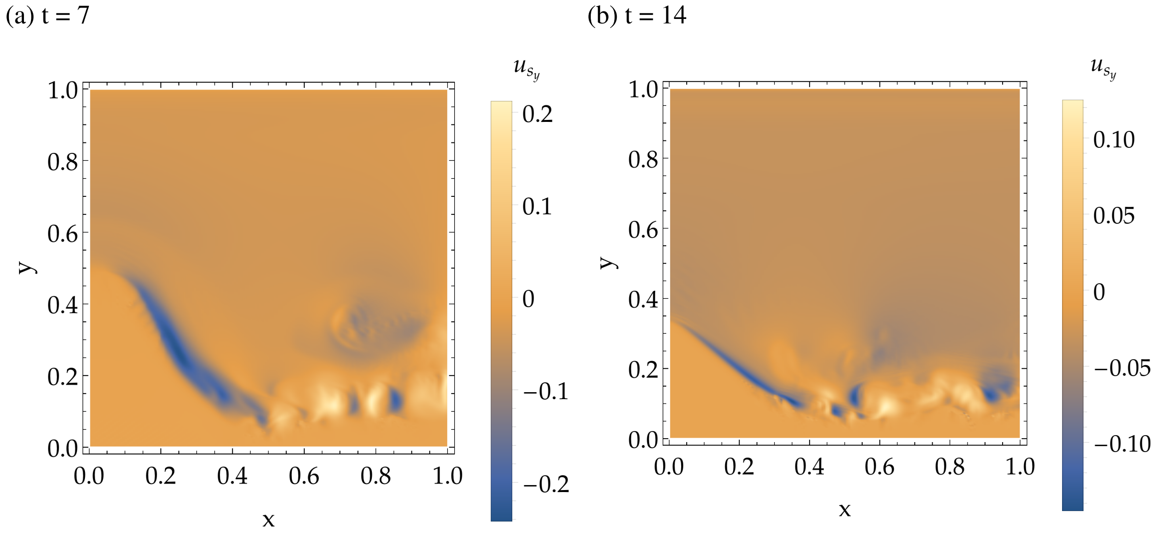


Figure 6.11: Collapse of a submarine granular column: vertical (y) component of the non-dimensional granular velocity $u_{s_y}$ at t = 7, 14. (a) at t = 7, the mobile region has widened, while the maximum of the velocity is reduced due to the decreased slope. One the surface of the adjacent bed, the velocity profile with alternating peaks is typical of a train of vortices. (b) at t = 14, the mobile region is significantly reduced and only a thin moving layer remains.

## 6.5 Conclusions

This Chapter presented a numerical study of dense stratified flows of granular suspensions; this study is based on the numerical algorithm developed in Chapter 5, which is used to solve the flow equations provided by the two-phase continuum model derived in Chapter 3.

First, results have been shown for the compaction of a dense granular bed under water, obtained with a specific numerical treatment of the integranular stress which allows to capture the transition of the flow to hydrostatic equilibrium. In particular, the flow exhibits a relaxation dynamic, with the granular phase settling downwards and the fluid phase moving upwards, which continues until the bed is sufficiently compacted and the flow stops. In addition, the performance of the numerical solver has been evaluated with a grid-convergence study.

Subsequently, the sedimentation of a uniform suspension into a granular bed has been studied; this is a particularly challenging problem from the computational standpoint, as there are significant variations of the granular volume fraction with time. The suspension settles to the bottom of the flow domain, creating a compacted bed close to maximum packing; the flow is controlled by interphasial drag. In addition, this flow naturally generates a sharp interface corresponding to the top of the compacted granular bed; for this reason it has also been used as a benchmark in order to evaluate the performance of the interface regularization treatment which is implemented by the numerical algorithm of Chapter 5.

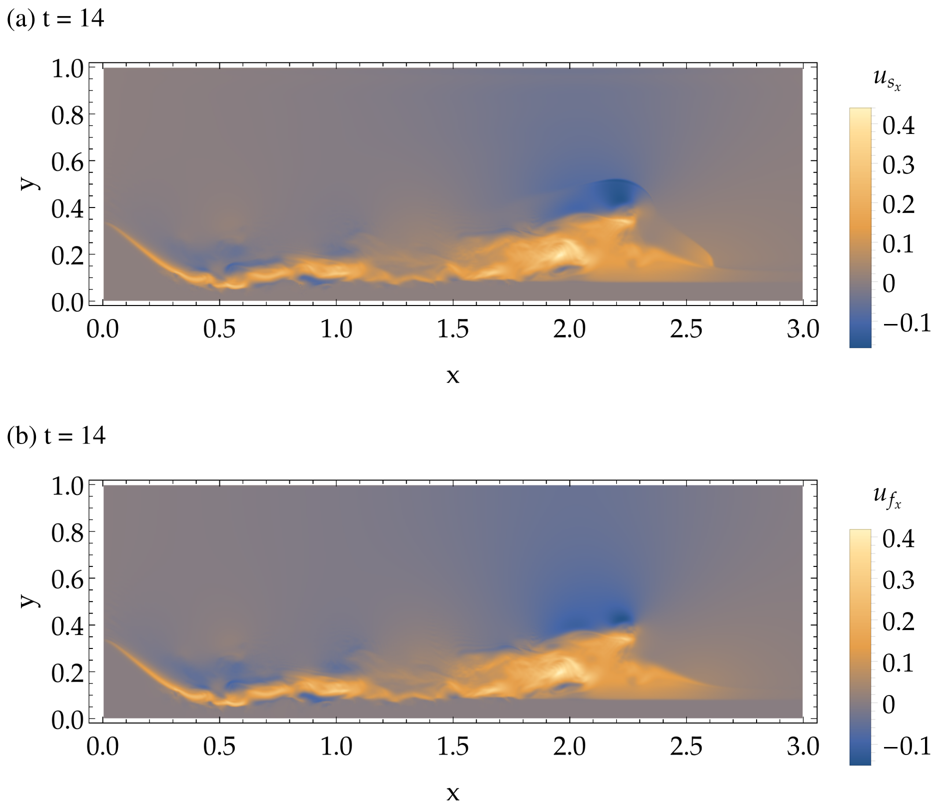


Figure 6.12: Collapse of a submarine granular column: streamwise (x) component of the non-dimensional phasial velocities $u_{s_x}$ and $u_{f_x}$ t = 14. A dense basal layer is present which propagates away from the point of collapse with high velocity, and the velocities of the two phases are similar due to strong interphasial drag in the dense high-velocity region.

Finally, the collapse of a submerged granular column has been simulated. The computations capture accurately the complex flow structure observed in experiments, and match the angle of repose for the granular pile that is left behind when the collapse is completed. It is more difficult to match the final height of the remaining pile, due to the high sensitivity of this parameter with respect to the initial volume fraction inside the granular column. With regards to practical applications, it is particularly noteworthy that a dense basal layer with high horizontal velocity is observed after the collapse; this type of flow structure is known to appear in submarine collapse events such as submarine landslides [181, 182]. The propagation of a dense layer of mobilized sediments can be critical with respect to engineering installations located on the sea floor, such as submarine pipes and cables, since the dense sediment can impart significant forces on these installations. In turn, the full-field description developed in this thesis provides a way to resolve the internal structure of this dense layer, potentially allowing to compute the interaction with these installations without additional modelling assumptions.

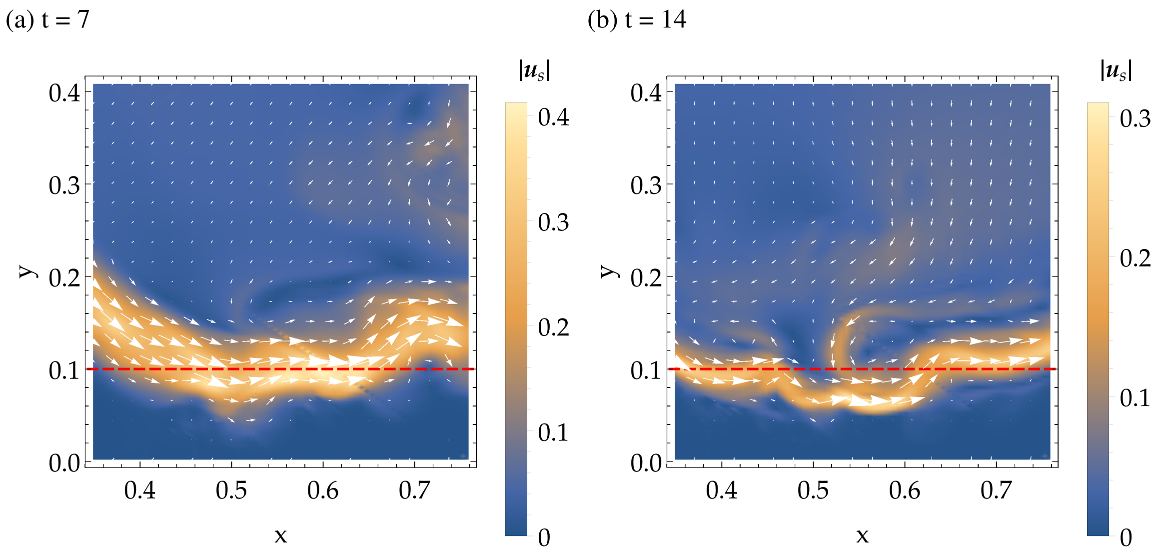


Figure 6.13: Collapse of a submarine granular column: magnitude of the non-dimensional granular velocity $|\mathbf{u}_s|$ in the adjacent granular bed at t = 7,14. The white arrows represent velocity vectors. The red dashed line at $y = 0.1$ corresponds to the initial height of the granular bed. Significant velocity can be observed under this line, indicating mobilization of the granular phase inside the bed.

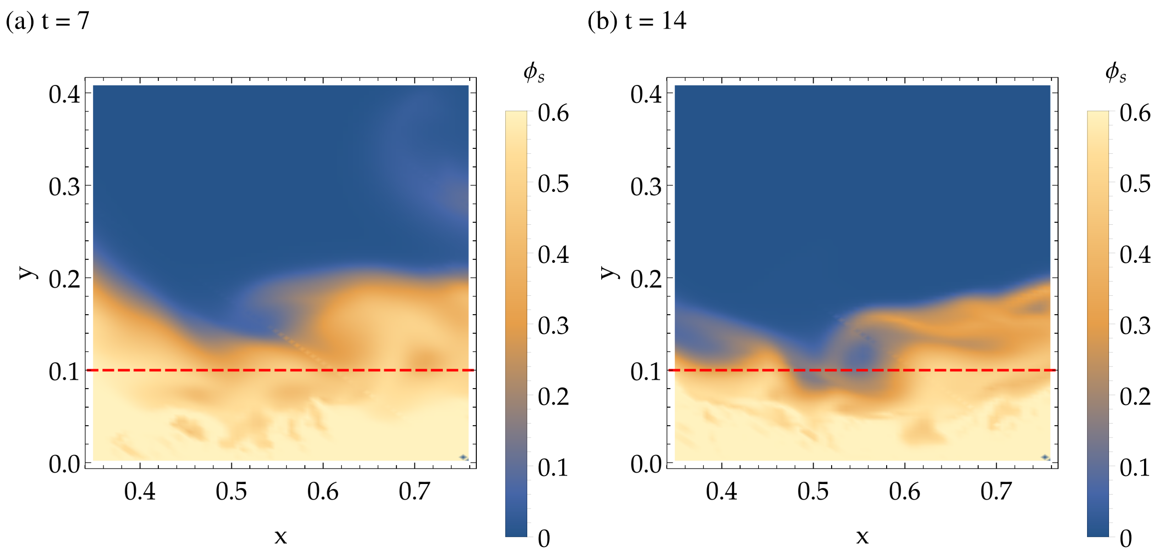


Figure 6.14: Collapse of a submarine granular column: distribution of volume fraction $\phi_s$ in the granular bed adjacent to the column at t = 7, 14. The red dashed line at $y = 0.1$ corresponds to the initial height of the bottom layer. Significant volume-fraction variations can be observed inside this layer, which is partly advected away during the collapse.

# Chapter 7

# Concluding remarks

## 7.1 Summary of results

This thesis concerns the theoretical and numerical analysis of granular flows, with emphasis on the description of sedimentation processes in constant-density flows. In Chapter 2, numerical results have been presented for fluid flow over compacted granular beds. These results are obtained with a flow model that provides a simplified (Newtonian) description of granular rheology and does not account for compaction. The analysis of the results shows that this simplified description is able to capture a number of relevant flow features. However it also shows that a more general approach, which considers compaction, is required in order to describe physical processes such as sedimentation and shear-induced particle migration, which can play an important role in granular transport.

In order to develop a more accurate description of particle migration, a novel two-phase continuum theory for granular suspensions has been derived. This theory, presented in Chapter 3, is the first to incorporate a non-Newtonian suspension rheology in a thermodynamically-consistent formalism. Further, the governing equations have been specialized to the case of constant-density, which is of great importance in practical applications. The constant-density equations agree with state-of-the-art rheological models when applied to Couette flow, and provide a rheology formulation which is directly applicable to general flow. This is a notable achievement, as models for granular rheology are often experiment-based and rely on a specific flow geometry.

The proposed theory has been validated against experiments in Chapter 4, which presents an analysis of pressure-driven flow of a dense suspension in a microchannel (a flow which depends crucially on the non-Newtonian properties of the suspension). To this end, a specific iterative algorithm has been developed. The computations match accurately the available experimental data for the volume fraction and velocity distributions, which is a challenging task for continuum descriptions due to the fact that the particle size is not negligible with respect to the width of the channel.

Subsequently, a general numerical algorithm has been developed for the integration of the governing equations, which can be applied to arbitrary flow. This algorithm, presented in Chapter 5, is based on a fractional-step projection method and is tailored to the structure of the governing equations. In fact, the compaction equation for the proposed model is coupled directly with the phasial pressures; this is a new feature in the literature of projection methods. A specific numerical treatment has been derived, which allows to cope with this new feature and to integrate this equation in a stable manner.

Finally, in order to provide further validation, in Chapter 6 the proposed algorithm has been applied to example problems concerning sedimentation processes. The numerical results demonstrate the predictive capabilities of the algorithm, and show that it can capture granular compaction and the transition to hydrostatic equilibrium. Further, computations have been performed for the collapse of a submerged granular column, a flow where granular rheology plays a dominant role; the numerical predictions match available experimental data with good accuracy, and showcase the capability of the proposed description with respect to unsteady granular flows with large volume-fraction variations.

## 7.2 Future work and perspectives

### Theoretical developments

The two-phase theory developed in this thesis includes a complex rheological description, which conforms with state-of-the-art rheological models for simple flows such as Couette flow, while proposing a generalization to arbitrary flows which is thermodynamically-consistent. However, similarly to other models it predicts that the first normal-stress difference (NSD) vanishes, as detailed in the relative discussion at the end of Chapter 3. This is known from experiments to be only an approximation, since the first NSD can assume a small non-vanishing value. Presently, there is not sufficient experimental data to characterize the behaviour of this quantity; once this data becomes available, it will be possible to obtain a generalization of the proposed formalism through the inclusion of order parameters that describe additional microstructural degrees of freedom.

In addition, the continuum description of turbulent suspensions requires further theoretical exploration. At high concentration flow is laminar due to strong dissipation, and at the other end of the concentration spectrum the granular phase evolves as a passive scalar. However, one can expect an intermediate concentration range where turbulence is present and there is strong coupling between the fluid and granular phases. In this case, the smallest scales of fluid motion can be smaller than the particle diameter, a length scale which is not directly accessible to continuum modelling; it is not clear yet how to incorporate turbulence at the sub-grain scale into a consistent continuum description. Further, a clear understanding of this flow regime is a necessary step towards the development of turbulence models for large-scale flows.

### Numerical developments

The numerical results for flow in a microchannel show that a continuum description can be practically useful even at a scale which is not too distant from the grain diameter; in particular, a channel with a half-width of 20 grain diameters was considered herein. Due to sedimentation, even in large-scale flows material interfaces can form, where the volume fraction changes abruptly over a distance of few grain diameters. While it may in principle be possible to resolve the narrow transition region with a continuum model, the target of a continuum description is to employ a resolution which is significantly larger than the grain diameter. In fact, this is the case of the numerical studies of sedimentation flows presented in this thesis, where an interface-regularization method is used. It is important to assess the impact of interface-regularization procedures in more complex flow geometries, as granular transport in stratified flows happens in close proximity of material interfaces. In particular, further characterization of the interplay between the granular rheology and the regularization treatment will allow to significantly improve the efficiency of numerical simulations of large-scale flows.

In addition, a detailed investigation of material interfaces will provide an important test of the theory with respect to particle entrainment from compacted granular beds, a phenomenon which is particularly important in sediment-transport applications. It is known from experiments that in certain flow conditions entrainment can be quite modest, and is due to turbulent fluctuations of the fluid velocity around individual particles protruding from the top of the granular bed. As previously mentioned, a continuum description of sub-grain turbulence is still an open problem, so that capturing particle entrainment in these circumstances is challenging. Nevertheless, the proposed flow model has not been tested in these conditions, and in any case it might be possible to introduce ad hoc modifications on empirical grounds. In order to evaluate the capabilities of the proposed theory, it will be instrumental to perform numerical simulations of fully-developed turbulent fluid flows over compacted granular beds.

Another useful development concerns the integration of the compaction equation. It has been shown that this equation requires a specific treatment, due to the fact that it contains explicitly the phasial pressures (which affects the projection method used for time integration). A treatment of this equation has been proposed and employed succesfully in the computations of this thesis; however, there is still considerable room for performance improvements. In particular, it has been shown that common time-integration schemes can exhibit very weak stability in this context, with an attenuation coefficient for the numerical error that does not depend on the time increment $\Delta t$. It is desirable to further investigate the numerical integration of the compaction equation, in order to derive robust integration schemes applicable to general flow.

Finally, it is important to investigate extensions of the proposed algorithm which are fully second-order with respect to time integration. As mentioned in Chapter 5, the proposed algorithm computes the phasial pressures with first-order accuracy in time unless suitable countermeasures are introduced; a possible remedy is to cast the algorithm in a predictor-corrector procedure. The numerical results of Chapter 6 indeed suggest that the mass-conservation error increases linearly with the time-step $\Delta t$; this can be a limitation for sufficiently long simulations, so that it is important to further assess the time-dependency of the numerical errors for the case of higher-order implementations.

**Experimental developments**

The development of theoretical models for complex materials goes hand in hand with the availability of accurate experimental measurements; in fact, it is often more difficult to derive a description that is unambiguously constrained by existing experimental observation, rather than providing a good fit of available results. The theory that was developed in this thesis rests on fairly general physical assumptions which are not flow specific; nevertheless it contains a large number of material coefficients, and for some of these coefficients direct experimental measurements are not available. While particular attention was dedicated in this work, so as to avoid using these coefficients as fitting parameters on a case-specific basis, to the best of the author's knowledge there are currently no direct measurements of the bulk viscosity $\zeta_s$ and of the compaction viscosity $\mu_c$ for general volume fractions. Further, the thermodynamic derivatives $\beta_s$ and $\gamma_s$ require additional experimental characterization in order to clarify the impact of particle deformation and fracturing. The experimental investigation of flows where these coefficients can be measured directly will contribute significantly towards a rigorous validation of the proposed theory.

Finally, it has been mentioned that the current theory, similarly to several contemporary modelling attempts, predicts that the first NSD should vanish (in fact, it can be shown that this is a consequence of the assumed isotropy of the constitutive relations). While sufficient data is available to assert that this is only an approximation, presently there is not enough information to unambiguously characterize this behaviour from the theoretical standpoint. Experimental studies that precisely identify the role of the relevant microstructural order parameters will directly enable a more accurate modelling of suspension rheology.

# Appendices

# Appendix A

# A projection algorithm for solenoidal granular flows

This appendix outlines the main steps of the algorithm, originally proposed in [42], that has been used for the computations of Chapter 2. This algorithm is a fractional-step two-phase projection method,based on a generalization of the classical Chorin-Temam approach [70, 71]. The governing equations (2.1)–(2.6), expressing the model of [26] for the case of constant density, constitute a superset of the incompressible Navier-Stokes equations and share a similar structure; in particular, equation (2.3) predicts the velocity of the granular phase to be solenoidal. It has been shown in [42] that a suitable generalization of the projection method, based on Ladyzhenskaya's decomposition theorem, [161], can be succesfully applied to equations (2.1)–(2.6).

## A.1 Selection of unknown variables

Projection algorithms for the Navier-Stokes equations typically solve these equations for the velocity and pressure unknowns. One can in principle proceed along these lines and attempt to solve (2.1)–(2.6) for the phasial velocities $\mathbf{u}_f$ and $\mathbf{u}_s$, the phasial pressures $p_f$ and $p_s$ and volume fractions $\phi_s$ and $\phi_f$. However, as thoroughly discussed in [42], such choice might not be desirable for a number of reasons. Most notably, the momentum equations (2.2) and (2.4) contain the non-conservative product $p_f \nabla \phi_s$ on the right-hand side; this can jeopardize the performance of a projection method because, in general, $p_f$ is not bounded in the $L^\infty$-norm; cf. [161] for theoretical and [77] for numerical evidence. In addition, hydrostatic pressure due to gravity is often a dominant term for stratified flows, so that it is useful to remove this component from the phasial pressures before solving the system. To this end, the system

The content of this Appendix has been published in: C. Varsakelis, D. Monsorno, and M.V. Papalexandris, (2015), "Projection methods for two-velocity, two-pressure models for flows of heterogeneous mixtures", *Computers & Mathematics with Applications*, Vol.70, pp. 1024-1045.

(2.1)–(2.6) can be rearranged. More specifically, one can define the auxiliary variables $p$ and $p'_f$ as follows,

$$p = \frac{(p_s - p_f)\phi_s}{\rho_s}, \qquad p'_f = p_f - \rho_f \Phi, \quad \text{with} \quad \nabla\Phi = \rho_f \mathbf{g}. \tag{A.1}$$

The system (2.1)–(2.6) can then be cast into the following equations for the unknowns $\mathbf{u}_f$, $\mathbf{u}_s$, $p'_f$, $p$, $\phi_f$ and $\phi_s$,

$$\begin{aligned}
\nabla \cdot (\phi_f(\mathbf{u}_s - \mathbf{u}_f)) \ &= 0\,, && \text{(A.2)}\\
\frac{\partial \phi_f \mathbf{u}_f}{\partial t} + \nabla \cdot (\phi_f \mathbf{u}_f \otimes \mathbf{u}_f) + \phi_f \nabla p'_f \ &= \frac{1}{\mathrm{Re}} \nabla \cdot (2\phi_f\, \mathbf{V}_f^d) \\
&\quad - \delta\,(\mathbf{u}_f - \mathbf{u}_s)\,, && \text{(A.3)}\\
\nabla \cdot \mathbf{u}_s \ &= 0\,, && \text{(A.4)}\\
\frac{\partial \phi_s \mathbf{u}_s}{\partial t} + \nabla \cdot (\phi_s \mathbf{u}_s \otimes \mathbf{u}_s) + \nabla p \ &= \frac{1}{\rho_s \mathrm{Re}} \nabla \cdot (2\mu_s \phi_s\, \mathbf{V}_s^d) \\
&\quad - \nabla \cdot \left( \frac{\gamma_s}{\rho_s} \nabla\phi_s \otimes \nabla\phi_s \right) \\
&\quad - \phi_s \nabla \left( \frac{p'_f}{\rho_s} \right) + \frac{\delta}{\rho_s} (\mathbf{u}_f - \mathbf{u}_s) \\
&\quad + \left( 1 - \frac{1}{\rho_s} \right) \phi_s \boldsymbol{g}\,, && \text{(A.5)}\\
\frac{\partial \phi_s}{\partial t} + \mathbf{u}_s \cdot \nabla \phi_s \ &= 0\,, && \text{(A.6)}\\
\phi_f + \phi_s \ &= \ 1\,. && \text{(A.7)}
\end{aligned}$$

In this system the state of the fluid phase has been chosen as reference state for the non-dimensionalization, so that $\rho_f = 1$, $\mu_f = 1$.

It can be observed that in equations (A.3) and (A.5) only the gradients of the phasial pressures appear. In addition, gravity does not enter the equations for the fluid phase, and its effect is limited to a buoyancy term appearing on the right-hand side of equation (A.5); in particular, if the two phases have the same density, this term vanishes.

## A.2 Time discretization

Similarly to most projection algorithms, this algorithm is a fractional-step method. To this end it employs a second-order semi-implicit time-marching scheme; the flowchart of this scheme is summarized now for the case of an equidistant temporal mesh with time-step $\Delta t$. The superscripts $n$, and $n+1$ are used to denote values computed at time $n\,\Delta t$ and $(n+1)\Delta t$, respectively.

1) The updated value of the volume fraction $\phi_s^{n+1}$ is computed from the compaction equa-

tion (A.6),

$$\frac{\phi_s^{n+1} - \phi_s^n}{\Delta t} \;=\; -\,\mathbf{u}_s^n \cdot \nabla \phi_s^n \,. \tag{A.8}$$

2) The time-integration scheme for the granular phase has the following form,

$$\begin{aligned}\frac{\phi_s^{n+1}\mathbf{u}_s^{n+1} - \phi_s^n\mathbf{u}_s^n}{\Delta t} + \nabla p^{n+1/2} \;&= \frac{1}{\mathrm{Re}}\nabla\cdot\left(\mu_s^{n+1}\phi_s^{n+1}(\mathbf{V}_s^d)^{n+1} + \mu_s^n\phi_s^n(\mathbf{V}_s^d)^n\right) \\ &\qquad \mathbf{Res}_s^{n+1/2} + \phi_s^{n+1}\left(1 - \frac{1}{\rho_s}\right)\mathbf{g}\,,\end{aligned} \tag{A.9}$$

where $\mathbf{Res}_s$ is given by the following expression,

$$\begin{aligned}\mathbf{Res}_s \;=&\; -\,\nabla\cdot(\phi_s\mathbf{u}_s\otimes\mathbf{u}_s) + \nabla\cdot\left(\frac{\gamma_s}{\rho_s}\nabla\phi_s\otimes\nabla\phi_s\right) - \phi_s\nabla\left(\frac{p_f'}{\rho_s}\right) \\ &+ \frac{\delta}{\rho_s}\left(\mathbf{u}_f - \mathbf{u}_s\right).\end{aligned} \tag{A.10}$$

In order to avoid the inversion of the nonlinear equation (A.9) a fractional projection is employed. In a preliminary "advection–diffusion step", a provisional value of the granular velocity $\tilde{\mathbf{u}}_s$ is computed as follows,

$$\begin{aligned}\phi_s^{n+1}\tilde{\mathbf{u}}_s - \frac{\Delta t}{\mathrm{Re}}\nabla\cdot\left(\mu_s^{n+1}\phi_s^{n+1}\tilde{\mathbf{V}}_s^d\right) \;&= \phi_s^n\mathbf{u}_s^n + \frac{\Delta t}{\mathrm{Re}}\nabla\cdot\left(\mu_s^n\phi_s^n(\mathbf{V}_s^d)^n\right) \\ &\quad + \Delta t\,\mathbf{Res}_s^{n+1/2}\,.\end{aligned} \tag{A.11}$$

It can be observed from equation (A.11) that the proposed method belongs to the class of pressure-free methods.

Subsequently, the projection step is performed,

$$\phi_s^{n+1}\tilde{\mathbf{u}}_s \;=\; \phi_s^{n+1}\mathbf{u}_s^{n+1} + \Delta t\nabla q^{n+1} - \Delta t\phi_s^{n+1}\left(1 - \frac{1}{\rho_s}\right)\mathbf{g}\,. \tag{A.12}$$

The quantity $q^{n+1}$ is not the same as the pressure $p^{n+1/2}$ appearing in (A.9). Rather, it is an auxiliary numerical variable that enforces the realization of the Helmholtz decomposition and is denoted as " granular auxiliary pressure" in this Chapter. Of course, $q^{n+1}$ and $p^{n+1/2}$ are closely related; this relation is quantified below. The presence of the gravity term on the right-hand side of the above equation might come as a surprise because its presence is not customary in the literature of projection methods; typically, this term is incorporated in the computation of the provisional velocity. The rationale behind this choice is given below, when the boundary conditions of the various quantities are discussed. Moreover, it can be observed that (A.12) constitutes the Helmholtz–Marsden decomposition of the vector field $\tilde{\mathbf{u}}_s + \Delta t\left(1 - \frac{1}{\rho_s}\right)\mathbf{g}$, [156].

The granular auxiliary pressure $q^{n+1}$ is computed as the solution to the elliptic problem that emerges upon projecting equation (A.12) over the solenoidal fields. More specifically, by virtue of equation (A.4), at every time step $\nabla \cdot \mathbf{u}_s$ has to satisfy the following relation,

$$\nabla \cdot \mathbf{u}_s^{n+1} \; = 0. \tag{A.13}$$

Consequently, one can divide each member of equation (A.12) by $\phi_s$ and then take the divergence of this equation to enforce the solenoidality constraint (A.13). One can then compute $q^{n+1}$ as follows,

$$\nabla \cdot \left( \frac{1}{\phi_s^{n+1}} \nabla q^{n+1} \right) \; = \frac{\nabla \cdot \tilde{\mathbf{u}}_s}{\Delta t} \, . \tag{A.14}$$

Once the granular auxiliary pressure $q^{n+1}$ has been calculated, the granular velocity is updated via (A.12),

$$\mathbf{u}_s^{n+1} \; = \; \tilde{\mathbf{u}}_s^{n+1} - \Delta t \frac{1}{\phi_s^{n+1}} \nabla q^{n+1} + \Delta t \left( 1 - \frac{1}{\rho_s} \right) \mathbf{g} \, . \tag{A.15}$$

3) In analogy to the granular phase, the time–integration scheme for the fluid phase reads,

$$\begin{aligned} \frac{\phi_f^{n+1} \mathbf{u}_f^{n+1} - \phi_f^n \mathbf{u}_f^n}{\Delta t} + \phi_f^{n+1} \nabla p_f^{\prime n+1/2} \; &= \frac{1}{\mathrm{Re}} \nabla \cdot \left( \phi_f^{n+1} (\mathbf{V}_f^d)^{n+1} + \phi_f^n (\mathbf{V}_f^d)^n \right) \\ &\quad + \mathbf{Res}_f^{n+1/2} \, , \end{aligned} \tag{A.16}$$

where $\mathbf{Res}_f$ is given by the following expression,

$$\mathbf{Res}_f \; = \; -\nabla \cdot \left( \phi_f \mathbf{u}_f \otimes \mathbf{u}_f \right) - \delta \left( \mathbf{u}_f - \mathbf{u}_s \right) . \tag{A.17}$$

In the "advection–diffusion" step of the fluid phase, the provisional fluid velocity $\tilde{\mathbf{u}}_f$ is computed as follows,

$$\begin{aligned} \phi_f^{n+1} \tilde{\mathbf{u}}_f - \frac{\Delta t}{\mathrm{Re}} \nabla \cdot (\phi_f^{n+1} \tilde{\mathbf{V}}_f^d) \; &= \phi_f^n \mathbf{u}_f^n + \frac{\Delta t}{\mathrm{Re}} \nabla \cdot (\phi_f^n (\mathbf{V}_f^d)^n) \\ &\quad + \Delta t \, \mathbf{Res}_f^{n+1/2} \, , \end{aligned} \tag{A.18}$$

The projection step for the fluid phase assumes the following form,

$$\phi_f^{n+1} \tilde{\mathbf{u}}_f \; = \; \phi_f^{n+1} \mathbf{u}_f^{n+1} + \Delta t \phi_f^{n+1} \nabla q_f^{\prime n+1} \, , \tag{A.19}$$

where, analogously to the granular phase, $q_f'$ is the "fluid auxiliary pressure". In view of equation (A.2), the term $\nabla \cdot (\phi_s \mathbf{u}_f)$ has to satisfy the following relation,

$$\nabla \cdot (\phi_f^{n+1} \mathbf{u}_f^{n+1}) \ = \nabla \cdot (\phi_f^{n+1} \mathbf{u}_s^{n+1}). \tag{A.20}$$

Since $\mathbf{u}_s^{n+1}$ has been already updated, equation (A.20) can be used to compute the fluid auxiliary pressure directly. More precisely, the fluid auxiliary pressure is computed as the solution to the following elliptic problem,

$$\nabla \cdot (\phi_f^{n+1} \nabla q_f'^{n+1}) \ = \ \frac{\nabla \cdot (\phi_f^{n+1} \tilde{\mathbf{u}}_f)}{\Delta t} - \frac{\nabla \cdot (\phi_f^{n+1} \mathbf{u}_s^{n+1})}{\Delta t} \,. \tag{A.21}$$

Following the computation of the fluid auxiliary pressure $q_f'^{n+1}$, the fluid velocity is updated via (A.19) as follows,

$$\mathbf{u}_f^{n+1} \ = \ \tilde{\mathbf{u}}_f^{n+1} - \Delta t \nabla q_f'^{n+1} \,. \tag{A.22}$$

#### Explicit integration of the $\mathrm{Res}_\alpha$ terms

The time-marching scheme just described is essentially a Crank-Nicolson method for the integration of the viscous fluxes of both phases, which is employed in order to circumvent the following quite-restrictive parabolic-type constraint,

$$\Delta t \ \lesssim \ \min_{\alpha=s,f} \frac{\mathrm{Re} \min \Delta {x_j}^2}{\max(\mu_\alpha)} \,, \qquad j = 1, ..., 3 \,, \tag{A.23}$$

which may be become stringent since the ratio between $\mu_s$ and $\mu_f$ can be gargantuan.

On the other hand the remaining terms, expressed by the multi-component expressions $\mathbf{Res}_\alpha$ in equations (A.9) and (A.16), are evaluated explicitly at $n + 1/2$. These terms contain the convective fluxes $\nabla \cdot (\phi_\alpha \mathbf{u}_\alpha \otimes \mathbf{u}_\alpha)$ as well as source terms that describe the momentum exchange between the phases, and the divergence of the configuration stress tensor $\gamma_s \nabla \phi_s \otimes \nabla \phi_s$. Following [163], the approximation of ${\mathbf{Res_a}}^{n+1/2}$ is performed with a second-order Adams-Bashforth scheme so that,

$$\mathbf{Res}_a^{n+1/2} \ \approx \ \frac{3}{2} \mathbf{Res}_a^{n} - \frac{1}{2} \mathbf{Res}_a^{n-1} \,. \tag{A.24}$$

#### Boundary conditions

The use of a Crank-Nicolson scheme, and actually of any implicit or semi-implicit scheme, for the time integration of the viscous fluxes presumes that the provisional velocities $\tilde{\mathbf{u}}_a$ are endowed with appropriate boundary conditions. Although not frequently mentioned, the choice of proper boundary conditions for the provisional velocity in the Navier–Stokes is crucial for enforcing correct tangential boundary conditions for the true velocity and to secure second-order convergence of the pressure field in time [162].

A generalization of the analysis of [162] to equations (A.2)–(A.7) dictates that the tangential components of the provisional velocities be assigned the following boundary conditions,

$$\tilde{\mathbf{u}}_s^{n+1}|_{\partial\Omega}\cdot\boldsymbol{\tau} \;= \mathbf{u}_s^{n+1}|_{\partial\Omega}\cdot\boldsymbol{\tau} + \Delta t\frac{1}{\phi_s^{n+1}}\nabla q^{n+1}|_{\partial\Omega}\cdot\boldsymbol{\tau} - \Delta t\,(1-1/\rho_s)\,\mathbf{g}\cdot\boldsymbol{\tau}\,, \tag{A.25}$$

$$\tilde{\mathbf{u}}_f^{n+1}|_{\partial\Omega}\cdot\boldsymbol{\tau} \;= \mathbf{u}_f^{n+1}|_{\partial\Omega}\cdot\boldsymbol{\tau} + \Delta t\nabla q_f'^{n+1}|_{\partial\Omega}\cdot\boldsymbol{\tau}\,, \tag{A.26}$$

where $\boldsymbol{\tau}$ is a versor oriented as the velocity component tangential to the boundary.

The quantities $\mathbf{u}_s^{n+1}|_{\partial\Omega}\cdot\boldsymbol{\tau}$ and $\mathbf{u}_f^{n+1}|_{\partial\Omega}\cdot\boldsymbol{\tau}$ are known since they are specified as boundary conditions; $\phi_s^{n+1}$ is also known, as the volume fraction is the first variable to be updated. However, neither $q^{n+1}$ nor $q_f'^{n+1}$ are known at this stage of the algorithm and, therefore, they need to be approximated. It was shown in [163] that employing $q^n$ and $q_f'^n$ instead of $q^{n+1}$ and $q_f'^{n+1}$ in (A.25) still results in a second-order-accurate scheme; this choice is followed here. Thus, the boundary conditions for the tangential components of $\tilde{\mathbf{u}}_s$ and $\tilde{\mathbf{u}}_f$ read,

$$\tilde{\mathbf{u}}_s^{n+1}|_{\partial\Omega}\cdot\boldsymbol{\tau} \;= \mathbf{u}_{s_b}\cdot\boldsymbol{\tau} + \Delta t\frac{1}{\phi_s^{n+1}}\nabla q^{n}|_{\partial\Omega}\cdot\boldsymbol{\tau} - \Delta t\,(1-1/\rho_s)\,\mathbf{g}\cdot\boldsymbol{\tau}\,, \tag{A.27}$$

$$\tilde{\mathbf{u}}_f^{n+1}|_{\partial\Omega}\cdot\boldsymbol{\tau} \;= \mathbf{u}_{f_b}\cdot\boldsymbol{\tau} + \Delta t\nabla q'^{n}_f|_{\partial\Omega}\cdot\boldsymbol{\tau}\,. \tag{A.28}$$

On the other hand, the boundary conditions for the normal components of $\tilde{\mathbf{u}}_s$ and $\tilde{\mathbf{u}}_f$ are inherited from the Helmholtz decomposition and, in particular, from the requirement that the decomposition is orthogonal. One obtains

$$\tilde{\mathbf{u}}_s^{n+1}|_{\partial\Omega}\cdot\boldsymbol{n} \;= \mathbf{u}_s^{n+1}|_{\partial\Omega}\cdot\boldsymbol{n} \;=\; \mathbf{u}_{s_b}\cdot\mathbf{n}\,, \tag{A.29}$$

$$\tilde{\mathbf{u}}_f^{n+1}|_{\partial\Omega}\cdot\boldsymbol{n} \;= \mathbf{u}_f^{n+1}|_{\partial\Omega}\cdot\boldsymbol{n} \;=\; \mathbf{u}_{f_b}\cdot\mathbf{n}\,. \tag{A.30}$$

Finally, as regards the boundary conditions for the phasial pressures, they are directly induced by combining (A.29), (A.30) with (A.14) and (A.21), respectively. This yields,

$$\nabla q^{n+1}|_{\partial\Omega}\cdot\boldsymbol{n} \;= \phi_s^{n+1}\left(1-\frac{1}{\rho_s}\right)\mathbf{g}\cdot\mathbf{n},\,, \tag{A.31}$$

$$\nabla q_f'^{n+1}|_{\partial\Omega}\cdot\boldsymbol{n} \;= 0\,. \tag{A.32}$$

In other words, each phase is endowed with a different Neumann problem.

**Updating the pressure**

The relation of $q^n$ and $q_f'^n$ to $p^n$ and $p_f'^n$ and $p(n\Delta t)$, $p'_f(n\Delta t)$ is quite delicate and constitutes one of the most difficult parts in the analysis of projection methods. First, in the Navier–Stokes equations, the pressure term computed by projection methods typically exhibits artificial boundary layers due to the boundary conditions that it inherits from the Helmholtz decomposition, see [164] that also establishes the thickness of such layers as a function of $\Delta t$. Still, as shown in [165], the computed pressure does converge to the solution but only on the average, a type of convergence for which boundary layers are inconsequential. The manifestation of boundary layers in the pressure fields is expected herein as well.

It should now be stressed that the time-integration algorithm described in Section A.2 does not require the values of the pressures $p^{n+1/2}$, $p'^{n+1/2}$. However, knowledge of the phasial pressures is often useful; a relevant example consists of inertial rheology laws such as the $\mu(I)$-rheology of [83], which requires the pressure field as an input. In order to express the relation between $q^n$, $q_f'^n$, $p^{n+1/2}$ and $p_f'^{n+1/2}$ one has to combine (A.9) with (A.15) and (A.11) as well as (A.16) with (A.22) and (A.18), respectively; The following relations are obtained.

$$
\begin{aligned}
\nabla p^{n+\frac{1}{2}} &= \nabla q^{n+1} - \frac{\Delta \mathrm{t}}{2\mathrm{Re}} \nabla \cdot \left( \mu_s^{n+1} \phi_s^{n+1} \mathbf{Q}_s \right) && \text{(A.33)} \\
\nabla p_f'^{n+\frac{1}{2}} &= \nabla q_f'^{n+1} - \frac{\Delta \mathrm{t}}{2\mathrm{Re}\, \phi_f} \nabla \cdot \left( \mu_f^{n+1} \phi_f^{n+1} \mathbf{Q}_f \right) \,, && \text{(A.34)}
\end{aligned}
$$

where,

$$
\begin{aligned}
\mathbf{Q}_s &= \nabla \left( \frac{\nabla (q^{n+1})}{\phi_s^{n+1}} \right) + \nabla \left( \frac{\nabla (q^{n+1})}{\phi_s^{n+1}} \right)^T - \frac{2}{3} \nabla \cdot \left( \frac{\nabla (q^{n+1})}{\phi_s^{n+1}} \right) \mathbf{I} \,, \\
\mathbf{Q}_f &= \nabla \nabla q_f'^{n+1} + \left( \nabla \nabla q_f'^{n+1} \right)^T - \frac{2}{3} \nabla \cdot (\nabla q_f'^{n+1}) \mathbf{I} \,.
\end{aligned}
$$

## A.3 Spatial discretization

In order to describe spatial discretization, a uniform mesh is introduced on a rectangular domain; more precisely this mesh consists of a finite collection of equidistant 3-dimensional rectangles $K_{i,j,k}$, $i = 1, ...M_{x_1}$, $j = 1, ..., M_{x_2}$, $k = 1, ..., M_{x_3}$, lexicographically ordered with respect to the Cartesian coordinates of their cell centers $(x_{1_i}, x_{2_j}, x_{3_k})$. The length of the cells in each dimension is denoted by $\Delta x_1$, $\Delta x_2$ and $\Delta x_3$, respectively. Throughout this Section, the following standard notation convention is adopted: for every quantity $f$,

$$
\begin{aligned}
f(i,j,k) &\equiv f(x_{1_i}, x_{2_j}, x_{3_k}) \,, && \text{(A.35)} \\
f(i \pm \tfrac{1}{2}, j \pm \tfrac{1}{2}, k \pm \tfrac{1}{2}) &\equiv f(x_{1_i} \pm \tfrac{\Delta x_1}{2}, x_{2_j} \pm \tfrac{\Delta x_2}{2}, x_{3_j} \pm \tfrac{\Delta x_3}{2}) \,. && \text{(A.36)}
\end{aligned}
$$

Further, two discrete operators are introduced. First, the finite-difference operator acting on a function $f(x_{1_i}, x_{2_j}, x_{3_k})$. When applied to the $x_1$-direction is given by,

$$
\frac{\delta_n f(i,j,k)}{\delta x_1} = \frac{f(x_{1_i} + n\frac{\Delta x_1}{2}, x_{2j}, x_{3_k}) - f(x_{1i} - n\frac{\Delta x_1}{2}, x_{2j}, x_{3k})}{n \Delta x_1} \,. \qquad \text{(A.37)}
$$

Second, the linear interpolation operator, whose action along the $x_1$-direction reads,

$$\overline{f}^{nx_1}(i,j,k) \; = \frac{f(x_{1_i} + n\frac{\Delta x_1}{2}, x_{2_j}, x_{3_k}) + f(x_{1_i} - n\frac{\Delta x_1}{2}, x_{2_j}, x_{3_k})}{2} \,. \tag{A.38}$$

Expressions for the above operators acting on the other directions can be directly obtained by symmetry.

**Compaction equation & regularization**

The accurate and efficient integration of the compaction equation (A.6) is of profound importance for the overall performance of the numerical method; this algorithm employs the Corner-Transport-Upwind (CTU) algorithm proposed in [166]. This well-known algorithm constitutes a second-order generalization of the standard upwind scheme to multiple dimensions.

From a formal standpoint, the volume fraction $\phi_s$ is, generally, a discontinuous function; even from a physical standpoint experience shows that this quantity can exhibit very sharp variations, for instance in the case of stratified flows. In turn, this can trigger severe numerical instabilities that may not be remedied unless a prohibitively small time–step $\Delta t$ is adopted. Moreover, from the analysis point of view, there is no *a priori* guarantee that such discontinuities will not affect the well–posedness of the equations of interest. For these reasons, a treatment of these instabilities and hence the avoidance of such well-posedness issues is performed with a regularization method.

The idea behind any regularization method is to replace the values of the discontinuous function in the vicinity of the discontinuity by those of a smoother, and preferably compactly supported, one. These methods, usually referred to as *diffuse–interface* methods, are backed with a solid theoretical framework; see, for example, the recent discussions of [167, 168] and references therein. This asserts that the perturbations induced by the use of the regularization lead to well-posed problems whilst the corresponding numerical schemes converge to the original solutions as the support of the regularization approaches zero.

However, despite their conceptual simplicity, regularization methods are not easy to implement when the interface is multi-dimensional and time-evolving. Moreover, the width of the regularization and its dependence on the spatial resolution of the numerical method remain a contentious topic, [77, 169].

In the present case a very simple regularization technique is employed, which is easy to implement and able to treat complicated geometries: the so-called parabolic regularization. More specifically, at every step of the algorithm, and following the update of the volume fraction $\phi_s^{n+1}$, the next sequence of operations is performed.

1) For every computational cell $K_{ijk}$, the differences between the value of $\phi_s^{n+1}$ in $K$ with the values of $\phi_s^{n+1}$ in the adjacent cells $|\phi_s^{n+1}(K_{ijk}) - \phi_s^{n+1}(K')|$ , is computed,

*i.e.* compute for all cells $K'$ that possess a common face with $K_{ijk}$. An interface exists in the direction normal to the common face of $A$ and $B$ if,

$$|\phi_s^{n+1}(K_{ijk}) - \phi_s^{n+1}(K')| > \delta\,,$$

where $\delta > 0$ is the parameter that differentiates between a discontinuity and a regular transition.

2) Regularized values $\phi_s^r$ are computed by iterating the following parabolic problem,

$$\frac{\phi_s^{r+1} - \phi_s^r}{\Delta t} = \epsilon\, \nabla^2 \phi_s^r\,, \tag{A.39}$$

$$\phi_s^0 = \phi_s^{n+1}\,, \tag{A.40}$$

where $\epsilon$ is a suitably chosen regularization parameter until,

$$|\phi_s^{r+1}(K_{ijk}) - \phi_s^{r+1}(K')| \;\leq\; \delta\,, \quad \forall K_{ijk}. \tag{A.41}$$

3) The regularized values $\phi_s^{r+1}$ are used as updated values of the volume fraction.

**Convective fluxes and odd-even decoupling instability**

The numerical computations discussed in Chapter 2 have been performed on a collocated grid. It is well known that this type of spatial discretization requires additional treatment in order to cope with the odd-even decoupling numerical instability. In this case a particular interpolation of the convective fluxes is employed, the so-called Rhie-Chow interpolation, which addresses this issue in a systematic way [170–174].

The core idea is to compute the velocity at the cell interfaces by combining values of both the velocity and the gradient of the pressure. In this case, an interpolation scheme can be deduced from equations (A.12) and (A.19). Indeed, conservation of momentum dictates that (A.12) and (A.19) are valid both at the cell centers and interfaces. For the sake of brevity, the consequences of this fact are listed below for an interface normal to the $(x_1, x_2)$ plane. At such interface, equations (A.12) and (A.19) assume the following form,

$$\begin{aligned}\phi_s^n(i,j,k\pm\tfrac{1}{2})u_{s3}^n(i,j,k\pm\tfrac{1}{2}) &= \phi_s^n(i,j,k\pm\tfrac{1}{2})\tilde{u}_{s3}^n(i,j,k\pm\tfrac{1}{2}) \\ &\quad - \Delta t\frac{\partial q^n}{\partial x_3}(i,j,k\pm\tfrac{1}{2}) \\ &\quad + \Delta t\left(1 - \frac{1}{\rho_s}\right)\phi_s^n(i,j,k\pm\tfrac{1}{2})\mathbf{e}_3\cdot\mathbf{g}\,, \end{aligned} \tag{A.42}$$

$$\begin{aligned}\phi_f^n(i,j,k\pm\tfrac{1}{2})u_{f3}^n(i,j,k\pm\tfrac{1}{2}) &= \phi_f^n(i,j,k\pm\tfrac{1}{2})\tilde{u}_{f3}^n(i,j,k\pm\tfrac{1}{2}) \\ &\quad - \Delta t\phi_f^n(i,j,k\pm\tfrac{1}{2})\frac{\partial q_f'^n}{\partial x_3}(i,j,k\pm\tfrac{1}{2})\,. \end{aligned} \tag{A.43}$$

The quantities on the right-hand side of the above equations can be approximated as follows,

$$\phi_s^n(i,j,k\pm\tfrac{1}{2})\tilde{u}_{s_3}^n(i,j,k\pm\tfrac{1}{2}) \approx \overline{\phi_s^n(i,j,k\pm\tfrac{1}{2})\,\tilde{u}_{s_3}^n(i,j,k\pm\tfrac{1}{2})}^{1x_3}\,, \tag{A.44}$$

$$\phi_f^n(i,j,k\pm\tfrac{1}{2})\tilde{u}_{f_3}^n(i,j,k\pm\tfrac{1}{2}) \approx \overline{\phi_f^n(i,j,k\pm\tfrac{1}{2})\,\tilde{u}_{f_3}^n(i,j,k\pm\tfrac{1}{2})}^{1x_3}\,, \tag{A.45}$$

$$\frac{\partial q^n}{\partial x_3}(i,j,k\pm\tfrac{1}{2}) \approx \frac{\delta^1 q^n(i,j,k\pm\tfrac{1}{2})}{\delta x_3}\,, \tag{A.46}$$

$$\phi_f^n(i,j,k\pm\tfrac{1}{2})\frac{\partial q_f'^n}{\partial x_3}(i,j,k\pm\tfrac{1}{2}) \approx \overline{\phi_f^n(i,j,\pm\tfrac{1}{2})}^{1x_3}\,\frac{\delta^1 q_f'^n(i,j,k\pm\tfrac{1}{2})}{\delta x_3}\,, \tag{A.47}$$

$$\phi_s^n(i,j,k\pm\tfrac{1}{2})\mathbf{e}_3\cdot\mathbf{g} \approx \overline{\phi_s^n(i,j,k\pm\tfrac{1}{2})}^{1x_3}\mathbf{e}_3\cdot\mathbf{g}\,. \tag{A.48}$$

Next, the following short-hand notation is introduced,

$$\begin{aligned} M_s^3(i,j,k\pm\tfrac{1}{2}) &= \overline{\phi_s^n(i,j,k\pm\tfrac{1}{2})\,\tilde{u}_{s_3}^n(i,j,k\pm\tfrac{1}{2})}^{1x_3} - \Delta t\frac{\delta^1 q^n(i,j,k\pm\tfrac{1}{2})}{\delta x_3} \\ &\quad + \Delta t\left(1-\frac{1}{\rho_s}\right)\overline{\phi_s^n(i,j,\pm\tfrac{1}{2})}^{1x_3}\mathbf{e}_3\cdot\mathbf{g}\,, \end{aligned} \tag{A.49}$$

$$\begin{aligned} M_f^3(i,j,k\pm\tfrac{1}{2}) &= \overline{\phi_f^n(i,j,k\pm\tfrac{1}{2})\,\tilde{u}_{f_3}^n(i,j,k\pm\tfrac{1}{2})}^{1x_3} \\ &\quad - \Delta t\overline{\phi_f^n(i,j,k\pm\tfrac{1}{2})}^{1x_3}\,\frac{\delta^1 q_f'^n(i,j,\pm\tfrac{1}{2})}{\delta x_3}\,. \end{aligned} \tag{A.50}$$

Then, by combining (A.42), (A.43) with (A.49) and (A.50), one readily obtains the following interpolation for $\phi_a\mathbf{u}_a$,

$$\phi_s(i,j,k\pm\tfrac{1}{2})u_{s_3}(i,j,k\pm\tfrac{1}{2}) \approx M_s^3(i,j,k\pm\tfrac{1}{2})\,, \tag{A.51}$$

$$\phi_f(i,j,k\pm\tfrac{1}{2})u_{f_3}(i,j,k\pm\tfrac{1}{2}) \approx M_f^3(i,j,k\pm\tfrac{1}{2})\,. \tag{A.52}$$

The quantities $M_\alpha^1(i,j,k)$ and $M_\alpha^2(i,j,k)$ can be defined by direct analogy. Then, the final expressions for cell interfaces normal to the other planes assume the following form,

$$\phi_\alpha(i\pm\tfrac{1}{2},j,k)u_{\alpha_3}(i\pm\tfrac{1}{2},j,k) \approx M_\alpha^1(i\pm\tfrac{1}{2},j,k)\,, \tag{A.53}$$

$$\phi_\alpha(i,j\pm\tfrac{1}{2},k)u_{\alpha_3}(i,j\pm\tfrac{1}{2},k) \approx M_\alpha^2(i,j\pm\tfrac{1}{2},k)\,,\quad \alpha=s,f\,. \tag{A.54}$$

The interpolation scheme provided by equations (A.51)–(A.54) introduces a coupling between the phasial velocities and pressures that is sufficient to remedy the odd-even decoupling problem. In particular, the divergence theorem is applied on an arbitrary cell $K_{ijk}$, which yields,

$$\int_{K_{i,j,k}} \nabla\cdot(\phi_\alpha\mathbf{u}_\alpha\otimes\mathbf{u}_\alpha)\mathrm{d}\mathbf{x} = \int_{\partial K_{i,j,k}} \phi_\alpha\mathbf{u}_\alpha\otimes\mathbf{u}_\alpha\cdot\,\mathrm{d}\mathbf{S}\,,\quad \alpha=s,f\,. \tag{A.55}$$

Then, by combining (A.51)–(A.54) with the right-hand side of (A.55), the following discretization scheme for the convective fluxes is obtained,

$$\int_{\partial K_{i,j,k}} \phi_\alpha \mathbf{u}_\alpha \otimes \mathbf{u}_\alpha \cdot \mathrm{d}\mathbf{S} \approx \frac{M^1_\alpha(i+\frac{1}{2},j,k)\overline{\mathbf{u}}^{1x_1}_\alpha(i+\frac{1}{2},j,k) - M^1_\alpha(i-\frac{1}{2},j,k)\overline{\mathbf{u}}^{1x_1}_\alpha(i-\frac{1}{2},j,k)}{\Delta x_1} + \frac{M^2_\alpha(i,j+\frac{1}{2},k)\overline{\mathbf{u}}^{1x_2}_\alpha(i,j+\frac{1}{2},k) - M^2_\alpha(i,j-\frac{1}{2},k)\overline{\mathbf{u}}^{1x_2}_\alpha(i,j-\frac{1}{2},k)}{\Delta x_2} + \frac{M^3_\alpha(i,j,k+\frac{1}{2})\overline{\mathbf{u}}^{1x_3}_\alpha(i,j,k+\frac{1}{2}) - M^3_\alpha(i,j,k-\frac{1}{2})\overline{\mathbf{u}}^{1x_3}_\alpha(i,j,k-\frac{1}{2})}{\Delta x_3} . \tag{A.56}$$

### Viscous fluxes

For the discretization of the viscous fluxes, conservative second-order finite differences are employed; this is the typical choice in the literature of projection methods. The only matter of debate concerns the computation of the phasial partial viscosities $\mu_s\phi_s$ and $\mu_f\phi_f$ at the cell interfaces. Indeed, these functions support considerable variations. Further, $\mu_s$, which accounts for the rheology of the granular material, is nonlinear in the volume fraction $\phi_s$ and can become arbitrarily large near the jamming limit. Consequently, the appropriateness of using standard linear interpolation should be put under scrutiny, [183]. In the results of Chapter 2, both linear and harmonic interpolations have been tested. However, the numerical results have indicated that the differences in the performances of both interpolations are minor for the flows under examination.

### Configuration stress tensor

The divergence of the configuration stress tensor $\nabla \cdot (\gamma_s \nabla\phi_s \otimes \nabla\phi_s)$ is a highly nonlinear differential operator and, as such, its discretization requires particular attention. Herein the following identity is employed,

$$\nabla \cdot (\gamma_s \nabla\phi_s \otimes \nabla\phi_s) = \left(\nabla \cdot (\gamma_s \nabla\phi_s)\mathbf{I} + \gamma_s \mathbf{H}(\phi_s)\right)\nabla\phi_s \, , \tag{A.57}$$

where $\mathbf{H}(\phi_s)$ is the Hessian of $\phi_s$; the discretization is then performed as follows. The diagonal tensor $\nabla \cdot (\gamma_s \nabla\phi_s)\mathbf{I}$ is approximated via the divergence theorem,

$$\begin{aligned}
&\nabla \cdot (\gamma_s(i,j,k)\nabla\phi_s(i,j,k))\mathbf{I} \simeq \\
&\left( \frac{\overline{\gamma}^{1x_1}(i+\frac{1}{2},j,k)\frac{\delta^1\phi_s(i+\frac{1}{2},j,k)}{\delta x_1} - \overline{\gamma_s}^{1x_1}(i-\frac{1}{2},j,k)\frac{\delta^1\phi_s(i-\frac{1}{2},j,k)}{\delta x_1}}{\Delta x_1} \right. \\
&+ \frac{\overline{\gamma_s}^{1x_2}(i,j+\frac{1}{2},k)\frac{\delta^1\phi_s(i,j+\frac{1}{2},k)}{\delta x_2} - \overline{\gamma_s}^{1x_2}(i,j-\frac{1}{2},k)\frac{\delta^1\phi_s(i,j-\frac{1}{2},k)}{\delta x_2}}{\Delta x_2} \\
&\left. + \frac{\overline{\gamma_s}^{1x_3}(i,j,k+\frac{1}{2})\frac{\delta^1\phi_s(i,j,k+\frac{1}{2})}{\delta x_3} - \overline{\gamma_s}^{1x_3}(i,j,k-\frac{1}{2})\frac{\delta^1\phi_s(i,j,k-\frac{1}{2})}{\delta x_3}}{\Delta x_3} \right) \mathbf{I} \, .
\end{aligned} \tag{A.58}$$

Both the diagonal and the off-diagonal components of the Hessian operator $\mathbf{H}(\phi_s)$ are approximated via cell centered, second-order finite differences. Finally, the multiplier $\nabla\phi_s$ is also approximated via the divergence theorem as follows,

$$\begin{pmatrix} \frac{\partial \phi_s(i,j,k)}{\partial x_1} \\ \frac{\partial \phi_s(i,j,k)}{\partial x_2} \\ \frac{\partial \phi_s(i,j,k)}{\partial x_3} \end{pmatrix} \approx \begin{pmatrix} \frac{1}{2}\left(\frac{\delta^1\phi_s(i+\frac{1}{2},j,k)}{\delta x_1} + \frac{\delta^1\phi_s(i-\frac{1}{2},j,k)}{\delta x_1}\right) \\ \frac{1}{2}\left(\frac{\delta^1\phi_s(i,j+\frac{1}{2},k)}{\delta x_2} + \frac{\delta^1\phi_s(i,j-\frac{1}{2},k)}{\delta x_2}\right) \\ \frac{1}{2}\left(\frac{\delta^1\phi_s(i,j,k+\frac{1}{2})}{\delta x_3} + \frac{\delta^1\phi_s(i,j,k-\frac{1}{2})}{\delta x_3}\right) \end{pmatrix} \tag{A.59}$$

# Appendix B

# A simple algorithm for steady one-dimensional flow

This appendix outlines the main steps of the algorithm that has been used for the computations of Chapter 4, and more precisely for the integration of the system (4.6)–(4.9). It is an iterative under-relaxation method that employs second-order centered differences for the computation of the differential operators.

1. First-guess values are introduced for the unknown $u_f$, $u_s$, $p_s$, $\phi_s$,

$$u_f = 0,\ u_s = 0,\ \phi_s = \overline{\phi}_s,\ p_s = \beta_s(\overline{\phi}_s), \tag{B.1}$$

   where $\overline{\phi}_s$ is the average granular volume fraction.

2. An intermediate value ${\phi_s}^\star$ is computed for the volume fraction from the compaction equation (4.9), via the following semi-implicit scheme,

$$\begin{aligned}&\left(\gamma_{s_i}^{\,n} + \gamma_{s_{i+1}}^{\,n}\right) \phi_{s_{i+1}}^{\,\star} - \\ &\left(\gamma_{s_{i+1}}^{\,n} + 2\gamma_{s_i}^{\,n} + \gamma_{s_{i-1}}^{\,n}\right) \phi_{s_i}^{\,\star} + \\ &\left(\gamma_{s_{i-1}}^{\,n} + \gamma_{s_i}^{\,n}\right) \phi_{s_{i-1}}^{\,\star} = \\ &-2(\Delta y)^2 \left(p_s - \beta_s\right)_i^n \ .\end{aligned} \tag{B.2}$$

   The superscript $n$ represents the iteration number and the index $i$ refers to the computational point.

3. An intermediate value ${u_f}^\star$ is computed for the fluid velocity from equation (4.6) via

the following semi-implicit discretization,

$$
\begin{aligned}
&- \left({\phi_s}_i^n + {\phi_s}_{i+1}^n\right) {u_f}_{i+1}^\star + \\
&\left({\phi_s}_{i+1}^n + 2{\phi_s}_i^n + {\phi_s}_{i-1}^n\right) {u_f}_i^\star - \\
&\left({\phi_s}_{i-1}^n + {\phi_s}_i^n\right) {u_f}_{i-1}^\star = \\
&2\,\mathrm{Re}\,(\Delta y)^2 \left(\delta(u_f - u_s) - F\,(1-\phi_s)\right)_i^n \;. \qquad \text{(B.3)}
\end{aligned}
$$

4. Similarly, an intermediate value ${u_s}^\star$ is computed for the velocity of the granular phase from (4.7) via the following discretization,

$$
\begin{aligned}
&\left((\mu_s\phi_s)_i^n + (\mu_s\phi_s)_{i+1}^n\right) {u_s}_{i+1}^\star - \\
&\left((\mu_s\phi_s)_{i+1}^n + 2(\mu_s\phi_s)_i^n + (\mu_s\phi_s)_{i-1}^n\right) {u_s}_i^\star + \\
&\left((\mu_s\phi_s)_{i-1}^n + (\mu_s\phi_s)_i^n\right) {u_s}_{i-1}^\star = \\
&-2\,\mathrm{Re}\,(\Delta y)^2 \left(\delta(u_f - u_s) + F\,\phi_s\right)_i^n \;. \qquad \text{(B.4)}
\end{aligned}
$$

5. An intermediate value ${p_s}^\star$ is computed for the granular pressure from equation (4.8). First the combined term $(p_s\phi_s)_i^\star$ is computed via quadrature of (4.8). Then the value of ${p_s}^\star$ follows from

$$
{p_s}_i^\star = \frac{(p_s\phi_s)_i^\star}{{\phi_s}_i^n}. \qquad \text{(B.5)}
$$

6. The relative error $\epsilon$ in the $l_2$-norm of the unknown variables is computed. For example, for $\phi_s$,

$$
\epsilon = \frac{||{\phi_s}^\star - {\phi_s}^n||_2}{||{\phi_s}^n||_2}. \qquad \text{(B.6)}
$$

7. The magnitude of the error is checked. The iterative procedure terminates when the relative error for all variables is smaller than a treshold value.

8. If the convergence criterion is not met, the variables are upgraded for the next iteration step $n+1$, with a small under-relaxation parameter $\lambda$ that is used to control convergence. For example, for $\phi_s$,

$$
{\phi_s}_i^{n+1} = (1-\lambda)\,{\phi_s}_i^n + \lambda\,{\phi_s}_i^\star. \qquad \text{(B.7)}
$$

# Bibliography


[1] J. Duran. *Sands, Powders, and Grains: An Introduction to the Physics of Granular Materials*. Springer, 2000.

[2] H.M. Jaeger and S.R. Nagel. Physics of the Granular State. *Science*, 255:1523–1531, 1992.

[3] P. Richard, M. Nicodemi, P. Ribière R. Delannay, and D. Bideau. Slow relaxation and compaction of granular systems. *Nat. Mater.*, 4:121–128, 2005.

[4] O. Reynolds. On the Dilatancy of Media composed of Rigid Particles in Contact, With Experimental Illustrations. *Phil. Mag.*, 20:469–481, 1885.

[5] H.M. Jaeger, S.R. Nagel, and R.P. Behringer. Granular solids, liquids, and gases. *Rev. Mod. Phys.*, 68:1259–1273, 1996.

[6] S. Matsusaka, H. Maruyama, T. Matsuyama, and M. Gadhiri. Triboelectric charging of powders: A review. *Chem. Eng. Sci.*, 65:5781–5807, 2010.

[7] H. Grosshans and M.V. Papalexandris. Direct numerical simulation of triboelectric charging in particle-laden turbulent channel flows. *J. Fluid Mech.*, 818:465–491, 2017.

[8] S. Herminghaus. *Wet Granular Matter: A Truly Complex Fluid*. World Scientific Publishing, 2013.

[9] X. Yan, Q. Shi, M. Hou, K. Lu, and C.K. Chan. Effects of Air on the Segregation of Particles in a Shaken Granular Bed. *Phys. Rev. Lett.*, 91:014302, 2003.

[10] M.E. Möbius, X. Cheng, G.S. Karczmar, S.R. Nagel, and H.M. Jaeger. Intruders in the Dust: Air-Driven Granular Size Separation. *Phys. Rev. Lett.*, 93:198001, 2004.

[11] G. Caballero, R. Bergmann, D. van der Meer, A. Prosperetti, and D. Lohse. Role of Air in Granular Jet Formation. *Phys. Rev. Lett.*, 99:018001, 2007.

[12] T. Homan, C. Gjaltema, and D. van der Meer. Collapsing granular beds: The role of interstitial air. *Phys. Rev. E*, 89:052204, 2014.

[13] J.E. Brady and F. Senese. *Chemistry Matter and Its Changes*. Wiley, 2004.

[14] I. Krieger and T. Dougherty. A mechanism for non-newtonian flow in suspensions of rigid spheres. *Trans. of the Soc. of Rheol.*, III:137–152, 1959.

[15] D. Quemada. Rheology of concentrated disperse systems II. A model for non-newtonian shear viscosity in steady flows. *Rheol. Acta*, 17:632–642, 1978.

[16] J.J. Stickel and R.L. Powell. Fluid mechanics and rheology of dense suspensions. *Annu. Rev. Fluid Mech.*, 37:129–149, 2005.

[17] J. Mewis and N.J. Wagner. Current trends in suspension rheology. *J. Non-Newton. Fluid*, 157:147 – 150, 2009.

[18] J. Mewis and N.J. Wagner. *Colloidal Suspension Rheology*. Cambridge University Press, 2012.

[19] P. Nott and J.F. Brady. Pressure-driven flow of suspensions: simulation and theory. *J. Fluid Mech.*, 275:157–199, 1994.

[20] K. Yeo and M. Maxey. Numerical simulations of concentrated suspensions of monodisperse particles in a poiseuille flow. *J. Fluid Mech.*, 682:491–518, 2011.

[21] A. Lefebvre-Lepot, B. Merlet, and T. N. Nguyen. An accurate method to include lubrication forces in numerical simulations of dense Stokesian suspensions. *J. Fluid Mech.*, 769:369–386, 2015.

[22] D.J. Pine, J.P. Gollub, J.F. Brady, and A.M. Leshanky. Chaos and threshold for irreversibility in sheared suspensions. *Nature*, 438:997–1000, 2005.

[23] I.M. Janosi, T. Tel, D.E. Wolf, and J.A.C. Gallas. Chaotic particle dynamics in viscous flows: The three-particle Stokeslet problem. *Phys. Rev. E*, 56:2858–2868, 1997.

[24] M.M. Denn and J.F. Morris. Rheology of non-brownian suspensions. *Annu. Rev. Chem. Biomol. Eng.*, 5:203–228, 2014.

[25] D. Gidaspow. *Multiphase flow and fluidization: continuum and kinetic theory descriptions*. Academic Press, 1994.

[26] M.V. Papalexandris. A two-phase model for compressible granular flows based on the theory of irreversible processes. *J. Fluid Mech.*, 517:103–112, 2004.

[27] M.A. Goodman and S.C. Cowin. A Continuum Theory for Granular Materials. *Arch. Rat. Mech. Anal.*, 44:249–266, 1972.

[28] S.L. Passman, J.W. Nunziato, P.B. Bailey, and K. Reed. Shearing motion of a fluid-saturated granular material. *J. Rheol.*, 20:167–192, 1986.

[29] J.B. Bdzil, R. Menikoff, S.F. Son, A.K. Kapila, and D.S. Stewart. Two-phase modelling of deflagration-to-detonation transition in granular materials: A critical examination of modelling issues. *Phys. Fluids*, 11:378–492, 1999.

[30] Y. Wang and K. Hutter. A constitutive model of multiphase mixtures and its application in shearing flows of saturated solid-fluid mixtures. *Granul. Matter*, 73:163–181, 1999.

[31] A.D. Drew and S.L. Passman. *Theory of Multicomponent Fluids*. Springer, 1999.

[32] C.E. Brennen. *Fundamentals of multiphase flow*. Cambridge Univ. Press, 2005.

[33] L.C. Van Rijn. *Principles of Sediment Transport in Rivers, Estuaries and Coastal Seas*. Aqua Publications, 1993.

[34] R. Bagnold. An empirical correlation of bedload transport rates in flumes and natural rivers. *Proc. R. Soc. Lond. A*, 372:453–473, 1980.

[35] Y. Zech, S. Soares-Frazão, B. Spinewine, C. Savary, and L. Goutière. Inertia effects in bed-load transport models. *Can. J. Civ. Eng.*, 36:1587–1597, 2009.

[36] G.A. Leftheriotis and A.A. Dimas. Coupled simulation of oscillatory flow, sediment transport and morphology evolution of ripples based on the immersed boundary method. In *ASME 2014 33rd International Conference on Ocean, Offshore and Arctic Engineering* , June 2014.

[37] H. Rouse. An analysis of sediment transport in the light of fluid turbulence. *Soil Conservation Service, Rep. SCS-TP*, 25, 1939.

[38] S. Soares-Frazão, R. Canelas, Z. Cao, L. Cea, H.M. Chaudhry, A. Die Moran, K. El Kadi, R. Ferreira, I.F. Cadórniga, N. Gonzalez-Ramirez, M. Greco, W. Huang, J. Imran, J. Le Coz, R. Marsooli, A. Paquier, G. Pender, M. Pontillo, J. Puertas, B. Spinewine, C. Swartenbroekx, R. Tsubaki, C. Villaret, W. Wu, Z. Yue, and Y. Zech. Dam-break flows over mobile beds: experiments and benchmark tests for numerical models. *J. Hydraul. Res.*, 50:364–375, 2012.

[39] L. Ouriemi, P. Aussillous, and E. Guazzelli. Sediment dynamics. Part 1. Bed–load transport by laminar shearing flows. *J. Fluid Mech.*, 636:295–319, 2009.

[40] T. Revil-Baudard and J. Chauchat. A two-phase model for sheet flow regime based on dense granular flow rheology. *J. Geophys. Res.: Oceans*, 118:619–634, 2013.

[41] F. Chiodi, P. Claudin, and B. Andreotti. A two-phase flow model of sediment transport: transition from bedload to suspended load. *J. Fluid Mech.*, 755:561–581, 2014.

[42] C. Varsakelis, D. Monsorno, and M.V. Papalexandris. Projection methods for two velocity-two pressure models for flows of heterogeneous mixtures. *Comput. Math. Appl.*, 70:1024–1045, 2015.

[43] C. Aussillous, J. Chauchat, M. Pailha, M. Médale, and E. Guazzelli. Investigation of the mobile granular layer in bedload transport by laminar shearing flows. *J. Fluid Mech.*, 736:594–615, 2013.

[44] M. Houssais, C.P. Ortiz, D.J. Durian, and D.J. Jerolmack. Onset of sediment transport is a continuous transition driven by fluid shear and granular creep. *Nature Communications*, 6, 2015.

[45] R. Jackson. Locally averaged equations of motion for a mixture of identical spherical particles and a newtonian fluid. *Chem. Eng. Sci.*, 52:2457–2469, 1997.

[46] GDR MiDi. On dense granular flow. *Eur. Phys. J. E*, 14:341—-365, 2004.

[47] J.J. Stickel, R.J. Phillips, and R.L. Powell. A constitutive model for microstructure and total stress in particulate suspensions. *J. Rheol.*, 50:379–413, 2006.

[48] M. Massoudi and M.M. Mehrabadi. A continuum model for granular materials: Considering dilatancy and the Mohr-Coulomb criterion. *Acta Mech.*, 152:121–138, 2001.

[49] I. E. Zarraga, D. A. Hill, and D. T. Leighton. The characterization of the total stress of concentrated suspensions of noncolloidal spheres in Newtonian fluids. *J. Rheol.*, 44: 185–220, 2000.

[50] A. Singh and P.R. Nott. Experimental measurements of the normal stresses in sheared stokesian suspensions. *J. Fluid Mech.*, 490:293–320, 2003.

[51] T. Moraczewski, H. Tang, and N.C. Shapley. Flow of concentrated suspensions through an abrupt axisymmetric expansion measured by nuclear magnetic resonance imaging. *J. Rheol.*, 49:1409–1428, 2005.

[52] W. Pabst, E. Gregorova, and C. Berthold. Particle shape and suspension rheology of short-fiber systems. *J. Eur. Ceram. Soc.*, 26:149–160, 2006.

[53] G. Ovarlez, F. Bertrand, and S. Rodts. Local determination of the constitutive law of a dense suspension of noncolloidal particles through magnetic resonance imaging. *J. Rheol.*, 50:259–292, 2006.

[54] S. Mueller, E.W. Llewellin, and H.M. Mader. The rheology of suspensions of solid particles. *P. Roy. Soc. London A: Math., Phys. Engn. Sc.*, 466:1201–1228, 2009.

[55] C. Gao, B. Xu, and J. F. Gilchrist. Mixing and segregation of microspheres in microchannels flows of mono- and bidispersed suspensions. *Phys. Rev. E*, 79:036311, 2009.

[56] C. Gao, S.D. Kulkarni, J.F. Morris, and J.F. Gilchrist. Direct investigation of anisotropic suspension structure in pressure-driven flow. *Phys. Rev. E*, 81:041403, 2010.

[57] F. Boyer, E. Guazzelli, and O. Pouliquen. Unifying suspension and granular rheology. *Phys. Rev. Lett.*, 107:188301, 2011.

[58] F. Boyer, O. Pouliquen, and E. Guazzelli. Dense suspensions in rotating-rod flows: normal stresses and particle migration. *J. Fluid Mech.*, 686:5–25, 2011.

[59] T. Dbouk, L. Lobry, and E. Lemaire. Normal stresses in concentrated non-brownian suspensions. *J. Fluid Mech.*, 715:239–272, 2013.

[60] R.M. Miller and J.F. Morris. Normal stress-driven migration and axial development in pressure-driven flow of concentrated suspensions. *J. Non-Newton. Fluid*, 135:149–165, 2006.

[61] P. Nott, E. Guazzelli, and O. Pouliquen. The suspension balance model revisited. *Phys. Fluids*, 23:043304, 2011.

[62] C. Varsakelis and M.V. Papalexandris. Low-Mach-number asymptotics for two-phase flows of granular materials. *J. Fluid Mech.*, 669:472–497, 2011.

[63] C. Varsakelis and M.V. Papalexandris. On the relevance of Low-Mach-number Asymptotics in Thermodynamics of Heterogeneous, Immiscible Mixtures. *J. Non-equil. Thermody.*, 42:99–112, 2017.

[64] S.R. De Groot and P. Mazur. *Non-equilibrium Thermodynamics*. Dover, 1984.

[65] D.G. Lebon, D. Jou, and J. Casas-Vázquez. *Understanding Non-equilibrium Thermodynamics: Foundations, Applications, Frontiers*. Springer, 2008.

[66] Y. Wang and K. Hutter. A constitutive theory of fluid-saturated granular materials and its application in gravitational flows. *Rheol. Acta*, 38:214–223, 1999.

[67] M.R. Baer and J.W. Nunziato. A two-phase mixture theory for the deflagration-to-detonation transition (DDT) in reactive granular materials. *Int. J. Multiphas. Flow*, 12:861–889, 1986.

[68] J.M. Powers. Two-phase viscous modeling of compaction of granular materials. *Phys. Fluids*, 16:2975–2990, 2004.

[69] G. Gallavotti. *Foundations of Fluid Dynamics*. Springer, 2002.

[70] A.J. Chorin. A numerical method for solving incompressible viscous flow problems. *J. Comput. Phys.*, 2:12–26, 1967.

[71] R. Temam. Une méthode d'approximation des solutions des équations de Navier-Stokes. *Bull. Soc. Math. France*, 98:115–152, 1968.

[72] S.B. Savage. Gravity flow of cohesionless granular materials in chutes and channels. *J. Fluid Mech.*, 92:53–96, 1979.

[73] C. Varsakelis and M.V. Papalexandris. The equilibrium limit of a constitutive model for two-phase granular mixtures and its numerical approximation. *J. Comput. Phys.*, 229:4183–4207, 2010.

[74] C. Varsakelis and M.V. Papalexandris. Numerical simulation of subaqueous chute flows of granular materials. *Eur. Phys. J. E*, 38:40, 2015.

[75] P.N. Rowe. Drag forces in a hydraulic model of a fluidised bed. Part II. *Trans. Int. Chem. Engng*, 48:175–180, 1961.

[76] A.E. Lobkovsky, A.V. Orpe, R. Molloy, A. Kudrolli, and D.H. Rothman. Erosion of a granular bed driven by laminar fluid flow. *J. Fluid Mech.*, 605:47–58, 2008.

[77] C. Varsakelis and M.V. Papalexandris. A numerical method for two-phase flows of dense granular mixtures. *J. Comput. Phys.*, 257:737–756, 2014.

[78] P.-Y. Lagrée, L. Staron, and S. Popinet. The granular column collapse as a continuum: validity of a two-dimensional Navier–Stokes model with a $\mu(I)$–rheology. *J. Fluid Mech.*, 686:378–408, 2011.

[79] E.L. Thompson and H.E. Huppert. Granular column collapses: further experimental results. *J. Fluid Mech.*, 575:177–186, 2007.

[80] L. Rondon, O. Pouliquen, and P. Aussillous. Granular collapse in a fluid: role of the initial volume fraction. *Phys. Fluids*, 23(7):073301, 2011.

[81] C. Wang, Y. Wang, C. Peng, and X. Meng. Dilatancy and compaction effects on the submerged granular column collapse. *Phys. Fluids*, 29(10):103307, 2017.

[82] F. Da Cruz, S., M. Prochnow, J.N. Roux, and F. Chevoir. Rheophysics of dense granular materials: discrete simulations of plane shear flows. *Phys. Rev. E*, 72:021309, 2005.

[83] P. Jop, Y. Forterre, and O. Pouliquen. A constitutive law for dense granular flows. *Nature*, 441:727–730, 2006.

[84] Y. Forterre and O. Pouliquen. Flows of dense granular media. *Annu. Rev. Fluid Mech.*, 40:1–24, 2008.

[85] T. Barker, D. Schaeffer, P. Bohorquez, and J. Gray. Well-posed and ill-posed behaviour of the $\mu(I)$-rheology for granular flow. *J. Fluid Mech.*, 779:794–818, 2015.

[86] D. Monsorno, C. Varsakelis, and M.V. Papalexandris. A thermomechanical model for granular suspensions. *J. Fluid Mech.*, 808:410–440, 2016.

[87] B. Svendsen and K. Hutter. On the thermodynamics of a mixture of isotropic materials with constraints. *Intl. J. Engng. Sci.*, 33:2021–2054, 1995.

[88] A. Briggs, C.C. Wang, and M. Massoudi. Flow of a dense particulate mixture using a modified form of the mixture theory. *Particul. Sci. Tech.*, 17:1–27, 1999.

[89] C. Fang, Y. Wang, and K. Hutter. A thermo-mechanical continuum theory with internal length for cohesionless granular materials. *Continuum Mech. Thermodyn.*, 17: 577–607, 2006.

[90] G.B. Wallis. *One-dimensional two-phase flow*. McGraw-Hill, 1969.

[91] H. Krier and S.S. Gokhale. Modeling of convective mode combustion through granulated propellant to predict detonation transition. *AIAA J.*, 16:177–183, 1978.

[92] P.S. Gough and F.J. Zwarts. Modeling heterogeneous two-phase reacting flow. *AIAA J.*, 17:17–25, 1979.

[93] R.J. Atkin and R.E. Craine. Continuum theories of mixtures: basic theory and historical development. *Q. J. Mech. Appl. Math.*, 29:209–244, 1976.

[94] J.H. Stuhmiller. The influence of interfacial pressure forces on the character of two-phase flow model equations. *Int. J. Multiphas. Flow*, 3:551–560, 1977.

[95] S.C. Cowin and M.A. Goodman. A variational principle for granular materials. *ZAMM - J. Appl. Math. Mech.*, 56:281–286, 1976.

[96] P. Ván. Weakly nonlocal continuum theories of granular media: restrictions from the second law. *Int. J. Solids Struct.*, 41:5921–5927, 2004.

[97] D. Leighton and A. Acrivos. The shear-induced migration of particles in concentrated suspensions. *J. Fluid Mech.*, 181:415–439, 1987.

[98] W.J. Frith, J. Mewis, and T.A. Strivens. Rheology of concentrated suspensions: experimental investigations. *Powder Technol.*, 51:27–34, 1987.

[99] J.F. Brady and G. Bossis. The rheology of concentrated suspensions of spheres in simple shear flow by numerical simulation. *J. Fluid Mech.*, 155:105–129, 1985.

[100] J.F. Brady and G. Bossis. Stokesian dynamics. *Annu. Rev. Fluid Mech.*, 20:111–157, 1988.

[101] T.N. Phung, J.F. Brady., and G. Bossis. Stokesian dynamics simulation of brownian suspensions. *J. Fluid Mech.*, 313:181–207, 1996.

[102] J.F. Brady and J.F. Morris. Microstructure of strongly sheared suspensions and its impact on rheology and diffusion. *J. Fluid Mech.*, 348:103–139, 1997.

[103] D.R. Foss and J.F. Brady. Structure, diffusion and rheology of Brownian suspensions by Stokesian Dynamics simulation. *J. Fluid Mech.*, 407:167–200, 2000.

[104] J.F. Brady. Computer simulation of viscous suspensions. *Chem. Eng. Sci.*, 56:2921–2926, 2001.

[105] A. Sierou and J.F. Brady. Rheology and microstructure in concentrated noncolloidal suspensions. *J. Rheol.*, 46:1031–1056, 2002.

[106] J.F. Brady, A.S. Khair, and M. Swaroop. On the bulk viscosity of suspensions. *J. Fluid Mech.*, 554:109–123, 2006.

[107] Y. Yurkovetsky and J.F. Morris. Particle pressure in sheared Brownian suspensions. *J. Rheol.*, 52:141–164, 2008.

[108] J.F. Morris and F. Boulay. Curvilinear flows of noncolloidal suspensions: The role of normal stresses. *J. Rheol.*, 43:1213–1237, 1999.

[109] M. Massoudi. A generalization of Reiner's mathematical model for wet sand. *Mech. Res. Commun.*, 38:378–381, 2011.

[110] M. Massoudi and P. Tran. The Couette-Poiseuille flow of a suspension modeled as a modified third-grade fluid. *Arch. Appl. Mech.*, pages 1–12, 2015.

[111] M. Trulsson, B. Andreotti, and P. Claudin. Transition from viscous to inertial regime in dense suspensions. *Phys. Rev. Lett.*, 109:118305, 2012.

[112] E.J. Hinch. The measurement of suspension rheology. *J. Fluid Mech.*, 686:1–4, 2011.

[113] K. Kamrin and G. Koval. Nonlocal constitutive relation for steady granular flow. *Phys. Rev. Lett.*, 108:178301, 2012.

[114] D.K. Henann and K. Kamrin. A predictive, size–dependent continuum model for dense granular flows. *PNAS*, 110:6730–6735, 2013.

[115] J.M.N.T. Gray and A.N. Edwards. A depth-averaged $\mu(I)$-rheology for shallow granular free-surface flows. *J. Fluid Mech.*, 755:503–534, 2014.

[116] D.L. Henann and K. Kamrin. Continuum thermomechanics of the nonlocal granular rheology. *Int. J. Plast.*, 60:145 – 162, 2014.

[117] D. Lhuillier. Internal variables and the non-equilibrium thermodynamics of colloidal suspensions. *J. Non-Newton. Fluid*, 96:19–30, 2001.

[118] Y. Wang and K. Hutter. Shearing flows in a Goodman–Cowin type granular material–Theory and numerical results. *Particul. Sci. Technol.*, 17:97–124, 1999.

[119] N. Kirchner. Thermodynamically consistent modelling of abrasive granular materials. I Non–equilibrium theory. *Proc. R. Soc. Lond. A*, 458:2015–20176, 2002.

[120] M. Massoudi. Constitutive modeling of flowing granular materials: A continuum approach. In S. J. Antony, W. Hoyle, and Y. Ding, editors, *In Granular Materials: Fundamentals and Applications,*, pages 63–107. The Royal Society of Chemistry, 2004.

[121] C. Josserand, P.-Y. Lagrée, and D. Lhuillier. Stationary shear flows of dense granular materials: A tentative continuum modelling. *Eur. Phys. J. E*, 14:127–135, 2004.

[122] C. Josserand, P.-Y. Lagrée, and D. Lhuillier. Granular pressure and the thickness of a layer jamming on a rough incline. *Europhys. Lett.*, 73:363, 2005.

[123] M.T. Cochran and J.M. Powers. Computation of compaction in compressible granular material. *Mech. Res. Commun.*, 35:96–103, 2008.

[124] W.L. Elban and M.A. Chiarito. Quasi-static compaction study of coarse HMX explosive. *Powd. Techn.*, 46:181–193, 1986.

[125] G. Mesri and B. Vardhanabhuti. Compression of granular materials. *Can. Geotech. J.*, 46:369–392, 2009.

[126] J.E. Dunn and J.B. Serrin. On the thermo-mechanics of interstitial working. *Arch. Rat. Mech. Anal.*, 88:95–133, 1985.

[127] C. Varsakelis and M.V. Papalexandris. Stability of wall bounded, shear flows of dense granular materials: the role of the Couette gap, the wall velocity and the initial concentration. *J. Fluid Mech.*, 791:384–413, 2016.

[128] C. Truesdell and W. Noll. *The Non-Linear Field Theories of Mechanics*. Springer-Verlag, 2004.

[129] Z. Fang, A. Mammoli, J.F. Brady, M. Ingber, L. Mondy, and A. Graham. Flow-aligned tensor models for suspension flows. *Int. J. Multiphas. Flow*, 28:137–166, 2002.

[130] R. Jackson. *The dynamics of fluidized particles*. Cambridge University Press, 2000.

[131] M.V. Papalexandris. Numerical simulation of detonations in mixtures of gases and solid particles. *J. Fluid Mech.*, 507:95–142, 2004.

[132] V. Deledicque and M.V. Papalexandris. An exact Riemann solver for compressible two-phase flow models containing non-conservative products. *J. Comput. Phys.*, 222: 217–245, 2007.

[133] J. K. Carson, S. J. Lovatt, D. J. Tanner, and A. C. Cleland. Thermal conductivity bounds for isotropic, porous materials. *Int. J. Heat Mass Tran.*, 48:2150–2158, 2005.

[134] P.K. Samantray, P. Karthikeyan, and K.S. Reddy. Estimating effective thermal conductivity of two-phase materials. *Int. J. Heat Mass Tran.*, 49:4209–4219, 2006.

[135] F. Soltani and Ü. Yilmazer. Slip velocity and slip layer thickness in flow of concentrated suspensions. *J. Appl. Polym. Sci.*, 70:515–522, 1998.

[136] R. Phillips, R. Armstrong, R. Brown, A. Graham, and J. Abbott. A constitutive equation for concentrated suspensions that accounts for shear-induced particle migration. *Phys. Fluids A*, 4:30–40, 1991.

[137] J.F. Brady and I.C. Carpen. Second normal stress jump instability in non-Newtonian fluids. *J. Non-Newton. Fluid*, 102:219–232, 2002.

[138] J.J. Stickel, R.J. Phillips, and R.L. Powell. Application of a constitutive model for particulate suspensions: Time-dependent viscometric flows. *J. Rheol.*, 51:1271–1302, 2007.

[139] J.F. Morris. A review of microstructure in concentrated suspensions and its implications for rheology and bulk flow. *Rheol. Acta*, 48:909–923, 2009.

[140] N. Phan-Thien. Constitutive equation for concentrated suspensions in Newtonian liquids. *J. Rheol.*, 39:679–695, 1995.

[141] H. Hinrichsen and D. E. Wolf. *The Physics of Granular Media*. Wiley-VCH, 2004.

[142] J.D. Goddard. A dissipative anisotropic fluid model for non-colloidal particle dispersions. *J. Fluid Mech.*, 568:1–17, 2006.

[143] D. Bedeaux and J.M. Rubi. Nonequilibrium thermodynamics of colloids. *Physica A*, 305:360–370, 2002.

[144] A. Karnis, H. L. Goldsmith, and S. G. Mason. The kinetics of flowing dispersions: I. concentrated suspensions of rigid particles. *J. Colloid Interf. Sci.*, 22:531–553, 1966.

[145] C.J. Koh, P. Hookham, and L.G. Leal. An experimental investigation of concentrated suspension flows in a rectangular channel. *J. Fluid Mech.*, 266:1–32, 1994.

[146] R.E. Hampton, A.A. Mammoli, A.L. Graham, N. Tetlow, and S.A. Altobelli. Migration of particles undergoing pressure-driven flow in a circular conduit. *J. Rheol.*, 41: 621–640, 1997.

[147] M.K. Lyon and L.G. Leal. An experimental study of the motion of concentrated suspensions in two-dimensional channel flow. part 1. monodisperse systems. *J. Fluid Mech.*, 363:25–56, 1998.

[148] P. Mills and P. Snabre. Rheology and structure of concentrated suspensions of hard spheres. shear induced particle migration. *J. Phys. II France*, 5:1597–1608, 1995.

[149] K. Yapici, R. L. Powell, and R. J. Phillips. Particle migration and suspension structure in steady and oscillatory plane Poiseuille flow. *Phys. Fluids*, 21:053302, 2009.

[150] S. Benyahia, M. Syamlal, and T. O'Brien. Extension of Hill-Koch-Ladd drag correlation over all ranges of Reynolds number and solids volume fraction. *Powder Technol.*, 162:166–174, 2005.

[151] M. Massoudi, K.R. Rajagopal, and T.X.Phuoc. On the fully developed flow of a dense particulate mixture in a pipe. *Powder Technol.*, 104:258–268, 1999.

[152] C. Varsakelis and M.V. Papalexandris. Stability analysis of Couette flows of spatially inhomogeneous complex fluids. *Proc. R. Soc. A*, 471:20150529, 2015.

[153] C. Varsakelis and M.V. Papalexandris. Existence of solutions to a continuum model for hydrostatics of fluid-saturated granular materials. *Appl. Math. Let.*, 35:77–81, 2014.

[154] M.A. Goodman and S.C. Cowin. Two problems in the gravity flow of granular materials. *J. Fluid Mech.*, 45:321–339, 1971.

[155] B. Lecampion and D. I. Garagash. Confined flow of suspensions modelled by a frictional rheology. *J. Fluid Mech.*, 759:197–235, 2014.

[156] J. E. Marsden. Well–posedness of the equations of a non-homogeneous perfect fluid. *Commun. Part. Diff. Eq.*, 1:215–230, 1998.

[157] F. Nicoud. Conservative high-order finite-difference schemes for low-Mach number flows. *J. Comput. Phys.*, 158:71–97, 2000.

[158] B. Lessani and M.V. Papalexandris. Time-accurate calculation of variable density flows with strong temperature gradients and combustion. *J. Comput. Phys.*, 212:218–246, 2006.

[159] P.D. Antoniadis and M.V. Papalexandris. Dynamics of shear layers at the interface of a highly porous medium and a pure fluid. *Phys. Fluids*, 27:014104, 2015.

[160] A.W. Cook and J.J. Riley. Direct numerical simulation of a turbulent reactive plume on a parallel computer. *J. Comput. Phys.*, 129:263–283, 1996.

[161] O.A. Ladyzhenskaya. *Mathematical theory of viscous, incompressible flow*. Gordon and Breach, 1969.

[162] D.L. Brown, R. Cortez, and M.L. Minion. Accurate projection methods for the incompressible Navier–Stokes equations. *J. Comput. Phys.*, 168:464 – 499, 2001.

[163] J. Kim and P. Moin. Application of a fractional step method to incompressible Navier–Stokes equations. *J. Comput. Phys.*, 59:308–323, 1985.

[164] E. Weinan and L. Jian-Guo. Projection method i: Convergence and numerical boundary layers. *SIAM J. Numer. Anal.*, 32:1017–1057, 1995.

[165] R. Temam. Remark on the pressure boundary condition for the projection method. *Theor. Comput. Fluid Dyn.*, 3:181–184, 1991.

[166] P. Colella. Multidimensional upwind methods for hyperbolic conservation laws. *J. Comput. Phys.*, 87:171–200, 1990.

[167] G. Grün. On convergent schemes for diffuse interface models for two–phase flow of incompressible fluids with general mass densities. *SIAM J. Numer. Anal.*, 51:3036–3061, 2013.

[168] H. Abels, L. Diening, and Y. Terasawa. Existence of weak solutions for a diffuse interface model of non–Newtonian two-phase flows. *Nonlinear0 Anal. Real World Appl.*, 15:149 – 157, 2014.

[169] A.-K. Tornberg and B. Engquist. Numerical approximations of singular source terms in differential equations. *J. Comput. Phys.*, 200:462–488, 2004.

[170] C.M. Rhie and W.L. Chow. Numerical study of the turbulent flow past an airfoil with trailing edge separation. *AIAA J.*, 21:1525–1532, 1983.

[171] T. Siikonen M.M. Rahman, A. Miettinen. Modified simple formulation on a collocated grid with an assessment of the simplified quick scheme. *Numer. Heat Transf. Part B, Fundam.*, 30:291–314, 1996.

[172] S.-K. Choi, S.-O. Kim, Ch.-H. Kim, and H.-K. Choi. Use of momentum interpolation method for flows with a large body force. *Numer. Heat Transf. Part B, Fundam.*, 43: 267–287, 2003.

[173] J. Mencinger and I. Zûn. On the finite volume dicretization of discontinuous body force field on collocated grids: Application to VOF method. *J. Comput. Phys.*, 221: 524–538, 2007.

[174] S. Zhang, X. Zhao, and S. Bayyuk. Generalized formulations for the Rhie–Chow interpolation. *J. Comput. Physics*, 258:880 – 914, 2014.

[175] S. Balay, S. Abhyankar, M.F. Adams, J. Brown, P. Brune, K. Buschelman, L. Dalcin, V. Eijkhout, W.D. Gropp, D. Kaushik, M.G. Knepley, L.C. McInnes, K. Rupp, B.F. Smith, S. Zampini, H. Zhang, and H.Zhang. PETSc Web page. `http://www.mcs.anl.gov/petsc`, 2017. URL `http://www.mcs.anl.gov/petsc`.

[176] S. Balay, S. Abhyankar, M.F. Adams, J.Brown, P. Brune, K. Buschelman, L. Dalcin, V. Eijkhout, W.D. Gropp, D. Kaushik, M.G. Knepley, L.C. McInnes, K. Rupp, B.F. Smith, S. Zampini, H. Zhang, and H. Zhang. PETSc users manual. Technical Report ANL-95/11 - Revision 3.8, Argonne National Laboratory, 2017. URL `http://www.mcs.anl.gov/petsc`.

[177] S. Balay, W.D. Gropp, L.C. McInnes, and B.F. Smith. Efficient Management of Parallelism in Object Oriented Numerical Software Libraries. In E. Arge, A. M. Bruaset, and H. P. Langtangen, editors, *Modern Software Tools in Scientific Computing*, pages 163–202. Birkhäuser Press, 1997.

[178] M.J. Holems, N.G. Parker, and M.J.W. Povey. Temperature dependence of bulk viscosity in water using acoustic spectroscopy. *J. Phys.: Conf. Ser.*, 269:012011, 2011.

[179] G. Lube, H.E. Huppert, R.S.J. Sparks, and M.A. Hallworth. Axisymmetric collapses of granular columns. *J. Fluid Mech.*, 508:175–199, 2004.

[180] G. Lube, H.E. Huppert, R.S.J. Sparks, and A. Freundt. Collapses of two-dimensional granular columns. *Phys. Rev. E*, 72:041301, 2005.

[181] D.G. Masson, C.B. Harbitz, R.B. Wynn, G. Pedersen, and F. Løvholt. Submarine landslides: processes, triggers and hazard prediction. *Phil. Trans. R. Soc. A*, 364: 2009–2039, 2006.

[182] F. Wang, Z. Dai, and S. Zhang. Experimental study on the motion behavior and mechanism of submarine landslides. *Bull. Eng. Geol. Environ.*, pages 1–10, 2017.

[183] K. Hayashi and A. Tomiyama. Effects of numerical treatment of viscous and surface tension forces on predicted motion of interface. *J. Comput. Multiphase Flow*, 6:11–126, 2014.